



HAL
open science

Mechanisms of hollow-fiber membrane fouling removal used in water treatment : critical backwash fluxes and membrane deformation for an enhanced backwash efficiency

Thomas Vroman

► **To cite this version:**

Thomas Vroman. Mechanisms of hollow-fiber membrane fouling removal used in water treatment : critical backwash fluxes and membrane deformation for an enhanced backwash efficiency. Polymers. Université Paul Sabatier - Toulouse III, 2020. English. NNT : 2020TOU30013 . tel-02978055

HAL Id: tel-02978055

<https://theses.hal.science/tel-02978055>

Submitted on 26 Oct 2020

HAL is a multi-disciplinary open access archive for the deposit and dissemination of scientific research documents, whether they are published or not. The documents may come from teaching and research institutions in France or abroad, or from public or private research centers.

L'archive ouverte pluridisciplinaire **HAL**, est destinée au dépôt et à la diffusion de documents scientifiques de niveau recherche, publiés ou non, émanant des établissements d'enseignement et de recherche français ou étrangers, des laboratoires publics ou privés.



THÈSE

En vue de **l'obtention** du
DOCTORAT DE L'UNIVERSITÉ DE TOULOUSE

Délivré par l'Université Toulouse 3 - Paul Sabatier

Présentée et soutenue par
Thomas VROMAN

Le 16 mars 2020

Mécanismes de décolmatage de membranes fibres creuses en traitement des eaux: Flux critique de rétrolavage et déformation de la membrane pour une amélioration de l'efficacité du rétrolavage

Ecole doctorale : MEGEP - Mécanique, Energétique, Génie civil, Procédés

Spécialité : Génie des Procédés et de l'Environnement

Unité de recherche :

LGC - Laboratoire de Génie Chimique

Thèse dirigée par

M. Jean-Christophe REMIGY - Professeur, LGC, Université de Toulouse

Jury

Mme Murielle RABILLER-BAUDRY - Professeur, ISCR, Université de Rennes (Rapporteur)

M. Philippe MOULIN - Professeur, Aix-Marseille Université (Rapporteur)

M. Marc HERAN - Professeur, IEM, Université de Montpellier (Examinateur)

M. Patrice BACCHIN - Professeur, LGC, Université de Toulouse (Examinateur)

Mme Christelle GUIGUI - Professeur, TBI, INSA Toulouse (Examinateur)

M. Jean-Christophe REMIGY - Professeur, LGC, Université de Toulouse (Directeur de thèse)

M. François BEAUME - Ingénieur, Arkema (Membre invité)



THESIS

Submitted in fulfilment of the
requirements for the degree of
**DOCTOR OF PHILOSOPHY OF THE
UNIVERSITY OF TOULOUSE**

Issued by the University of Toulouse 3 - Paul Sabatier

Presented and defended by

Thomas VROMAN

On 16 March 2020

Mechanisms of hollow-fiber membrane fouling removal used in
water treatment: Critical backwash fluxes and membrane
deformation for an enhanced backwash efficiency

Doctoral School : MEGEP - Mechanics, Energetics, Civil and Process Engineering

Speciality : Process and Environmental Engineering

Research unit :

LGC – Chemical Engineering Laboratory

Thesis directed by

Mr. Jean-Christophe REMIGY – Professor, LGC, University of Toulouse

Jury

Ms. Murielle RABILLER-BAUDRY – Professor, ISCR, University of Rennes (Rapporteur)

Mr. Philippe MOULIN – Professor, Aix-Marseille University (Rapporteur)

Mr. Marc HERAN – Professor, IEM, University of Montpellier (Examinator)

Mr. Patrice BACCHIN – Professor, LGC, University of Toulouse (Examinator)

Ms. Christelle GUIGUI – Professor, TBI, INSA Toulouse (Examinator)

Mr. Jean-Christophe REMIGY – Professor, LGC, University of Toulouse (Thesis director)

Mr. François BEAUME – Engineer, Arkema (Invited member)

Remerciements

Je tiens à remercier toutes les personnes qui ont rendu ce travail possible ainsi que celles qui m'ont soutenu pendant ces trois années de thèse et qui m'ont permis de vivre une expérience professionnelle et sociale inoubliable.

Dans un premier temps je remercie le Laboratoire de Génie Chimique qui m'a très bien accueilli ainsi que l'entreprise Arkema et l'ANRT qui ont financé ce projet CIFRE.

Je souhaite remercier les membres du jury de thèse, Murielle Rabiller-Baudry et Philippe Moulin qui ont rapporté ce travail ainsi que les examinateurs Marc Heran, Patrice Bacchin et Christelle Guigui. Cette soutenance défendue dans des circonstances exceptionnelles, en huis-clos, restera gravée dans ma mémoire. Je remercie tout particulièrement mon directeur de thèse Jean-Christophe Remigy et le directeur du laboratoire Pierre Aimar qui ont autorisé et permis le maintien de cette soutenance dans les meilleures conditions malgré l'épidémie COVID19.

Mes remerciements vont à mon directeur de thèse, Jean-Christophe, pour toutes ces discussions scientifiques très intéressantes et ses précieux conseils. En plus d'un apport scientifique, Jean-Christophe m'a toujours soutenu dans les moments difficiles de la thèse. Je remercie également Samuel Devisme et particulièrement François Beaume d'Arkema pour leur intérêt dans ce projet, et leurs remarques très enrichissantes.

Je souhaite également remercier le personnel du laboratoire : Jean-Christophe Rouch qui m'a formé dans les premiers mois à la fabrication des membranes et modules, Sandrine Desclaux qui est toujours là pour aider à résoudre les problèmes et pour les moments de discussion sympathiques, Sébastien Gaspard et Patrick Colombies pour l'aide au filage des membranes. Je remercie également les permanents du département GIMD pour les discussions intéressantes. Des personnes du site de Labège ont également contribué à ce projet : Gwénaëlle Guittier pour les mesures de porosimétrie, Marie-Line De Solan pour la formation microscopie et Lahcen Farhi et Quentin Ribière pour l'aide apportée sur le pilote de filtration. Je remercie Nicolas du Fablab pour l'aide à la modélisation 3D de la cellule de filtration et Vincent Loisel pour les finitions sur les modules. Egalement Le LAAS et en particulier Etienne Dague pour les mesures AFM. J'exprime également ma profonde gratitude à Valentine et Emilie, stagiaires de Master, qui ont fortement contribué aux

résultats expérimentaux et à la réussite de ce projet. Je remercie également Soufiane pour son travail de modélisation.

Dans un second temps je souhaite remercier toutes les personnes avec qui j'ai partagé de bons moments au laboratoire, des fous rires, des pauses repas et cafés mais aussi tous mes amis à Toulouse ou aux quatre coins de la France. Les doctorants et récents docteurs : Julien C., Nabiil, Julien P., Charaf, Yin, Pritam, Vincent, Lisa, Cecilia, Fatma, Christophe, Johanne, Guillaume, Jesus, Michelle, Yohann, Margot. Merci à mes collègues de bureau : Paul mon ancien collègue du MHT, qui est devenu mon ami et m'a intégré dans son cercle d'amis Toulousains. Chams qui a toujours été bienveillante avec moi. Chloé pas vraiment du bureau mais toujours là pour les pauses cafés pleines de potins. Ranine qui m'a toujours soutenu et était de mon côté face à Dihia ^^ Dihia qui est toujours là pour discuter, rigoler et m'aider dès que j'en ai besoin, et avec qui je me suis lié d'amitié « Sérieux ?! » oui oui ^^ « N'importe quoi ! ». Je n'oublie pas les anciens : Arthur, Paul et Clément mes compères de sorties aux bars, concerts et week-ends. Melissa et Pierre mes amis, Melissa, toi qui es restée pendant ma troisième année et devenue ma partenaire de café, confidences et semi-marathon, merci pour tout, besos. Ce fut également un plaisir de faire partie de l'asso des doctorants « l'Alambic », on a quand même passé de supers moments en particulier avec Lauren, Lucas, Marco et Claire. Claire ma grande pote de soirée et de week-end dans les Pyrénées mais aussi une personne rassurante sur qui on peut compter avec le cœur sur la main.

J'ai une pensée pour mes amis de toujours, mes amis d'enfance « Les Dix », celles de prépa Amandine et Faustine, ma besta Marie, mes potos de Belgique, mes amis d'école d'ingé et ceux que je me suis fait à Toulouse, Amélie & Nico, Andréa, Lancelot & Laura je vous adore.

Mes remerciements s'adressent à ma famille qui m'a toujours encouragé et cru en moi, en particulier à mes grands-parents, mes parents, mon frère et ma sœur que j'aime profondément. Ma mère qui est toujours là pour me remonter le moral et qui se soucie beaucoup trop de notre bien-être et ma sœur qui a toujours la blague pour faire rire, indispensable pour passer une bonne soirée.

Enfin pour conclure je remercie Jonathan qui m'accompagne depuis le premier jour de ma thèse et me soutient au quotidien. Merci d'avoir été là dans les épreuves et dans les bons moments parsemés de voyages et week-ends.

Merci à vous tous !

Abstract

Kynar® PVDF ultrafiltration hollow fiber membranes with various properties (permeability and mechanical properties) were selected for the study of fouling removal mechanisms in the case of model suspension filtrations (bentonite and humic acid cake). The aim of this project is to improve backwash efficiency by optimizing materials and operating conditions for an energy-efficient backwash process.

The deformation of the external surface of the hollow fiber during pressure operations was measured under camera. The deformation, which can reach 15% during backwash, was numerically calculated using a mechanical deformation model of a thick-walled cylinder under pressure.

The experimental study of the bentonite cake removal percentage, as a function of backwash pressure and the different membranes or feed suspension, showed the existence of a critical backwash flux from which the backwash reached its maximal efficiency. However, detachment of humic acid cake, which is more adherent and causes irreversible fouling, is not affected by the backwash flux but seems to be affected by the strong deformation of external surface of the hollow-fiber (>10%). Mechanisms of cake removal during backwash are therefore linked to the mechanical stresses (normal and shear stress) acting at the cake-membrane interface.

Résumé

Des membranes fibres creuses d'ultrafiltration Kynar® PVDF possédant diverses caractéristiques (perméabilité et propriétés mécaniques) ont été sélectionnées pour étudier les mécanismes de décolmatage dans le cas de filtration de suspensions modèles (dépôt de bentonite ou d'acide humique). L'objectif de ce travail est d'améliorer l'efficacité du rétrolavage en optimisant les matériaux et les conditions opératoires dans le but de réduire le coût énergétique de cette opération.

Des mesures expérimentales sous caméra ont permis d'étudier la déformation de la surface externe des fibres creuses lors des opérations sous pression. Ces déformations qui peuvent atteindre 15% lors des étapes de rétrolavage ont été modélisées par la déformation mécanique d'un tube cylindrique à paroi épaisse sous pression.

L'étude expérimentale du taux d'élimination de dépôt de bentonite, fonction de la pression de rétrolavage et des différentes membranes ou suspension filtrée, a permis de montrer l'existence d'un flux critique de rétrolavage pour lequel l'efficacité maximum est atteinte. En revanche, le détachement des dépôts d'acide humique qui sont plus adhérent et responsable d'un colmatage irréversible, n'est pas impacté par le flux de rétrolavage mais semble être affecté par la forte déformation (>10%) de surface externe de la fibre. Les mécanismes de décolmatage des dépôts lors du rétrolavage sont donc liés aux contraintes mécaniques (contrainte normale et de cisaillement) s'exerçant à l'interface dépôt-membrane.

Contents

NOMENCLATURE	8
GENERAL INTRODUCTION	18
CHAPTER 1 - LITERATURE STUDY	24
1.1 Membrane filtration	26
1.1.1 Membrane market	26
1.1.2 Inorganic membranes	26
1.1.3 Polymeric membranes	26
1.2 Membrane preparation by phase inversion	27
1.2.1 Dope preparation	28
1.2.2 Phase separation	28
1.2.3 Membrane morphology	30
1.2.4 Membrane properties	32
1.2.5 Conclusion	35
1.3 Ultrafiltration of particle suspension.....	35
1.3.1 Filtration mode.....	36
1.3.2 Fouling.....	38
1.3.3 Limiting fouling.....	41
1.3.4 Conclusion	45
1.4 Membrane cleaning	45
1.4.1 Physical cleaning	46
1.4.2 Chemical cleaning	51
1.4.3 Innovative physical cleaning approach: Membrane deformation	52
1.4.4 Conclusion	57
1.5 Fouling/fouling removal characterization methods	57
1.5.1 Backwash efficiency evaluation	58
1.5.2 Observation techniques for fouling/fouling removal analysis on hollow-fiber membranes	59
1.5.3 Conclusion	64

1.6	General conclusion.....	65
CHAPTER 2 - MATERIALS AND METHODS.....		66
2.1	Materials	68
2.1.1	Polymers.....	68
2.1.2	Solvents.....	68
2.1.3	Inorganic salts.....	68
2.1.4	Particles	69
2.2	Hollow-fiber membrane preparation	69
2.2.1	Dope solution and bore fluid preparation.....	69
2.2.2	Preparation of membranes by spinning and dry-wet phase inversion.....	69
2.2.3	Membrane storage	71
2.3	Experimental design.....	71
2.3.1	Filtration unit A.....	71
2.3.2	Filtration unit B.....	72
2.3.3	Filtration module/cell.....	74
2.4	Ultrafiltration of feed solutions and backwash cleaning	75
2.4.1	Feed preparation	75
2.4.2	Protocol for single filtration/backwash cycle	77
2.4.3	Protocol for several filtration/backwash cycles.....	79
2.4.4	Fouling analysis.....	80
2.4.5	Fouling removal analysis	83
2.5	Hollow-fiber membrane characterization.....	84
2.5.1	Morphology and internal structure.....	84
2.5.2	Mechanical properties.....	84
2.5.3	Ultrapure water permeability.....	87
2.5.4	Hydrophilicity	89
2.5.5	Porosity.....	89
2.5.6	Membrane deformation	89
2.6	Particle suspension characterization.....	90
2.6.1	Particle size and zeta potential analysis of model suspensions	90
2.6.2	Turbidity	90
2.6.3	Ultraviolet-visible spectroscopy.....	91
2.6.4	Analysis of wastewater feed solution.....	92
2.7	Mechanical properties of the filter cake	93
2.7.1	Camera measurement	93
2.7.2	Atomic force microscopy	93

CHAPTER 3 - PREPARATION AND CHARACTERIZATION OF PVDF HOLLOW-FIBER MEMBRANES.....	94
3.1 Introduction.....	96
3.2 Hollow-fiber membrane preparation	96
3.2.1 Dope composition and spinning process.....	96
3.2.2 Adjustment of compositions and spinning conditions to new spinning apparatus	97
3.2.3 Chlorine washing effect.....	100
3.3 Structural, mechanical and surface properties	100
3.3.1 Internal structure observation.....	101
3.3.2 Mechanical properties.....	103
3.3.3 Surface hydrophilicity.....	105
3.4 Membrane permeability	106
3.4.1 Comparison of membrane permeability	106
3.4.2 Time-dependence of the membrane permeability.....	107
3.4.3 Pressure-dependence of the membrane permeability.....	108
3.4.4 Membrane permeability during filtration and backwash process.....	109
3.5 General conclusion.....	111
CHAPTER 4 - MEMBRANE DEFORMATION UNDER PRESSURE: MODELLING AND EXPERIMENTAL STUDY	112
4.1 Introduction.....	114
4.2 Numerical model for the deformation of thick-walled cylinder.....	114
4.2.1 System definition.....	114
4.2.2 Lamé's equations.....	115
4.2.3 Model limits	120
4.2.4 Application of the model to membrane filtration	120
4.2.5 Influence of membrane properties on hollow-fiber deformation under pressure.....	121
4.2.6 Conclusion	123
4.3 In-situ observation of membrane deformation under pressure.....	124
4.3.1 Experimental deformation under external pressure	124
4.3.2 Experimental deformation under internal pressure	126
4.3.3 Conclusion	127
4.4 Model fitting	127
4.4.1 Comparison between theoretical and experimental data	127
4.4.2 Adjustment factor	128

4.4.3	Origin of the adjustment factor	130
4.4.4	Model of two-layer hollow-fiber membrane.....	131
4.4.5	Conclusion	134
4.5	Influence of the deformation on membrane properties	135
4.5.1	Elastic limit and deformation reversibility.....	135
4.5.2	Pore deformation	137
4.6	General conclusion.....	139
CHAPTER 5 - ULTRAFILTRATION OF PARTICLE SUSPENSIONS AND FOULING		
REMOVAL MECHANISMS.....		
140		
5.1	Introduction.....	142
5.2	Characterization of particle suspensions	142
5.2.1	Definitions	142
5.2.2	Influence of the ionic strength on model suspension properties	144
5.2.3	Properties of the prepared feed model solutions for ultrafiltration	148
5.3	Fouling analysis.....	150
5.3.1	Decrease of permeate flux.....	150
5.3.2	Selectivity and adsorption.....	151
5.3.3	Hydraulic resistance	154
5.3.4	Measurement of the cake thickness	160
5.3.5	Conclusions.....	162
5.4	Fouling removal analysis	163
5.4.1	Influence of the cake thickness	163
5.4.2	Study on a 17 μm thick bentonite (KCl) cake.....	165
5.4.3	Study on a 17 μm thick bentonite (CaCl_2) cake.....	168
5.4.4	Study on a 10 μm thick humic acid (CaCl_2) cake	169
5.4.1	Effect of cation valency and visual observation of cake removal	171
5.4.2	Conclusions.....	172
5.5	Fouling removal mechanisms	173
5.5.1	Existence of a critical backwash flux for bentonite filtration	173
5.5.2	Critical pressure for the detachment of bentonite cakes.....	175
5.5.3	Effect of membrane surface deformation on humic acid cake	180
5.5.4	Multiple and combined mechanisms.....	182
5.5.5	Calculation of critical strain.....	191
5.5.6	Analysis of membrane permeability on the long term in the case of humic acid filtration	192
5.5.7	Economic benefits.....	196

5.6	General conclusion.....	196
	GENERAL CONCLUSIONS AND PERSPECTIVES	200
	APPENDICES	206
	Appendix 1 Technical data sheets of Kynar® PVDF grades.....	208
	Appendix 2 Dope and bore fluid compositions and spinning operating conditions	214
	Appendix 3 Filtration cell design and hydrodynamic.....	215
	Appendix 4 Valve control for filtration of feed solutions.....	218
	Appendix 5 Pore size and pore distribution	220
	Appendix 6 Loading-unloading cycles.....	222
	Appendix 7 Estimation of the consumed energy and permeate	224
	REFERENCES.....	226

Nomenclature

Symbols

A	absorbance	-
A_0	cross-sectioned area of a cylinder	m^2
$BTMP$	backwash transmembrane pressure	bar
$BTMP_{crit}$	critical backwash transmembrane pressure	bar
C_{cake}	particle concentration in the cake	$kg.m^{-3}$
C_i	ion concentration	$mol.L^{-1}$
C_{feed}	feed particle concentration	$g.L^{-1}$
C_p	permeate particle concentration	$g.L^{-1}$
CR	cake removal amount	-
D_{ext}	hollow-fiber membrane external diameter	μm
D_{int}	hollow-fiber membrane internal diameter	μm
E	membrane Young's modulus	MPa
E_f	fouling layer Young's modulus	Pa
e_{bw}	energy consumption for a single backwash	J
E_{bw}	backwash energy released during backwash	J
$E_{bw,crit}$	critical backwash energy required for cake removal	J
e_f	energy consumption for a single filtration	J
$e_{elastic}$	stored elastic potential energy	$J.m^{-2}$
f	numerical model adjustment factor	-
F_t	tensile force	N
F	applied force	N
F_r	applied forces on wall element in the radial direction	N
G_p	permeability gain	-

ΔG_{f-s}	fouling layer-substrate adhesion energy per unit area	J.m ⁻²
ΔG_{mwf}^{AB}	AB free energy component	mJ.m ⁻²
ΔG_{mwf}^{LB}	LB free energy component	mJ.m ⁻²
ΔG_{mwf}^{Tot}	total membrane-foulant free energy of adhesion	mJ.m ⁻²
h	hollow-fiber membrane thickness	μm
h_f	fouling layer thickness	m
I	ionic strength	M
$ICMP$	inter cake-membrane pressure	bar
$ICMP_{crit}$	critical inter cake-membrane pressure	bar
J	permeate flux	L.m ⁻² .h ⁻¹
J_{bw}	backwash flux through the fouled membrane	L.m ⁻² .h ⁻¹
$J_{bw,crit}$	critical backwash flux	L.m ⁻² .h ⁻¹
k	membrane permeability	m ²
L	sample length	m
L_0	initial sample length or gauge length	m
l_p	pore length	m
Lp_0	outside-in initial membrane permeability	L.m ⁻² .h ⁻¹ .bar ⁻¹
Lp_{bw}	outside-in membrane permeability after backwash	L.m ⁻² .h ⁻¹ .bar ⁻¹
Lp_f	outside-in membrane permeability after filtration	L.m ⁻² .h ⁻¹ .bar ⁻¹
Lp_{TMP}	outside-in membrane permeability at specific TMP	L.m ⁻² .h ⁻¹ .bar ⁻¹
Lp'_{BTMP}	inside-out membrane permeability at specific BTMP	L.m ⁻² .h ⁻¹ .bar ⁻¹
Lp'_f	inside-out fouled membrane permeability	L.m ⁻² .h ⁻¹ .bar ⁻¹
m_{bw}	mass of bentonite cake collected in the backwash waters	kg
m_d	deposited mass on membrane external surface	kg

$n(r_i)$	pore number of radius r_i per membrane surface area	m^{-2}
$Norm. r_{im}$	normalized intermediate radius	-
$Norm. P_{im}$	normalized intermediate pressure	-
NTU	turbidity	NTU
P_e	external pressure	Pa
P_i	internal pressure	Pa
P_{im}	intermediate pressure	Pa
Q	flow rate	$m^3.s^{-1}$
Q_{memb}	flow rate through the membrane	$m^3.s^{-1}$
Q_{cake}	flow rate through the cake	$m^3.s^{-1}$
r_i	internal radius	m
r_e	external radius	m
r_{int}	intermediate radius	m
r_p	pore radius	m
\bar{r}_p	mean pore radius	m
R	particle retention	-
R_{TOC}	total organic carbon reduction	-
R_c	cake hydraulic resistance	$m^2.L^{-1}$
$R_{c,f}$	cake hydraulic resistance after filtration	$m^2.L^{-1}$
$R_{c,r}$	cake hydraulic resistance after rinsing	$m^2.L^{-1}$
R_D	ratio of internal diameter over external diameter	-
R_f	total fouling hydraulic resistance	$m^2.L^{-1}$
$R_{f,f}$	fouling hydraulic resistance after filtration	$m^2.L^{-1}$
$R_{f,r}$	fouling hydraulic resistance after rinsing	$m^2.L^{-1}$

R_m	outside-in membrane hydraulic resistance at specific TMP	$m^2.L^{-1}$
R'_m	inside-out membrane hydraulic resistance at specific BTMP	$m^2.L^{-1}$
R_p	membrane permeability recovery	-
R_{rev}	reversible fouling hydraulic resistance	$m^2.L^{-1}$
R_{irrev}	irreversible fouling hydraulic resistance	$m^2.L^{-1}$
S_{BET}	BET specific surface area	$m^2.g^{-1}$
S_{ext}	hollow-fiber membrane external surface	m^2
t	time	h
t_{bw}	backwash duration	h
T	temperature	$^{\circ}C$
TMP	transmembrane pressure	bar
TOC_{feed}	total organic carbon in the feed	$g.L^{-1}$
TOC_p	total organic carbon in the permeate	$g.L^{-1}$
u	radial displacement	m
V_{bw}	backwash volume	L
V_p	permeate volume	L
Vr_{LP}	inside-out permeability variation rate at specific BTMP compared to outside-in permeability at TMP=0.8 bar	-
WCA	water contact angle	$^{\circ}$
z_i	ion charge	-

Greek symbols

α	specific cake resistance	m.kg^{-1}
γ_i^{LW}	LW component of surface tension	mJ.m^{-2}
γ_i^{tot}	total surface tension	mJ.m^{-2}
γ_i^+	electron acceptor component of surface tension	mJ.m^{-2}
γ_i^-	electron donor component of surface tension	mJ.m^{-2}
δ	indentation depth	m
ε	strain	-
ε_{break}	elongation at break	-
ε_c	critical strain	-
$\varepsilon_{elastic\ limit}$	elongation at elastic limit	-
ε_θ	element elongation in the circumferential direction	-
ε_l	element elongation in the longitudinal direction	-
ε_r	element elongation in the radial direction	-
θ	half-cone angle	°
μ	water dynamic viscosity	bar.h
ν	membrane Poisson's ratio	-
ν_f	fouling layer Poisson's ratio	-
ξ	minimal residual error (least squares method)	-
σ_t	tensile stress	Pa
σ_{break}	stress at break	MPa
σ_θ	hoop or circumferential stress	MPa
σ_l	longitudinal stress	MPa
σ_r	radial stress	MPa

Abbreviations

AB	Lewis acid-base
AFM	atomic force microscopy
BET	Brunauer-Emmett-Teller
CA	cellulose acetate
CaCl ₂	calcium chloride
CEB	chemically enhanced backwash
C.C.C	critical coagulation concentration
C.C.I.S.	critical coagulation ionic strength
DMF	dimethylformamide
DMSO	dimethylsulfoxide
DLVO	Derjaguin–Landau–Verwey–Overbeek
EIPS	evaporation induced phase separation
EL	electrostatic double-layer
KCl	potassium chloride
LiCl	lithium chloride
LW	Lifshitz-van der Waals
MBR	membrane bioreactor
MF	microfiltration
M-LPX	low permeable hollow-fiber membrane with X MPa Young's modulus
M-HPX	high permeable hollow-fiber membrane with X MPa Young's modulus
NaN ₃	sodium azide
NIPS	non-solvent induced phase separation
NF	nanofiltration

NMP	N-methylpyrrolidone
NMR	nuclear magnetic resonance
NOM	natural organic matter
PAN	polyacrylonitrile
PEG	polyethylene glycol
PES	polyethersulfone
PG	1,2-propylene glycol
PMMA	polymethylmethacrylate
PSU	polysulfone
PVA	polyvinylalcohol
PVDF	polyvinylidene fluoride
PVDF-HFP	polyvinylidene-co-hexafluoropropylene
PVP	polyvinylpyrrolidone
RO	reverse osmosis
SEM	scanning electron microscopy
TIPS	thermal induced phase separation
TOC	total organic carbon
UF	ultrafiltration
VIPS	vapor induced phase separation
V _{1,2,3}	manual valve
XDLVO	extended DLVO theory

General introduction

Water treatment membranes were firstly used after the Second World War following the collapse of drinking water systems in Germany and Europe. Millipore Corporation has invested, with funding from US military, in research and development of filtration membranes for water treatment. However, industrial applications of these membranes have long been limited because of their low competitiveness: low trade-off permeability/selectivity, high cost and unreliable [1]. In the 1960's, the development of high permeability asymmetric membranes by Loeb and Sourirajan [2] was the breakthrough towards membrane industrialization for reverse osmosis and desalinization of seawater. By 1980, microfiltration (MF), ultrafiltration (UF) and reverse osmosis (RO) were sufficiently developed processes to be introduced in the global industrial market [3].

Even if membrane filtration is still experiencing a strong industrial development, fouling remains one of the major limitation in membrane filtration process. Backwash is the most conventional cleaning technique to remove the fouling layer and recover initial permeate flux. Many technological aids have been implemented in industry to improve backwash efficiency. For example, the injection of air bubbles in parallel with backwashing introduces shear stress at membrane surface which greatly helps for fouling removal [4]. Extensive works have been published on fouling, fouling mitigation and membrane cleaning [5][6][7] as shown on Figure 1. Literature study deals mainly with fouling phenomenon, however literature focusing on backwash is limited.

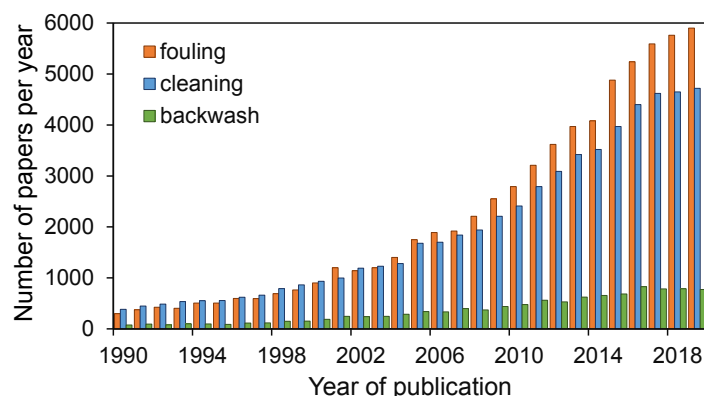


Figure 1: Evolution of number of scientific papers (articles and patents) published per year with emphasis on fouling and cleaning of ultrafiltration membranes. Data were collected between 1990 and 2019 from Google Scholar with the following searched keywords “ultrafiltration” and “membrane” with either “fouling” or “cleaning” or “backwash” (or “backflush” or “backpulse”) for each category.

Ultrafiltration in water treatment including domestic or industrial effluents, natural surface water, and seawater have been widely used to produce drinking water or recycling water for reuse in industry or release into the environment. Large efforts have been devoted to improve the permeate flux and manage fouling as membrane filtration has become a standard process for water production. The development of innovative materials and cleaning strategy is fostered by the ongoing demand of a more energy-efficient process. Moreover, limiting the environmental impacts of the whole filtration process is possible by selecting appropriate operating conditions and by reducing the need of chemical cleanings [8]. Optimization works on backwash operating conditions have been carried out, and in particular on backwash frequency, backwash duration and relaxation time to control fouling and reduce the long term decrease in permeability [9]. However, backwash pressures or fluxes are usually chosen by membrane manufacturers or industrials based on the experience [10]. Even if a few works have shown that backwash flux [11] or membrane deformation [12] might cause fouling removal, the mechanisms involved in fouling removal are not described and further investigation on the role of membrane properties is required.

The aim of this dissertation is to understand the mechanisms involved in fouling removal during the backwash process as illustrated on Figure 2. This research is a first approach to optimize materials and operating conditions for an energy-efficient backwash process.

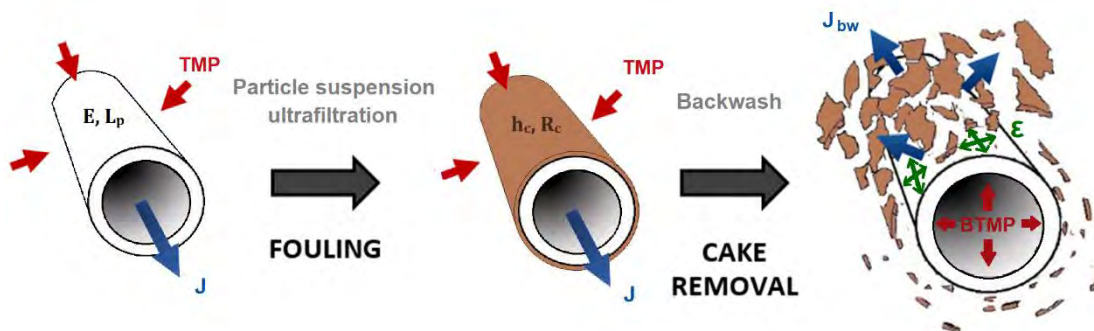


Figure 2: Schematic representation of mechanisms involved in cake removal during backwash

The first Chapter describes membrane preparation process and the mechanisms involved in particulate fouling and cake removal including a state of the art of the different physical methods for fouling mitigation and cleaning.

The second Chapter presents the materials and methods employed to evaluate membrane properties, fouling propensity and backwash efficiency.

In a third Chapter, a complete characterization of different ultrafiltration hollow-fiber membranes is provided with a focus on mechanical properties and pressure influence on membrane permeability.

The fourth Chapter presents a numerical simulation of the membrane deformation during backwash operations based on a mechanical deformation model and membrane properties. An experimental study by direct observation under digital camera is conducted to support the simulated results.

In a fifth Chapter, membrane behaviors during ultrafiltration of particle suspensions and backwash are investigated. Cake removal is analyzed through different characterization methods based on permeability measurements, mass balance and in-situ observations. Different fouling removal mechanisms related to critical parameters are exposed.

Finally, a general conclusion points out the fouling removal mechanisms and presents the positives and adverse effects of membrane elasticity during filtration and backwash process.

This research project was conducted in the Laboratoire de Génie Chimique (Toulouse) and funded by ANRT (Association Nationale Recherche Technologique) and Arkema S.A.. In this project, hollow-fiber membranes were made from Kynar® Polyvinylfluoride (PVDF) homopolymer and copolymers, marketed by Arkema. As technical specifications, the prepared ultrafiltration membranes should have high permeability and sufficient mechanical strength.

Chapter 1 - Literature study

1.1 Membrane filtration

1.1.1 Membrane market

Membrane filtration process is now used in 75% of the new water filtration facilities in the world [13]. Global membrane filtration market is estimated at \$13.5 billion in 2019 and is expected to reach \$19.6 billion in 2025 with an annual growth of 6.4% [14]. Industrial development and water quality regulations have promoted this global increase. Concerns about water scarcity and wastewater recycling will also bolster this growth for the next decades.

Membrane ultrafiltration is increasingly used for water treatment to remove suspended matter, colloidal particles, bacteria or viruses [15] from a wide range of water quality (i.e. domestic or industrial effluents, natural surface water). Two types of membrane materials have demonstrated great filtration performances described as high trade-off between permeability and selectivity: Polymeric and inorganic membranes.

1.1.2 Inorganic membranes

Most common inorganic membranes include silica, ceramic, zeolites and carbon membranes. They have found applications in harsh environment and aggressive conditions due to their excellent thermal and chemical stability. However, these materials are expensive, brittle and have a poor processability. Their use in water filtration processes have shown attracting interest but further research on membrane manufacturing and water separation mechanism is required [16].

1.1.3 Polymeric membranes

1.1.3.1 From various polymers

Membrane market for water treatment is driven by polymeric membranes mainly due to their low production cost and high filtration performances [17]. Moreover, a large number of commercial polymer materials are available for the preparation of polymeric

membranes. The choice of the appropriate polymer largely determines the ultimate membrane properties and therefore its field of application. In water treatment, hydrophilicity, permeability, fouling resistance, chemical stability, cost and durability are the main membrane properties of interest.

Most ultrafiltration membranes are made from polysulfone (PSU), polyethersulfone (PES), polyvinylidene fluoride (PVDF), polyacrylonitrile (PAN) or cellulose acetate (CA)[18]. These materials have different chemical, thermal, mechanical and surface properties.

1.1.3.2 Polyvinylidene fluoride

PVDF has become one of the most used polymer for the preparation of membrane for water treatment in recent years [18]. Indeed as a semi-crystalline polymer, PVDF has high mechanical strength withstanding pressure operations and physical cleaning steps (e.g. backwash, scouring). The degree of crystallinity of PVDF, comprised between 35% and 70%, has an impact on membrane morphology and mechanical properties [19]. Furthermore, PVDF possesses excellent thermal resistance and chemical stability, especially to chlorine agents. As chemical cleaning is an unavoidable step in filtration process, PVDF membranes demonstrates longer lifetime than most commercial polymeric membranes. PVDF is also highly compatible with other polymers (polymethylmethacrylate (PMMA), polyvinylalcohol (PVA)) increasing the variety of PVDF blend membranes and range of membrane properties [20][21]. Polyvinylidene-co-hexafluoropropylene (PVDF-HFP) copolymer has also been recently developed [22][23] in an attempt to increase membrane hydrophobicity for application in membrane contactor for example. Furthermore, PVDF and its copolymers easily dissolve in common organic solvents allowing membrane preparation by non-solvent induced phase separation detailed below.

1.2 Membrane preparation by phase inversion

Among the techniques used for membrane preparation, electrospinning [24] and particularly phase inversion [25][19] are the most common for the preparation of

ultrafiltration membranes for water treatment. Non-solvent induced phase separation (NIPS) remains though the most used technique for membrane manufacturing at industrial scale. Within the development of novel membranes, new phase inversion techniques have emerged such as thermal induced phase separation (TIPS). Indeed, some polymer blends might hardly solubilize in common solvent and TIPS is another alternative than NIPS as phase inversion process [26].

1.2.1 Dope preparation

The first step in the membrane preparation by phase inversion is to solubilize the polymer and additives in a common and good solvent (e.g. N-methylpyrrolidone (NMP), dimethylformamide (DMF) or dimethylsulfoxide (DMSO)) to obtain a homogenous dope solution. The addition of additives and pore-forming agents into the dope is essential to achieve membranes with high performances and desired properties for ultrafiltration. The role and effect of some of these compounds are described in the following section 1.2.4. The solvent choice can significantly affect the membrane morphology depending on polymer/solvent and solvent/non-solvent solubility parameters and diffusivity [27]. Furthermore, it has been observed in the case of semi-crystalline PVDF that increasing the dissolution temperature of the dope solution is decreasing the nucleation density resulting in different membrane morphology [28]. Therefore, dope solution composition and dissolution parameters have an influence on ultimate membrane properties.

1.2.2 Phase separation

Prior to phase separation, the dope solution has to be cast in tubular, flat-sheet or hollow-fiber shape. In the case of flat-sheet membrane, the dope solution is spread on a flat support (e.g. glass plate) while for hollow fiber membranes the dope is extruded through an annular spinneret to form the hollow-cylinder. Subsequently, phase separation takes place to solidify the shaped membranes.

Phase inversion consists in transforming a liquid solution to a porous solid by a demixing process. Phase separation occurs when the solubility limit of the polymer in the solvent is

exceeded. The polymer-rich phase forms then the dense matrix of the membrane while the polymer-poor phase becomes the pores after solvent elimination. The phase separation is caused either by thermal variation, evaporation, or solvent/non-solvent exchange [29][26]. The five classical phase separation processes for the preparation of ultrafiltration membranes are described below [25]:

- *Thermally Induced Phase Separation (TIPS)*: Cooling the dope solution results in a loss of solubility of the polymer in the solvent and lead to phase separation caused by thermal variation.

- *Evaporation Induced Phase Separation (EIPS)*: Dope solution initially contains non-solvent and the solvent is more volatile than the non-solvent. When leaving to evaporate, the membrane is formed by differential evaporation.

- *Vapor Induced Phase Separation (VIPS) or dry phase inversion*: Dope solution is in contact with vapor containing non-solvent (typically air). Membrane is formed by solvent/non-solvent exchange in the vapor phase.

- *Non-solvent Induced Phase Separation (NIPS) or wet phase inversion*: Dope solution is directly immersed in a coagulation bath essentially containing non-solvent (typically water). The membrane is formed by solvent/non-solvent exchanges in the liquid phase.

- *VIPS/NIPS or dry/wet phase inversion*: Dope solution is first exposed to vapor for a given time and then immersed in a coagulation bath of non-solvent to complete phase inversion. The membrane is formed by solvent/non-solvent exchanges (in vapor and liquid phase).

In general, phase inversion is governed by liquid-liquid demixing and is called instantaneous demixing for rapid separation kinetics or delayed demixing for slow kinetics. However, for semi-crystalline polymers (e.g. PVDF), the phase inversion process is governed by both liquid-liquid demixing and solid-liquid demixing (i.e. crystallization). Depending on the operating conditions and composition of dope and bore fluid, one mechanism could dominate another [30][31][19].

The dry/wet phase inversion process has been extensively used to prepare PVDF membranes [32][33][22]. Hollow-fiber membrane are prepared by spinning. A bore fluid composed of non-solvent or a mixture of solvent and non-solvent is co-extruded with the dope solution to maintain the tubular shape of the fiber. The nascent spun hollow-fiber

membrane is subsequently immersed into the coagulation bath composed of non-solvent where phase immersion takes place.

1.2.3 Membrane morphology

1.2.3.1 Asymmetric membrane structure

While symmetric membrane have a homogenous porous structure with uniform pore size, asymmetric membranes consist of a thin selective active layer called the skin onto a support sublayer of greater thickness (Figure 3). Differences in membrane density and morphology through the membrane wall is explained by a varying solution composition within the wall during the phase inversion process. Indeed, rapid solvent/non-solvent exchanges are taking place on the external surface of the nascent membrane as it is in first and direct contact with the non-solvent leading to the formation of a skin layer. Secondly, exchanges are controlled by diffusion of the non-solvent within the membrane wall forming the porous sub-layer.

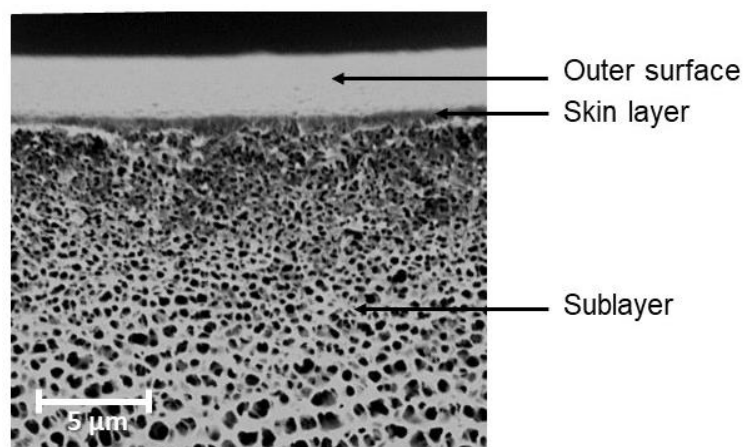


Figure 3: Cross-sectional SEM pictures of asymmetric PVDF ultrafiltration membrane.

1.2.3.2 Skin layer

The skin layer presents the smallest pores and acts therefore as the selective barrier. Membrane selectivity and permeability are thus governed by the skin layer. Its thickness depends on the phase separation process used (dry, wet, dry/wet) and might affect the membrane permeability. Dry/wet phase inversion process forms a very thin selective

layer of a few hundred nanometers [29][34]. In the case of hollow-fiber membranes, an inner skin layer may form if the bore fluid contains a high concentration of non-solvent.

1.2.3.3 Porous sublayer

The morphology of the sublayer extremely depends on the chemical composition and operating parameters. The structure of the inner morphology may influence mass transfer or mechanical properties of the membrane. As observed on Figure 4, they are different types of structures that are described below:

Sponge-like or cellular structure: Microporous sublayer formed by an interconnected network of regular pores of the order of a few microns (Figure 4, a). An enlargement of the pore size is observed with an increase in the distance from the outer and inner skin as observed on Figure 3.

Spherulitic or globular structure: Sublayer composed of packed uniform spheres or globules of micrometric size (Figure 4, b). The polymer has to be crystalline or semi-crystalline.

Macroporous structure: A sponge-like or spherulitic structure comprising a plurality of macrovoids (Figure 4, b and c). Macrovoids are big pores 100 to 1000 times larger than the selective pores of the skin layer. Structure with elongated macrovoids is also called *finger-like structure* (Figure 4, d).

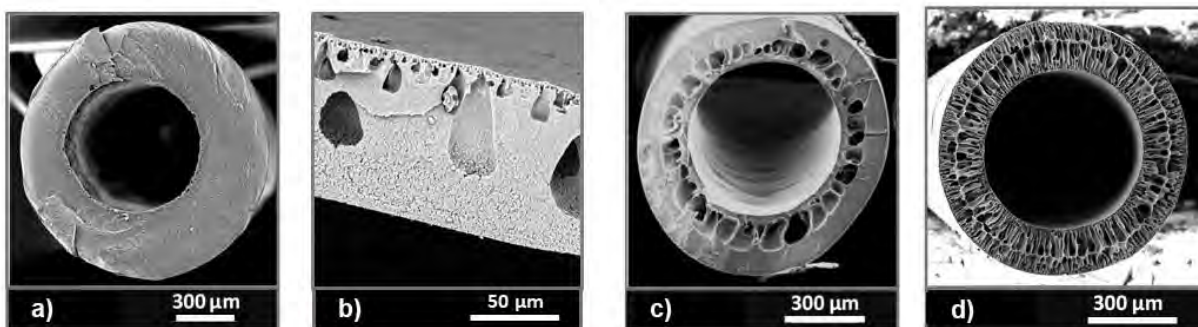


Figure 4: Various porous sublayer structures of ultrafiltration membranes. Structure: a) sponge-like; b) macroporous & spherulitic; c) macroporous & sponge-like; d) finger-like.

As PVDF is a semi-crystalline polymer, mixed cellular and spherulitic structures can be observed within the membrane wall [31]. PVDF membranes with a spherulitic

morphology are generally symmetrical and consist of a mixture of crystalline phase α and β [19].

1.2.4 Membrane properties

Membrane structure and properties are strongly dependent on the operating conditions during membrane preparation (e.g. temperatures, flow rates) and the chemical composition (solvent, polymers and additives) as all these parameters control the thermodynamics and the kinetics of phase inversion [35][30][31][19] [33]. In this section, the influence of some chemical compositions and some operating conditions on PVDF membrane permeability and mechanical properties is described. However, it is difficult to extrapolate these results to other polymers or other conditions than the one described.

1.2.4.1 Membrane hydrophilicity, permeability and selectivity

PVDF membranes are generally less hydrophilic than conventional polymeric membranes (PSU, PES or CA) as indicated by the water contact angle (WCA) found in the literature [36]–[39]. Increasing the hydrophilicity is generally associated with increasing the membrane permeability and the anti-fouling properties [40][41], therefore the permeate flux. Therefore, efforts have been made to improve PVDF hydrophilicity in order to compete with other polymeric membranes.

Table 1: Range of water contact angle for pristine membranes made from usual polymers

Membrane type	WCA (°)
PVDF	80-90
PSU	60-70
PES	50-70
CA	60-70

The contact angle is highly dependent of additives used during manufacturing of PVDF membranes as demonstrated by the measurement on different commercial PVDF

membranes (WCA=18° [42] for *Siemens* PVDF hollow-fiber or WCA= 65° for *Sepro* PVDF membrane [43]).

Tang *et al.* [32] have found that PVDF membrane permeability was firstly controlled by the concentration of polymer and additives and, to a lesser extent, by operating parameters. They have found that increasing the amount of polymer in the dope reduced the mass transfer properties. Several additives (e.g. polymer, surfactant, inorganic salt or filler) are added to the dope during membrane preparation in order improve the membrane properties and especially its permeability. Polyvinylpyrrolidone (PVP) and polyethylene glycol (PEG) are commonly used as pore-former additives in the preparation of PVDF membranes since they have shown significant enhancement of membrane hydrophilicity and permeability [40][23][44]. Wang *et al.* [33] have observed higher permeability and selectivity when adding low molecular weight PVP compared to high molecular weight PVP since lower molecular weight PVP are more prone to leach out from the membrane promoting permeability enhancement. Due to PVP leaching, membrane permeability might be not stable during use [45]. Membrane can therefore be intensively washed with a concentrated sodium hypochlorite solution after spinning to finalize the membrane preparation and obtain a stable membrane permeability. Soaking the membrane into hypochlorite solution contributed to a fast leaching out of PVP molecules from the membrane due to PVP degradation [46]. This soaking into hypochlorite allowed a strong increase of the ultrapure water membrane permeability [47][48] with possible pore size enlargement and increase in surface hydrophobicity [49] as adverse effects.

Lithium chloride (LiCl) has been largely used as inorganic salt additive for the preparation of membranes as it contributes to increase membrane permeability and selectivity [50][51]. However, its effect on membrane properties depends on its concentration in the dope and on the PVDF grade [52]. Other inorganic salts have been employed to improve hydrophilicity and membrane permeability. Membrane permeability was thus multiplied by 8 when adding 4 wt% of ferrous chloride without significant change in selectivity [53].

Regarding the solvent choice in the dope solution, Bottino *et al.* [27] have shown that replacing NMP by DMSO increases twice the permeability. Khayet *et al.* [54][55] have observed a significant enhancement of membrane permeability with adding non-solvent (water or 1,2-ethanediol) in a range of 2-8 wt.% into the dope solution. However, this

increase was accompanied by an increase in membrane pore size and therefore a decrease in selectivity.

Operating conditions during PVDF hollow-fiber membrane spinning have also been investigated as further membrane permeability enhancers. Khayet *et al.* [56] have observed a decrease of membrane permeability associated with an increase of solute rejection when increasing the air gap (distance between spinneret exit and coagulation bath). They explained that increasing the air gap induced more molecular chain orientation and chain package causing this decrease in permeability. Tang *et al.* [32] have found that decreasing the PVDF dope flow rate (shear stress in the spinneret) and increasing the take-up speed improved the mass transfer properties. Indeed, increasing dope flow rate results in higher shear stress in the spinneret inducing more molecular chain orientation and chain package. Therefore, a denser skin with lower permeability is formed under higher dope flow rate. Regarding the influence of take-up speed, they explained that accelerated phase inversion might result in porosity increase.

1.2.4.2 Mechanical properties

The grade of PVDF [57] and the composition of the dope or external coagulant [30] (concentration and additives) strongly influence the mechanical properties of the spun PVDF fiber. Shi *et al.* [51] observed a strong increase of the Young's modulus when adding LiCl to the PVDF dope. The Young's modulus of the spun fiber increased from 60 MPa for pure PVDF-HFP hollow-fiber membrane to 83 MPa and 118 MPa for PVDF-HFP with 2 wt.% LiCl and with 4 wt.% LiCl respectively. On the contrary, the addition of PVP into the PVDF-HFP dope resulted in a decrease of the tensile stress at break and Young's modulus of the spun hollow-fiber [22]. The Young's modulus of the spun hollow-fiber decreased from 60 to 40 MPa and 50 MPa when adding 5 wt.% and 10 wt.% PVP in the dope respectively. Wang *et al.* [58] also observed a decrease of the Young's modulus of pure Kynar® HSV 900 hollow-fiber membrane from 63 MPa to 24 MPa when adding 10 wt.% of PEG to the dope solution.

The degree of crystallinity of the forming PVDF membrane can vary during the process of membrane fabrication. Lin *et al.* [28] observed lower membrane mechanical properties when increasing the dissolution temperature of the dope solution. Furthermore, spinning

operating conditions (i.e. temperature [19], take-up speed [32] or shear stress in the spinneret [59]) affect the morphology and membrane crystallinity, which have a direct impact on the mechanical properties of the spun hollow-fiber [19].

1.2.5 Conclusion

A multitude of factors and parameters during the membrane preparation are affecting final PVDF membrane morphology and properties. Moreover, preparation of hollow-fiber membranes is even more complex than flat-sheet membranes due to additional parameters (e.g. bore fluid, stretch-speed ratio, air gap). Literature review on the effect of chemical composition and operating parameters on final membrane properties have revealed some driving parameters and key additives to improve membrane permeability and modify mechanical properties. However, prediction of ultimate properties remains a challenge in hollow-fiber membranes prepared by phase inversion.

In this work, membrane permeability and mechanical properties were the main properties of interest. Preparation of membrane was focused on different existing formulations of various PVDF grades and additives with adjustments on the operating conditions to achieve membranes with desired properties.

1.3 Ultrafiltration of particle suspension

Membrane filtration process is a separation technique based on a driving force where the membrane layer acts as a physical barrier retaining molecules depending on their size, characteristics, or affinity with the polymer matrix. Transmembrane pressure gradient is the most common driving force and is used in reverse osmosis (RO), nanofiltration (NF), ultrafiltration (UF) and microfiltration (MF). However, the separation process may be based on different driving forces such as electrical potential gradient (e.g. electrodialysis) or concentration gradient (e.g. dialysis, hemodialysis or pervaporation).

Pressure-driven membrane filtration processes are classified based on membrane pore size and the range of pressure used [60][61].

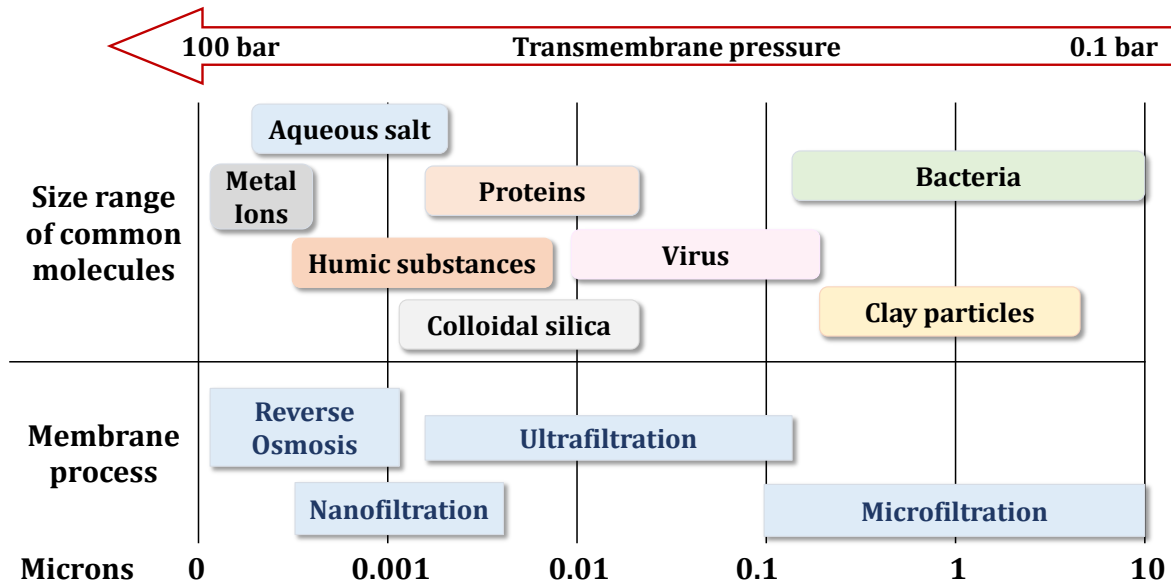


Figure 5: Classification of membrane processes and common molecules based on their size.

Ultrafiltration is the main energy-efficient process for water treatment as virus and bacteria are fully retained by the membrane at lower transmembrane pressure than nanofiltration or reverse osmosis. Particle suspensions (clay, silica or humic acid) are retained or partially retained by UF membranes as shown on Figure 5.

1.3.1 Filtration mode

In this research, the pressure-driven pressure was operated at constant pressure, in dead-end filtration and outside-in hollow-fiber modules.

1.3.1.1 Constant pressure/permeate flux

Pressure-driven membrane processes can be operated at constant transmembrane pressure (TMP) or constant permeate flux. At constant pressure, the permeate flux is decreasing through filtration time due to fouling whereas at constant filtration flux, the TMP is increasing. Wetterau *et al.* [62] have demonstrated that neither mode showed higher filtration performances. Therefore, the filtration mode depends more on the experimental design or operator's choice. Industrials tend to operate water treatment plants at constant flux to maintain a constant production rate of treated water.

1.3.1.2 Dead-end/cross-flow filtration

Depending on the feed quality (e.g. particle type and concentration) or experimental design, the filtration is operating in dead-end or cross-flow filtration mode.

In dead-end mode, the flow is perpendicular to the membrane surface and the entire feed solution is passing through the membrane (see Figure 6). Foulant materials are therefore directly accumulated on the membrane surface leading to rapid pressure increase (at constant permeate flux) or permeate flux fall (at constant pressure). Nevertheless, this filtration mode is often chosen because of its ease of implementation.

In cross-flow mode, the feed solution passes tangentially along the membrane surface (see Figure 7). Under pressure, a proportion of the feed is passing through the membrane surface (permeate) while particles larger than the pores are retained on the feed side (retentate) and usually recirculated. In cross-flow filtration, the tangential flow creates a shearing effect limiting the deposit growth.

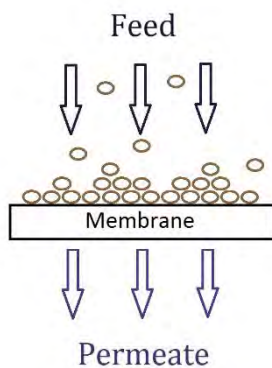


Figure 6: Dead-end filtration mode

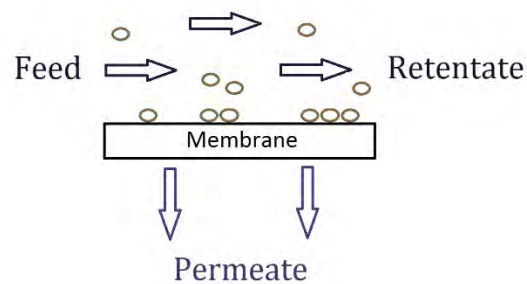


Figure 7: Cross-flow filtration mode

1.3.1.3 Inside-out/outside-in

In the case of hollow-fiber membrane, an additional filtration mode is involved. Indeed, the filtration can be conducted in outside-in or inside-out mode.

In inside-out mode, the filtration flow is circulating from the center of the fiber (lumen) to the outside of the fiber where permeate is collected.

In outside-in mode, feed solution passes from the external side of the fiber through the membrane to the inner lumen where permeate is collected. Xu *et al.* [63] have

demonstrated that outside-in mode showed higher performances for seawater desalination pretreatment than outside-in mode. Introduction of air bubbles helps to reduce or eliminate fouling in outside-in mode. Furthermore, in outside-in mode, the membrane surface area is higher and the lumen cannot be clogged by particles [64].

1.3.2 Fouling

Fouling is unavoidable during filtration and remains one of the most challenging issue in membrane filtration. During filtration of particle suspension at constant pressure, the permeate flux is decreasing due to the hydraulic fouling resistance developed at the membrane surface or within the membrane pores. Fouling is highly dependent on the water quality of the feed (e.g. particle nature, size and concentration, pH and ionic strength).

1.3.2.1 Fouling mechanisms

In water ultrafiltration, combined fouling mechanisms appear simultaneously causing a decrease of membrane permeability. They are several fouling mechanisms described in the literature [64][65]:

1) Particle deposition on membrane surface

As the membrane acts as a selective barrier retaining the particles larger than the pores, the local concentration of particles at the surface increases. When their limit of solubility or gel concentration is reached, the particles precipitate or form a gel resulting in the gradual formation of a filter cake. This cake deposition is usually the fouling mechanism that contributes the most to the additional hydraulic resistance and therefore the loss of permeability.

2) Blockage of membrane pores

Particles can partially or fully block the pores of the membrane either at the membrane surface or within the pores if the size of the pores is close to the particle size.

3) *Adsorption on membrane surface*

The adsorption of a solute on the membrane surface highly depends on the affinity and interactions between the molecules and membrane material. Adsorption is also related to exposure time and particle concentration and contributes to the fouling hydraulic resistance especially on the long-term. Adsorption can also be accentuated due the concentration of polarization at the membrane surface that shifts the concentration equilibrium [66].

4) *Pore constriction*

Pore constriction is due to the adsorption of small molecules within the pores reducing the apparent pore size. It occurs when the molecules are sufficiently small to penetrate through the membrane but large enough to constrict the pores when adsorbed in pores.

5) *Biofilm growth*

The development of microorganisms on the membrane surface forms a biofilm with low permeability and strongly adhered to the surface. As biofilm generally grows slowly, membrane permeability is slightly affected on the short-term. However, on the long term biofouling becomes a strong issue and causes significant permeability loss.

These fouling mechanisms make different contributions to the flux decline during filtration at constant pressure and act at different time scales. The degree of reversibility of fouling depends on the interactions between the foulant and the membrane. Reversible fouling is a term used to refer to fouling which is removed by physical cleaning whereas irreversible fouling refers to fouling which requires chemical cleaning to be eliminated.

1.3.2.2 Fouling behavior of typical foulant materials

Foulant materials may also be classified according to their nature and characteristics [67][68][64], the main categories are:

- *Inorganic particles*: Inorganic particles (clay particles) usually form a hydraulically reversible cake on the surface. Blockage of the pores occur for particles with similar size of the membrane pores and may be hydraulically reversible.

- *Natural Organic matter (NOM)*: Colloidal particles (humic substances, proteins) adsorb on the membrane surface and within the pores typically resulting in irreversible fouling. They also form a cake/gel on the membrane surface.
- *Microorganisms*: Microorganisms (bacteria, algae or fungi) develop a biofilm at the membrane surface with a strong adherence usually causing irreversible biofouling.

However, these fouling behaviors are also dependent of the chemical composition of feed water and especially of pH and ionic strength. Indeed, the addition of a bivalent cation such as calcium ion, will strongly modify the properties of the cake and even affect the fouling reversibility [69]. Yoon *et al.* [70] and Hong and Elimelech [71] have studied the influence of ionic strength, pH and calcium ion concentration on fouling propensity of humic substances. They demonstrated that calcium ion has a bridging effect between acidic functional groups of humic acids. This complexation reduces the negative charge of the NOM macromolecules and therefore increases the adsorption and deposition of humic acid. Yoon *et al.* [70] have shown that increasing pH led to an increase of repulsive forces between humic acid particles and fouled membrane, reducing fouling propensity. On the other hand, increasing pH increases bridging effect between humic acid and therefore adsorption and fouling. Hong and Elimelech [71] have shown that increasing the ionic strength of the humic acid feed solution resulted in higher fouling hydraulic resistance and denser cake. Compact layer is possible as high ionic strength decreases the interchain electrostatic repulsion leading to coiled humic macromolecules. They proposed a schematic representation of the influence of the chemical composition on the NOM fouling cake layer (Figure 8).

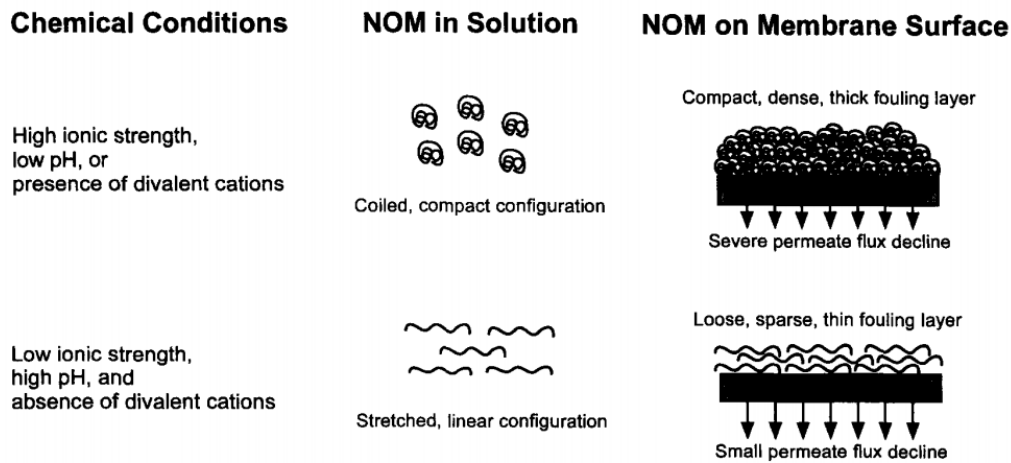


Figure 8: Schematic representation of the influence of the chemical composition on the NOM fouling cake layer, adapted from [71].

The effect of calcium ion is not limited to NOM and binding effect might also be observed on clay particles [72]. However, even in filtration conditions less prone to fouling, high permeate flux is leading to severe NOM fouling suggesting a balance between hydrodynamic and feed electrostatic interactions [71].

1.3.3 Limiting fouling

Preventive solutions to limit fouling have been developed and implemented in water treatment. Optimization of the operating conditions and membrane materials can indeed drastically reduce fouling.

1.3.3.1 Shearing effect at membrane surface

Many methods and technologies have been implemented to modify the flow near the membrane surface in order to create shear stress. As explained in 1.3.1, cross-flow filtration mode limits the deposition of particle due to the applied tangential flow to the membrane surface. Cross-flow velocity can also be increased to further reduce fouling [73][74]. The introduction of helical inserts [75] or feed spacers [76] are also implemented to create turbulent flow near the membrane and prevent the build-up of particulate cake or foulant concentrations.

The introduction of an external media (particles or gas) in the filtration module in order to promote the shearing effect at membrane surface has also shown high performances in fouling control. Gas bubbling inside or outside of hollow-fiber membranes (on feed side) generates transient shear profiles along membrane surface [77][78]. Air sparging has demonstrated great improvement in permeate flux stability [79][80][81] and has found industrial applications, especially in membrane bioreactors.

The use of scouring agents has also attracted interest in fouling mitigation. Scouring agents are mainly made from polymeric materials of spherical shape and millimeter size [82]. Granular media promotes shearing at membrane surface and take away foulants from the membrane. Contrary to air bubbles, scouring media cross the laminar boundary layer and hit membrane surface causing membrane shaking, which helps to control fouling [83]. However, membrane could be damaged in inappropriate hydraulic conditions [84] or non-adapted granular media [85]. This technique involves lower energy consumption while maintaining same efficiency than other fouling control methods such as air sparging or increase in cross-flow velocity (see on Figure 9) [82].

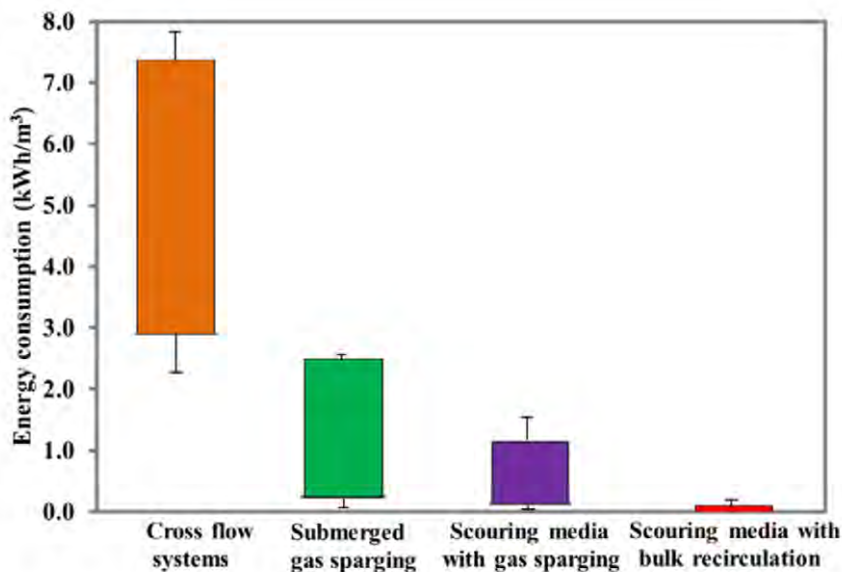


Figure 9: Comparison of energy consumption for different fouling control methods, adapted from [82].

In terms of mechanical cleaning, dynamic filtration systems have shown also their effectiveness in limiting fouling. Jaffrin *et al.* [86] compared permeate flux between rotating disk module and vibrating membrane. They found that rotating disks generated more shear rates than vibrating membrane resulting in higher permeate flux. In these systems, rotation speed and vibration amplitude have a great effect on shear rates, which

governed the permeate flux. Li *et al.* [87] demonstrated that vibrations were effectively reducing fouling beyond a critical vibration amplitude and/or frequency. They also showed that fiber looseness can increase further the permeate flux under vibrations due to the additional lateral movements and dynamic shear enhancement.

1.3.3.2 Sub-critical operating condition

One of the main strategy to control fouling and avoid permeate flux decrease is to operate the filtration at sub-critical flux [88]. In cross-flow filtration, the critical flux is the permeate flux at which fouling become noticeable. It can be defined as the transition flux between the concentration of polarization and the particle aggregation on the surface [89]. The concentration of polarization which is the boundary layer adjacent to the membrane surface where particles are concentrated can slightly affect the permeate flux but when the pressure is reduced the polarized layer is removed. Increasing the flux above the critical flux will overcome the repulsive barrier between particles and lead to permanent fouling cake layer.

The concept of critical filtered volume is similar than critical flux but applied to dead-end filtration system. As the entire feed solution is forced to pass through the membrane, there is a critical volume at which particles are aggregating and below which no fouling occurs [90].

As illustrated on Figure 10, delimited zones where fouling occurs in cross-flow or dead-end filtration can be represented for a given membrane/particle suspension solution. Critical flux and critical filtered volume are strongly dependent on hydrodynamics, feed conditions and process time.

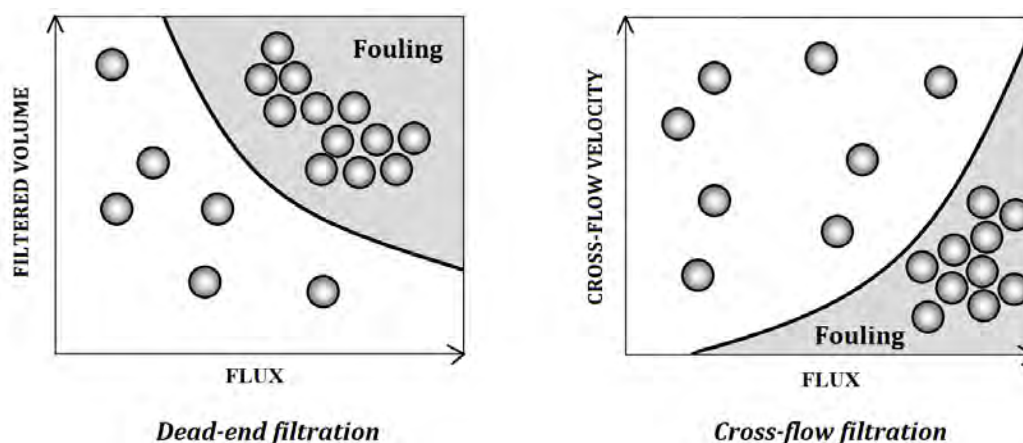


Figure 10 : Graphical representation of fouling zones in cross-flow and dead-end filtration. Adapted from [90][91].

1.3.3.3 Low-fouling membranes

Another strategy to reduce fouling is to develop low-fouling membranes. Low-fouling membranes have a surface having low adhesion or adsorption of foulants retarding fouling. Different approaches can be used to prepare low-fouling surfaces such as surface modification by grafting or coating layer or direct modification of membrane material.

Hydrophilic membranes have been largely studied for their low fouling ability and high permeate flux. Whereas hydrophobic membrane are more prone to fouling with higher wetting-resistance [41]. As PVDF is hydrophobic polymer, efforts have been devoted to make its surface more hydrophilic.

1.3.3.3.1 Modification of membrane composition

Hydrophilicity can be improved by modifying the chemical composition of the dope solution during membrane preparation by means of hydrophilic polymers [40][92] (PVP, PEG) or inorganic particles [93][94] addition. Blending with amphiphilic block copolymer has also attracting interest as it offers a stable hydrophilicity of the membrane surface [35][95][96]. Indeed, as amphiphilic block copolymer is composed of hydrophobic and hydrophilic moieties, it plays a significant role in hydrophilicity enhancement. The hydrophobic moiety presents high compatibility with the polymer matrix whereas the hydrophilic part tends to migrate to the external surface, increasing surface

hydrophilicity. This dual function prevents the amphiphilic block copolymer from leaching out.

1.3.3.3.2 Modification of surface layer

Different techniques can modify the surface and enhance hydrophilicity of membrane surface such as UV-grafting, interfacial polymerization, chemical reaction or corona treatment [97]. Hydrophilic monomers can be UV-grafted directly on membrane surface using photoinitiators on the surface or photopolymer [98][99]. Ma *et al.* have shown that the incorporation of zwitterionic monomers in the selective layer by interfacial polymerization lead to fouling-resistant RO membranes [100]. Abedi *et al.* [101] modified the surface of polyacrylonitrile hollow fiber membranes by chemical reaction with hydroxylamine forming hydrophilic groups on the surface.

1.3.4 Conclusion

Membrane fouling during ultrafiltration of particles is known to be an inherent issue in membrane filtration limiting the production of treated water. Fouling and its mechanisms have therefore been widely studied in the literature. However, predicting the fouling rate and fouling reversibility is challenging due to the complexity of the real wastewaters. Indeed, particle-particle and particle-membrane interactions strongly depend on the type of matter, water ionic strength and pH. Various methods have been employed to prevent fouling such as continuous shear stress at the membrane surface, sub-critical operating conditions or low-fouling membranes. However, membrane cleanings on the short or long-term are unavoidable.

1.4 Membrane cleaning

Due to the loss of production of treated water or the higher energy consumption, membranes are regularly cleaned. Membrane cleaning aims to recover the initial permeability of the pristine membrane without modifying the membrane material. Indeed, the cleaning step should not interfere with membrane selectivity or affect

membranes properties (i.e. mechanical, surface, permeability). Furthermore, the cleaning process has to be cost-effective and easy to implement to gain productivity. Membrane cleaning includes different techniques to eliminate each type of fouling. Physical cleaning intends to remove loosely attached foulants on membrane surfaces (reversible fouling) whereas chemical cleaning aims to eliminate strongly attached foulants (irreversible fouling). In most membrane systems, both physical and chemical cleanings are used to restore the initial flux. Typical evolution of membrane permeability with time during several filtration/cleaning cycles is represented on Figure 11.

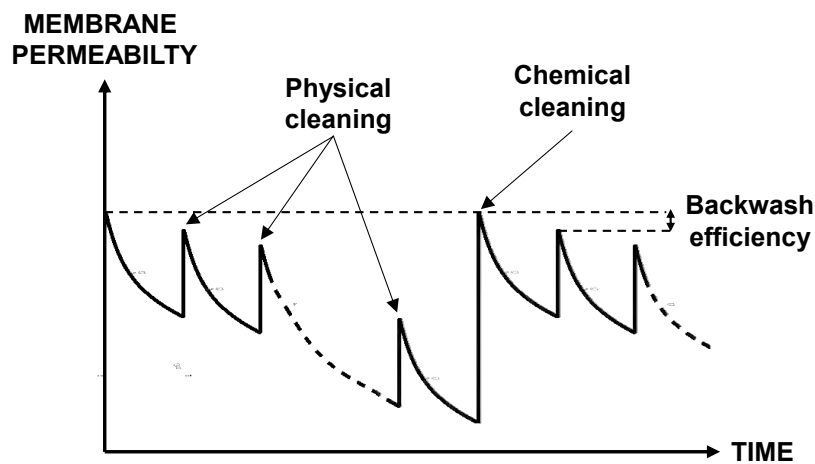


Figure 11: Representative evolution of the membrane permeability with time during several filtration/cleaning cycles.

1.4.1 Physical cleaning

Physical cleaning is performed on the short term to eliminate the reversible fouling. It is mostly based on a change of hydrodynamic to cause fouling removal. Other techniques include the application of mechanical stress or, more rarely, ultrasonic and electrical fields [102]. Some mechanisms causing the fouling removal have been mentioned in the literature but they have not been investigated in detail.

1.4.1.1 Backwash

One of the most conventional and used physical process is backwash. Backwashing consists in reversing the flow direction through the membrane, from the permeate side to

the feed side. In outside-in filtration mode, backwash pressure is thus applied on the lumen side generating a backwash flux that lifts and takes away the formed deposit from the external membrane surface and dislodge particles from the membrane pores. Backwash performances and operating conditions (i.e. frequency, duration or pressure) highly depends on the quality of the feed water [103][9]. In industry, backwash has been generally fully automated and is triggered when pressure or permeate flux reaches a set point (maximum pressure or minimum flux) according to the filtration mode (constant flux or pressure). The current strategy is to optimize backwash initiation and operating conditions to be more effective and energy-efficient [104][103]. Several studies have been carried out to improve the backwash efficiency by adjusting backwash operating parameters and backwash water composition.

Firstly, increasing the backwash duration [11] and backwash frequency [103][5] have shown evidence of backwash enhancement, especially a reduction of irreversible fouling. However, the positive impacts are generally offset by the loss of productivity due to the higher permeate consumption and loss of time during backwash. Therefore, optimization of these backwash parameters are required to have a better control on permeate flux [103][105][9].

Secondly, Huang *et al.* [106] have shown that backwash efficiency was not, or slightly, improved when increasing backwash flux for membranes fouled with natural organic matter whereas Hwang *et al.* [11] have found higher backwash efficiency for membrane fouled with PMMA particles. Remize *et al.* [107] and Ferrer *et al.* [5] have demonstrated that increasing the backwash pressure, which is related to the backwash flux by the membrane permeability, increased fouling removal. Chang *et al.* [9] compared the strength of the backwash (i.e the ratio of the backwash flux to permeate flux under constant flux, or the ratio of backwash pressure to filtration pressure under constant pressure) between different fouling removal studies and found out an optimal backwash strength between 1.5 and 2.5.

Finally, backwash performances can be directly optimized by changing the ionic strength of the water used for backwash. Replacing the ultrafiltrated permeate by demineralized water during backwash has indeed led to higher backwash efficiency whereas adding Ca^{2+} in backwash waters reduced backwash efficiency due to bridging effect of Ca^{2+} with NOM

[108][109][110]. Abrahamse *et al.* [111] have shown that irreversible fouling was increased when using backwash water with high ionic strength due to the compression of the double layer.

However, in all cases, treated water production has to be interrupted to perform the backwash. Backwashing is also a costly process due to permeate and energy requirements. In MBR, the amount of permeate used for backwash operations is evaluated between 5 and 30% of the produced permeate [112].

1.4.1.2 Air sparging

Air sparging has been described in the previous section (1.3.3.1) as fouling mitigation method. However, it is also extensively used to clean fouled membranes [113]. The preponderant fouling removal mechanism remains the shear stress generated at the membrane surface. However, studies on mechanisms are still needed as many parameters are involved [102][9]. Indeed, the membrane module [114], the duration of the process [115] and the size, velocity or direction of air bubbles [116] can greatly affect the fouling removal.

In most cases, air sparging is combined with backwash and has a key role in the enhancement of backwash efficiency [113][107]. Serra *et al.* [117] have demonstrated that backwash was improved in combination of air sparging. They showed that the duration of the rinsing step and the backwash could be shortened when using air bubbles, increasing the production rate. Bessiere *et al.* [118] compared air-assisted backwash to single phase backwash. They have shown that the additional energy consumption when using air was counterbalanced by the increase in backwash efficiency leading to energy savings on several filtration cycles. Remize *et al.* [107] have demonstrated that the percentage of particle removed was higher during air-assisted backwash than backwash alone. Furthermore, the enhancement of backwash efficiency was particularly observed on the long-term (after several filtration cycles) as shown on Figure 12 [107]. Indeed, the membrane permeability at the beginning of the cycle normalized to initial pristine membrane permeability was decreasing slower with the number of cycles for air-assisted backwash than for single-phase backwash.

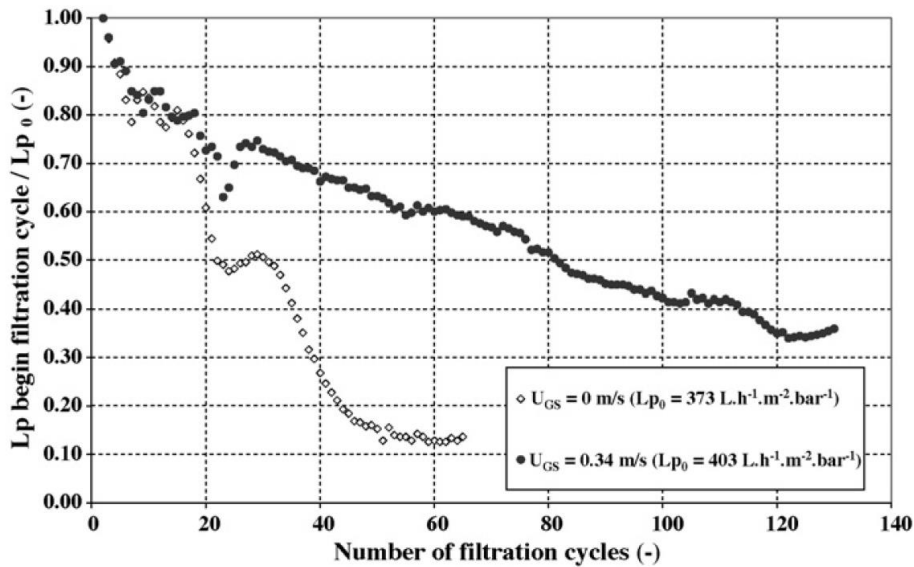


Figure 12: Membrane permeability at the beginning of the cycle normalized to initial pristine membrane permeability as a function of the number of filtration cycles for a simple backwash \diamond and for an air-assisted backwash \bullet (with U_{GS} the air velocity), adapted from [107]

1.4.1.3 Rotation

Novel physical cleaning may be based on combination of several processes to enhance shear conditions. Membrane rotation used to prevent fouling and described in 1.3.3.1, can also found applications as physical cleanings process. Indeed, Ruigómez *et al.* [119] have shown that membrane rotation combined with backwash was efficiently removing fouling cake, especially at high rotating speeds. They have also found higher backwash efficiency when combined with rotation than with gas scouring.

1.4.1.4 Relaxation and rinsing

Commonly used in membrane bioreactors, relaxation consists in stopping the filtration for a short period to allow the foulants to diffuse or be transported away from the membrane surface. Relaxation greatly contributes to permeability recovery especially when used after backwash and in synergy with other physical cleanings (e.g. air scouring or rotation) [119][120][121].

After physical cleaning, debris remain in the module and could rapidly rebuild a cake when filtrating again. Therefore, rinsing may be performed to evacuate the cake

fragments [122][118]. Feed water can be used to perform this additional cleaning step avoiding permeate loss [123].

1.4.1.5 Non-conventional techniques

Non-conventional techniques presented below have the main advantage, compared to backwash process, to be performed without interruption of the filtration process leading to time and permeate savings. However, due to complex or expensive design, process industrialization may be limited.

The use of electric field pulse as a physical cleaning technique during cross-flow ultrafiltration showed great permeate flux enhancement [124]. When applying voltage pulse, micro-bubbles may form at the cake-membrane interface causing fouling removal [125]. This innovative technique requires reasonable electrical energy and could compete with conventional cleanings. However, electrical process requires two electrodes to apply the electrical field. The membrane can be used as electrode if made from electrically conductive material (inorganic membrane or conductive polymer)[126].

Ultrasonic cleaning has also been used to clean fouled hollow-fiber membrane after ultrafiltration of clay suspension [127]. Several mechanisms that might be responsible for fouling removal when using ultrasounds have been reported by Masselin *et al.* [128]: Firstly, successive compression and rarefaction causing acoustic stress might fracture the fouling layer. Furthermore, phenomenon of acoustic cavitation, which consists in small bubble formation followed by rapid bubble collapse, may disperse aggregate. Finally, particles are dispersed in the feed stream due to turbulence generated by acoustic waves (acoustic streaming). However, ultrasounds have to be used with care and at suitable frequency since they might also cause the degradation of the membrane material [127]. Stability studies [128][129] have revealed that PVDF has greater ultrasonic resistance compared to PES membranes.

1.4.2 Chemical cleaning

Due to irreversible fouling phenomenon (e.g. adsorption, biofilm formation), the membrane permeability tends to decrease on the long term even if physical cleaning are regularly performed as observed on Figure 11.

In addition of physical cleanings, chemical cleanings are performed in an attempt to recover initial pristine membrane permeability. Chemical cleaning consists in changing the chemical composition of the solution on the feed side to degrade or solubilize foulants. Prevalent chemical agents are sodium hypochlorite that oxidizes organic foulants and citric acid that dissolves inorganic compound and chelates divalent ions [130].

Chemical cleaning is generally carried out once the membrane permeability is no longer recovered with physical cleaning. Filtration is then stopped to chemically clean and rinse the membrane. In some cases chemical cleaning is directly combined with backwash [131], called chemically enhanced backwash (CEB), chemical agents are therefore added into the backwash waters, usually at lower concentrations [9] [132].

However, strong oxidants or pH variations could also degrade the membrane material. Indeed, sodium hypochlorite can cause chain scission of polymer matrix or additives such as PVP leading to the degradation of the membrane [47][133]. A modification of the membrane surface properties could result as instance in higher fouling rate for the next filtration cycle after chemical cleaning. Membrane materials have different chemical resistances but most of them may lose their integrity during chemical cleaning process (PSU [134], PES [47][135] and PVDF [136]). Furthermore, chemical cleaning generates chemical wastes that are harmful for the environment and that require therefore a post-treatment. Indeed, sodium hypochlorite leads, for example, to the formation of toxic by-products such as absorbable organic halogen and trihalomethane compounds [137][121].

Even if chemical cleaning can eliminate irreversible fouling and allows great permeability recovery, intensive use of chemical agents have numerous adverse effects. Frequency of chemical cleanings are therefore minimized. Exploring innovative physical cleaning strategies and their effectiveness seems a viable solution to limit chemical cleanings.

1.4.3 Innovative physical cleaning approach: Membrane deformation

To the best of our knowledge, the study of mechanisms on fouling removal caused by surface deformation of filtration membrane has not been conducted yet. However, biofouling detachment caused by surface deformation have been studied in recent works.

1.4.3.1 Pore deformation for better fouling control

It has been reported in the literature that elasticity of membranes could play a role in the fouling removal during cleaning. Indeed, a few studies on microfiltration membranes [12][138][139][140] have suggested that reversible pore deformation, and particularly pore expansion, during backwash helps to dislodge clogged particles. However, measurement of pore deformation was not performed to support this assumption in the above studies.

Akhondi *et al.* [141] have focused on the measurement of pore deformation by evapoporometry [142] to understand hollow-fiber UF membrane pore deformation during filtration and backwash. According to pore-size distribution measurements, pore size was only modified during backwash where larger pores expanded while smaller pores were compressed. They firstly explained that in outside-in mode (during filtration) membrane external surface is subjected to compressive hoop stress whereas in inside-out mode (during backwash) internal surface is subjected to tensile hoop stress. Therefore, pore enlargement could only be observed during backwash in inside-out mode. Secondly, this opposing deformation between larger and small pore originated from a balance in a confined volume. Akondhi *et al.* explained that large pores are subjected to higher strain at same stress than small pores and their expansion resulted in a decrease of the size of small pores. Consequently, bulk porosity appeared constant before and after backwash. Furthermore, larger deformations were measured for PVDF than PAN membranes. As PVDF membranes have a lower Young's modulus than PAN membranes, PVDF membrane pores experienced larger deformation under same stress conditions according to Hooke's law (Eq. 9). Regarding fouling removal results, backwash efficiency would be higher on large pore than on small ones. Indeed, as the flow rate through a pore increases with pore size (Hagen-Poiseuille law, Eq. 32), the induced shear stress on the wall of the large pores will be higher leading to better fouling removal [141].

Zhao *et al.* [12] have studied the effect of backwash pressure on polyurethane-based microfiltration membrane. They observed by camera that the external surface of the hollow-fiber membrane was increasingly expanding with backwash pressure increase in inside-out mode, but they did not measure the membrane deformation. They suggested that the expansive pore and surface deformation cracked and loosed the cake layer leading to its removal as they observed higher fouling removal at higher backwash pressure. However, these results have to be considered with care as higher backwash flux or pressure also lead to higher fouling removal without surface deformation mentioned [11][107][5].

1.4.3.2 Polymeric substrate deformation for biofilm detachment

Systems composed of a polymeric substrate that can elastically deform under external stimuli (mechanical, pneumatic, hydraulic or electrical actuation) were used to demonstrate how surface deformation is causing the detachment of biofouling formed by micro-organisms (algae or bacteria) [143][144][145][146].

Firstly, Limbert *et al.* [145] have studied the attachment and detachment of biofilms on surgical sutures made from polyester using a numerical model. Based on a finite element model and microscopic images, the mechanical behavior of the structure was simulated when subjected to non-uniform macroscopic loads (tension, bending and twisting) considering a Young's modulus of 500 MPa. The generated strain could reach 10% and might lead to the detachment of biofilm as induced shear stresses at the biofilm-suture interface are sufficient to cause biofilm sliding. Bending case demonstrated the highest tensile stresses at the surface of the suture meaning the highest probability to lead to biofilm detachment from the surface.

Following these theoretical predictions, Levering *et al.* [146] demonstrated that stretching a biofilm-covered silicon flat substrate promotes the biofilm detachment. The biofilm debonding was related to the applied strain and strain rate. A minimum of 25% strain (strained 10 times consecutively) and strain rate of 40% per second were indeed required to detach 80% of the biofilm (as seen on Figure 13). At lower strain or strain rate only a small amount (<20%) was removed from the surface. They demonstrated that there is a critical strain, at high strain rate, from which the biofilm debonded as large

fragments from the surface (Figure 13 (c)). Whereas at low strain rate, the biofilm was fractured in little pieces but remained on the surface even at high strain as represented on Figure 13 (b) [146].

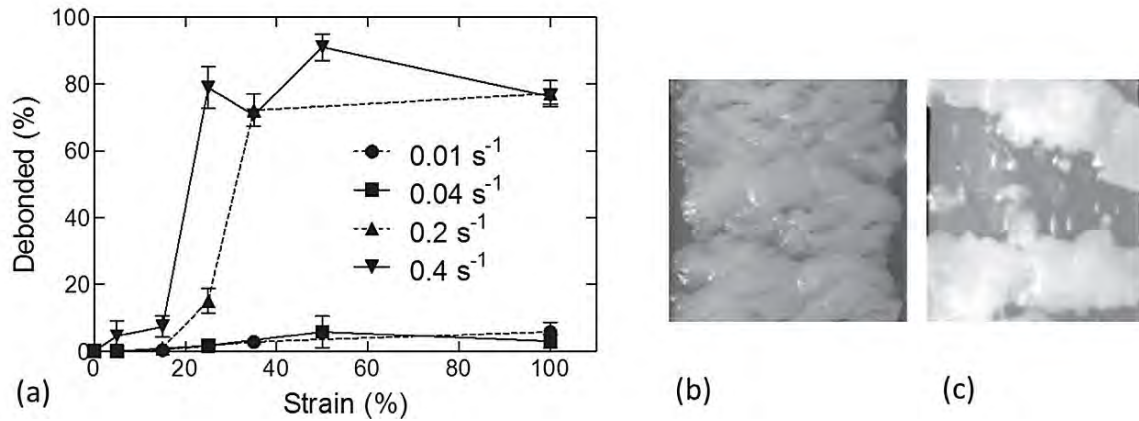


Figure 13: Biofilm debonding as a function of strain and strain rate (a). Pictures of biofilm fragments debonded at 100% strain and 1% strain rate (b) or 40% strain rate(c). Adapted from [146].

Levering *et al.* have further investigated the biofilm debonding when applying axial strain on a biofilm-covered tubular device as observed on Figure 14 [146]. The tube was made from silicone with a Young's modulus of 0.2 MPa and found application as urinary catheter. They demonstrated that stretching the tubular silicone substrate 10 times consecutively at a strain of 50% efficiently removed the biofilm from the lumen surface.

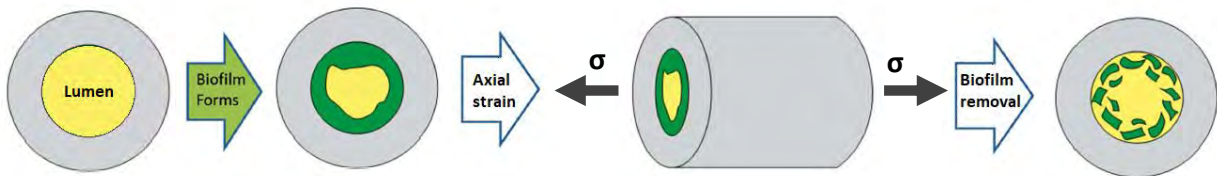


Figure 14: Biofilm debonding caused by axial strain on a urinary catheter prototype, adapted from [146].

Furthermore, the composition of the biofilm had an impact on its debonding. Indeed, more crystalline biofilm generates higher shear stress at the biofilm-substrate interface leading to a better detachment of the biofilm at a given deformation [146]. Chaudhury *et al.* [147] also observed this behavior in release of algae spores and sporelings from silicon surface when subjected to shear stress due to different biofouling rigidities.

Chaudhury *et al.* [147] have demonstrated that the Young's modulus of the silicon substrate influenced biofouling removal when subjected to shear stress. They assumed that the generated shear stress might deform substrates with different elasticities at

different strain amplitudes. Indeed, a softer substrate (with lower Young's modulus) is more likely to deform at constant stress leading to higher fouling release.

Biomimicry has attracted interest in the recent years contributing to the development of innovative technologies. There are some biological surfaces that are able to self-clean, as instance, coral polyps possess ability to clear sediments by tissue expansion [148]. Shivapooja *et al.* [143] developed bioinspired elastomeric surface for active control of biofouling. They have shown that the removal of biofilm when deforming silicon substrate was strongly affected by the biofilm thickness as observed on Figure 15.

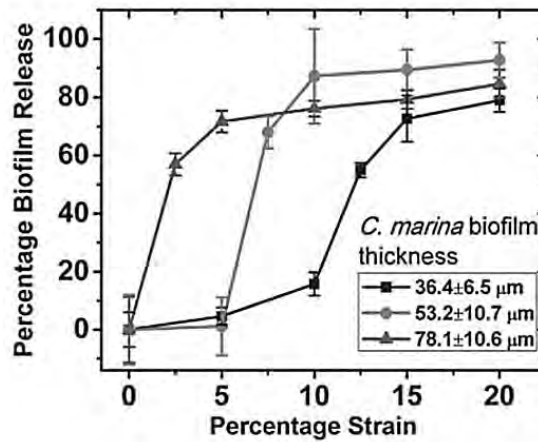


Figure 15 : Percentage of biofilm release as a function of strain and biofilm thickness, adapted from [143].

They also explained that for a linearly elastic biofilm (made from bacteria), elastomeric substrate and biofilm were simultaneously deforming during substrate stretching up to a critical strain. At this critical strain, the elastic energy of the biofilm exceeds the adhesion energy between the biofilm and the substrate leading to its release. This critical strain is expressed by Eq. 1:

$$\varepsilon_c = \left(\frac{2\Delta G_{f-s}(1 - \nu_f^2)}{h_f E_f} \right)^{\frac{1}{2}} \quad \text{Eq. 1}$$

With ε_c the critical strain, E_f the Young's modulus of the fouling layer (Pa), h_f the fouling layer thickness (m), ν_f the Poisson's ratio of the fouling layer and ΔG_{f-s} the energy of adhesion per unit area between the fouling layer and the substrate ($\text{J}\cdot\text{m}^{-2}$).

Therefore, recent works have shown promising results of biofouling removal caused by substrate deformation in the biology, marine or health area. Mechanisms for fouling release was explained by potential induced shear stress at the biofilm-substrate

interface during substrate strain. An energetic approach showed also a critical strain for an efficient detachment of the biofilm. However, further investigations are required to understand the removal mechanisms as many parameters are involved in the biofilm debonding (e.g. strain, strain rate, substrate and biofilm properties).

1.4.3.3 Analogy with hollow-fiber membrane during the backwash process

By analogy with the area of membrane filtration, hollow-fiber membrane surface deformation caused by hydraulic pressure (during backwash) might lead to greater fouling and biofouling removal.

Membrane materials are however different from the tested elastomeric surfaces mentioned in the above section (1.4.3.2). Indeed, while the Young's modulus of silicon substrates is about 0.2 MPa [146][143][144], the Young's modulus of commercial membranes is usually above 40 MPa to ensure good mechanical resistance [136][22]. As silicone substrates are much softer, at the same applied stress they deform to higher extent than typical membranes.

Indeed, according to Hooke's law (Eq. 9) and Young's modulus values mentioned above, to achieve equivalent strain on membrane than on silicon substrate, the stress applied on the membrane has to be 200 times higher. Levering *et al.* [146] have found high fouling removal from silicon catheter surface when a minimum stress (inflated pressure) of 5 kPa was applied. For typical membrane, this critical stress would then reach 1000 kPa that is 10 bar. However, current UF membranes could not withstand such high pressures. Indeed, membranes are not made from elastomeric polymers, making them more prone to plastic deformation or bursting under high stress. Therefore, to achieve similar membrane deformation, the Young's modulus of the membranes has to be reduced without hindering membrane filtration ability and hollow-fiber integrity.

One of the main objective of this dissertation is to study membranes that possess ability to deform under backwash in order to prove that surface deformation might be an innovative physical cleaning method to remove fouling. The deformation of the fouled surface during backwash would occur either if the membrane is used in outside-in or inside-out mode. However, a backwash in inside-out mode might lead to higher deformation of the external fouled layer (expansion) resulting in higher fouling removal.

In this research, membrane filtration was performed in outside-in and backwash process in inside-out.

1.4.4 Conclusion

Membrane cleanings are always performed for drinking water treatment and are increasingly automated processes in industry. Physical cleanings are preferred to chemical cleanings as they avoid the use of chemical agents (e.g. sodium hypochlorite) that might cause membrane degradation and require post-treatment. Due to its easy processing and great cleaning performances, backwash has become the most conventional cleaning process. Several studies have been conducted to optimize the backwash parameters to improve its efficiency but fouling removal mechanisms are still poorly understood. Other physical cleaning methods are used to induce shear stress at the membrane surface such as air scouring or rotation, but most of them are used in combination with backwash to enhance cleaning performances.

A new physical cleaning process consisting in deforming a biofilm-covered substrate to cause biofilm detachment has drawn our attention. Indeed, an analogy with the expansion of deformable hollow-fiber membranes during the backwash step might lead to the same fouling detachment. In this work, the surface deformation and its consequence on fouling removal have been measured and discussed.

1.5 Fouling/fouling removal characterization methods

They are a multitude of available characterization methods to observe and quantify the cake formation on membrane surface during filtration, and its removal during backwash. Choosing the appropriate method depends on the needed information but also on the operator's expertise and experimental environment. This research was focused on the study of fouling removal during backwash and in particular on the evaluation of backwash efficiency. Backwash efficiency is generally assessed by flux or permeability recovery. However, mass balance calculations have shown interesting results providing supplementary information on short-term filtration.

1.5.1 Backwash efficiency evaluation

Backwash efficiency can be evaluated by different methods to highlight the reversible and irreversible part of the fouling [9]. Some calculation methods depends on the filtration mode (constant pressure or flux) and are therefore related to pressure and permeate flux recovery. Others are independent and based on membrane property variation or mass balance calculation. Calculations based on permeability characterize the elimination of hydraulic resistance and recovery of permeate flux whereas quantification of the real amount of matter eliminated during the backwash is performed by mass balance.

1.5.1.1 Permeability recovery or gain

Membrane permeability recovery (R_p) is usually used as first indicator to evaluate backwash performance. The ratio of permeability after cleaning on the initial pristine membrane permeability gives relevant information on the loss of permeate flux due to irreversible fouling [107].

$$R_p = \frac{Lp_{bw}}{Lp_0} \quad \text{Eq. 2}$$

With R_p the membrane permeability recovery, Lp_{bw} the outside-in permeability after backwash ($\text{L}\cdot\text{m}^{-2}\cdot\text{h}^{-1}\cdot\text{bar}^{-1}$) and Lp_0 the outside-in initial membrane permeability ($\text{L}\cdot\text{m}^{-2}\cdot\text{h}^{-1}\cdot\text{bar}^{-1}$).

The gain of permeability from fouled to backwashed membrane is expressed by Eq. 3 [149][150]. Contrary to permeability recovery (Eq. 2), the gain of permeability takes into account the membrane permeability after filtration.

$$G_p = \frac{Lp_{bw} - Lp_f}{Lp_0 - Lp_f} \quad \text{Eq. 3}$$

With G_p the gain of permeability and Lp_f the outside-in permeability after filtration ($\text{L}\cdot\text{m}^{-2}\cdot\text{h}^{-1}\cdot\text{bar}^{-1}$).

These equations based on permeability measurements provide rapid and efficient results on long-term operations but it remained difficult to predict accurate backwash efficiency on a single or a few filtration/backwash cycles [107].

1.5.1.2 Mass balance method

Mass balance method have been used to quantify the amount of removed matter during backwash [107][117][115][12]. Contrary to permeability calculation, this method is appropriate for single (or a few) filtration/backwash cycle. Measurement of the matter concentration in the backwash waters and estimation of deposited mass of matter on the surface are required to calculate the amount of cake removed during single backwash as follows:

$$CR = \frac{m_{bw}}{m_d} \quad \text{Eq. 4}$$

with CR the amount of cake removed during the backwash, m_d the deposited mass on membrane external surface (kg) and m_{bw} the mass of cake collected in the backwash waters (kg).

This method is therefore more complex to implement than permeability recovery. Mass balance provides accurate percentage of cake removal that may significantly differ from permeability recovery percentage. Indeed, Remize et al. [107] have measured a permeability recovery of 99 % whereas the percentage of cake removal reached only 25%. One of the explanation is that a filter cake with a low hydraulic resistance slightly contributes to the change of permeability and does not affect the calculation of permeability recovery whereas it is included in mass balance calculation. Therefore, if the cake was not removed during the backwash low cake removal is obtained whereas high permeability recovery might still be observed.

Moreover, the remaining fouling layer on the membrane surface after backwash may increase the fouling rate for the next cycle as the new cake would build up on the previous one. Therefore, in this case, backwash efficiency seem to be better assessed by mass balance than permeability recovery.

1.5.2 Observation techniques for fouling/fouling removal analysis on hollow-fiber membranes

Observations at the local scale offer additional information on the fouling and fouling removal mechanisms. The observation can also be compared to the backwash evaluation

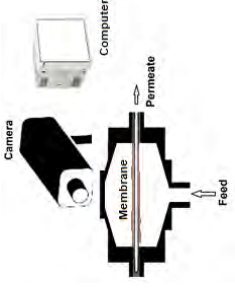
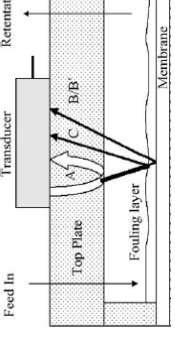
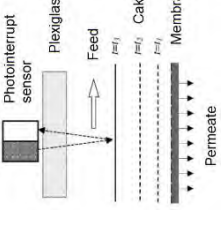
method to support backwash efficiency calculations. Local measurements are either performed using in-situ or ex-situ observation techniques with micrometric or even lower resolution. Visual direct observation with microscope and camera was focused in this work and detailed in this section.

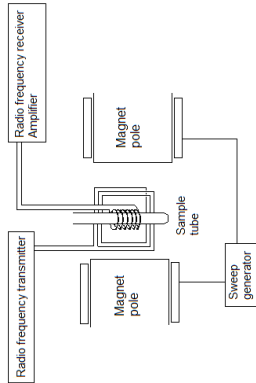
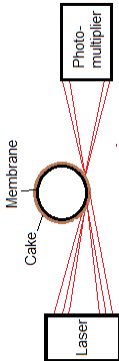
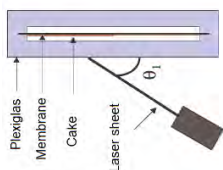
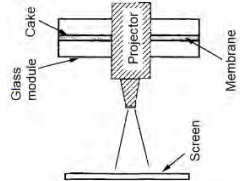
1.5.2.1 Overview of the different techniques

Ex-situ measurements such as Scanning Electron Microscopy (SEM) is typically used to observe deposited particles on surfaces or to measure deposit thicknesses [151][152] after filtration or backwash. However, cryofracture and vacuum mode, required for sampling and analysis, may modify the cake structure and thickness. Cleaning efficiency can be evaluated by Fourier transform infrared spectroscopy with attenuated total reflectance (FTIR-ATR). This ex-situ technique allowed a quantitative analysis of the residual fouling on the membrane surface after the use of different cleaning agents [153].

Contrary to ex-situ characterization techniques, in-situ techniques provide real-time information throughout the filtration and backwash duration. Furthermore, in-situ characterization methods are non-invasive, and therefore, do not affect cake growth or removal. Table 2 summarizes some of these in-situ characterization techniques including technique resolution, schematic and brief description of the measurement and its limitation. Optical methods have been widely used but transparent module is necessary for measurement whereas ultrasonic or nuclear magnetic resonance (NMR) imaging can be performed on non-transparent system. Most techniques can only be used in external mode (fouling on external surface), except in the case of NMR imaging.

Table 2: Summary of fouling and fouling removal characterization techniques for hollow-fiber membranes: Principle, limitation and schematic.

Technique	Filtration mode		Resolution	Principle	Limitation	Schematic
	Outside-in	Inside-out				
Direct observation [154][155][156] [157]	x	(x)	μm	Observation of deposit growth or removal at the membrane-solution interface using an optical camera or microscope.	<ul style="list-style-type: none"> - Detection of deposit-membrane interface - Clear or low turbid water - Low depth of field - Tight and still hollow-fiber 	
Ultrasonic [152][158]	x		μm	At the interface between two medium, ultrasonic wave is partially reflected and flight time and received signal amplitude are measured.	Theoretical data are required for calculations (sound velocity in the fouling layer).	
Photointerrupt sensor [159]	x		$10 \mu\text{m}$	IR light emitted and reflected into the collector at the interface. Measurement of reflective current.	Sensitive to the color of the solution.	

<p><i>Nuclear magnetic resonance imaging</i> [160][161]</p>	<p>x</p>	<p>20 μm</p>	<p>Measurement of mobile protons in sample layers. No NMR signal for bentonite and silica particles (black area in image analysis).</p>	<p>- Complex equipment - Difficulty to extract information - Artefacts during cake growth</p>	
<p><i>Laser beam</i> [162]</p>	<p>x</p>	<p>μm</p>	<p>Laser beam (He-Ne) is emitted tangentially onto the membrane surface. Signal intensity variation gives information on deposit thickness.</p>	<p>- Low particle concentration in the solution - Limit for cake height</p>	
<p><i>Laser sheet at grazing incidence</i> [163]</p>	<p>x</p>	<p>3 μm</p>	<p>Laser sheet is focused on the membrane. The reflected laser light is recorded by CCD camera.</p>	<p>- Particulate concentration range : 0-3 g.L⁻¹ - Transparent module - Specific θ angle</p>	
<p><i>Projection</i> [164]</p>	<p>x</p>	<p>10 μm</p>	<p>Fouled membrane is projected on a screen (4 meters away). Measurement by resizing.</p>	<p>- Detection of membrane-cake interface - Space for projection</p>	

1.5.2.2 In-situ direct observation by optical device

Marselina *et al.* [154][155] have observed filter cake formation and removal on PVDF membrane during bentonite cross-flow filtration and backwash. These observations were carried out using a filtration set-up working in cross-flow mode at constant flux and equipped with a microscope objective lens and video camera (Figure 16). The filtration cell was designed with a 4 mm channel height and a glass transparent window. One of the system limitation is the fiber movement during observation. Therefore, the fiber was well tight to stay still during the process. Turbidity in the cell (high feed concentration) may also be a limiting factor for visual observation. As observed on Figure 16, the cake growth on membrane surface was measured on different pictures. Cake height was calculated by the difference in height between fouled membrane and virgin membrane as cake-membrane interface remained stationary (still membrane) and difficult to detect.

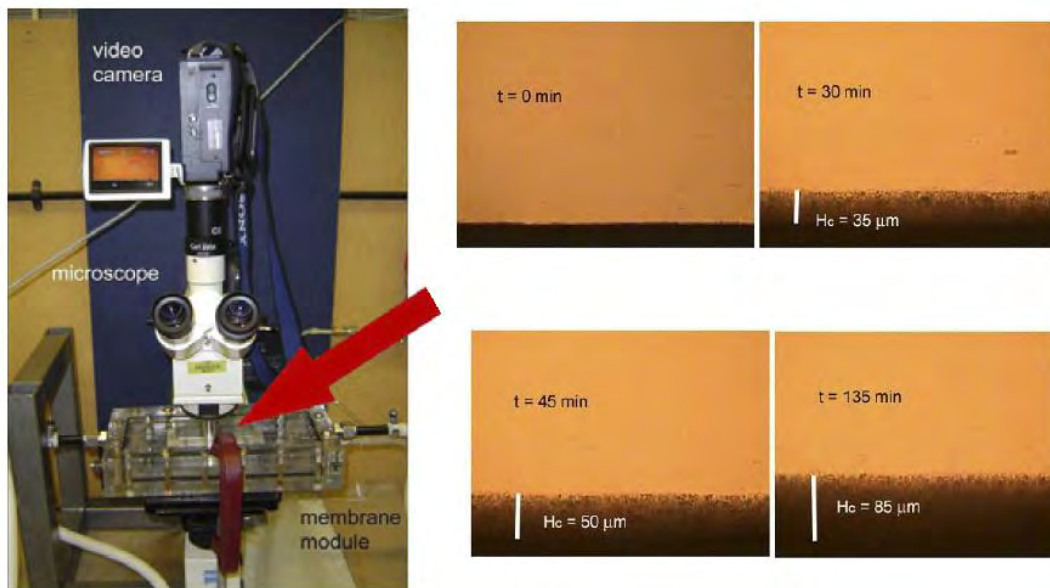


Figure 16: Experimental set-up for direct observation of hollow-fiber membrane under microscope (left) and bentonite cake growth pictures on membrane external surface during filtration (right). Adapted from [154].

Fouling removal was also observed during backwash, Marselina *et al.* described a gradual loosening of the cake taking a few minutes. The cake layer was expanded and became fluidized prior to be eliminated due to shearing effect induced by cross-flow velocity as observed on Figure 17.

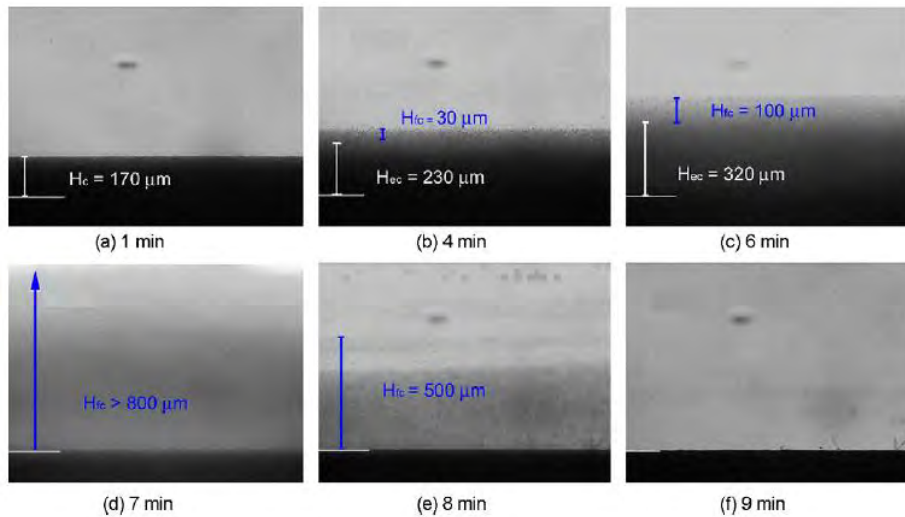


Figure 17: Fouling removal pictures during backwash at different time intervals with H_c the stagnant cake height, H_{ec} the expanded cake height and H_{fc} the fluidized cake height. Adapted from [155].

Chang and Fane [157] have used the same optical device to observe filtration performance enhancement using air scouring on polypropylene hollow-fiber membrane during yeast filtration. Limiting fouling when using air bubbles was confirmed by visual observation. They could also measure the critical flux (defined in 1.3.3.2) through direct observation. Other studies by direct observation of fouling and fouling removal on PVDF hollow-fiber membranes have been conducted during filtration of different particles (polymeric charged particles [156], bentonite and alginate mixture [165]). These observations were coupled with hydraulic resistance measurements. Direct observation through the membrane to evaluate inside fouling is also possible in the case of transparent membrane [166].

1.5.3 Conclusion

Quantification of the cake removal by mass balance seems to be a more accurate method to assess the backwash efficiency than permeability recovery, especially on short-term filtration/backwash cycle. Furthermore, analysis at the local scale by in-situ and real-time characterization techniques is essential to support backwash efficiency calculations and to understand the mechanisms involved during filtration and backwash. Optical methods such as direct observation technique under microscope and camera have shown interesting results that help to explain fouling removal mechanisms as a function of operating conditions and feed composition.

1.6 General conclusion

It can be concluded from this chapter that ultimate hollow-fiber membrane properties are difficult to predict as many parameters influence the membrane formation and its morphology. They are some operating parameters and additives, which help to the preparation of high permeable membranes with specific mechanical properties. However due to the complexity of phase inversion mechanisms, producing a membrane with target properties remains challenging.

Extensive studies on fouling with model and real suspensions have been conducted in the literature. Even if multiple preventive solutions have been developed to limit the fouling rate, cleaning of the membrane remains an essential step in membrane filtration. Physical and chemical cleanings are therefore largely employed to manage fouling in water treatment. As the main cleaning process, backwash has been improved by the optimization of operating parameters or combination with other processes (e.g. air scouring) to increase its efficiency and reduce its cost. However, fouling removal mechanisms are still poorly understood and there is lack of optimization criteria for an efficient backwash process.

This work proposes to study these mechanisms using different characterization methods (i.e. mass balance, permeability and hydraulic resistance measurements, and direct observation under camera) in order to compare backwash efficiency to the membrane properties. It is suggested that the backwash flux and the membrane surface strain during backwash might help to remove the fouling layer from the surface due to the introduction of various stresses at the cake-membrane interface. This innovative physical cleaning approach by optimizing the membrane materials and backwash operating parameters could lead to greater backwash efficiency and filtration performances.

Chapter 2 - Materials and methods

2.1 Materials

2.1.1 Polymers

Different grades of Kynar[®] polyvinylidene fluoride (PVDF) homopolymer (Kynar[®] HSV 900 and Kynar[®] MG15) and Kynar[®] polyvinylidene-co-hexafluoropropylene (PVDF-HFP) copolymer (Kynar Flex[®] 2801-00 and Kynar[®] RC10,312) were provided by Arkema S.A. (France) and used as membrane-forming polymers. Homopolymers are formed from a single type of monomer but grades have different molecular weights. Copolymers are formed by copolymerization of two types of monomer (PVDF and HFP) and copolymer grades have different molecular weights and/or monomer fractions. Technical data sheets of these Kynar[®] PVDF grades are provided in Appendix 1. Polyvinylpyrrolidone (PVP) and polyethylene glycol (PEG, $M_w=10,000 \text{ g}\cdot\text{mol}^{-1}$) were purchased from Sigma Aldrich (France) and used as pore-forming additives. 1,2-propylene glycol (PG) was purchased from Sigma Aldrich (France) and used as additive.

2.1.2 Solvents

N-methyl-2-pyrrolidone (NMP) was purchased from Gaches Chimie SAS (France) and dimethyl sulfoxide (DMSO) provided from Arkema (France). Both were used as solvents.

2.1.3 Inorganic salts

Lithium chloride (LiCl) was purchased from Sigma Aldrich (France) and used as pore forming agent. Potassium chloride (KCl) was purchased from Carlo Erba (France) and dihydrated calcium chloride ($\text{CaCl}_2 \cdot 2\text{H}_2\text{O}$) from Acros Organics (France). Both were used as ionic compounds for the preparation of particle suspensions. Sodium azide (NaN_3) was purchased from Sigma Aldrich (France) and sodium bisulfite was purchased from Acros Organics (France). Both were used as bacteriostatic agents.

2.1.4 Particles

Bentonite (montmorillonite) Clarsol FB2 was purchased from CECA (France) and humic acid from Sigma Aldrich (France). Both were used for the preparation of particle suspensions.

2.2 Hollow-fiber membrane preparation

2.2.1 Dope solution and bore fluid preparation

The dope solution was prepared by dissolving Kynar[®] PVDF and additives (e.g. PVP, PG, PEG and/or LiCl) into a solvent (NMP or DMSO). The components were mixed in a temperature-controlled vessel at 70°C under mechanical agitation for at least 6 hours. The homogenous dope solution was degassed at 70°C in a vacuum tank overnight. The bore fluid was tap water or a mixture of solvent (NMP) and non-solvent (water, PG).

Detailed chemical compositions of the dope solution and bore fluid for M-LP19 and M-LP91 are given in Appendix 2 . Other chemical compositions were confidential. Dope and bore fluid formulations were provided by Arkema S.A. (U.S.A) and the Laboratoire de Génie Chimique (France).

2.2.2 Preparation of membranes by spinning and dry-wet phase inversion

Hollow-fiber membranes were produced by the phase inversion process using a spinning apparatus (Figure 18). Dope and bore solutions were placed in separate pressurized tanks set at the chosen temperature. The dope solution and bore fluid were co-extruded through an annular spinneret using gear pumps to form a hollow-cylinder. Spinneret dimensions and design are presented in Figure 18. The nascent hollow fiber was then immersed in a tap water coagulation bath where the phase inversion took place. The fiber was pulled out, at a controlled take-up speed, from the bath by a set of rollers and was placed in a storage water bath to complete solvent release.

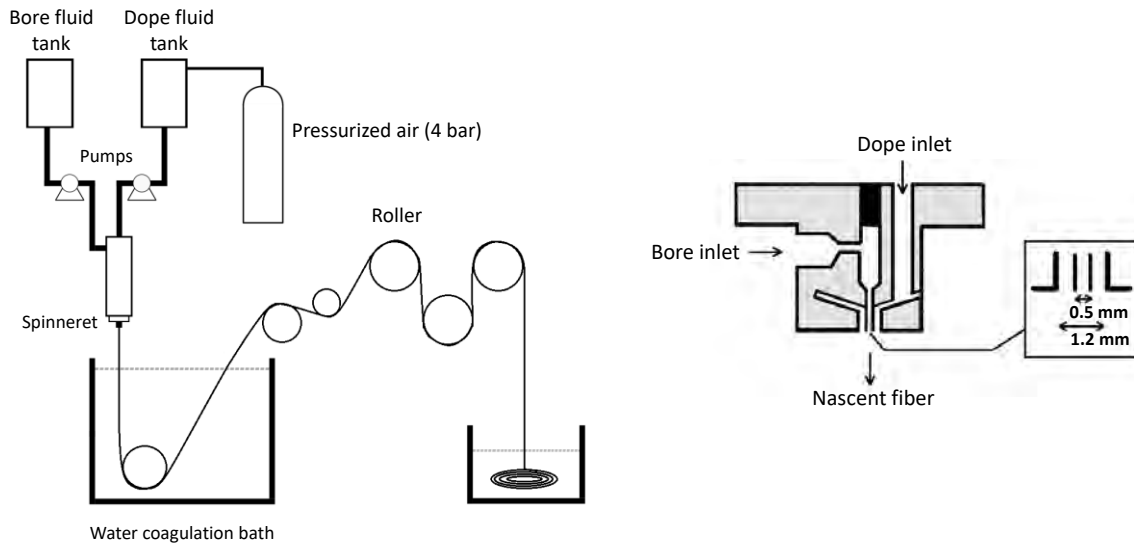


Figure 18: Spinning apparatus (left) and spinneret design (right) in the Laboratoire de Génie Chimique

Spinning operating conditions were given by Arkema S.A. and Laboratoire de Génie Chimique and were adjusted in the lab to produce proper membrane with various properties. M-LP19, M-LP91 and M-HP32 were spun in Laboratoire de Génie Chimique, Toulouse, France. Others were imported from Arkema (King of Prussia, USA): M-HP47, M-HP45 and M-LP59. Spinning operating parameters are shown in Table 3 and a range of values was given for the preparation of the hollow-fiber membranes. Detailed spinning operating conditions for M-LP19 and M-LP91 are given in Appendix 2 .

Table 3: Spinning operating conditions given in a range of values used for the preparation of the hollow-fiber membranes.

Operating conditions	Range
Bore fluid	
<i>Temperature</i>	20-80°C
<i>Flow rate</i>	1-20 ml.min ⁻¹
Dope fluid	
<i>Temperature</i>	20-80°C
<i>Flow rate</i>	3-30 ml.min ⁻¹
Water coagulation bath	
<i>Temperature</i>	20-60°C
Air gap	
<i>Distance</i>	0-40 cm
Roller	
<i>Take-up speed</i>	3-30 m.min ⁻¹

The spun membranes containing PVP additive were washed out using a bleach solution. Membranes were soaked in a 15,000 ppm chlorine bath at pH 11 for 6 hours. Membranes were then thoroughly rinsed with ultrapure water and soaked for 2 hours in two successive water baths to eliminate residual chlorine.

2.2.3 Membrane storage

The hollow-fiber membranes spun in Laboratoire de Génie Chimique were kept wet in water. Membranes were stored in a cool place into an airtight plastic bag containing a sodium bisulfite solution. The storage solution was used to prevent from bacterial growth and was prepared by dissolving 10 g.L⁻¹ of sodium bisulfite in ultrapure water.

The hollow-fiber membranes imported from Arkema S.A. were stored in glycerol in an airtight plastic bag in a cool place.

2.3 Experimental design

Two filtration units were designed in the lab: filtration unit A and filtration unit B. Both were working at constant pressure in dead-end and outside-in mode. The flow could be reversed to perform a backwash at constant pressure.

2.3.1 Filtration unit A

Filtration unit A (Figure 19) was used to measure the cake removal percentage by the method of mass balance and the permeability recovery on a single filtration/backwash cycle and on several cycles. Time and pressure dependence of the membrane permeability was also explored on filtration unit A. Module comprising single or several hollow-fiber membranes (see Figure 21) was mounted in the filtration unit. Temperature, pressure, and permeate mass were continuously recorded with ABB Model SM1000 instrument.

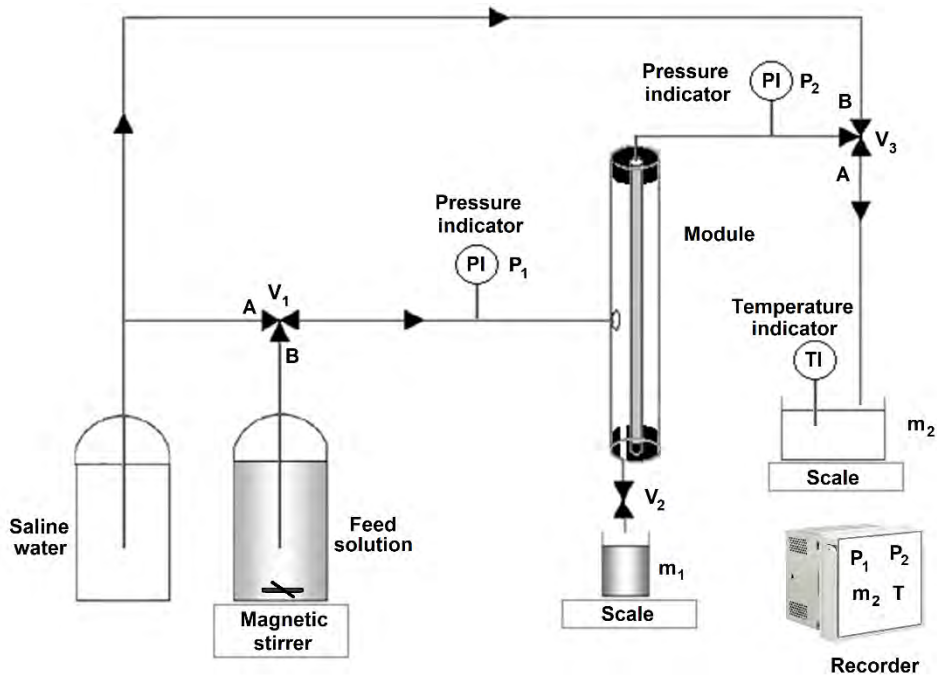


Figure 19: Experimental design of filtration unit A (schematic at the top and picture at the bottom): Filtration in dead-end filtration and outside-in mode under constant pressure and backwash under constant pressure. Experimental pilot equipped with a temperature, pressure and mass recorder.

2.3.2 Filtration unit B

Filtration unit B (Figure 20) was used to observe cake growth (during filtration), cake deformation and cake removal (during backwash) and to measure the membrane deformation under external and internal pressure. Filtration cell comprising single hollow-fiber membrane (see Figure 21) was mounted in the filtration unit. A digital camera Model Manta G-1236, Allied Vision, equipped with an optical system with a lens RODAGON (50 mm, F2, 8) was focus on the

membrane interface and used to take pictures and record videos of the hollow-fiber membrane. The camera has a resolution of $0.7 \mu\text{m}$ per pixel and a field of vision of $4 \times 3 \text{ mm}$. Pictures and movies were processed with Vimba Viewer and ImageJ software. A source of light was added below the cell to clearly observe the membrane interface. In this configuration, the hollow-fiber membrane and the cake deposition appeared in black while the feed solution remained white.

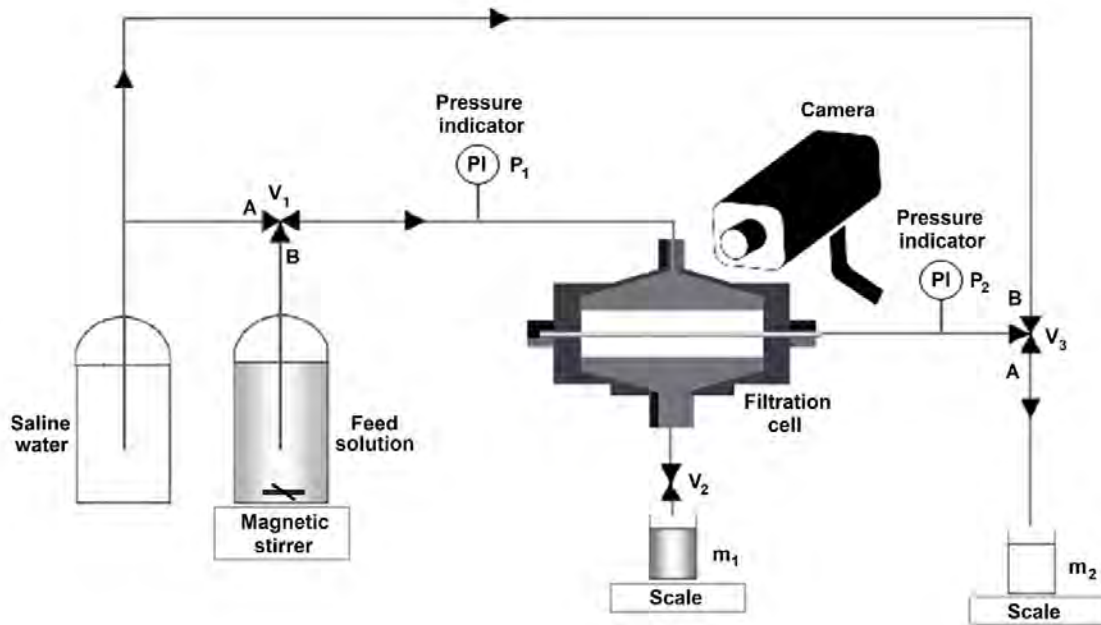


Figure 20: Experimental design of filtration unit B (schematic at the top and picture at the bottom): Filtration in dead-end filtration and outside-in mode under constant pressure and backwash under constant pressure. Pilot equipped with digital camera.

2.3.3 Filtration module/cell

A module comprising a single, centered and tight hollow-fiber membrane (see on Figure 21, A) was used for fouling/fouling removal analysis with model suspensions on filtration unit A. The module was made from PVC tube of 30 cm length and 1.3 cm diameter. The membrane was potted at both ends into epoxy glue: one fiber extremity was open to collect permeate whereas the other was close with epoxy glue for experimental design. The effective fiber length was 27 cm. The effective volume of the filtration module was 40 ml.

A module comprising four hollow-fiber membranes in “U-configuration” (see on Figure 21, B) was used for permeability measurement and filtration/backwash cycles on filtration unit A. The membrane was potted at one extremity into epoxy glue and left open for permeate collection. The effective fiber length was 27 cm.

A filtration cell was used for observations under camera on filtration unit B. The filtration cell model was designed in 3D on Blender software and optimized to have a homogenous liquid flow inside the cell and outside the hollow-fiber (details are given in Appendix 3). The cell was made from aluminum by 3D-printing technique. The printed cell dimensions were 106 x 66 mm and the effective volume was 7 ml. The observation window dimensions were 66 x 16 mm. The filtration cell was completely waterproof below 1.5 bar (sealing was no longer effective above 1.5 bar). The filtration cell comprised a single, centered and tight hollow-fiber membrane potted at both ends into epoxy glue: one fiber extremity was open to collect permeate whereas the other was close with epoxy glue for experimental design (see on Figure 21, C). The effective fiber length was 7 cm.

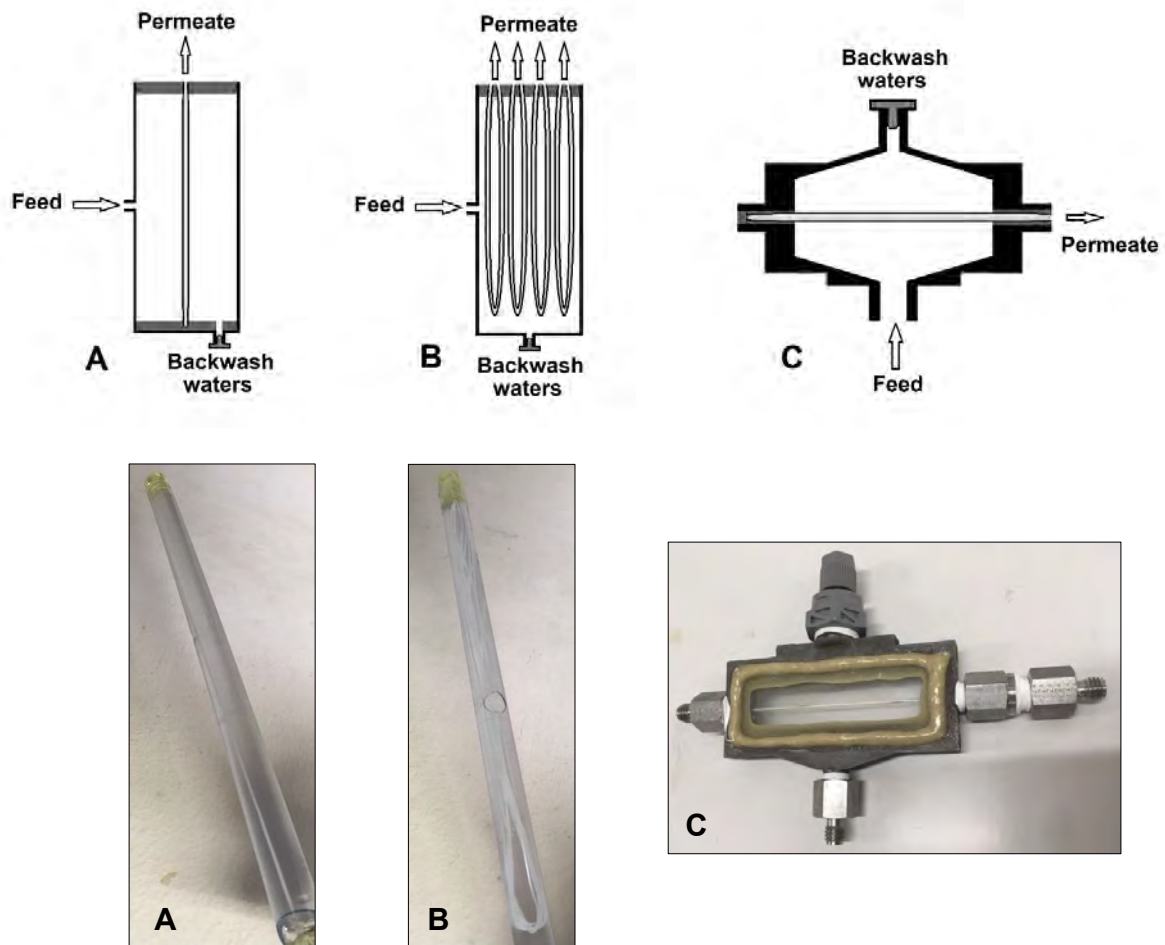


Figure 21: Sectional drawings (at the top) and pictures (at the bottom) of the filtration modules/cell, A: Single centered hollow-fiber membrane in PVC module, B: Four hollow-fiber membranes in "U-configuration" in PVC module and C: Single hollow-fiber membrane in aluminum 3D-printed filtration cell.

2.4 Ultrafiltration of feed solutions and backwash cleaning

2.4.1 Feed preparation

2.4.1.1 Model suspensions

Model suspensions were prepared from particle powder (bentonite and humic acid). Potassium chloride (KCl) or calcium chloride (CaCl_2) were added to the suspensions to modify the interaction between particles [72], and therefore change the cake properties during the filtration process [167]. The ionic strength of the suspensions was chosen below the critical coagulation concentration for higher control of ultrafiltration and cake deposition. Therefore, the ionic strength was adjusted to 10^{-3} M for all prepared suspensions.

2.4.1.1.1 Bentonite suspension

Bentonite clay solution was prepared by dispersing 30 g of bentonite powder in 1 L of sodium azide solution (1 mg.L^{-1} of NaN_3 in ultra-pure water to prevent from bacterial growth) under mechanical agitation for 15 hours. The clay solution was left to settle and only supernatant was collected. A stock solution of 18.1 g.L^{-1} was obtained by successive settlings [168] (twice for 4 hours and once overnight) of the bentonite clay solution and was stored in a cool place. The particle concentration of the stock solution was measured using a Sartorius, Model MA 100 gravimetric moisture analyzer.

Feed solution with a bentonite particle concentration of 0.05 g.L^{-1} was prepared from the stock solution (18.1 g.L^{-1}) in ultrapure water. The ionic strength was adjusted to 10^{-3} M by adding monovalent (KCl) or bivalent salt (CaCl_2) and the suspension was placed under mechanical agitation for at least 4 hours. Two feed solutions were prepared and filtered: a suspension of 0.05 g.L^{-1} of bentonite with a concentration in KCl of $10^{-3} \text{ mol.L}^{-1}$, called bentonite (KCl), and a suspension of 0.05 g.L^{-1} bentonite with a concentration in CaCl_2 of $3.3 \times 10^{-4} \text{ mol.L}^{-1}$ (calculated from Eq. 33) called bentonite (CaCl_2).

2.4.1.1.2 Humic acid suspension

Humic acid solution with particle concentration of 0.05 g.L^{-1} was prepared in ultrapure water. The ionic strength was adjusted to 10^{-3} M by adding CaCl_2 salt and the suspension was placed under mechanical agitation (moderate stirring to avoid foam) for at least 4 hours. The prepared feed solution of 0.05 g.L^{-1} of humic acid with a concentration in CaCl_2 of $3.3 \times 10^{-4} \text{ mol.L}^{-1}$ was called humic acid (CaCl_2).

2.4.1.2 Real fluids

Domestic wastewaters were collected from a water treatment plant from Veolia (Brax, France). The activated sludge was stored in a cool place under aeration for a maximum duration of 3 days. The feed solution was prepared by sieving the activated sludge through a 0.5 mm metal mesh to remove any residual particles able to clog the filtration unit. Feed solution was placed under mechanical agitation for 2 hours before use.

2.4.2 Protocol for single filtration/backwash cycle

Each hollow-fiber membrane, mounted in a module or filtration cell, was first fouled during filtration of model suspensions at constant pressure and then backwashed at constant pressure. A new module with a new single hollow fiber membrane was used for each filtration/backwash cycle. In addition of the prepared feed (section 2.4.1), a saline solution made from ultrapure water with ionic strength adjusted to 10^{-3} M with KCl or CaCl₂ (salt of the filtration) was prepared. This saline solution was used for permeability measurements, rinsing and backwash to prevent from modifying electrostatic interactions in the filter cake. Experimental protocol for filtration/backwash cycle of model suspensions is described in Table 4 and protocol for valve control in Appendix 4 .

Table 4: Experimental protocol for single filtration/backwash cycle of model suspensions (bentonite and humic acid) at constant filtration pressure TMP=0.8 bar and constant backwash pressures BTMP=[0.2-2.5] bar.

Step	Solution	Pressure (bar)	Duration (min)
Conditioning	Saline solution	TMP=0.8	45
Permeability measurement			5
<i>Draining and refilling with feed solution</i>			
Filtration	Feed solution	TMP=0.8	15-120
<i>Rinsing step with saline solution</i>			
Permeability measurement	Saline solution	TMP=0.8	5
1st Backwash		BTMP=[0.2 - 0.8]	1
<i>Rinsing step with saline solution</i>			
Permeability measurement	Saline solution	TMP=0.8	5
2nd Backwash		BTMP=[0.8 - 2.5]	1
<i>Rinsing step with saline solution</i>			
Permeability measurement	Saline solution	TMP=0.8	5

2.4.2.1 Permeability measurement

Membrane permeability was measured at different stages of filtration/backwash cycle at constant transmembrane pressure (TMP) at 0.8 bar in outside-in mode:

- After conditioning with saline solution for initial membrane permeability
- At the end of filtration with feed solution for fouling resistance calculation

- After rinsing with saline solution to check the integrity of the fouling cake
- After each backwash for permeability recovery calculation at each backwash pressure

2.4.2.2 Conditioning

Before each filtration of model suspensions (bentonite and humic acid) the membrane was conditioned for 45 minutes at TMP=0.8 bar with the saline solution.

2.4.2.3 Filtration procedure

The module was drained from saline solution (by the introduction of air) and refilled with feed suspension. Model feed solutions (bentonite (KCl), bentonite (CaCl₂) and humic acid (CaCl₂) suspensions) were filtered at TMP=0.8 bar. A permeate volume of 60 L.m⁻² was filtered for each membrane. The cake thickness was measured by difference in height between fouled membrane and virgin membrane using pictures taken by video camera [154]. Filtration duration depended on the membrane permeability and fouling propensity.

2.4.2.4 Rinsing procedure

The rinsing step was required to calculate precisely cake removal using mass balances. It consisted in draining slowly the module either to replace the feed solution by saline solution (after filtration) or to evacuate the detached cake fragments (after each backwash). A quick draining of the module by the introduction of air would cause the cake removal in case of low adhered deposit such as bentonite cake. Membrane was therefore rinsed with 250 ml of saline solution at low flow ($\sim 2 \text{ L h}^{-1}$) for approximately 7 minutes. Saline solution was used to avoid fouling cake modification (after filtration) or elimination of the remaining cake (after backwash). Rinsing waters after backwash were collected and considered as backwash waters.

2.4.2.5 Backwash procedure

Flow of permeate was reversed to perform a backwash at constant pressure to remove the cake and recover the permeability. Backwashing at fixed transmembrane pressure (BTMP) was chosen to study the influence of the membrane mechanical properties, as membrane

deformation (pore and diameter) is function of the applied stress or pressure. Backwash was performed at different pressures from 0.2 to 2.5 bar. The backwash pressure was applied for a duration of 1 minute during which backwash waters were collected.

Backwash was performed in two steps at two different pressures. The first backwash was performed at 0.2 or 0.4 bar in the case of bentonite fouling and at 0.2, 0.4 or 0.8 bar in the case of humic acid fouling. The second backwash was performed at 0.8 or 1.5 bar in the case of bentonite fouling and at 1.5, 2.0 or 2.5 in the case of humic acid fouling. The removed cake mass during the second backwash was added to the removed cake mass during the first backwash for mass balance calculation. A few initial tests have demonstrated that first and second backwash could be considered independent from each other meaning that the removed cake mass of the second backwash (at higher pressure) is similar if performed without first backwash. This observation reduced by half the number of experiments since the cake removal percentage was measured at two backwash pressures instead of one for one fiber module.

2.4.3 Protocol for several filtration/backwash cycles

Several filtration/backwash cycles were performed on some hollow-fiber membranes with as feed: humic acid (CaCl_2) model suspension or wastewaters. Experimental protocol for filtration/backwash cycles is described in Table 5 and protocol for valve control in Appendix 4 .

Membrane was first conditioned for 45 minutes at $\text{TMP}=0.5$ bar with the saline solution for humic acid filtration and with water from tap for the wastewater filtration. Feed solution (humic acid suspension or wastewaters) was then filtered at $\text{TMP}=0.5$ bar. A permeate volume of 40 L.m^{-2} was filtered for each membrane. Backwash was finally performed at constant backwash pressure of 2.0 bar for 1 minute. The filtration/backwash cycle was successively repeated 14 times (maximum number of cycles in a working day). The rinsing step between each cycle allowed the evacuation of the detached cake fragments (after each backwash).

Table 5: Experimental protocol for several filtration/backwash cycles for humic acid (CaCl₂) and wastewaters at constant filtration pressure TMP=0.5 bar and constant backwash pressures BTMP=2.0 bar.

Step	Solution	Pressure (bar)	Duration (min)
Conditioning			45
Permeability measurement	Saline solution/water	TMP=0.5	5
<i>Draining and refilling with feed solution</i>			
1st Filtration cycle	Feed solution	TMP=0.5	5-45
1st Backwash cycle	Saline solution/water	BTMP=2.0	1
<i>Rinsing step with feed solution</i>			
2nd Filtration cycle	Feed solution	TMP=0.5	5-45
2nd Backwash cycle	Saline solution/water	BTMP=2.0	1
<i>Rinsing step with feed solution</i>			
⋮			
14th Filtration cycle	Feed solution	TMP=0.5	5-45
14th Backwash cycle	Saline solution/water	BTMP=2.0	1
<i>Rinsing step with feed solution</i>			

2.4.4 Fouling analysis

2.4.4.1 Hydraulic resistance

In some phrases, “hydraulic resistance” was abbreviated in “resistance” to lighten the text.

2.4.4.1.1 Darcy' Law

In ultrafiltration, the permeate flux is modelled by the resistance-in-series model based on Darcy's Law Eq. 5. A flux decline is observed when fouling occurs during suspension filtration with the increase of fouling resistance.

$$J = \frac{1}{S_{ext}} * \frac{dV_p}{dt} = \frac{TMP}{\mu * (R_m + R_f)} \quad \text{Eq. 5}$$

with J the permeate flux ($\text{L}\cdot\text{m}^{-2}\cdot\text{h}^{-1}$), t the time (h), R_m the membrane hydraulic resistance in outside-in mode ($\text{m}^2\cdot\text{L}^{-1}$) measured at specific TMP (bar), μ the water viscosity ($\text{bar}\cdot\text{h}$) and R_f the total fouling hydraulic resistance ($\text{m}^2\cdot\text{L}^{-1}$).

The total fouling resistance is composed of a hydraulically reversible fouling and an irreversible fouling.

$$R_f = R_{rev} + R_{irrev}$$

R_{rev} the reversible fouling hydraulic resistance ($\text{m}^2\cdot\text{L}^{-1}$) and R_{irrev} the irreversible fouling hydraulic resistance ($\text{m}^2\cdot\text{L}^{-1}$)

2.4.4.1.2 Membrane hydraulic resistance

The membrane hydraulic resistance for each membrane was obtained when saline solution was filtered (Eq. 5, with $R_f = 0$). As explained for permeability measurements in section 2.5.3, the membrane resistance varied with the pressure, time and flow direction.

2.4.4.1.3 Bentonite cake hydraulic resistance

Bentonite was fully retained by each membrane (i.e. rejection rates equal to 100%) and only cake deposition was observed during membrane fouling. It was assumed that there was no pore blocking nor adsorption nor biofilm. The total fouling resistance was then assumed exclusively caused by the cake formation ($R_f = R_c$, with R_c the cake hydraulic resistance in $\text{m}^2\cdot\text{L}^{-1}$ or m^{-1}). The hydraulic resistance of bentonite cake was determined for each bentonite feed suspension. As identical cake resistances were found at the end of the filtration and between the different membranes, mean cake resistance was calculated for all membranes for bentonite (KCl) and for bentonite (CaCl₂).

2.4.4.1.4 Bentonite specific cake resistance

The specific cake resistance provides information on the cake structure and its properties. The specific cake resistance can be expressed by Eq. 6 since the deposited mass calculated by Eq. 7 increases linearly with filtered permeate volume due to dead-end filtration mode [169]. Full bentonite retention ($R=1$) was measured for each hollow-fiber membrane whereas various humic acid retention were measured.

$$\alpha = \frac{R_c * S_{ext}}{m_d} \quad \text{Eq. 6}$$

$$m_d = R * C_{feed} * V_p \quad \text{Eq. 7}$$

with α the specific cake resistance (m.kg^{-1}), R_c the cake hydraulic resistance (m^{-1}), R the particle retention, C_{feed} the particle concentration of the feed (g.L^{-1}) and V_p the permeate volume (L).

2.4.4.1.5 Humic acid fouling resistance

Due other fouling mechanisms such as adsorption or pore blocking in the case of humic acid filtration, the total fouling resistance was calculated using Eq. 5 but cake resistance alone was not determined.

2.4.4.2 Humic acid adsorption

Membrane were rinsed with ethanol and then with ultrapure water. An 80 cm long sample of each hollow-fiber membrane was placed in a 0.05 g.L^{-1} humic acid solution for 200 hours. Absorbance of the solution was measured, after moderate stirring, by UV/vis spectroscopy (detailed in 2.6.3) at different times (between 1 and 200 h). Kinetics and equilibrium of static adsorption of humic acid on the external membrane surface were determined from absorbance measurements and calibration curve for humic acid suspension (Figure 25).

2.4.4.3 Retention

The retention of model feed solutions for each hollow-fiber membrane was calculated by:

$$R = 1 - \frac{C_p}{C_{feed}}$$

With C_p the concentration of particle in the permeate (g.L^{-1}).

Particle concentration was measured by turbidity for bentonite suspension and by UV/vis spectroscopy for humic acid suspensions. Retention was averaged for each feed and membrane.

In the case of wastewaters, the retention efficiency was assessed by the total organic carbon reduction.

$$R_{TOC} = 1 - \frac{TOC_p}{TOC_{feed}}$$

With R_{TOC} the total organic carbon reduction, TOC_p the total organic carbon in the permeate (g.L^{-1}) and TOC_{feed} the total organic carbon in the feed solution (g.L^{-1}).

Total organic carbon (TOC) concentration was determined using a Shimadzu TOC analyzer, TOC-L series.

2.4.5 Fouling removal analysis

2.4.5.1 Backwash flux densities

As backwash pressure was kept constant, the backwash flux was increasing during the backwash step due to the gradual elimination of the cake, and was difficult to measure due to short time scale (\sim seconds) of the cake removal. The backwash flux (J_{bw}) was calculated using the Darcy's law and was only valid for the fouled membrane before cake removal. The cake hydraulic resistance was assumed constant in outside-in or inside-out mode. However, the membrane resistance was dependent on the mode and the pressure due to membrane deformation, the backwash flux was therefore calculated for each backwash pressure by Eq. 8.

$$J_{bw} = Lp'_f * BTMP = \frac{BTMP}{\mu * (R'_m + R_f)} \quad \text{Eq. 8}$$

with J_{bw} the backwash flux through the fouled membrane ($\text{L.m}^{-2}.\text{h}^{-1}$), Lp'_f the permeability of the fouled membrane in inside-out mode ($\text{L.m}^{-2}.\text{h}^{-1}.\text{bar}^{-1}$) and R'_m the membrane hydraulic resistance in inside-out mode ($\text{m}^2.\text{L}^{-1}$) measured at specific BTMP.

2.4.5.2 Mass balance method

The backwash efficiency was assessed by the percentage of cake removed during a single backwash and was calculated by the mass balance method [107], [117] using Eq. 4.

Rinsing waters obtained after backwash were included in the backwash waters. Cake removal amount of the second backwash (Table 4) was added to the first backwash to calculate cake removal percentage at the second backwash pressure. Cake removal percentages were averaged for each backwash pressure on a minimum of 3 measurements.

2.5 Hollow-fiber membrane characterization

2.5.1 Morphology and internal structure

Hollow-fiber membrane samples were cryofractured in liquid nitrogen and coated with gold under vacuum before being observed with scanning electron microscopy (SEM, Phenom XL Desktop). Pictures of the cross-sectional area of the membranes were taken to measure the hollow-fiber dimensions (external diameter D_e , internal diameter D_i and thickness h). The global morphology (tubular shape) and the inner structure (sponge-like, finger like or macroporous structure) were observed under SEM. The skin layer layer was also observed to check that the membrane surface was free of defects.

2.5.2 Mechanical properties

2.5.2.1 Tensile test

Hollow-fiber membranes were mechanically tested using the testing machine Instron 3342 equipped with pneumatic grips for cord and yarn. The initial gauge length was fixed at 85 mm and the elongation rate at 50 mm/min. Specimen was axially elongated up to breaking. Tensile force and displacement were recorded by BlueHill 2 software. Young's modulus E , stress at break σ_{break} , elongation at break ε_{break} and elongation at elastic limit $\varepsilon_{elastic\ limit}$ of the membranes were measured in wetted-conditions and ambient temperature from stress-strain curves (Figure 22). Measurements were repeated 5 times for each sample.

The tensile force was measured and the tensile stress was calculated by BlueHill 2 software using the provided hollow-fiber dimensions. When a hollow-fiber membrane is subjected to tensile force along its axis, the applied stress is calculated by:

$$\sigma_t = \frac{F_t}{\pi(r_e^2 - r_i^2)}$$

With σ_t the tensile stress (Pa), F_t the tensile force (N), r_e the external radius of the fiber (m) and r_i the internal radius of the fiber (m).

The displacement during elongation was measured and strain was calculated by BlueHill 2 software using:

$$\varepsilon = \frac{L - L_0}{L_0}$$

With ε the strain, L the sample length (m), L_0 the initial sample length or gauge length (m).

The stress at break σ_{break} and elongation at break ε_{break} were measured at the breakage of the fiber (as illustrated on Figure 22).

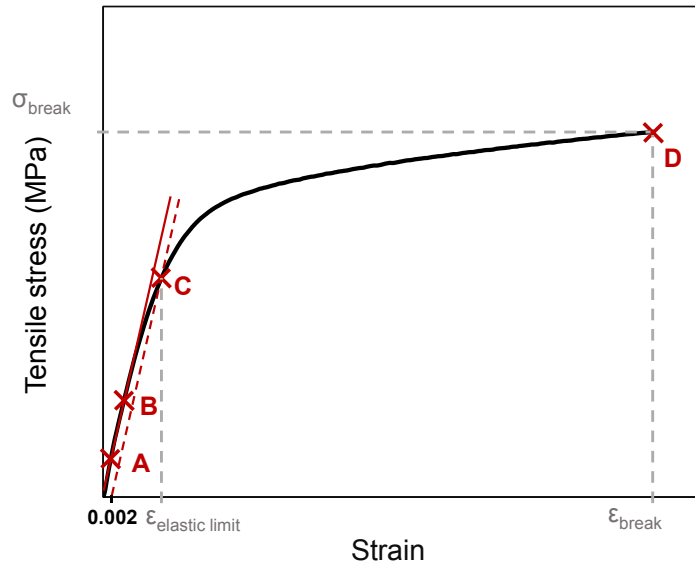


Figure 22: Stress-strain representative curve of polymeric membrane for mechanical properties analysis. A-B: Young's modulus slope, C: Elastic limit at 0.2% $\varepsilon_{elastic\ limit}$ and D: Breakage at σ_{break} and ε_{break} .

2.5.2.2 Young's modulus

The tensile Young's modulus E describes the tensile elasticity of a material. It was calculated on Excel using the Hooke's law:

$$E = \frac{\sigma_t}{\varepsilon} \quad \text{Eq. 9}$$

With E the tensile Young's modulus (MPa).

The Young's modulus was calculated in the linear elastic slope of the stress-strain curve in a range of strain from 0.4% to 0.9% ($\varepsilon=0.004-0.009$) over 10 measuring points (between A and B on Figure 22).

2.5.2.3 Elastic limit

The elastic limit is defined as the limit of the linear elastic behavior. Below the elastic limit, the strain is reversible when stress is no longer applied whereas it becomes plastic (no longer completely reversible) once the elastic limit is exceeded. When limit of the elastic behavior is difficult to detect, the elongation at elastic limit $\epsilon_{elastic\ limit}$ can be measured at the intersection between a line drawn parallel to the Young's modulus slope (red dashed line) at 0.2% strain with the stress-strain curve as illustrated on Figure 22.

2.5.2.4 Loading-unloading cycle

Loading-unloading cycle was carried out using the same testing machine and same initial conditions (i.e. gauge length, elongation rate). Specimen was axially elongated up to a maximum strain (comprised between 0.3% and 10%) before returning to the initial gauge length. The cycle was repeated 10 times successively. Tensile force and displacement were continuously recorded with BlueHill 2 software. The software feature "Preliminary cycle" was used to reproduce loading-unloading cycle as there was no cyclic feature on the software. Elastic recovery and residual strain for loading-unloading cycle can be determined from stress-strain curves as shown on Figure 23 [170].

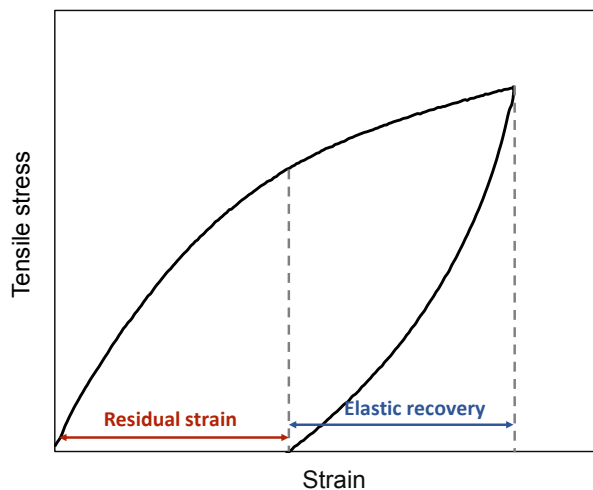


Figure 23: Representation of the elastic recovery and plastic deformation on stress-strain curve for loading-unloading cycle.

2.5.3 Ultrapure water permeability

2.5.3.1 Membrane permeability equations

Membrane permeability was assed using filtration unit A (Figure 19) and a module with four hollow-fiber membranes in “U-configuration” (see on Figure 21, B) in both outside-in and inside-out modes. Each membrane permeability was calculated and temperature corrected at 20°C using Eq. 10 and Eq. 11 for the applied pressure. The external surface was used for both permeability calculations since the filtration was performed in outside-in mode.

$$Lp_{TMP} = \frac{V_p}{S_{ext} * t * TMP} * (1 - 0,025 * (20 - T)) \quad Eq. 10$$

With Lp_{TMP} the membrane permeability ($L \cdot m^{-2} \cdot h^{-1} \cdot bar^{-1}$) in outside-in mode measured at specific TMP, S_{ext} the hollow-fiber membrane external surface (m^2), t the time (h) and T the temperature ($^{\circ}C$).

$$Lp'_{BTMP} = \frac{V_p}{S_{ext} * t * BTMP} * (1 - 0,025 * (20 - T)) \quad Eq. 11$$

With Lp'_{BTMP} the membrane permeability ($L \cdot m^{-2} \cdot h^{-1} \cdot bar^{-1}$) in inside-out mode measured at specific BTMP, $BTMP$ the backwash transmembrane pressure (bar).

2.5.3.2 Influence of membrane conditioning

Membrane permeability was measured during the conditioning for 3 hours at constant pressure TMP or BTMP=0.8 bar with ultrapure water in both outside-in and inside-out modes to evaluate the effect of conditioning on permeability.

2.5.3.3 Pressure-dependence of membrane permeability

Prior to measure the permeability variations with the applied pressure in inside-out and outside-in mode, the membrane was conditioned for 45 minutes at TMP or BTMP=0.2 bar with ultrapure water in outside-in or inside-out mode respectively. The ultrapure water permeability measured under 0.2 bar pressure was taken as reference value for a membrane assuming no deformation and no pore compaction. Water membrane permeability was then measured at different pressures from 0.4 to 2.4 by incremental pressures of 0.2 bar (as described in Table 6) in both outside-in and inside-out modes. Comparison was made between

permeability measurements in outside-in and inside-out modes and the reference value measured under 0.2 bar. The reversibility of the permeability was assessed at 1.4 and 2.4 bar by comparing $Lp_{1.4}$ to $Lp_{0.2}$ and $Lp_{2.4}$ to $Lp_{0.2}$, with $Lp_{0.2}$ the permeability at $TMP=0.2$ bar.

Table 6: Experimental protocol for measurement of permeability variations and its reversibility in both inside and outside modes, with pressure comprised between 0.2 and 2.4 bar.

Step	Pressure (bar)	Time (min)
Conditioning	0.2	45
Measurement	0.2-0.4-0.6-0.8-1.0-1.2-1.4	5 for each pressure
Relaxation	0.2	10
Measurement	0.2	5
Measurement	1.6-1.8-2.0-2.2-2.4	5 for each pressure
Relaxation	0.2	10
Measurement	0.2	5

2.5.3.4 Membrane permeability and hydraulic resistance variation during single filtration/backwash cycle

Ultrapure water membrane permeability was varying with operating pressures ($TMP=0.8$ and $BTMP=[0.2-2.5]$) during the different steps of the filtration/backwash cycle due to membrane deformation. However, membrane hydraulic resistances obtained from permeability measurements are required for the calculation of backwash flux (Eq. 8). These permeability variations under pressure were therefore accurately measured for a clean fiber during filtration/backwash cycle using only ultrapure water (protocol described in Table 4). A permeability variation rate, calculated for each fiber and at each backwash pressure, is expressed by:

$$Vr_{LP} = \frac{Lp'_{BTMP} - Lp_{0.8}}{Lp_{0.8}} \quad Eq. 12$$

With Vr_{LP} the variation rate of the membrane permeability measured in inside-out at given $BTMP$ to the membrane permeability measured in outside-in at $TMP=0.8$ bar.

The permeability variation rate was assumed independent of the initial membrane water permeability for a given membrane. However, as initial water membrane permeability can vary with storage time and therefore for the different fouling studies with bentonite and humic acid,

water membrane permeability and hydraulic resistance during backwash were recalculated using the following equations:

$$Lp'_{BTMP} = Lp_{0.8}(Vr_{LP} + 1)$$

$$R'_m = \frac{1}{\mu L p'_{BTMP}} = \frac{1}{\mu L p_{0.8}(Vr_{LP} + 1)} \quad Eq. 13$$

2.5.4 Hydrophilicity

Hollow-fiber membrane were cut along the length, flattened and mounted on a support with double-sided adhesive tape. Static contact angle from air captive bubble in ultrapure water was measured on flattened membrane surface at room temperature by a Krüss drop shape analyzer, Model DSA30, equipped with image-processing software. A micro-syringe injected a 10 μ L air bubble on the surface. Measurement of the contact angle was made 300 ms after the drop contacted the surface. Water contact angle for each hollow-fiber membrane was averaged over 10 measurements.

2.5.5 Porosity

Brunauer-Emmett-Teller (BET) analysis was carried out on MicrotracBel nitrogen adsorption analyzer, Model Belsorp-max. Dry membranes were cut down, placed into a glass tube and outgassed before analysis. Nitrogen adsorption was measured at 77 K. Pore size distribution and specific surface area were determined from nitrogen adsorption/desorption isotherms using NLDFT model and BET method.

2.5.6 Membrane deformation

External diameter of the membrane was measured under digital camera on filtration unit B at different pressures. Pictures of hollow-fiber membrane were taken at incremental pressure comprised between TMP=[0-1.5] bar and BTMP=[0-2.4 bar]. Diameter of the membrane was measured using ImageJ software on the picture taken at the center of the cell for each pressure. Two measurements were made at two random locations of the picture to confirm reproducibility. Deformation reversibility was measured after relaxation of 10 min at zero pressure (for deformation at 0.8, 1.5 and 2.4 bar).

2.6 Particle suspension characterization

All samples were sonicated 5 minutes in ultrasonic bath (frequency was 37 kHz and power was 90 W) at ambient temperature before analysis. Particle size, zeta potential, turbidity and UV/vis spectroscopy were measured for each model feed solutions (bentonite (KCl), bentonite (CaCl₂) and humic acid (CaCl₂) suspension). Total organic carbon, dry matter concentration and turbidity were measured for the wastewaters feed solution.

2.6.1 Particle size and zeta potential analysis of model suspensions

Particle size and zeta potential were determined using the instrument Malvern Zetasizer Nano ZS90. The sample was placed in appropriate vial (DTS1070 vial for potential zeta and DTS0012 for particle size) and analyzed at ambient temperature and neutral pH. Particle size and zeta potential were averaged on three successive measurements for each sample.

Prior to zeta potential analysis, the refractive index of particle suspension was measured with a refractometer, as this value was required for measurement.

As particles were not spherical, the so-called particle size was not fully correct and used for comparison. Indeed, the instrument measured the hydrodynamic equivalent diameter of bentonite and humic acid particles assimilated to spherical particles.

These analyses were also performed on prepared suspensions with particle concentration of 0.05 g.L⁻¹ and of varying ionic strength from 10⁻⁵ to 1 M by adding KCl or CaCl₂.

2.6.2 Turbidity

2.6.2.1 Analysis

Turbidity was measured using a HACH turbidimeter, Model 2100N. The sample was placed into an appropriate vial and agitated just before analysis. Turbidity measurement was recorded after stabilization or after 2 minutes.

This analysis was also performed on bentonite suspensions with particle concentration of 0.05 g.L⁻¹ and of varying ionic strength from 10⁻⁵ to 1 M by adding KCl or CaCl₂.

2.6.2.2 Calibration curves for bentonite suspensions by turbidity

Calibration curves of the turbidity as a function of the particle concentration were established for KCl and CaCl₂ and at ionic strength of 10⁻³ M (see on Figure 24). Particle concentration was varied between 0.005 and 0.1 g.L⁻¹, the maximal value during experiments. The calibration curves were used to calculate the particle concentration in the prepared feed solution and in the collected backwash waters.

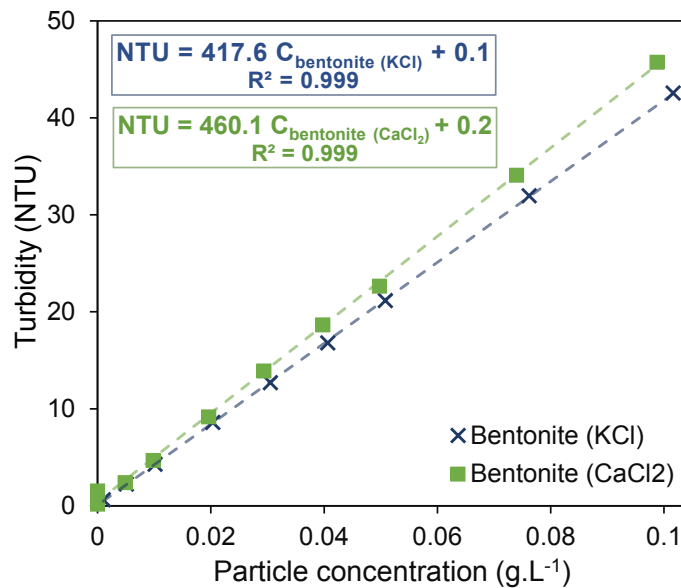


Figure 24: Turbidity calibration curves for particle concentration calculation for bentonite (KCl) and bentonite (CaCl₂) suspensions, $I=10^{-3}$ M

2.6.3 Ultraviolet-visible spectroscopy

2.6.3.1 Analysis

Absorbance spectroscopy was measured using a UV/Vis spectrophotometer, Model PerkinElmer Lambda 365. The sample was placed in a quartz cell and spectra was measured in the range between 190 and 400 nm. Absorbance was measured at wavelength of 254 nm.

This analysis was also performed on humic acid suspensions with particle concentration of 0.05 g.L⁻¹ and of varying ionic strength from 10⁻⁵ to 1 M by adding CaCl₂.

2.6.3.2 Calibration curve for humic acid suspension by UV-spectroscopy

Calibration curve of the absorbance as a function of the humic acid (CaCl_2) concentration (Beer-Lambert law) was established at a wavelength of 254 nm and ionic strength of 10^{-3} M (Figure 25). Humic acid concentration was varied between 0.001 and 0.05 g.L^{-1} , the maximal value during experiments. The calibration curve was used to calculate the humic acid concentration in the prepared feed solution and in the collected backwash waters.

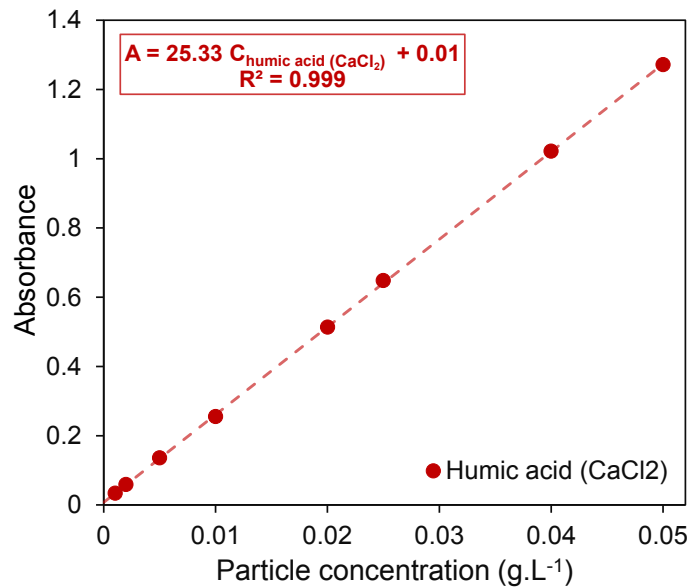


Figure 25: UV absorbance calibration curve for humic acid (CaCl_2) suspension, at a wavelength of 254 nm, $I=10^{-3}$ M

2.6.4 Analysis of wastewater feed solution

Total Organic Carbon (COT) concentration was measured using a Shimadzu TOC analyzer, TOC-L series. Dry matter concentration was measured using a Sartorius gravimetric moisture analyzer respectively. Turbidity was measured using HACH turbidimeter. Mean values are reported in Table 7.

Table 7: Analysis of wastewater feed solution.

Feed	COT (g.L^{-1})	Dry matter (g.L^{-1})	Turbidity (NTU)
Wastewaters	4.1	12	3570

2.7 Mechanical properties of the filter cake

2.7.1 Camera measurement

The deformation of the wet filter cake during backwash was measured under digital camera on filtration unit B. A cake was firstly formed on the membrane surface during filtration of particle suspensions as described previously (2.4.2). Backwash pressure was then gradually applied from zero to the pressure at which the cake is removed. Deformation of the cake was measured from pictures taken at different backwash pressures (before the pressure of detachment and rupture) and processed with ImageJ. Stress-strain curve was constructed for each cake by plotting the calculated ICMP (Eq. 36) as a function of the measured cake elongation. Only one measurement on a single fiber was performed for each cake.

2.7.2 Atomic force microscopy

A Nanowizard III (JPK Instruments) was used to perform atomic force microscopy measurements (AFM) on deposit samples to determine mechanical properties and particularly Young's modulus of wet filter cakes. The sample was prepared by particle suspension filtration on PVDF flat-sheet membrane to form a thick filter cake. The sample size was 3x3 cm. Prior to AFM measurement, the sample was wetted with the saline solution (salt of the filtration). The measurements were performed using a Bruker conic cantilever (model MLCT, made from silicon nitride) with a nominal spring constant of 0.031 N.m⁻¹ determined by thermal noise method. Deflection sensitivity was 46.17 nm.V⁻¹, ramp size was set to 2 μm and peak force to 1.5 nN. Force curves were processed on JPKSPM Data processing software. The Young's modulus was calculated from the force curves using the following expression (Hertz-Sneddon model):

$$F = \frac{E_f}{(1 - \nu_f^2)} * \frac{2 \tan \theta}{\pi} * \delta^2 \quad \text{Eq. 14}$$

With F the applied force (N), θ the half-cone angle (°) ($\theta = 17.5^\circ$ for MLCT cantilevers), and δ the indentation depth (m).

Chapter 3 - Preparation and
characterization of PVDF
hollow-fiber membranes

3.1 Introduction

Hollow-fiber membranes were prepared by dry/wet phase inversion, a process that has been extensively used for PVDF membranes [32][33][22]. However, preparing a hollow-fiber membrane with specific properties is still challenging as many operating parameters influence the final membrane properties. Indeed, the formation of the membrane morphology is the result of thermodynamic and kinetic exchange of solvent and non-solvent during the phase inversion [19][171].

In this research work, membrane preparation was focused on the membrane permeability and mechanical properties of the spun hollow-fiber since they were the main properties of interest. A complete characterization of the membrane (structure, permeability, mechanical and surface properties) was carried out on the different spun hollow-fibers. As a few membranes were expected to deform under filtration and backwash, the influence of pressure on the membrane permeability was extensively studied.

M-LP91, M-HP47, M-HP32 and M-LP19¹ were fully characterized as they were selected for fouling and fouling removal analysis (Chapter 5) whereas M-HP45 and M-LP59 were partially characterized (no surface measurement or extensive permeability study).

3.2 Hollow-fiber membrane preparation

3.2.1 Dope composition and spinning process

The dope solution was composed of a membrane-forming polymer (PVDF) mixed with a pore-forming agent (PEG, PVP or LiCl) dissolved into a solvent (NMP or DMSO). Dope compositions used to spin the selected hollow-fiber membranes are described in Table 8 (detailed composition for M-LP91 and M-LP19 can be found in Appendix 2). Different grades of Kynar[®] PVDF, additives and solvent were chosen to produce membrane with various properties and controlled mechanical properties in a range of Young's modulus comprised between 19 and 91 MPa (as seen on Table 12).

¹ Identification of the fiber code name: M for Membrane, LP for Low Permeability, HP for High Permeability and last two digits for Young's modulus of the membrane. For example, M-LP91 was a membrane with a low permeability and a Young's modulus of 91 MPa.

Table 8: Dope compositions for the preparation of PVDF blend membranes

Fiber Name	Polymer	Additive	Solvent
M-LP91	Kynar® HSV 900 <i>Homopolymer</i>	LiCl	NMP
M-HP47	Kynar® MG15 <i>Homopolymer</i>	PVP	NMP
M-HP32			
M-LP19	Kynar Flex® 2801-00 <i>HFP-copolymer</i>	PEG	DMSO
M-LP59	Kynar® RC10,312 <i>HFP-copolymer</i>	PVP	NMP
M-HP45			

The dope solutions (from Table 8) were spun through a spinneret in a tubular shape. The spinning conditions were fully described for M-LP91 and M-LP19 in Appendix 2 but were confidential for the other membranes. The nascent hollow-fibers were then immersed in a water coagulation bath at elevated temperature ($>50^{\circ}\text{C}$) where phase inversion took place. Spun membranes were then stored in sodium bisulfite solution (1 wt.% in ultrapure water) in a cool place.

3.2.2 Adjustment of compositions and spinning conditions to new spinning apparatus

In this project, formulations and spinning conditions for M-HP32 hollow-fiber membrane were provided by Arkema S.A. . However, the existing spinning apparatus in the laboratory was different from the one in Arkema, specifically with regard to the spinneret dimensions. Works have been carried out to adapt the composition and spinning operating conditions from Arkema to the lab spinning apparatus.

3.2.2.1 Shape control

As observed on Figure 26, irregularities were formed in the inner contour of the spun hollow-fiber membrane when using the dope and bore formulations provided by Arkema. Due to the viscoelastic properties of PVDF, rapid phase inversion would prevent the polymer chains from

relaxing and the accumulated back stress in the nascent hollow-fiber might cause these irregularities [22]. One of the strategy to suppress these inner irregularities was to increase the amount of solvent (NMP) in the bore fluid to slow down the solvent/non-solvent exchanges [22]. Effective suppression of the waves and proper tubular shape was observed by increasing the amount of solvent (NMP) of 10% in the bore fluid (as seen on Figure 26).

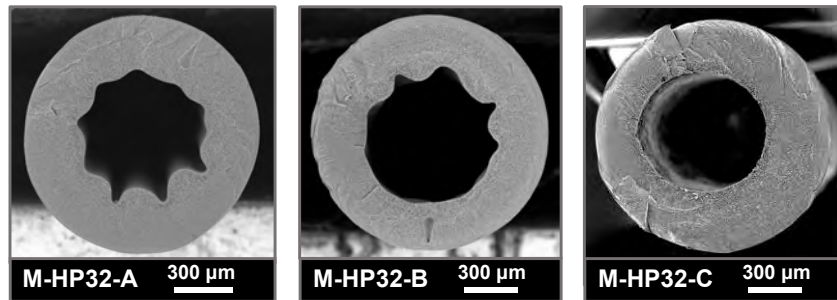


Figure 26: Influence of bore fluid composition on the tubular shape of the lumen of PVDF hollow-fiber membrane. Weight fraction of NMP in bore fluid: 50 wt.% in M-HP32-A; 55 wt.% in M-HP32-B; 60 wt.% in M-HP32-C.

Due to different spinneret dimensions between the two spinning units, the flow rates provided by Arkema could not be implemented in the lab unit. Adjustment of the flow rate was made to prepare membranes with similar dimensions and properties than the spun fibers from Arkema. Firstly, the flow rates of dope and bore fluid (in $\text{ml}\cdot\text{min}^{-1}$) were converted in speed rates (in $\text{m}\cdot\text{min}^{-1}$) based on spinneret dimensions (needle and die). The ratio of dope to bore fluid speed rate was then kept constant between the two units to produce membranes with close dimensions (outer diameter, inner diameter and thickness). Morphology and dimensions of the spun membrane (M-HP32C) was similar to the one from Arkema (M-REF) as observed on SEM pictures on Figure 27. However, mechanical properties were lower than the ones given by Arkema. The Young's modulus of M-HP32-C was 50% lower than M-REF. One of the assumption to explain this difference was the different shear stress induced in the spinneret during hollow-fiber membrane spinning as explained in the following section (3.2.2.2).

3.2.2.2 Shear stress in the spinneret

During dope extrusion through the spinneret, the polymer chains are subjected to shear stresses that force the chain to align in the direction of the shear increasing molecular orientation [172]. It has been reported in the literature that shear stress greatly affects the membrane properties such as permeability [173] or mechanical properties [59]. Chung *et al.*

[59] observed an increase of the Young's modulus from 58 to 104 MPa when the shear rate was multiplied by 10 (from 245 to 2568 s⁻¹).

Shear stress and shear rate profiles in the spinneret were calculated using the model described by Shilton [174] for each membrane. Shear values at the external wall of the spinneret are listed in Table 9. It was observed much higher shear stress and shear rate for M-HP32-C than M-REF. The lab spinneret had indeed narrower annular channels than the spinneret in Arkema resulting in higher shear. The dope and bore flow rate can be reduced to decrease the shear rate, while keeping the constant ratio of dope to bore fluid speed rate to have the same dimensions. M-HP32-D was spun with the same calculated shear stress than M-REF whereas M-HP32-C had higher shear (Table 9).

Table 9: Shear stress and shear rate at the external wall of the spinneret for M-REF, M-HP32-C and M-HP32-D.

Fiber Name	Shear stress T (N.m ⁻²)	Shear rate $\dot{\gamma}$ (s ⁻¹)
M-REF	7,200	1,500
M-HP32-C	10,700	2,500
M-HP32-D	7,200	1,500

As observed on Figure 27, M-HP32-D showed a comparable morphology and same dimensions than M-HP32-C. However, the mechanical properties were also the same than M-HP32-C (lower than M-REF) meaning that the shear rate here did not affect the mechanical properties. A critical shear rate was demonstrated in the literature from which molecular orientation is at its maximum [172]. At high shear values (in the range of values from Table 9), mechanical properties were therefore slightly or no longer impacted [175][59]. It was then assumed that the shear rate when spinning M-HP32-C and M-HP32-D was higher than critical shear rate since identical Young's modulus was found between the two spun membranes. The difference in Young's modulus between M-REF (spun in Arkema) and M-HP32-C or M-HP32-D (spun in lab) was not explained here, but other parameters such as chemical suppliers or other spinning conditions (i.e. time in coagulation bath or temperature at the outlet of the spinneret) should be considered.

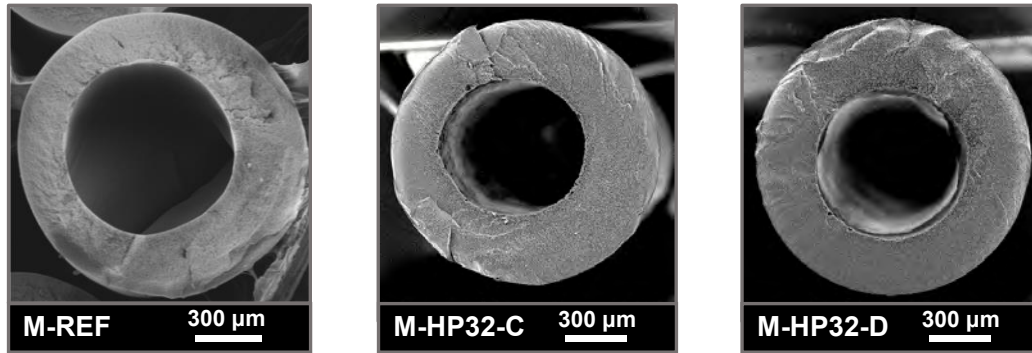


Figure 27: Preparation of membranes at same dope to bore speed ratio but different shear rate at the external wall of spinneret. Shear rates: $1,500\text{ s}^{-1}$ for M-REF; $2,500\text{ s}^{-1}$ for M-HP32-C; $1,500\text{ s}^{-1}$ for M-HP32-D.

3.2.3 Chlorine washing effect

It has been reported in the literature that PVP molecules are prone to leach out due to its small size during the filtration and the membrane permeability was not stable during use [45]. High dose of chlorine was therefore used to accelerate the ageing of PVDF/PVP blend membranes. While PVDF was almost not affected by chlorine in these conditions, the degradation of PVP involving chain scission mechanism increased the membrane permeability [47][49]. From Table 10, it can be observed that M-HP32 membrane permeability increased with the soaking time in sodium hypochlorite solutions. The membrane permeability was multiplied by more than 3 times when soaking the spun fiber in 15,000 ppm chlorine bath at pH 11 for 6 hours compared to the non-treated membrane.

Table 10: Effect of chlorine dose during the washing step of the PVDF/PVP membrane preparation on the membrane permeability. Membrane were soaked in 15,000 ppm chlorine bath for several hours (0-6 hours) at pH 11.

Fiber Name	Dose of Chlorine (ppm.h)	L_p (L.m ² .h ⁻¹ .bar ⁻¹)
M-HP32	0	150
	60,000	200
	90,000	500

3.3 Structural, mechanical and surface properties

A first selection of the spun membranes was based on the basic appearance (i.e. tubular shape and defect free) and dimensions of the fiber (ratio of the inner diameter to outer diameter

comprised between 0.5 and 0.7). Then, permeability and mechanical properties were measured and further selection was based on the Young's modulus of the hollow-fiber membranes and membrane permeability. Membranes with different mechanical properties and different, but sufficient, permeabilities were targeted in order to explore the influence of these properties on the filtration/ backwash process.

3.3.1 Internal structure observation

Cross sectional area of each spun hollow-fiber membrane was observed under SEM (Figure 28). Even if PVDF was the polymer used for the preparation of all membranes, very different inner morphology was obtained for each membrane. The water coagulation bath, at elevated temperature, induced a rapid liquid-liquid demixing of the polymeric solution preventing from crystallization [30][31] and leading to sponge-like, finger-like or macrovoid structure as observed on Figure 28. M-HP32 was the only fiber that presents a sponge-like structure without macrovoid while M-LP19 had a finger-like structure through the entire membrane wall. For some membranes, the membrane wall was divided into two layers: M-LP91 had for instance a macrovoid structure in the inner layer of the membrane wall and sponge-like structure in the outer layer whereas M-LP59 has a sponge-like structure in the inner layer of the membrane wall and a finger-like structure in the outer layer.

Dope composition and spinning operating parameters greatly influenced the thermodynamic and the kinetic of the solvent/non-solvent exchange during phase separation resulting in the formation of various inner structures [19][171][176][23][30]. Further investigation on the morphology was not the focus of this work. Nevertheless, pore size and pore distribution were measured on M-LP91, M-HP47, M-HP32 and M-LP19 by BET analysis and results are presented in Appendix 5 .

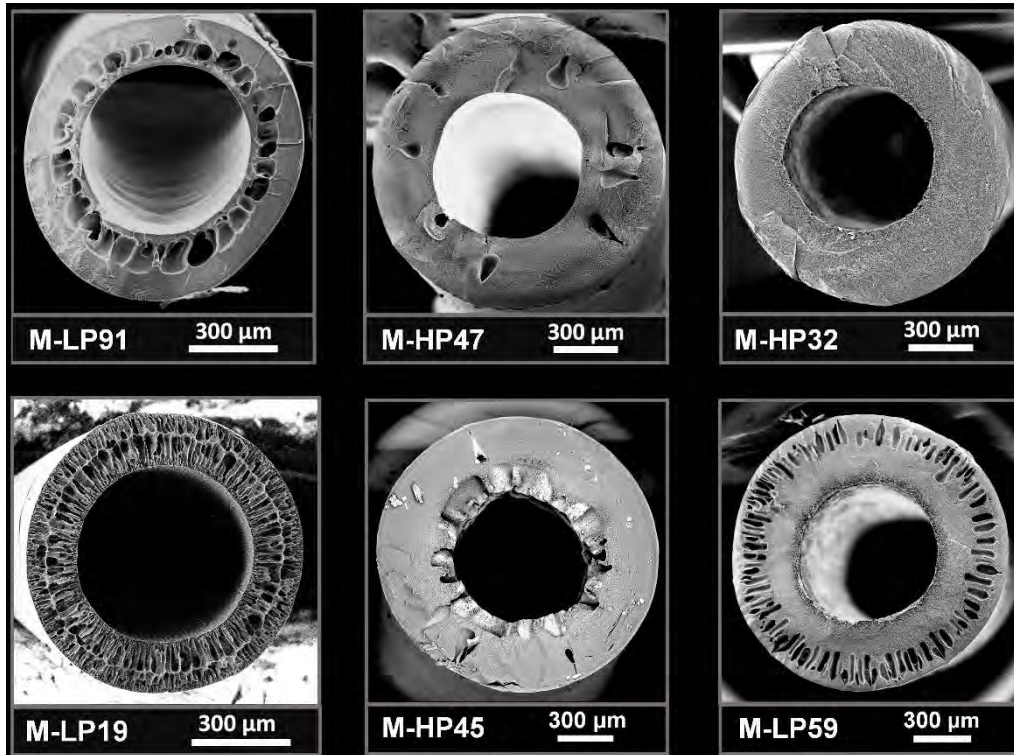


Figure 28: Cross-sectional SEM pictures of PVDF hollow-fiber membranes

External (D_e) and internal (D_i) diameter of the hollow-fiber membrane were measured on the SEM pictures and reported in Table 11. Membrane wall thickness (h) and diameter ratio (R_D), defined by the ratio of internal diameter over external diameter, were calculated from these measurements. Dimensions were also very different between the hollow-fibers: M-LP19 and M-LP91 had an outer diameter between 0.8 and 1.0 mm and a wall thickness below 200 μm while the other membranes had an outer diameter comprised between 1.3 and 1.5 mm and a thickness above 250 μm . Membrane diameters were mainly controlled by the extrusion rates of the dope and bore fluid, and especially by the take-up speed. The outer diameter was for instance increased when increasing the dope flow rate whereas inner diameter was increased when increasing the flow rate of bore fluid. Diameter ratio could be therefore adjusted with the ratio of dope to bore fluid flow rates. Increasing the take-up speed stretched the nascent fiber and decrease the dimensions of the spun fiber. However, the effect of these operating parameters was in an ideal case and dimensions of the fiber were more difficult to adjust in reality. Indeed, the main objective was to prepare membrane with a proper hollow-fiber shape and specific properties (e.g. high permeability and various mechanical properties).

Table 11: Dimensions of PVDF hollow-fiber membranes

Fiber Name	D_e (μm)	D_i (μm)	h (μm)	R_D
M-LP91	925	565	180	0.61
M-HP47	1390	840	275	0.60
M-HP32	1350	670	340	0.50
M-LP19	840	530	155	0.63
M-LP59	1430	700	365	0.49
M-HP45	1500	700	400	0.47

3.3.2 Mechanical properties

In this research study, the selection of the membranes was focused on the final mechanical properties of the spun fiber, and especially on the Young's modulus that described the tensile elasticity. Commercial PVDF membranes have generally Young's modulus above 40 MPa and tensile strength above 2 MPa [136][22] to allow good mechanical resistance during filtration and cleaning steps. However, a couple of membranes with lower Young's modulus was selected in this study as they were suspected to deform to a greater extent under pressure. As described in the literature, dope composition [57][51][22] and spinning operating conditions [19][32][59] had a large influence on the Young's modulus of PVDF hollow-fiber membranes. In this work, the dope composition, and especially the grade of Kynar® PVDF and type of additives (Table 8), was changed to obtain different PVDF membranes with a large range of mechanical properties (Table 12).

The tensile stress-strain curve was established for each hollow-fiber on Figure 29. All mechanical properties such as the Young's modulus E , the stress at break σ_{break} , the elongation at break ε_{break} and the elongation at elastic limit $\varepsilon_{elastic\ limit}$ of each spun fiber were taken from these stress-strain curves and reported in Table 12. A large range of Young's modulus from 19 MPa to 91 MPa was obtained for the different PVDF membranes. The stress at break was higher for membranes with higher Young's modulus. M-LP91 had the highest tensile strength with $\sigma_{break}=5.6$ MPa and highest Young's modulus with $E=91$ MPa whereas M-LP19 had the weakest mechanical properties with a stress at break of 1.6 MPa and a Young's modulus of 19 MPa. All PVDF membranes were highly deformable with elongation at break above 100%,

but the deformation was considered partially irreversible when elongation exceeded the elastic limit (approximately 2%). M-LP91 and M-LP19 had the lowest elastic limit with an elongation at elastic limit of 1.5% and 1.8% respectively. This low elastic limit might be due to the thin membrane wall (<200 μm) of the two membranes.

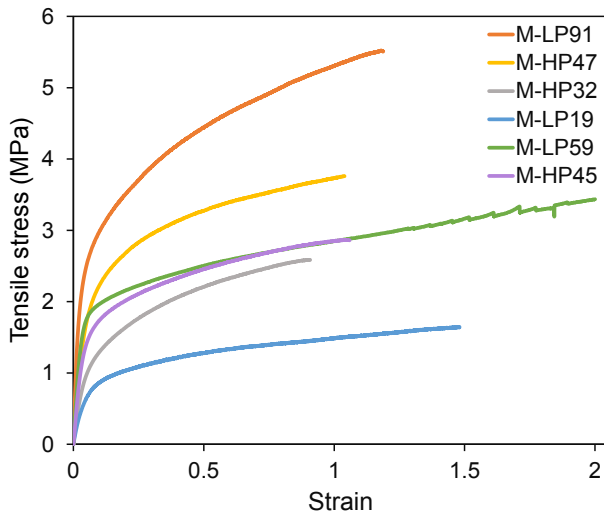


Figure 29: Tensile stress-strain curves for the spun PVDF hollow-fiber membranes at an elongation rate of $50 \text{ mm}\cdot\text{min}^{-1}$ and for a gauge length of 85 mm.

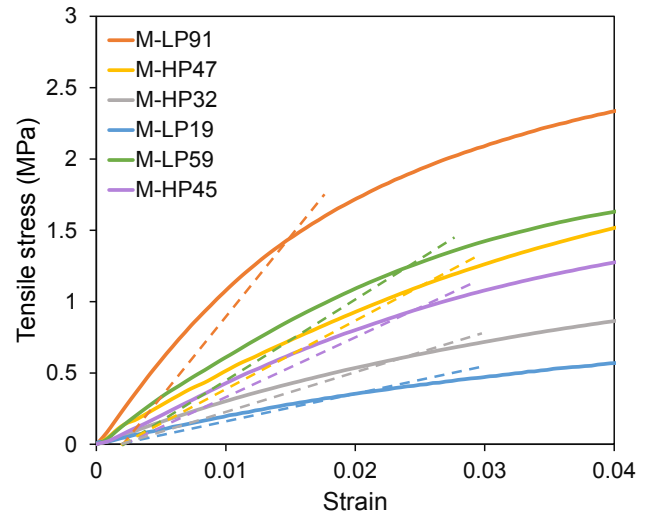


Figure 30: Zoom on elastic domain from tensile stress-strain curves (Figure 29). Dotted lines are indicative curves for the determination of elastic limit.

Table 12: Mechanical properties of the PVDF hollow-fiber membranes determined from tensile stress-strain curves (Figure 29).

Fiber Name	E (MPa)	σ_{break} (MPa)	ϵ_{break} (%)	$\epsilon_{elastic\ limit}$ (%)
M-LP91	91 ± 5	5.6 ± 0.2	125 ± 6	1.5 ± 0.2
M-HP47	47 ± 2	3.7 ± 0.3	104 ± 18	2.6 ± 0.8
M-HP32	32 ± 2	2.6 ± 0.1	92 ± 6	2.3 ± 0.4
M-LP19	19 ± 1	1.6 ± 0.1	140 ± 12	1.8 ± 0.2
M-LP59	59 ± 2	3.4 ± 0.2	200 ± 17	2.3 ± 0.4
M-HP45	45 ± 1	2.8 ± 0.1	107 ± 6	2.4 ± 0.3

Several loading-unloading cycles were performed on hollow-fiber membranes in and out of the elastic domain (Table 12) to show the reversibility of the deformation on the long term. As observed in Appendix 6, even when the deformation remained in the elastic domain (below

1.5%), a residual strain was observed when stress was no longer applied. This residual strain was composed of a viscoelastic strain, which recovers with time and a plastic strain, which is irreversible [177][178]. However, the testing machine and the software was not adapted to accurately measure microstrains and loading-unloading cycles (no cyclic testing feature with the software).

3.3.3 Surface hydrophilicity

The membrane surface hydrophilicity was characterized by water contact angle (WCA) measurement. The membrane is considered hydrophobic when the contact angle exceed 90° and hydrophilic when this one is below 90° . Water contact angle was measured on wet PVDF blend membranes through the captive air bubble method and reported in Table 13. Contact angle measurement was only performed on M-LP91, M-HP47, M-HP32 and M-LP19 since they were selected for fouling analysis (Chapter 5).

Even if PVDF is considered as a hydrophobic polymer [19], all measured contact angles on the PVDF membranes were lower than 56° (value found for pristine Kynar[®] HSV 900 [35]) indicating a hydrophilic membrane. The crystallinity and the roughness of the membrane might be responsible of this low contact angle [35].

The measured contact angle for PVDF/LiCl blend membrane was very similar to the pure Kynar[®] HSV 900 while a lower value of approximatively 40° was found for M-HP47 and M-HP32 indicating a more hydrophilic membrane surface. According to the literature, lithium chloride do not affect the membrane surface hydrophilicity [35] and the addition of PEG could slightly decrease the water contact angle [23]. However, the use of PVP can significantly increase the surface hydrophilicity [40][44]. The addition of PVP in the preparation of M-HP47 and M-HP32 membranes (Table 8) might be therefore responsible for the lowest measured contact angles. As different grades of PVDF (homopolymer or copolymer) were used (see Table 8), the effect of each additive on the contact angle could not be confirmed here.

Table 13: Water contact angle on PVDF membrane surface

Fiber Name	WCA (°)
M-LP91	54 ± 3
M-HP47	37 ± 3
M-HP32	40 ± 2
M-LP19	50 ± 3

3.4 Membrane permeability

In Chapter 5, all filtrations of the model suspensions were carried out under constant pressure at TMP=0.8 bar in outside-in mode for different filtration times. The membranes were then backwashed at different pressures (BTMP= [0.2-2.5 bar]) for 1 minute. Due to various mechanical properties, an extensive study on the membrane permeability was performed in outside-in and inside-out mode. It was important to analyze the influence of time and pressure on each membrane permeability when ultrapure water was passed through the membrane due to compaction phenomenon and membrane deformation. This preliminary study of the membrane permeability was essential to explain the fouling and fouling removal mechanisms during filtration and backwash step.

3.4.1 Comparison of membrane permeability

Membranes were first conditioned with ultrapure water, in outside-in mode at 0.8 bar, for 45 min prior to measure the stable membrane permeability for each hollow-fiber at the same pressure. Average permeability of each membrane was reported in Table 14. M-LP19, M-LP91 and M-LP59 hollow-fiber membranes had a low permeability (LP) below 200 L.m⁻².h⁻¹.bar⁻¹ compared to M-HP32, M-HP47 and M-HP45, which had high permeability (HP) above 400 L.m⁻².h⁻¹.bar⁻¹. The presence of PVP in M-HP32, M-HP47 and M-HP45 (see on Table 8) greatly contributed to the increase in permeability [40].

Table 14: Average membrane permeability of Kynar® PVDF hollow-fiber in outside-in mode at TMP=0.8 bar ($Lp_{0.8}$) after 1 h of conditioning with ultra-pure water.

Fiber Name	$Lp_{0.8}$ (L.m ⁻² .h ⁻¹ .bar ⁻¹)
M-LP91	260 ± 20
M-HP47	490 ± 40
M-HP32	500 ± 30
M-LP19	150 ± 30
M-LP59	190 ± 20
M-HP45	830 ± 50

3.4.2 Time-dependence of the membrane permeability

Before measuring the membrane permeability and before filtration, the membrane was conditioned with ultrapure water to eliminate residual impurities or remaining solvent in the hollow-fiber membrane and have a stabilized flux. Furthermore, phenomenon of compaction are observed on polymeric membrane under pressure and the conditioning step allows the precompaction of the membrane [179][180]. Degree of compaction and its reversibility depend on the membrane material and structure [181].

The membrane permeability was plotted as a function of the conditioning time with ultrapure water for each membrane (Figure 31). Conditioning was performed in outside-in (Lp) and inside-out (Lp') modes under constant pressure at TMP or BTMP=0.8 bar. A strong difference in membrane permeability was observed for M-LP19 and M-HP32 when comparing in outside-in and inside-out mode whereas there was no difference for M-HP47 and M-LP91 between the two modes. The M-LP19 membrane permeability at 0.8 bar was indeed 3.5 times higher in inside-out than in outside-in mode. M-LP19 and M-HP32 were the membranes the most prone to compaction [182] when subjected to external pressure due to their low Young's modulus (Table 12).

Furthermore, all membrane permeabilities in outside in mode were completely stable after 45 min of conditioning with ultra-pure water (Figure 31) except M-LP19 that showed a slight decrease over time of its permeability after 45 min as shown on Figure 32. This low decrease

of the permeability might be attributed either to a continuous compaction of pore or to a creep behavior of the polymeric membrane under constant pressure. Regarding the measurements in inside out, the membrane permeability was stabilized after 90 min even for M-LP19. In particular, M-HP32 demonstrated a strong change of its permeability during conditioning.

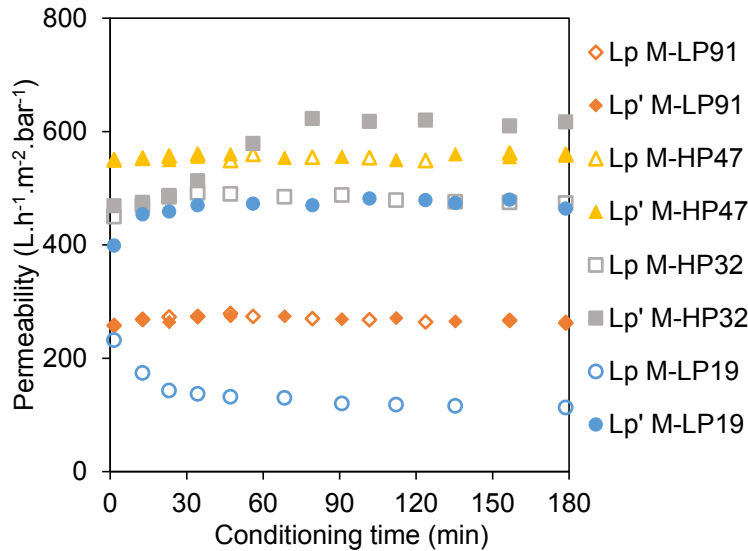


Figure 31: Time-dependence of membrane ultrapure water permeability in outside-in (L_p) and inside-out (L_p') modes at constant TMP or BTMP=0.8 bar.

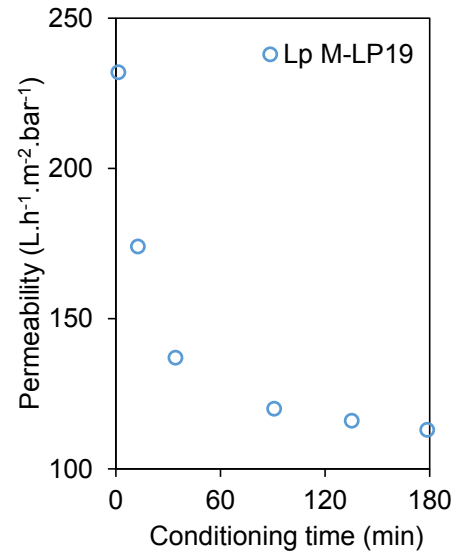


Figure 32: Zoom on membrane ultrapure water permeability of M-LP19 in outside-in (L_p) at constant TMP=0.8 bar

3.4.3 Pressure-dependence of the membrane permeability

Compaction phenomenon and membrane surface deformation were also dependent of the applied pressure. Compaction of the pores is assumed to be responsible for a permeability loss of the membrane with increasing the pressure [181][183] especially for elastic materials [182]. Due to various mechanical properties of the hollow-fibers, the permeability behavior of each membrane versus the pressure in outside-in and inside-out modes are reported in Figure 33. Membrane were firstly conditioned at 0.2 bar for 45 minutes and the flux was stabilized for 5 min at each pressure before membrane permeability measurement. The membrane permeability in outside-in mode was always below the permeability in inside-out mode suggesting a compaction effect due to external pressure. At a TMP or BTMP of 2.0 bar, the relative difference of the ultra-pure water permeability in inside-out mode ($L_{p'2.0}$) to the permeability in outside-in mode ($L_{p2.0}$) was 6%, 14%, 35% and 94% for M-LP91, M-HP47, M-HP32 and M-LP19 respectively. These results showed that a membrane with a low Young's modulus was more sensitive to pressure and deformed to a greater extent.

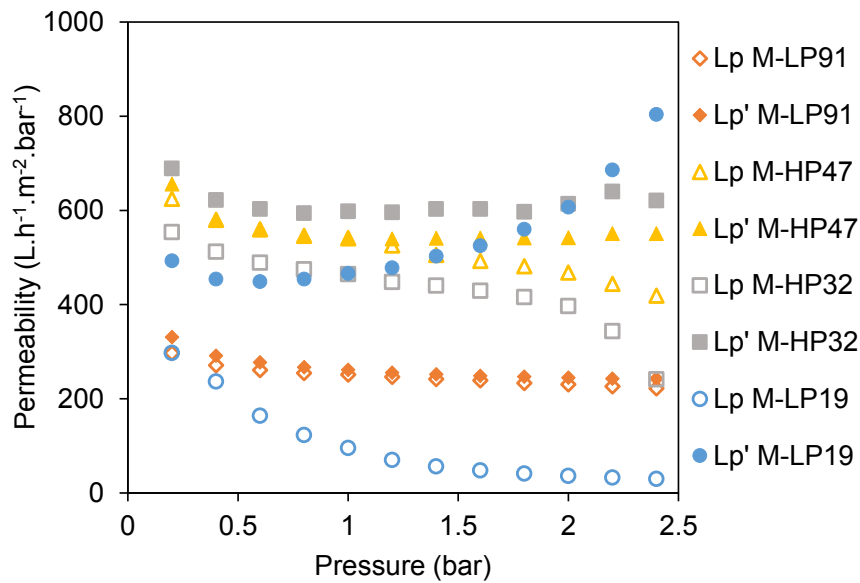


Figure 33: Pressure-dependence of membrane ultrapure water permeability in outside-in (L_p) and inside-out (L_p') modes.

High recovery of the initial permeability was observed for M-LP91, M-HP47 and M-HP32 (reversibility from 97 to 100%) when the pressure was reduced from 2.5 to 0.2 bar indicating a completely reversible compaction. Regarding M-LP19, 95% of reversibility was measured when the pressure was reduced from 1.5 to 0.2 bar. However, the reversibility of the membrane permeability was lower (up to 85%) when reducing the pressure from 2.5 to 0.2 bar, indicating an irreversible compaction and plastic deformation of the material. In inside-out mode, the permeability was constant when increasing the pressure for most membranes and was increasing for M-LP19. Enlargement of the pores was responsible for this increase in permeability for the most elastic fiber [184][141] as the pore density was assumed unchanged (free of new defect).

3.4.4 Membrane permeability during filtration and backwash process

Membrane permeability was depending on the flux direction, the conditioning time and the pressure but also on the operating steps. Indeed, the membrane permeability measured in inside-out with a continuous increase of the pressure (as seen on Figure 33) was different than the membrane permeability measured during short backwash (for 60 seconds) and performed just after the filtration cycle, especially for M-LP19. Furthermore, membrane permeability might also slightly vary with storage time especially for M-LP19 for which permeability changed during the year (as shown in Table 15). This permeability change could be attributed

to membrane ageing (i.e. additive leaching) or eventually due to non-uniform material in the batch.

Table 15: Initial membrane permeability measured with ultrapure water in outside-in mode at TMP=0.8 bar for the different studies performed at different time of the year: bentonite (KCl), bentonite (CaCl₂) and humic acid (CaCl₂).

Fiber Name	Lp_{0.8}(L.m⁻².h⁻¹.bar⁻¹) with ultrapure water <i>In the case of study with:</i>		
	bentonite (KCl) <i>September 2018</i>	bentonite (CaCl ₂) <i>April 2019</i>	humic acid (CaCl ₂) <i>July 2019</i>
M-LP91	280 ± 30	250 ± 20	250 ± 20
M-HP47	510 ± 40	450 ± 50	510 ± 30
M-HP32	490 ± 60	530 ± 60	490 ± 50
M-LP19	160 ± 30	175 ± 30	115 ± 10

Consequently, more accurate measurements of membrane permeability were made on filtration/backwash cycle with ultrapure water (as described in 2.5.3.4). The permeability variation rate measured at different backwash pressures during filtration/backwash cycle was obtained using Eq. 12 for the different fibers and is given in Table 16.

Table 16: Membrane permeability variation rates measured with ultrapure water in inside-out mode at different backwash pressures compared to permeability measured in outside-in mode at TMP=0.8 bar.

Fiber Name	Permeability variation rate Vr_{LP} for each BTMP					
	0.2 bar	0.4 bar	0.8 bar	1.5 bar	2 bar	2.5 bar
M-LP91	23%	12%	7%	6%	3%	1%
M-HP47	29%	15%	10%	12%	11%	14%
M-HP32	29%	15%	10%	11%	11%	14%
M-LP19	110%	106%	118%	153%	189%	284%

Membrane hydraulic resistances (R'_m) for the different fouling studies were calculated from Table 15 and Table 16 using Eq. 13. These values were used for the calculation of backwash fluxes (Eq. 8).

3.5 General conclusion

Hollow-fiber membranes made from various grades of PVDF and additives were successfully prepared by spinning and phase inversion, by adapting the spinning operating conditions, and dope and bore compositions. Membranes were selected for further investigation according to their shape, permeability and mechanical properties.

Complete characterization of morphology, mechanical and surface properties, and permeability was carried out on four membranes: M-LP91, M-HP47, M-HP32 and M-LP19. The selected membranes had Young's modulus comprised between 19 and 91 MPa, water contact angle between 37 and 54° and permeability between 150 and 500 L.m⁻².h⁻¹.bar⁻¹ (at TMP=0.8 bar). The permeability of the membrane was affected by the conditioning time and the storage time but particularly by the applied pressure and the flow direction (outside-in or inside-out mode) leading to strong variations of the permeability during process operations. Compaction phenomenon and membrane surface deformation were mainly responsible of the decrease or increase in the membrane permeability. Compaction was reversible for all membranes except M-LP19 that was irreversibly compacted or deformed under high pressure (>1.5 bar).

The extensive characterization of mechanical and mass transfer properties for each hollow fiber membrane was a preliminary step for the calculation of the membrane deformation under pressure (Chapter 4) and the understanding of the fouling removal mechanisms (Chapter 5).

Chapter 4 - Membrane

deformation under pressure:

Modelling and experimental
study

4.1 Introduction

Most polymeric materials are able to reversibly deform (up to a certain limit) under mechanical stress. Polymeric membranes are therefore experiencing deformations under pressure operations. During water filtration in outside-in mode, hollow-fiber membrane is subjected to external pressure and compaction phenomenon is observed [183]. Whereas during the backwash, the flow is reversed and the membrane is subjected to internal pressure leading to an expansion of the membrane external surface [12]. The hollow-fiber membrane is therefore subjected to numerous compressive stresses during filtration-backwash cycles, which cause the membrane deformation. In the literature, a few studies have investigated the deformation of the membrane with a focus on the compaction of membrane during the filtration [183] and pore deformation during backwash [141]. However, no complete analysis of the circumferential deformation of hollow-fiber membranes during pressure operation has been conducted yet.

In this chapter, the membrane deformation was numerically calculated by a model based on the mechanical deformation of thick-walled cylinders [185][186] and theoretical strain curves were compared with the external diameter strain of the hollow-fibers measured under digital camera. Membranes with a lower Young's modulus were expected to undergo more significant deformation under pressure.

4.2 Numerical model for the deformation of thick-walled cylinder

4.2.1 System definition

The initial hollow-fiber membrane was represented by a thick-walled cylinder having an inner radius r_i and an outer radius r_e , with a cross-sectioned area A_0 . Membrane wall was considered thick since the ratio of the inner diameter to the wall thickness was below 20 [187] (equations could be simplified in the case of thin-walled cylinder). During the filtration and backwash step, the membrane deformed as represented on Figure 34. External pressure (P_e) compressed the membrane and caused a reduction of the external and internal diameter of the hollow-fiber while internal pressure (P_i) expanded the membrane and caused an expansion of the internal and external diameter. The variation of the membrane wall thickness was uncertain. A non-porous material would compress and the membrane wall would be thinner in both cases, but

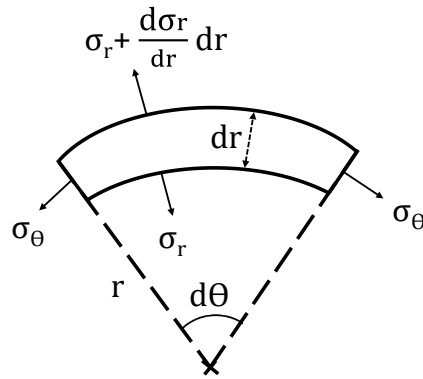


Figure 35: Circumferential and radial stress on an element of the membrane wall

At equilibrium, the sum of all the forces in the radial direction gives:

$$\sum F_r = 0$$

With F_r the forces (N) applied on the wall element in the radial direction at the equilibrium.

The radial force equilibrium of the element gives after neglecting the small terms and higher order:

$$\sigma_\theta - \sigma_r - r \frac{d\sigma_r}{dr} = 0 \quad \text{Eq. 15}$$

With σ_θ the circumferential stress (MPa), σ_r the radial stress (MPa) and r the radius position (m)

In order to solve Eq. 15, the Hooke's generalized law is used:

$$\begin{aligned} \varepsilon_r &= \frac{1}{E} (\sigma_r - \nu\sigma_l - \nu\sigma_\theta) \\ \varepsilon_\theta &= \frac{1}{E} (\sigma_\theta - \nu\sigma_r - \nu\sigma_l) \\ \varepsilon_l &= \frac{1}{E} (\sigma_l - \nu\sigma_r - \nu\sigma_\theta) \end{aligned} \quad \text{Eq. 16}$$

With ε_r the elongation of the element in the radial direction, ε_θ the elongation of the element in the circumferential direction, ε_l the elongation in the longitudinal direction, σ_l the longitudinal stress (MPa), E the Young's modulus (MPa) and ν the Poisson's ratio.

σ_r and σ_θ are expressed as function of the elongations and σ_l

From Eq. 16:

$$\sigma_r = E \varepsilon_r + \nu(\sigma_l + \sigma_\theta) \quad \text{Eq. 17}$$

Eq. 18 is obtained by substituting Eq. 17 in Eq. 16.

$$\varepsilon_\theta = \frac{1}{E} (\sigma_\theta - \nu(E \varepsilon_r + \nu(\sigma_l + \sigma_\theta)) - \nu\sigma_l) \quad \text{Eq. 18}$$

σ_θ is obtained from Eq. 18 after simplifying:

$$\sigma_\theta = \frac{E}{1 - \nu^2} (\varepsilon_\theta + \nu\varepsilon_r) + \frac{\nu}{1 - \nu} \sigma_l \quad \text{Eq. 19}$$

Eq. 20 is obtained by substituting Eq. 19 in Eq. 17 after simplifying:

$$\sigma_r = \frac{E}{1 - \nu^2} (\varepsilon_r + \nu\varepsilon_\theta) + \frac{\nu}{1 - \nu} \sigma_l \quad \text{Eq. 20}$$

The radius displacement of a cylindrical surface of radius r is denoted u was introduced to continue the resolution of the stress equations. The radial displacement of a surface of radius $r + dr$ is $u + \frac{du}{dr} dr$. According to the strain-displacement relationship, a wall element undergoes a deformation in the radial and circumferential direction of:

$$\varepsilon_r = \frac{du}{dr} \quad \text{Eq. 21}$$

$$\varepsilon_\theta = \frac{2\pi(r + u) - 2\pi r}{2\pi r} = \frac{u}{r}$$

The radial displacement is constant in the circumferential direction but varies in the radial direction. The change in diameter was given by the circumferential strain and not the radial strain.

Expressing the radial and circumferential elongations as a function of the radial displacement in Eq. 19 and Eq. 20 yields an equation system (Eq. 22) with one fewer unknown.

$$\sigma_\theta = \frac{E}{1 - \nu^2} \left(\frac{u}{r} + \nu \frac{du}{dr} \right) + \frac{\nu}{1 - \nu} \sigma_l \quad \text{Eq. 22}$$

$$\sigma_r = \frac{E}{1 - \nu^2} \left(\frac{du}{dr} + \nu \frac{u}{r} \right) + \frac{\nu}{1 - \nu} \sigma_l$$

Substituting Eq. 22 in Eq. 15 and after simplifying:

$$\frac{d^2u}{dr^2} + \frac{du}{rdr} - \frac{u}{r^2} = 0 \quad \text{Eq. 23}$$

The general solution of this equation is:

$$u = C_1 r + \frac{C_2}{r} \quad \text{Eq. 24}$$

Substituting Eq. 24 in Eq. 22 gives:

$$\sigma_\theta = \frac{E}{1-\nu^2} \left(C_1(1+\nu) + C_2 \frac{(1-\nu)}{r^2} \right) + \frac{\nu}{1-\nu} \sigma_l$$

$$\sigma_r = \frac{E}{1-\nu^2} \left(C_1(1+\nu) - C_2 \frac{(1-\nu)}{r^2} \right) + \frac{\nu}{1-\nu} \sigma_l$$

The constants C_1 and C_2 are determined using boundary conditions at the inner and outer surface of the cylinder where the pressures and therefore the normal stress are known.

At the external surface: $r = r_e$ and $\sigma_r = -P_e$

At the internal surface: $r = r_i$ and $\sigma_r = -P_i$

The sign of the stress is negative for compressive stresses and positive for tensile stresses.

And therefore from boundary conditions,

$$C_2 = \frac{1+\nu}{E} * \frac{r_i^2 r_e^2 (P_i - P_e)}{r_e^2 - r_i^2}$$

$$C_1 = \frac{1-\nu}{E} * \frac{r_i^2 P_i - r_e^2 P_e}{r_e^2 - r_i^2} - \frac{\nu}{E} \sigma_l$$

σ_l is different from zero in the case of a close ends cylinder subjected to internal and external pressure. The longitudinal stress is assumed uniformly distributed over the wall thickness far from the ends and is developed by pressure load on the close end as shown in Figure 36.

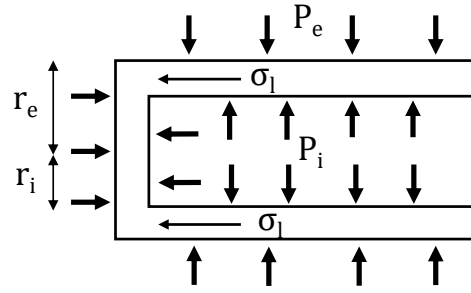


Figure 36: Force acting on the close end of the cylinder

The longitudinal force equilibrium gives:

$$\sigma_l * \pi(r_e^2 - r_i^2) = P_i * \pi r_i^2 - P_e * \pi r_e^2$$

Therefore,

$$\sigma_l = \frac{r_i^2 P_i - r_e^2 P_e}{r_e^2 - r_i^2} \quad \text{Eq. 25}$$

The final expressions of the different stresses σ_r , σ_θ and σ_l in the case of a thick-walled cylinder with close ends and subjected to external and internal pressures are:

$$\sigma_\theta = \frac{r_i^2 P_i - r_e^2 P_e}{r_e^2 - r_i^2} + \frac{r_i^2 r_e^2 (P_i - P_e)}{r^2 (r_e^2 - r_i^2)}$$

$$\sigma_r = \frac{r_i^2 P_i - r_e^2 P_e}{r_e^2 - r_i^2} - \frac{r_i^2 r_e^2 (P_i - P_e)}{r^2 (r_e^2 - r_i^2)} \quad \text{Eq. 26}$$

$$\sigma_l = \frac{r_i^2 P_i - r_e^2 P_e}{r_e^2 - r_i^2}$$

These equations are valid for isotropic and non-porous material in the case of small strains. The combination of these stresses results in the deformation of the hollow cylinder and in particular the deformation of the external diameter, which is calculated by the circumferential strain ε_θ expressed by:

$$\varepsilon_\theta = \frac{u}{r} = C_1 + \frac{C_2}{r^2} = \frac{1}{E} (\sigma_\theta - \nu \sigma_r - \nu \sigma_l)$$

The general expression for the diameter strain after simplifying is:

$$\varepsilon_{\theta} = \frac{1}{E} \left[(1 - 2\nu) \frac{r_i^2 P_i - r_e^2 P_e}{r_e^2 - r_i^2} + (1 + \nu) \frac{r_i^2 r_e^2 (P_i - P_e)}{r^2 (r_e^2 - r_i^2)} \right] \quad \text{Eq. 27}$$

4.2.3 Model limits

This model could be used to estimate the deformation of hollow-fiber membrane during the filtration under external pressure and during the backwash under internal pressure. However, in Timoshenko's book [185] the Lamé's equations were used to describe structural materials with strong stiffness (i.e. steel). The model could be limited for elastic material with very low Young's modulus such as membranes. The problem is also solved by linear-elastic approach. The deformation should therefore remain within the elastic range of the membrane.

Furthermore, the Lamé's equation are assumed valid for isotropic, homogenous and non-porous material. This represents the strongest assumption made in this deformation model. Membrane are indeed composed of porous structure comprising macrovoids and a skin layer, thus often referred to anisotropic and asymmetric materials.

4.2.4 Application of the model to membrane filtration

The deformations were only calculated on the external surface $r = r_e$ since fouling and fouling removal were studied on the membrane external surface.

The diameter ratio was defined by:

$$R_D = \frac{r_i}{r_e}$$

During filtration, the internal pressure is zero (relative pressure): $P_i = 0$. Thus, Eq. 27 becomes:

$$\varepsilon_{\theta} = -\frac{P_e}{E(1 - R_D^2)} [(1 - 2\nu) + R_D^2(1 + \nu)]$$

During backwash, the external pressure is zero (relative pressure): $P_e = 0$. Thus, Eq. 27 becomes:

$$\varepsilon_{\theta} = \frac{P_i (2 - \nu) R_D^2}{E (1 - R_D^2)}$$

For both cases, the deformation of the membrane was proportional to the pressure and inversely proportional to the Young's modulus of the membrane. Therefore, the lower the Young's modulus, the higher the deformation of the membrane under pressure. Furthermore, when R_D tends to 1, ε_θ tends to infinity whereas if R_D tends to 0, ε_θ tends to 0. Therefore, the closer R_D was to 1, the greater the deformation would be. Membrane initial dimension and wall thickness would greatly influence the membrane deformation. Finally, the Poisson's ratio plays a role in the deformation of the material but in the case of PVDF membranes it was considered constant and was found in literature at $\nu = 0.34$ [188]. Poisson's ratio for PVDF membranes varied from 0.32[188] to 0.4 [177] in the literature, however in this narrow range of values the calculated deformation was almost not affected.

4.2.5 Influence of membrane properties on hollow-fiber deformation under pressure

The model for thick-walled cylinder described in the previous section (4.2.2) was used to simulate the deformation of a membrane of varying properties to demonstrate the influence of each parameter on the diameter strain when subjected to external or internal pressure.

The influence of the transmembrane pressure on the membrane deformation was showed on Figure 37 and Figure 38, in the range of common pressure used in filtration (TMP=[0-2]bar). The deformation was calculated for typical membranes with Young's modulus in the range of 5-120 MPa and a constant diameter ratio of 0.6 (Figure 37). A negative diameter stain was found confirming that the membrane was compressed under external pressure as expected. Membranes with a lower Young's modulus should demonstrate higher membrane strain. The diameter ratio also influenced the computed membrane deformation as shown on Figure 38. Deformation was focused on membranes with Young's modulus of 10 and 30 MPa since high deformation were expected in this range. Increasing the diameter ratio to 0.9 (thin-walled membrane) would result in a great increase of the membrane deformation. Indeed, for a membrane with a Young's modulus of 10 MPa and a diameter ratio of 0.9, the external membrane diameter was expected to reduce to more than 7% under external pressure at TMP=1 bar.

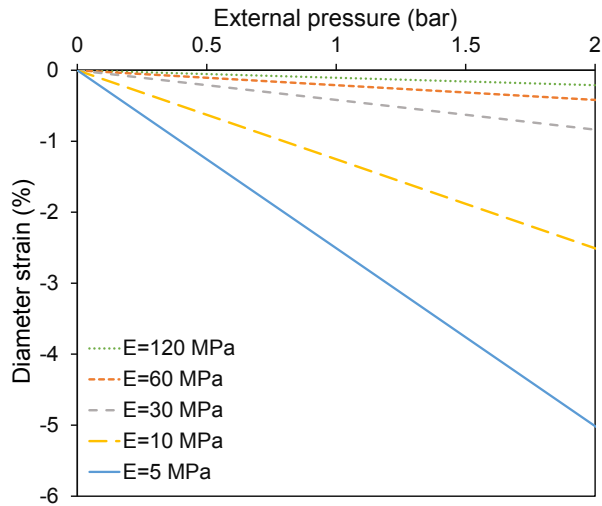


Figure 37: Numerical membrane deformation during filtration under external pressure for various Young's modulus, $E=[5-120]$ MPa and constant diameter ratio $R_D=0.6$

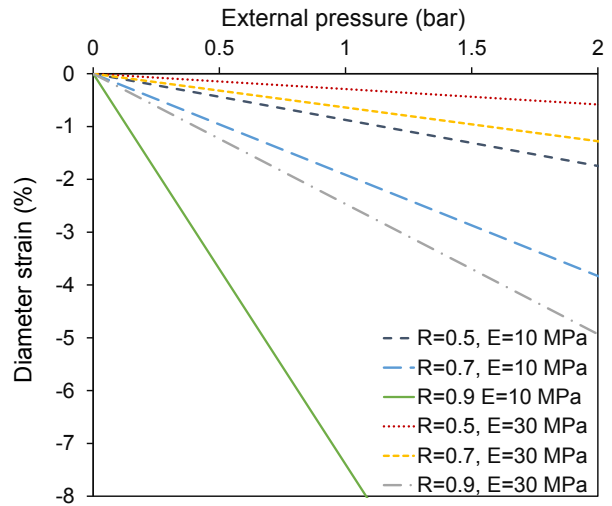


Figure 38: Numerical membrane deformation during filtration under external pressure for various diameter ratio, $R_D=[0.5-0.9]$ MPa and Young's modulus, $E=10$ or 30 MPa

The calculated deformation of the membrane under internal pressure (BTMP=[0-3]bar) during backwash was showed on Figure 39 and Figure 40. As previously, the influence of Young's modulus and diameter ratio was investigated. The positive deformation confirmed an expansion of the external membrane diameter during the backwash. This deformation could become $> 6\%$ at a backwash pressure of 3.0 bar but only for a membrane with a Young's modulus < 30 MPa and a diameter ratio > 0.9 or for a membrane with a Young's modulus < 10 MPa and a diameter ratio > 0.7 . According to the model, the same deformation at constant backwash pressure was expected for a membrane with a Young's modulus of 10 MPa and a diameter ratio of 0.5 and for a membrane with a Young's modulus of 30 MPa and a diameter ratio of 0.7.

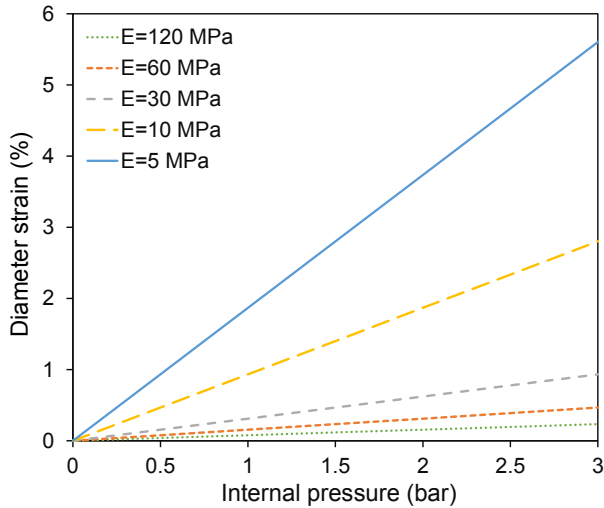


Figure 39: Numerical membrane deformation during backwash under internal pressure for various Young's modulus, $E=[5-120]$ MPa and constant diameter ratio $R_D=0.6$

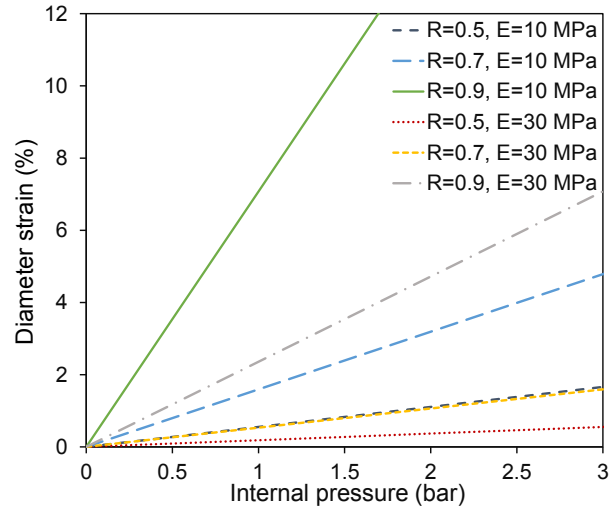


Figure 40: Numerical membrane deformation during backwash under internal pressure for various diameter ratio, $R_D=[0.5-0.9]$ MPa and Young's modulus, $E=10$ or 30 MPa

The membrane deformation could therefore be controlled by both the applied pressure and membrane properties (diameter ratio and Young's modulus). The deformation predicted by the Lamé's equation were small, the external diameter deformation was expected below 2 % since typical membranes have a Young's modulus above 30 MPa and a diameter ratio below 0.9. The same order of magnitude of diameter deformation was obtained in filtration and backwash with the applied pressure. However, the membrane should compress during filtration and expand during backwash.

4.2.6 Conclusion

The deformation of hollow-fiber membranes under pressure was simulated by a deformation model of thick-walled cylinder using the Lamé's equations. The deformation of the fiber diameter was the result of radial stress, circumferential stress and longitudinal stress (for close ends cylinder). The theoretical deformation was dependent on the applied pressure and also on the membrane properties (i.e. Young's modulus, Poisson's ratio and diameter ratio). According to the model, the deformations were predicted small (<2%) for most simulated membranes. Only membrane with very low Young's modulus and diameter ratio close to 1 would be able to reach deformation above 10%. However, calculated deformation should be carefully interpreted since the model was assumed valid for isotropic and non-porous material.

4.3 In-situ observation of membrane deformation under pressure

In order to check the validity of the predicted deformation by the model of deformation of thick-walled cylinder, the deformation of the hollow-fiber membrane under external and internal pressure was experimentally measured. Each hollow-fiber membrane was placed in the designed observation cell (Figure 21, C) to measure the deformation under external and internal pressure in the range of transmembrane and backwash pressures commonly used in ultrafiltration. Measurements were performed on two samples for each fiber and at two different locations along the fiber length to verify the reproducibility of the results.

4.3.1 Experimental deformation under external pressure

The diameter reduction was measured under external pressure by digital camera allowing $0.7 \mu\text{m}$ of resolution per pixel and the diameter strain was calculated at several backwash pressures (from 0.2 to 1.5 bar). As observed on Figure 41, the external radius (r_e) of the hollow-fiber membrane decreased by $11 \mu\text{m}$ at 0.8 bar and $18 \mu\text{m}$ at 1.5 bar.

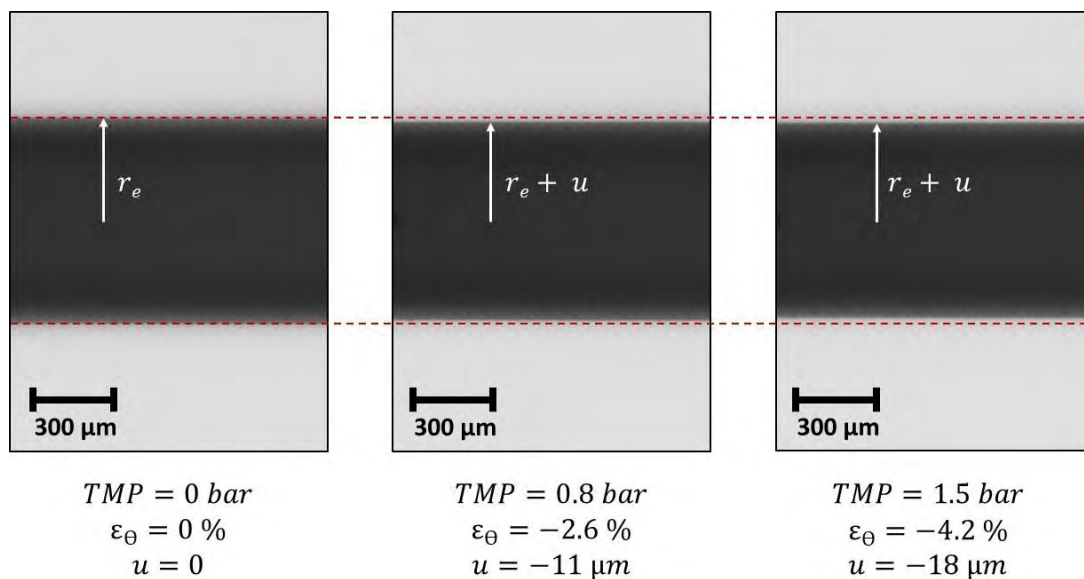


Figure 41: Observation of M-LP19 deformation under external pressure by digital camera at 0.8 and 1.5 bar. Red dotted lines are reference lines.

The diameter deformations under external pressure were measured on M-LP91, M-HP47, M-HP32 and M-LP19 between 0 and 1.5 bar (Figure 42).

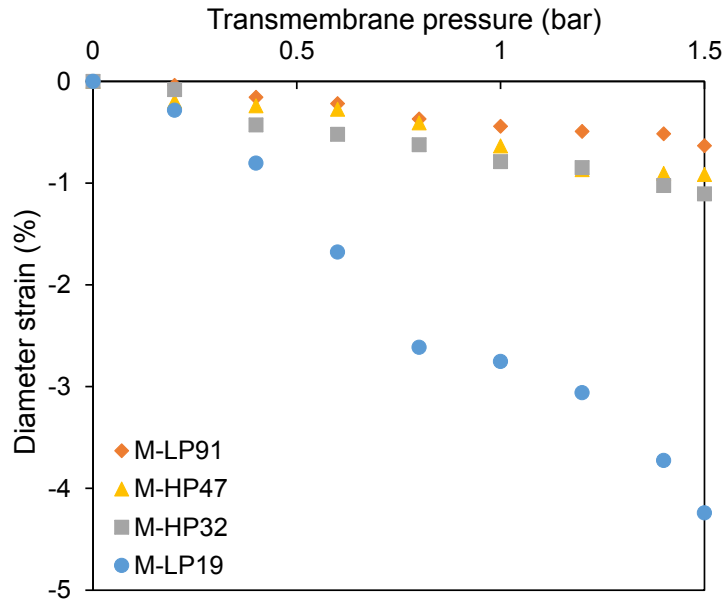


Figure 42: Experimental membrane deformation during filtration under external pressure for the selected membranes M-LP91, M-HP47, M-HP32 and M-LP19.

As calculated by the Lamé's equations the membranes were compressed with the applied pressure. The measured deformations for M-HP47, M-HP32 and M-LP91 were similar and below 1%. However, M-LP19 showed much higher deformation and the membrane strongly compressed with the pressure. In some tests on M-LP19, pinch points appeared on the hollow-fiber once the pressure exceeded 0.8 bar (as seen on Figure 43). This pinch was not studied in more details but it might come from the collapse of the structure under pressure or the pressure loss in the fiber lumen. The unintended rotation when placing the membrane in the observation cell could also cause the formation of pinch point when subjected to pressure. Diameter strain was measured far from this pinch point.

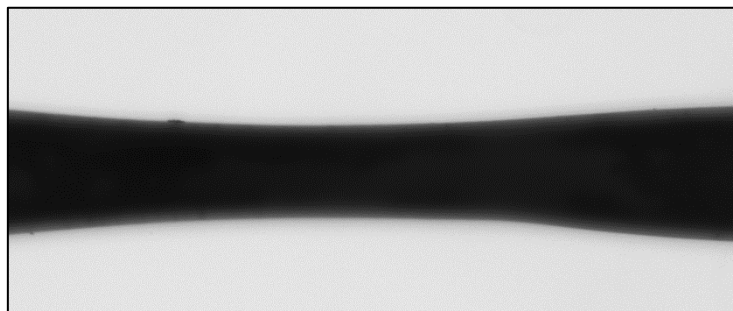


Figure 43: Pinch point observed on M-LP19 at a single location (middle of the fiber) at TMP=0.8 bar

4.3.2 Experimental deformation under internal pressure

Diameter expansion of M-LP19 under internal pressure was measured by digital camera and the diameter strain was calculated at several backwash pressures (from 0.2 to 2.4 bar). As observed on Figure 44, the radius of the hollow-fiber membrane increased by $32\ \mu\text{m}$ at 1.6 bar and by $62\ \mu\text{m}$ at 2.4 bar.

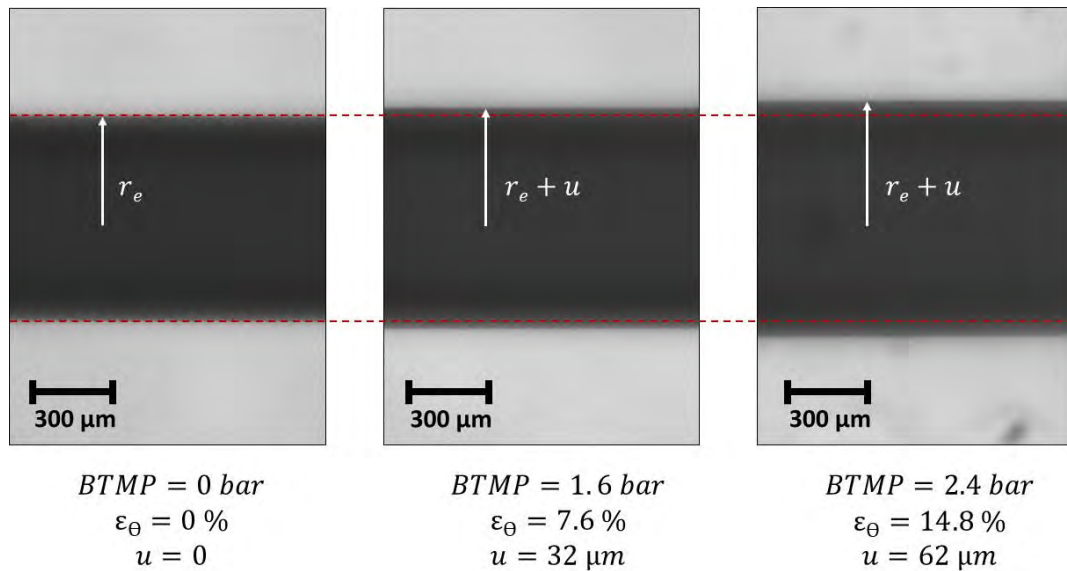


Figure 44: Observation of M-LP19 deformation under backwash pressure by digital camera at 1.6 and 2.4 bar. Red dotted lines are reference lines.

The deformations under backwash pressure were measured on M-LP91, M-HP47, M-HP32, M-LP19, M-HP45 and M-LP59 between 0 and 2.4 bar and results are plotted on Figure 45.

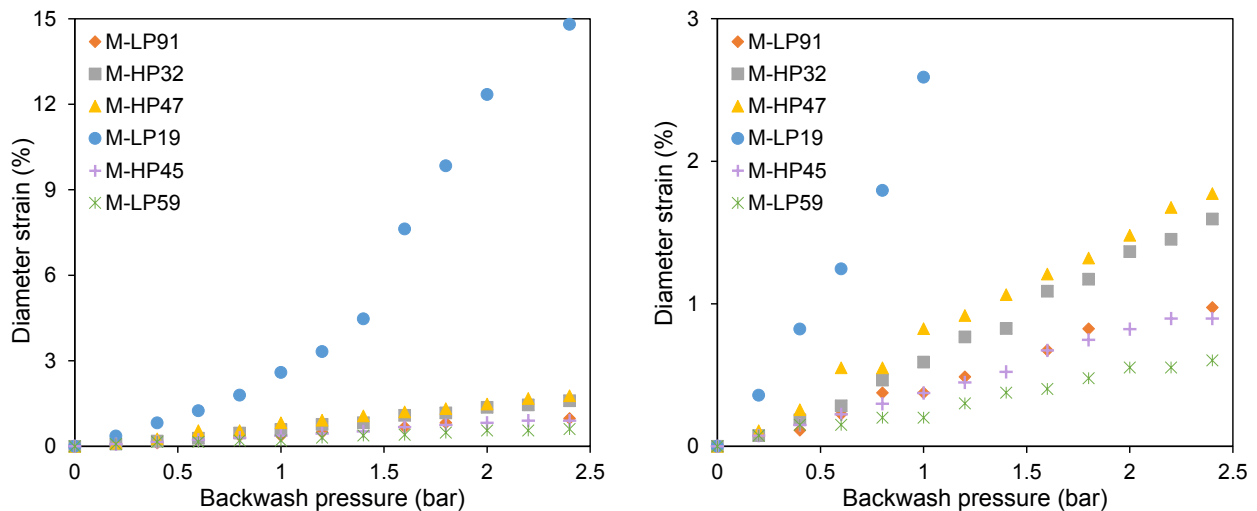


Figure 45: Experimental membrane deformation (left) with a zoom on small deformation (right) during backwash under internal pressure for the selected membranes M-LP91, M-HP47, M-HP32, M-LP19, M-HP45 and M-LP59.

An expansion of the external diameter of the hollow-fiber membrane was observed for all fibers when increasing the internal pressure. M-LP19 could be distinguished from the other

membranes due to its larger deformation. A linear strain of M-LP19 membrane diameter was observed at low pressure but when the backwash pressure exceeded 1 bar the deformation was deviated from linearity suggesting a plastic deformation, and therefore irreversible deformation of the fiber. M-LP19 sometimes even burst when backwash pressure exceeded 2.5 bar. Furthermore, the membrane with the highest Young's modulus was not the least deformable membrane, M-LP59 (with $E=59$ MPa) was indeed less deformed than M-LP91 (with $E=91$ MPa) at the same backwash pressure. As explained by the thick-walled model (4.2.2), the deformation depends on both the Young's modulus and the diameter ratio. The diameter ratio of M-LP91 ($R_D = 0.61$) was closer to 1 than the diameter ratio of M-HP59 ($R_D = 0.49$) conducting to higher deformation.

4.3.3 Conclusion

Micrometric deformations under external and internal pressure were measured using a digital camera. Measurements on each hollow-fiber membranes were very reproducible from one sample to another, homogenous along the fiber length and consistent with the membrane properties. The diameter strain was related to the pressure, the Young's modulus and the diameter ratio as described by the Lamé's equations. Only M-LP19 showed strong deformation with the pressure (formation of pinch points or bursting) and deformation might be irreversible at high pressures.

4.4 Model fitting

4.4.1 Comparison between theoretical and experimental data

The model for the deformation of thick-walled cylinder calculated for M-LP91, M-HP47, M-HP32, M-LP19, M-HP45 and M-LP59 was compared to the experimental deformation. Both under internal and external pressure, the model significantly underestimated the measured deformations as observed on Figure 46 and Figure 47. However, the theoretical deformation variations were related to the experimental ones. As predicted by the theory, membrane deformations were ranked as follows: M-LP19 >> M-HP32 ~ M-HP47 > M-LP91 (Figure 46 and Figure 47) with a calculated strain for M-LP19 much higher than the other membranes.

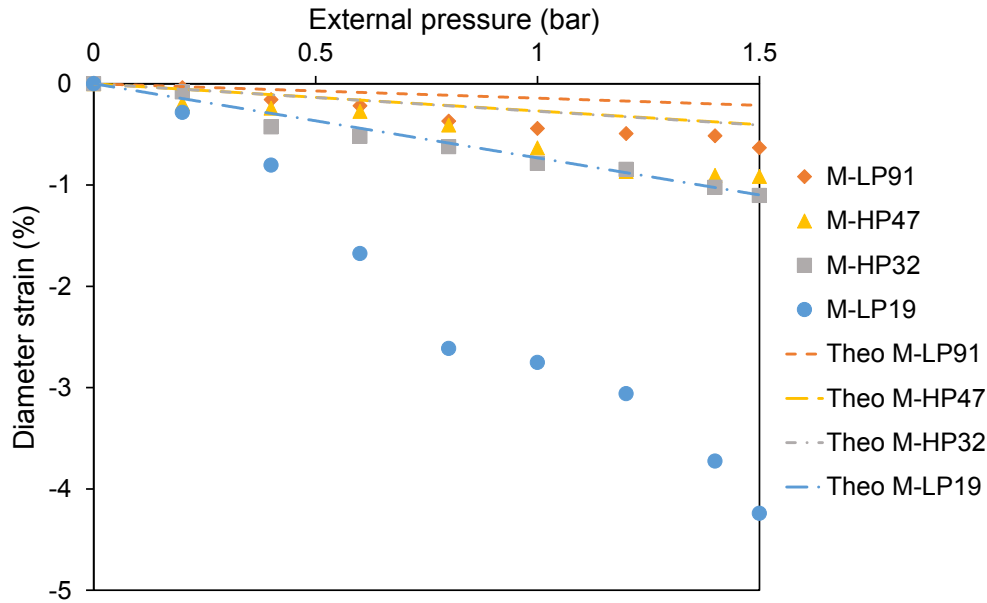


Figure 46: Comparison between the model for the deformation of thick-walled cylinder and experimental deformation of hollow-fiber membranes under external pressure.

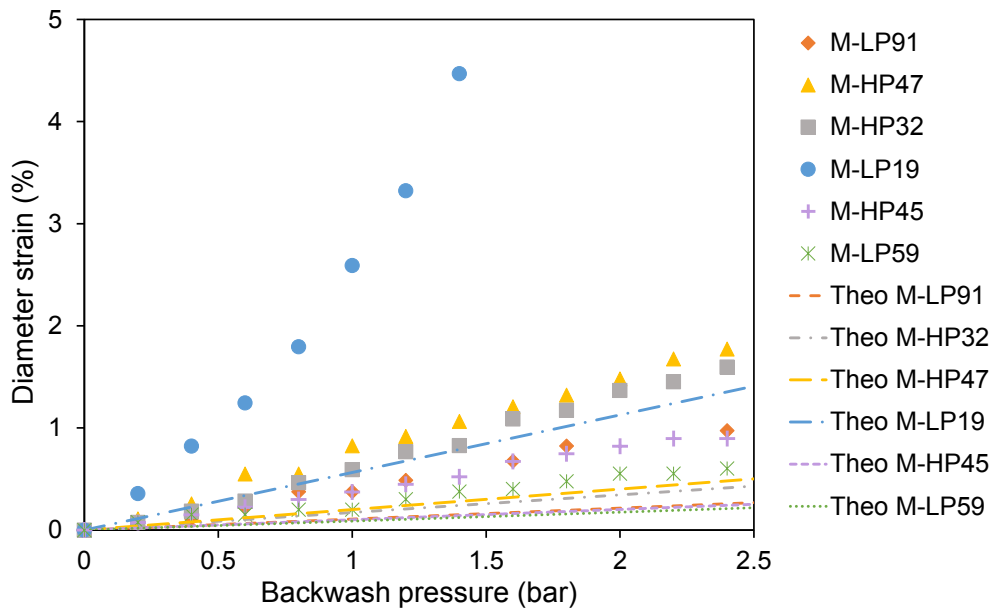


Figure 47: Comparison between the model for the deformation of thick-walled cylinder and experimental deformation of hollow-fiber membranes under internal pressure.

4.4.2 Adjustment factor

The calculated deformations were linearly proportional to the measured deformations and a single and unique adjustment factor fitted the model to the experimental data. This adjustment factor corrected all the calculated deformation and provided an excellent fit with all measured deformations, under both external pressure (Figure 48) and internal pressure (Figure 49). The factor f was 3.5 and was obtained using the method of least squares, which minimizes the sum

of the square of the difference between the corrected theoretical data points and experimental data points (Eq. 28), denoted ξ .

$$\xi = \sum [f \cdot \varepsilon_{\theta}(\text{model}) - \varepsilon_{\theta}(\text{experimental})]^2 \rightarrow 0 \quad \text{Eq. 28}$$

The data points for residual error calculations were chosen in the range of external and internal pressure between 0 and 0.8 bar for both external and internal to remain in the elastic domain. The minimal ξ was 0.9. The relationship between the experimental and theoretical data was:

$$\varepsilon_{\theta}(\text{experimental}) = f \cdot \varepsilon_{\theta}(\text{model})$$

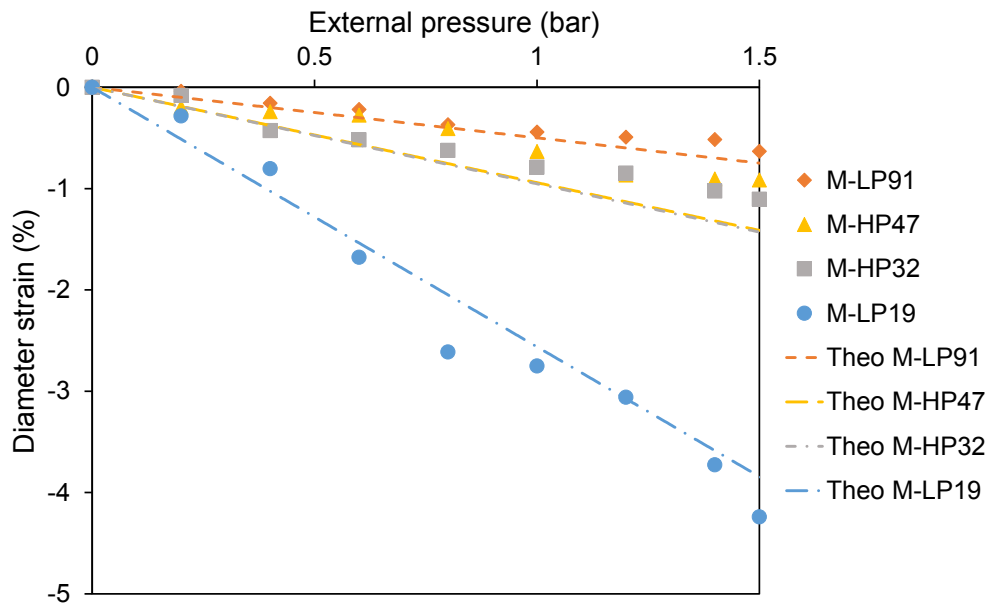


Figure 48: Model fitting with experimental deformation of the membrane diameter under external pressure, model adjustment factor $f=3.5$.

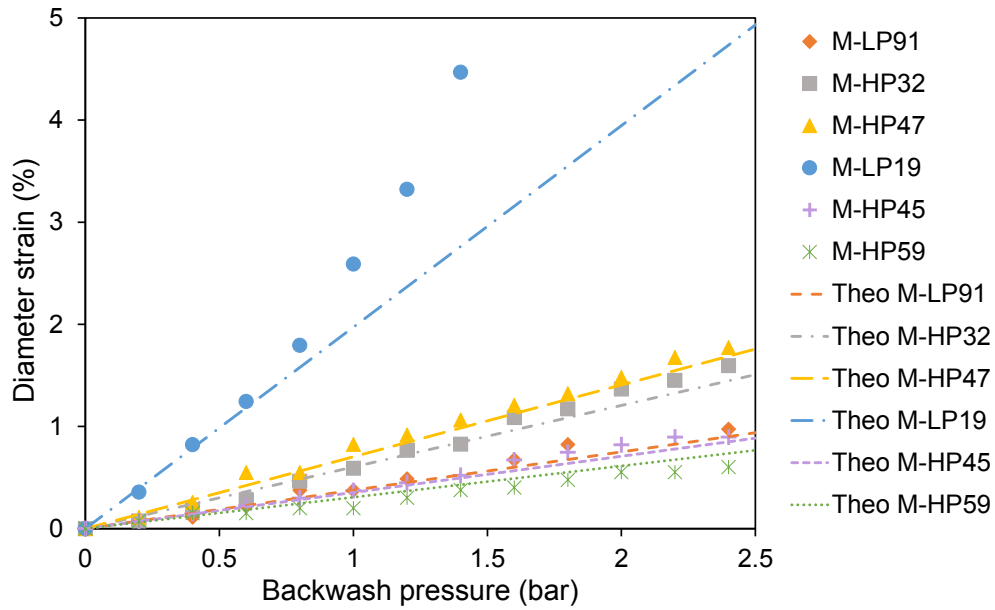


Figure 49: Model fitting with experimental deformation of the membrane diameter under internal pressure, model adjustment factor $f=3.5$.

As observed on Figure 49, M-LP19 deviated from the corrected model for backwash pressures higher than 0.8 bar confirming that the membrane plastically deformed as the model was based on a linear-elastic approach.

4.4.3 Origin of the adjustment factor

A single and common adjustment factor was found to fit all membrane deformations under external or internal pressure. To understand its origin, it was important to analyze the assumptions of the model. The model was described for non-porous hollow cylinder but in the case of porous membrane, a pressure gradient was formed within the membrane wall. Indeed, the Darcy's law through a porous media is expressed by:

$$J = -\frac{k}{\mu} \frac{\partial P}{\partial r}$$

with J the permeate flux ($\text{m}\cdot\text{s}^{-1}$), k the permeability of the membrane (m^2), μ the water dynamic viscosity ($\text{Pa}\cdot\text{s}$) and $\frac{\partial P}{\partial r}$ the pressure gradient through the porous membrane ($\text{Pa}\cdot\text{m}^{-1}$)

As explained in 4.2.1 the wall thickness might also deform during the filtration and backwash step. In the model, the calculations are made on the external surface with a pressure exerted either on the external or internal surface as shown on Figure 34. However, it could be consider that the pressure was deforming the porous structure and therefore that the model

underestimated the deformation as observed on Figure 46 and Figure 47. The deformation of hollow-fiber membranes would be better illustrated by Figure 50.

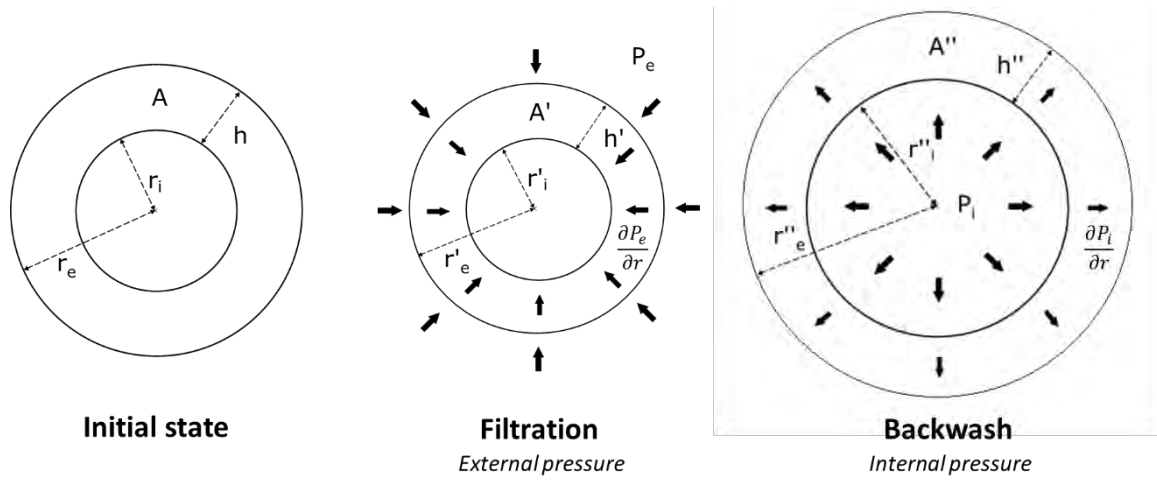


Figure 50: Deformation of hollow-fiber membrane under external and internal pressure, with pressure gradient within the membrane wall.

4.4.4 Model of two-layer hollow-fiber membrane

As the pressure gradient in the membrane wall might be responsible of the larger observed deformation. The numerical model was refined by dividing the membrane wall into two cylindrical layers. The layers were defined as an intermediate layer of inner radius r_i and outer radius r_{im} and an external layer of inner radius r_{im} and outer radius r_e . The intermediate pressure between the two layers was defined by P_{im} . The two-layer hollow-fiber membrane is represented on Figure 51.

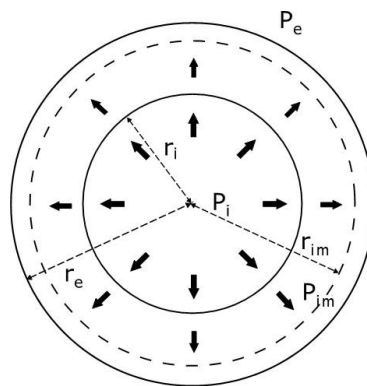


Figure 51: Deformation of the two-layer hollow-fiber membrane during backwash, with pressure gradient within the membrane wall.

This second model was also based on Lamé's equation as expressed previously by Eq. 26. The intermediate layer was subjected to both inner (P_i) and outer pressure (P_{im}) whereas the external layer was subjected to inner pressure (P_{im}) and outer pressure (P_e). The boundary conditions were:

At the external surface: $r = r_e$ and $P = P_e$

At the internal surface: $r = r_i$ and $P = P_i$

At the intermediate radius: $r = r_{im}$ and $P = P_{im}$

The pressure and the deformation were continuous at the interface.

The two-layer model was solved only in the case of the backwash step (under internal pressure only). The external layer deformation was calculated from Eq. 27 with $P_e = 0$ and $r_i = r_{im}$.

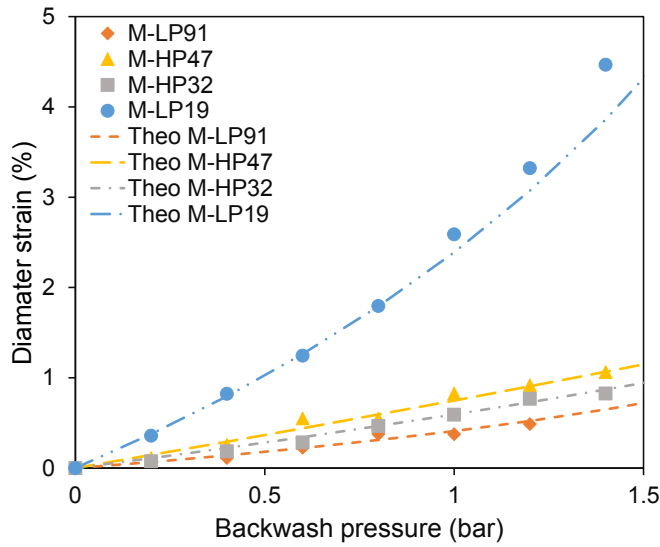
$$\varepsilon_\theta = \frac{1}{E} \left[(2 - \nu) \frac{r_{int}^2 P_{im}}{r_e^2 - r_{im}^2} \right] \quad \text{Eq. 29}$$

Eq. 29 was solved by Excel's Solver to fit the experimental data, choosing r_{im} and P_{im} as variables with $r_i < r_{im} < r_e$ and $P_i > P_{im} > 0$. Best fit was obtained by the method of least squares calculated in the range of pressure from 0 to 0.8 bar for each fiber. There was a single intermediate radius (r_{im}) and a single pressure (P_{im}) but different for each membrane that solved Eq. 29, met the boundary conditions and fitted the experimental data with $\xi < 0.05$ (Eq. 28) as shown on Figure 52.

The variables r_{im} and P_{im} , calculated by the solver, were normalized for comparison between fibers of different dimensions (Figure 52). The calculated intermediate radius was normalized to the membrane wall thickness using Eq. 30 and the intermediate pressure was normalized to the internal pressure using Eq. 31.

$$Norm. r_{im} = \frac{r_{im} - r_i}{r_e - r_i} \quad \text{Eq. 30}$$

$$Norm. P_{im} = \frac{P_{im}}{P_i} \quad \text{Eq. 31}$$



Fiber	$Norm. r_{im}$	$Norm. P_{im}$
M-LP91	0.62	0.88
M-HP47	0.65	0.74
M-HP32	0.67	0.54
M-LP19	0.76	0.52

Figure 52: Fitting of the two-layer deformation model on experimental data under internal pressure (on left) with the calculated normalized parameters (on right).

A qualitative profile of the pressure gradient within the wall could be plotted on Figure 53 based on the solutions of Eq. 29 for each membrane. Different pressure profiles through the wall were obtained since the internal structure was specific to each membrane. Furthermore, the morphology was also different at different positions of the membrane wall on a same membrane (as illustrated on Figure 53). It was interesting to notice that the pressure profile seemed related to the membrane wall morphology. M-LP91 showed indeed a small pressure decrease in the part of the wall comprising large macrovoids (with low mass transfer resistance) and a strong decrease of the pressure in the sponge-like structure (higher mass transfer resistance). Whereas M-HP32 had the most linear decrease of the pressure through the membrane wall and presented an homogenous sponge-like structure. The external thin skin layer is also assumed to contribute the most to the mass transfer resistance resulting in higher pressure decrease when getting closer to the external surface. However, this interpretation was questionable since other properties (Young's modulus, Poisson's ratio) could also differ between the different layers.

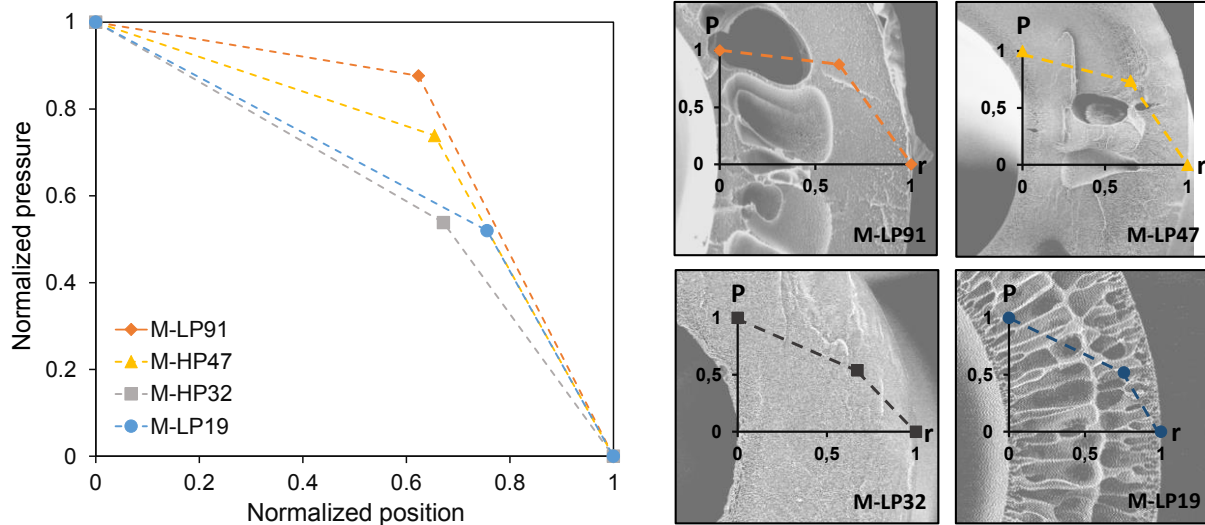


Figure 53: Qualitative representation of the pressure gradient profile within the membrane wall when subjected to internal pressure. The normalized position was 0 at the internal surface and 1 at the external surface of the hollow-fiber membrane. The normalized pressure was 1 at the internal surface and 0 at the external surface. Comparison with the membrane wall morphology (on the right).

This second model was developed to further understand the impact of the existing pressure gradient within the wall on the membrane deformation and explained the underestimated deformations obtained by the thick-walled cylinder model proposed in 4.2. From this two-layer model, the membrane wall deformation would also contribute to the external surface deformation of the hollow-fiber membrane during operating pressure.

4.4.5 Conclusion

The model of deformation of thick-walled cylinder underestimated the real deformations of hollow-fiber membranes. However, a single and common adjustment factor of 3.5 corrected the Lamé's equations and provided an excellent fit of the measured deformations. Furthermore, this factor was identical to fit the membrane compression and expansion under external pressure and internal pressure respectively. Larger observed deformations of the external diameter might be due to the extra deformation of the porous membrane wall subjected to a pressure gradient. A model based on a two-layer cylinder showed that the pressure gradient would lead to higher deformation of the external membrane surface. The simulated profile of pressure gradient was also dependent on the membrane wall morphology.

4.5 Influence of the deformation on membrane properties

4.5.1 Elastic limit and deformation reversibility

The elastic limit determined from tensile stress-strain curves (described in 2.5.2.3) was the strain from which the tensile stress deviated from the linear-elastic slope. At higher strain than the elastic limit the deformation was considered partially reversible and became plastic. The tensile elastic limit could be assimilated to the axial elastic limit but might be different from the radial elastic limit. Compression tests were not performed on the hollow-fiber membranes and only the axial elastic limit was measured for the selected membranes (listed in Table 17).

Table 17: Elastic limit of the selected hollow-fiber membranes measured on tensile stress-strain curves

Fiber name	$\epsilon_{elastic\ limit}$ (%)
M-LP91	1.5
M-HP47	2.6
M-HP32	2.3
M-LP19	1.8
M-LP59	2.3
M-HP45	2.4

The measured elastic limits were similar between the membranes, with slightly lower elastic limits for M-LP91 and M-LP19. The smaller diameter and wall thickness of these membranes may be responsible for the lower values. According to the experimental deformation measured under external and internal pressure (Figure 42 and Figure 45), the maximal deformation for each membrane was below the axial elastic limit, except for M-LP19. Indeed, M-LP19 reached the axial elastic limit at TMP=0.6 bar (under external pressure) and at BTMP=0.8 bar (under internal pressure). Therefore, higher pressures would result in a plastic and irreversible deformation (if axial elastic limit is close to the radial elastic limit). It could be noticed that the strain from which M-LP19 deviated from the linear-elastic theory (Figure 49) corresponded to the axial elastic limit of M-LP19 determined by tensile test (Table 17). Therefore, axial elastic limit was assumed very close to the radial elastic limit supporting the assumption that membrane could be considered as isotropic and homogenous materials.

Following the section 4.3 on the experimental observation of the deformation, hollow-fiber membrane were left to recover at zero pressure for ten minutes after being deformed at 0.8, 1.5 and 2.4 bar. The measurement of the irreversible deformation after recovering was given in Table 18 when subjected to external pressure and in Table 19 when subjected to internal pressure.

Table 18: Diameter strain at TMP of 0.8 and 1.5 bar and irreversible strain after recovering for ten minutes at zero pressure.

Fiber name	Diameter strain (%) at		Irreversible strain (%) after	
	TMP (bar)		deforming at TMP (bar)	
	0.8	1.5	0.8	1.5
M-LP19	-2.6	-4.2	-0.2	-0.5
M-HP32	-0.6	-1.1	-0.1	-0.1
M-HP47	-0.4	-0.9	-0.1	-0.1
M-LP91	-0.4	-0.6	-0.1	-0.3

Table 19: Diameter strain at BTMP of 0.8, 1.5 and 2.4 bar and irreversible strain after recovering for ten minutes at zero pressure.

Fiber name	Diameter strain (%) at			Irreversible strain (%) after		
	BTMP (bar)			deforming at BTMP (bar)		
	0.8	1.5	2.4	0.8	1.5	2.4
M-LP19	1.8	5.4	14.8	0.1	0.5	10.3
M-HP32	0.5	1.0	1.6	0	0.3	0.3
M-HP47	0.6	1.2	1.9	0.4	0.4	0.7
M-LP91	0.3	0.6	1.0	0.1	0	0.1
M-HP59	0.2	0.4	0.6	0	0.1	0.1
M-HP45	0.3	0.6	1.0	0	0.1	0.1

Most of deformations were completely reversible when decreasing the pressure at zero. However, M-LP19 showed irreversible deformations especially when subjected to 2.4 bar internal pressure. The diameter strain of M-LP19 at 1.5 bar was 5.4% and was therefore well above the elastic limit (1.8%), even though the irreversible deformation was only 0.5%. However, at 2.4 bar M-LP19 deformed up to 14.8% and the irreversible strain was 10.3%,

indicating a strong plastic deformation. High deformation of hollow-fiber membranes would therefore generate plastic deformations.

4.5.2 Pore deformation

The membrane diameter strain was the same than the external surface strain where the selective layer is located. The surface deformation was then certainly causing the deformation of membrane pores on a different scale. Microscopic techniques have been used to measure the pore deformation of microfiltration membrane [177], [178] but were limited for the measurement of ultrafiltration membrane pore size. Iio *et al.* [177] measured the pore size of PVDF microfiltration membranes under different strain and observed an increase of the membrane permeability with the pore growth.

The pore diameter strain could be estimated from permeability measurements under a range of pressure. The flow rate through a cylindrical pore could be estimated using the Hagen-Poiseuille law:

$$Q = \frac{\pi * TMP * r_p^4}{8 * \mu * l_p} \quad Eq. 32$$

With Q the flow rate ($m^3.s^{-1}$), TMP the transmembrane pressure (Pa), r_p pore radius (m), μ the water dynamic viscosity (Pa.s) and l_p the pore length (m)

By combining the pore size distribution and the Hagen-Poiseuille law [189], the membrane permeability could be expressed by:

$$Lp_0 = \frac{\pi}{8 * \mu * l_p} * \sum_i n(r_i) * r_{p,i}^4$$

With Lp_0 the pure water permeability at 20°C ($m.Pa^{-1}.s^{-1}$), $n(r_{p,i})$ the number of pores of radius $r_{p,i}$ per membrane surface area (m^{-2})

Therefore, the permeability was proportional to the fourth power of the mean pore radius:

$$Lp_0 \propto \bar{r}_p^4$$

With \bar{r}_p the mean pore size (m)

The pure water permeability, the average pore radius and pore length were dependent on the transmembrane pressure but pore length deformation was assumed negligible compared to the other terms.

The estimated deformation of the pore size was calculated for each hollow-fiber membrane under external and internal pressure (Figure 54) based on membrane permeability measurements under pressure (Figure 33) and normalizing the average pore size to the initial pore size at 0.2 bar pressure. Membranes were compressed under external pressure and the pore size was reduced for all membranes. The pore size of M-LP19 decreased much more than other membranes, however the membrane structure collapsed under pressure (see on Figure 43), and measurements might not be reliable. Under the range of internal pressure, the pore size was also lower than the initial pore size (measured at BTMP=0.2 bar) for all membranes except for the most deformable membrane. M-LP19 was indeed the only membrane that showed an expansion of its pore size when the internal pressure exceeded 1.2 bar. The pore size underwent an expansion of 13% at 2.4 bar (Figure 54) leading to a strong increase of membrane permeability (Figure 33). This calculated deformation of the pore size was extremely consistent with measured membrane surface deformation of 15% at 2.4 bar.

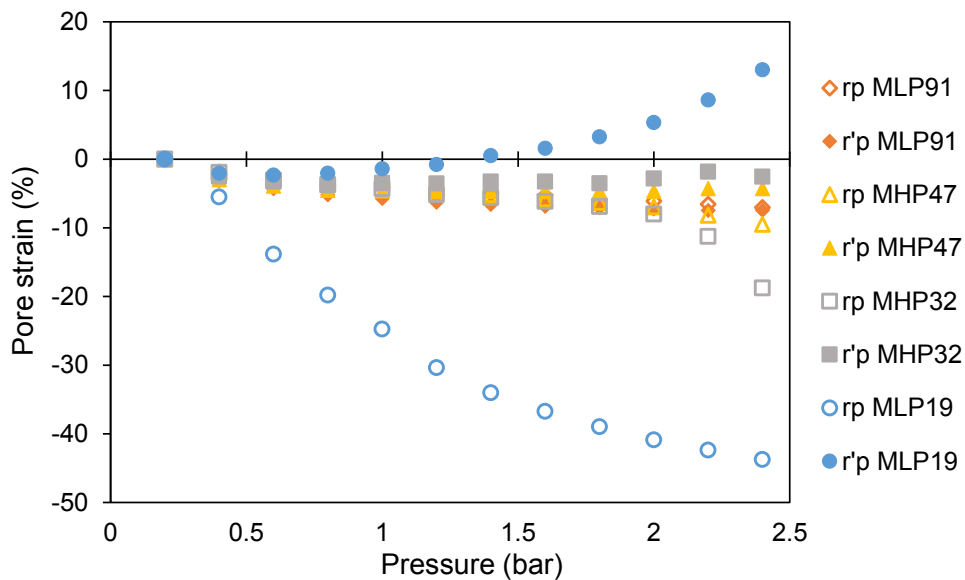


Figure 54: Estimation of pore radius deformation under external pressure r_p and internal pressure for r'_p

4.6 General conclusion

In this chapter, the hollow-fiber membrane compression during filtration and expansion during backwash was observed under digital camera and simulated by the Lamé's equations. A simple model on the deformation of thick-walled cylinder under pressure demonstrated an excellent correlation with the experimental measurements of the external membrane surface deformation under both internal and external pressure when using an adjustment factor of 3.5. This factor might be related to the pressure gradient within the porous membrane that would also deform the membrane wall increasing therefore the calculated diameter strain. The membrane M-LP19, with the lowest Young's modulus of 19 MPa, demonstrated much larger deformation under pressure than all other membranes. Indeed, while most membrane deformations were below 2% at the considered pressures, M-LP19 diameter strain reached 15% at BTMP=2.4 bar. This measured deformation was however small if compared to the required deformation for the detachment of biofilm from silicon surface (minimum deformation of 25% to detach 80% of biofilm [146]) but sufficiently high to exceed the elastic limit of the M-LP19 membrane. Even though the deformations were reversible for most membranes, the deformation of M-LP19 was however highly irreversible at 2.4 bar. Furthermore, according to the permeability measurements the pore deformation was closely linked to the deformation of the membrane external surface.

Chapter 5 - Ultrafiltration of particle suspensions and fouling removal mechanisms

5.1 Introduction

In this chapter, the selected membranes (M-LP91, M-HP47, M-HP32 and M-LP19) were used for the ultrafiltration of model solutions and real fluids (wastewaters). Model solutions were chosen to carry out controlled filtrations and obtain homogenous filter cakes on the external surface of the membrane. Bentonite suspensions and humic acid suspension were selected as model feed solutions since they were the most representative particle solutions of the real fluid (natural surface water). Furthermore, fouling and fouling removal mechanisms were expected to be different in the case of bentonite (inorganic particles) and humic acid (organic particles) filtrations. Indeed, during filtration bentonite particles usually form a hydraulically reversible cake on the surface [190] whereas humic acid filtration generally leads to hydraulically irreversible fouling due to adsorption and pore blockage [69][110].

In a first part, the model suspensions were characterized with focusing on the influence of ionic strength on particle suspension stability. In a second part, the study of fouling mechanisms was compared on different membranes and with the different feed suspensions. In a third section, the fouling removal results obtained by mass balance method are presented at different backwash pressures and backwash efficiency was compared between the membranes. The final part consists in explaining the fouling removal mechanisms for different particle suspensions and the difference in backwash efficiencies.

5.2 Characterization of particle suspensions

5.2.1 Definitions

Bentonite, mainly composed of montmorillonite, is a smectite clay from the phyllosilicate group of minerals. Bentonite particles are made from several clay layers, which are composed of two silica tetrahedral sheets (SiO_4) and one aluminum octahedral sheet (Al^{3+}). They form a plate-shaped particle with a ratio length to thickness of approximately 100 (illustrated on Figure 55). Van der Waals forces are holding the layers together but electrostatic interactions are the predominant forces due to negative charge on the layer surface [191]. Overall particle charge is negative. Dispersion of bentonite particles in water forms a colloidal suspension after settling because the suspension is stable and the particle size is micron-sized or less [190].

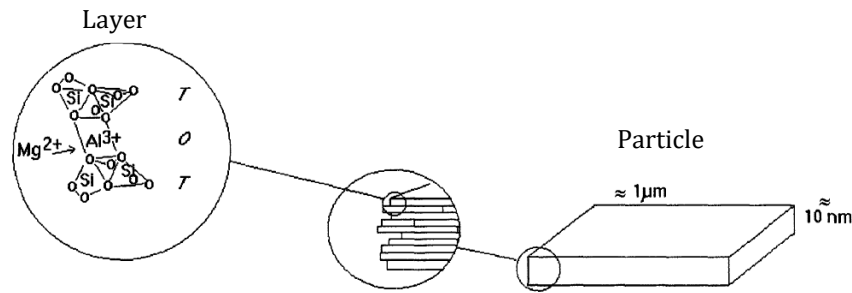


Figure 55: Plate-shaped bentonite particle [190]

Humic acid is the principle component of humic substances present in humus, the major organic fraction of soil extract. Humic acids are insoluble at low pH values but soluble in water at pH higher than 2. They have different molecular weights, solubility and size depending from their origin, age or extraction method [192]. Humic acids are mainly composed of aromatic cycles and carboxylic acids or alcoholic hydroxyls as functional groups (see on Figure 56). Dispersing humic acid in water solution results in a colloidal solution with properties greatly influenced by pH, humic acid concentration and ionic strength [192].

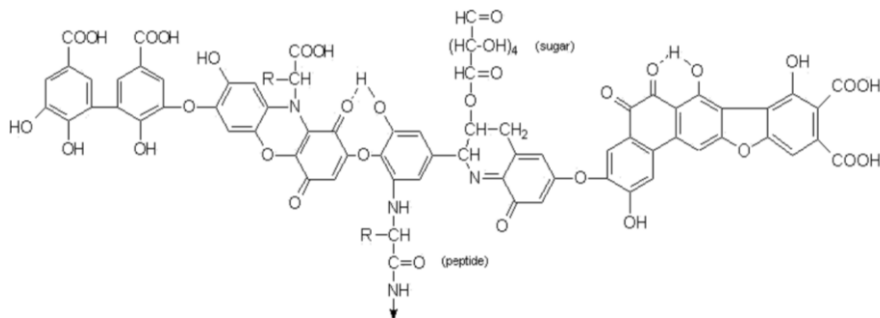


Figure 56: Model structure of humic acid [193]

For both particle suspensions, the ionic strength plays a major role in electrostatic interaction or complexation of particles resulting in the formation of different cake structure during ultrafiltration [194]. Katsoufidou et al. [69] have shown the influence of ionic strength of humic acid suspension on fouling propensity and its reversibility. Santiwong et al. [167] and Bacchin [190] have shown how ionic strength can modify bentonite suspensions properties and change the deposit structure and resistance during filtration. Increasing the ionic strength conducts to the destabilization of the suspension and the aggregation of the particles. The critical coagulation concentration defines the salt concentration from which particles will aggregate and is dependent of the nature of salt and particles. This concentration can be estimated with the DLVO theory based on interaction energy and depends on the ion valency [195].

The ionic strength is related to the ion concentration using the following equation:

$$I = \frac{1}{2} \sum_i C_i z_i^2 \quad \text{Eq. 33}$$

With I the ionic strength in M or mol.L⁻¹, C_i the ion concentration in mol.L⁻¹ and z_i the ion charge.

In the case of monovalent salt (i.e. KCl), $C_i = I$ whereas for a divalent salt (i.e. CaCl₂), $C_i = \frac{I}{3}$.

5.2.2 Influence of the ionic strength on model suspension properties

The particle suspensions are stable in the dispersant in specific conditions of pH, ionic strength, temperature, and particle concentration. Finding out the limits of stability of the model suspensions was relevant to have a better control on the filtration process. Indeed, as ionic strength affects the suspension properties (zeta potential, conductivity, particle size, turbidity and absorbance) it was important to determine at which ion concentration the experiments should be carried out. The bentonite and humic acid suspensions were prepared (as described in 2.4.1.1) and ionic strength was varied between 10⁻⁵ M and 1 M by adding KCl or CaCl₂.

5.2.2.1 Zeta potential and conductivity

Measurements of particle charge (Figure 57) were performed on bentonite (KCl), bentonite (CaCl₂) and humic acid (CaCl₂).

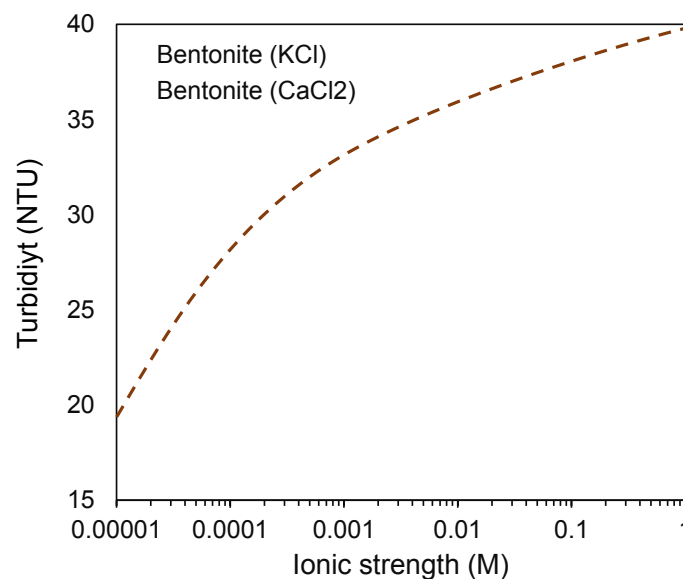


Figure 57: Zeta potential of particles of bentonite (KCl), bentonite (CaCl₂) and humic acid (CaCl₂) suspensions as function of ionic strength with $I = [10^{-5}-1]$ M, at neutral pH.

The measured charge of the particles was negative for all prepared suspensions. The zeta potential (absolute value) was decreasing and approximating zero value when increasing the ionic strength indicating the destabilization of the suspension. The adsorption of cation on the charged surface compressed the electric double layer and caused the decrease of the zeta potential [102]. This decrease is also higher with higher cation valency ($\text{Ca}^{2+} > \text{K}^+$) [169]. From Figure 57, a larger decline of the zeta potential of approximately 30 mV was indeed observed for bentonite (CaCl_2) and humic acid (CaCl_2) compared to only 15 mV for bentonite (KCl).

5.2.2.2 Particle size and size distribution

Colloidal suspensions are characterized by the size of the suspended particles, and parameters such as the size distribution and the critical coagulation concentration. As explained in 2.6.1 the so-called particle size was actually a measurement of the hydrodynamic equivalent diameter of bentonite and humic acid particles (assimilated to spherical particles)

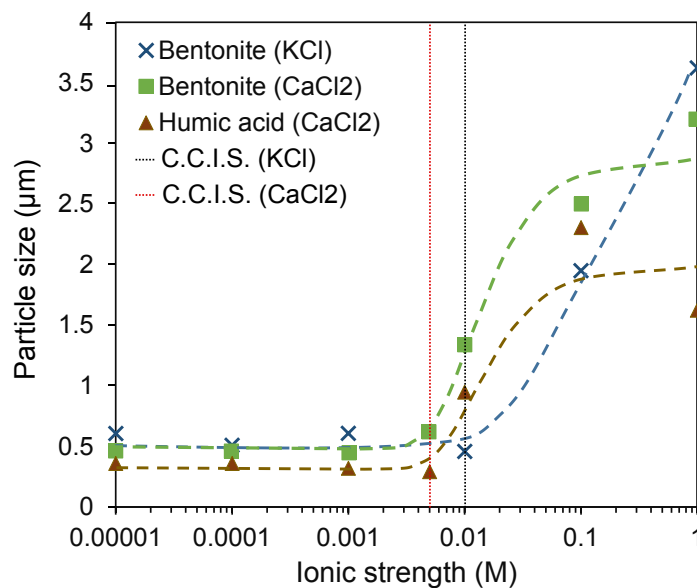


Figure 58: Evolution of the particle size with increasing the ionic strength, $I = [10^{-5} - 1]$ M, for bentonite (KCl), bentonite (CaCl_2) and humic acid (CaCl_2) suspensions. Determination of the critical coagulation ionic strength (C.C.I.S.) for each suspension.

The average size of particles was kept constant in the range of ionic strength from 10^{-5} to $5 \cdot 10^{-3}$ M. However, when exceeding $I = 5 \cdot 10^{-3}$ M the particle size was rapidly increasing. The sharp increase of the particle size with ionic strength was explained by the aggregation of particles. In the case of the addition of a bivalent salt (CaCl_2), the particle aggregation was triggered at lower ionic strength than in the case of monovalent salt (KCl). The critical

coagulation ionic strength (C.C.I.S.), at which the aggregation begins, can be determined from Figure 58 and the critical coagulation concentration (C.C.C) was calculated using Eq. 33.

Table 20: Critical coagulation ionic strength and concentration for bentonite (KCl), bentonite (CaCl₂) and humic acid (CaCl₂) suspensions.

Feed	Experimental		Theoretical [190]
	C.C.I.S. (M)	C.C.C. (M)	C.C.C. (M)
Bentonite (KCl)	1.10^{-2}	1.10^{-2}	4.10^{-3}
Bentonite (CaCl ₂)	5.10^{-3}	2.10^{-3}	6.10^{-4}
Humic acid (CaCl ₂)	5.10^{-3}	2.10^{-3}	6.10^{-4}

As shown on Table 20, the C.C.I.S. was 2 times lower for bentonite (CaCl₂) than bentonite (KCl), and the C.C.C. was therefore 6 times lower. Theoretical C.C.C can be calculated using the rule of Schulze-Hardy, theoretical values for monovalent salt (KCl) and bivalent salt (CaCl₂) were found in Bacchin work [190]. The theoretical critical coagulation concentrations underestimated the real C.C.C for all prepared suspensions.

5.2.2.3 Turbidity for bentonite suspensions

Bentonite particle concentration was determined by turbidity measurement and using the calibration curves presented in Figure 24. The influence of the ionic strength on suspension turbidity was studied between 10^{-5} and 1 M for both bentonite suspensions (see on Figure 59).

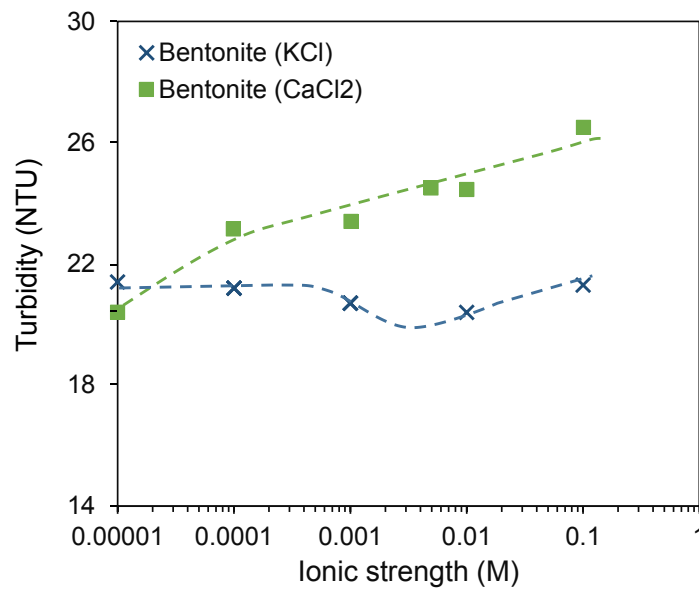


Figure 59: Evolution of the turbidity with the ionic strength, $I= [10^{-5}-1]$ M, for bentonite (KCl) and bentonite (CaCl₂)

Due to particle aggregation, bentonite (CaCl₂) turbidity increased from 20 to 26 NTU when increasing ionic strength from 10⁻⁵ to 1 M while bentonite (KCl) turbidity remained constant around 21 NTU. A slight decrease in turbidity was represented on the curve for bentonite (KCl) between $I=10^{-3}$ and $I= 10^{-2}$ M. This decrease was also observed in the work of Bacchin [190] and seems to be related to the C.C.C.

5.2.2.4 UV-Spectroscopy for humic acid suspension

Humic acid particle concentration was determined by UV-spectroscopy measurement and using the calibration curve presented in Figure 25. The influence of the ionic strength on suspension absorbance was studied between 10⁻⁵ and 1 M (see on Figure 60).

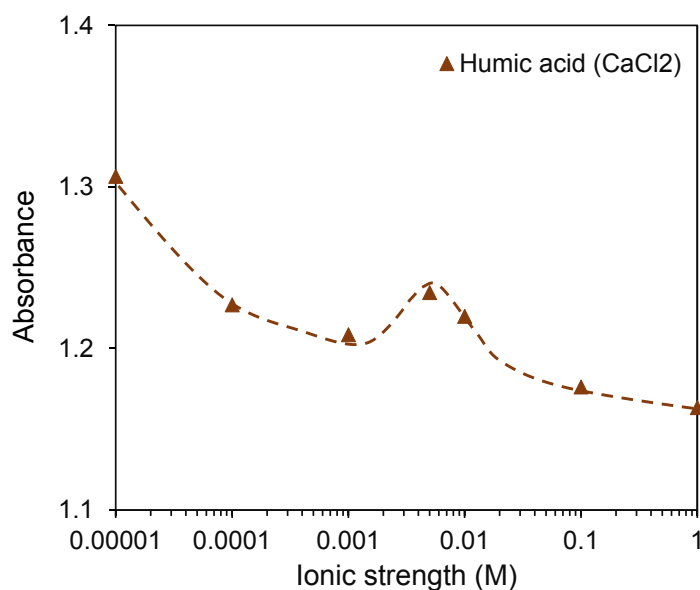


Figure 60: Evolution of the absorbance with the ionic strength, $I = [10^{-5}-1]$ M, for humic acid (CaCl_2), at a wavelength of 254 nm

The presence of CaCl_2 lowered the absorbance of humic acid suspension. The absorbance was indeed decreasing from 1.31 to 1.16 when increasing the ionic strength from 10^{-5} to 1 M. However, a slight rise of the absorbance was observed at $I = 5 \cdot 10^{-3}$ M, which was the exact C.C.I.S. (Table 20) of humic acid (CaCl_2) suspension.

5.2.3 Properties of the prepared feed model solutions for ultrafiltration

Van der Waals and electrostatic interactions control the stability of colloidal suspensions and a change in pH or ionic strength can cause the aggregation of particles. This study on the influence of the ionic strength on different suspension properties was a preliminary work to have a complete understanding of fouling and fouling removal mechanisms. In order to have a better control on these mechanisms, diluted concentration of particles and ion concentration below the critical coagulation concentration were chosen.

All feed suspensions were prepared in ultra-pure water with a particle concentration of $0.05 \text{ g}\cdot\text{L}^{-1}$ and an ionic strength of 10^{-3} M (adjusted with KCl or CaCl_2). Characteristics of the prepared suspensions are detailed in Table 21 and Figure 61. The suspensions were used at room temperature ($15-25^\circ\text{C}$) and neutral pH (comprised between 6.5 and 7.0).

Table 21: Characteristics of the prepared feed suspensions. Particle concentration of 0.05 g.L^{-1} and ionic strength adjusted to 10^{-3} M with KCl or CaCl_2 .

Feed	Turbidity (NTU)	Absorbance	Average Particle size (nm)	Zeta potential (mV)
Bentonite (KCl)	20.7	0.18	610	-16
Bentonite (CaCl_2)	26.9	0.19	490	-18
Humic acid (CaCl_2)	15.1	1.27	326	-21

According to analytical results of the feed suspensions, the bentonite (CaCl_2) particles had a smaller average size (Table 21) and narrower size distribution (Figure 61) than bentonite (KCl) particles. However, humic acid particles were smaller with an average size of 326 nm. The estimated particle size of humic acid (CaCl_2) suspension was comprised between 90 nm and 830 nm. As presented in the following results (Table 22), humic acid particles were not completely retained by the membranes suggesting that the smallest particles were passing through the membrane pores.

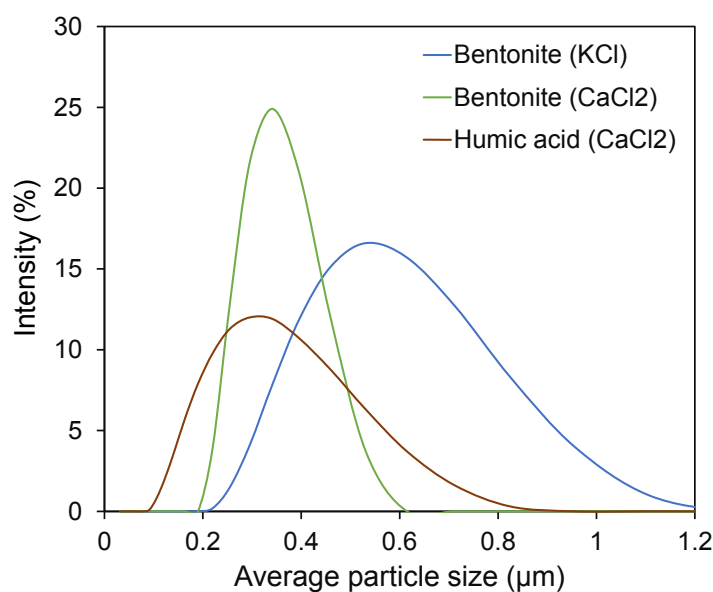


Figure 61: Size distribution of particles in the prepared feed suspensions

5.3 Fouling analysis

0.05 g.L⁻¹ bentonite (KCl or CaCl₂) or 0.05 g.L⁻¹ humic acid (CaCl₂) suspensions were filtered in dead-end filtration in outside-in mode on each selected hollow-fiber membranes. The permeate volume was chosen at 60 L.m⁻² to form a deposit of identical thickness on membrane surface.

5.3.1 Decrease of permeate flux

During the particle suspension filtration, the permeate flux was decreasing at different speed rates (as illustrated on Figure 62) depending on the nature of the foulant, the cake structure, and particle-particle or/and particle-membrane interactions.

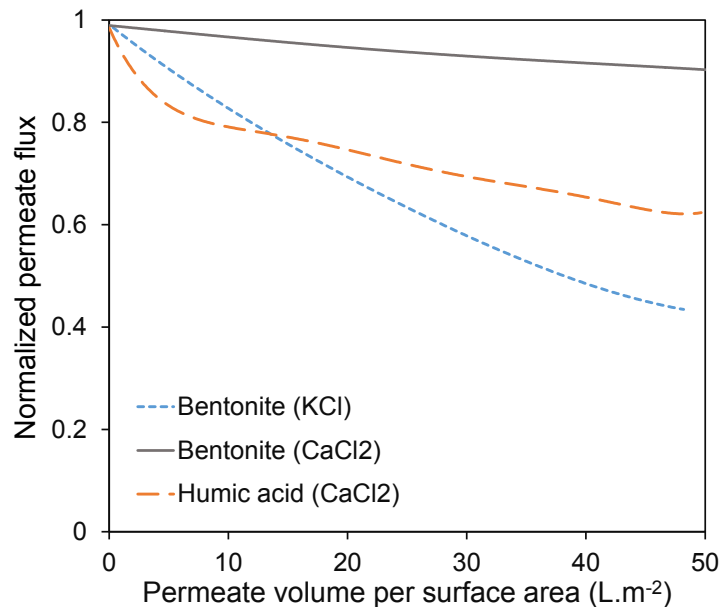


Figure 62: Normalized permeate flux when filtrating different feed solutions on M-LP91 at constant pressure, $TMP=0.8$ bar

For bentonite (KCl) filtration (see on Figure 63), the decrease of permeate flux was faster for the most permeable membranes M-HP32 and M-HP47 than for M-LP91 and M-LP19 but at the end of the filtration the permeate flux converged to a common value [100-150] L.m⁻².h⁻¹ for each fouled membrane. It indicates that the resistance of the bentonite (KCl) cake overcame the membrane hydraulic resistance and governed the permeate flux. In the case of bentonite (CaCl₂) filtration (see on Figure 64), the permeate flux was slightly decreasing for the most permeable membranes but remained constant for M-LP91 and M-LP19. Due to low resistance of the bentonite (CaCl₂) cake, the membrane hydraulic resistance seemed to govern the permeate flux. Regarding the permeate flux decrease during humic acid filtration (see on Figure

65), a decrease was observed at the very beginning of the filtration then the permeate flux was quasi-constant especially for M-LP19 and M-LP91. Indeed, in addition of the cake deposition, pore blockage was largely contributing to the permeate flux decline in the early stage of filtration [196].

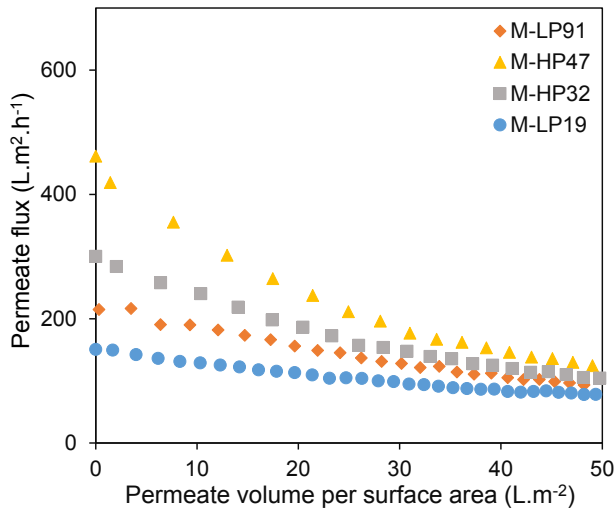


Figure 63: Permeate flux during bentonite (KCl) filtration at constant pressure, $TMP=0.8$ bar

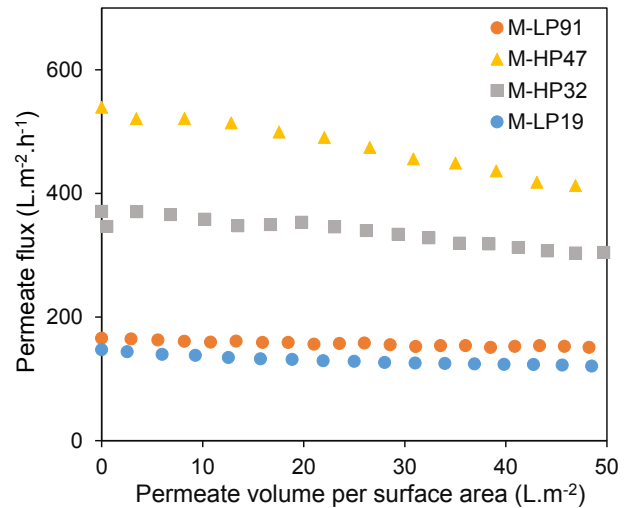


Figure 64: Permeate flux during bentonite ($CaCl_2$) filtration at constant pressure, $TMP=0.8$ bar

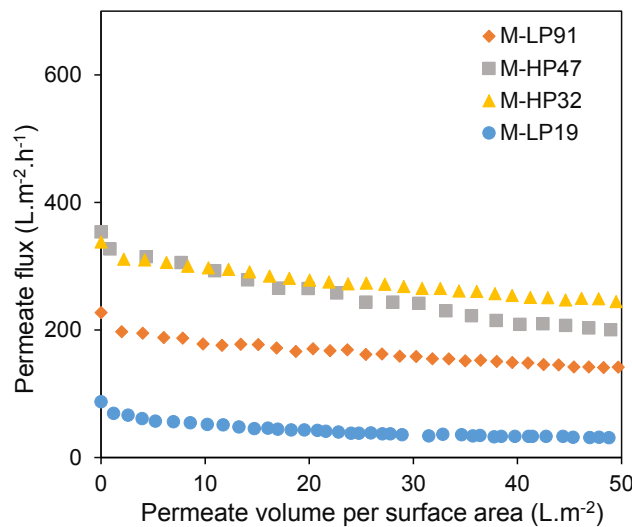


Figure 65: Permeate flux during humic acid ($CaCl_2$) filtration at constant pressure, $TMP=0.8$ bar

5.3.2 Selectivity and adsorption

Bentonite particles were completely retained by the different membranes with a measured retention higher than 99 %. However, during the filtration of humic acid suspensions at constant transmembrane pressure ($TMP=0.8$ bar), the retention was not total and depended on

the hollow-fiber membrane. The various retentions during humic acid filtration are reported in Table 22. As observed on Figure 61, a broader distribution of particle size was measured for humic acid particles than bentonite ones. The larger particles with a size close to the bentonite particle size should be retained but the smallest particles were not retained by the membrane.

Table 22: Humic acid retention during filtration at constant pressure $TMP=0.8$ bar

Fiber	Retention
M-LP91	89 %
M-HP47	68 %
M-HP32	72 %
M-LP19	74 %

The retention varied from 68 % for M-HP47 to 89% for M-LP91. Different pore size would lead to different retention but the humic acid adsorption was certainly affecting the retention.

The kinetics and equilibrium of static adsorption of humic acid on the external membrane surface was measured and plotted on Figure 65.

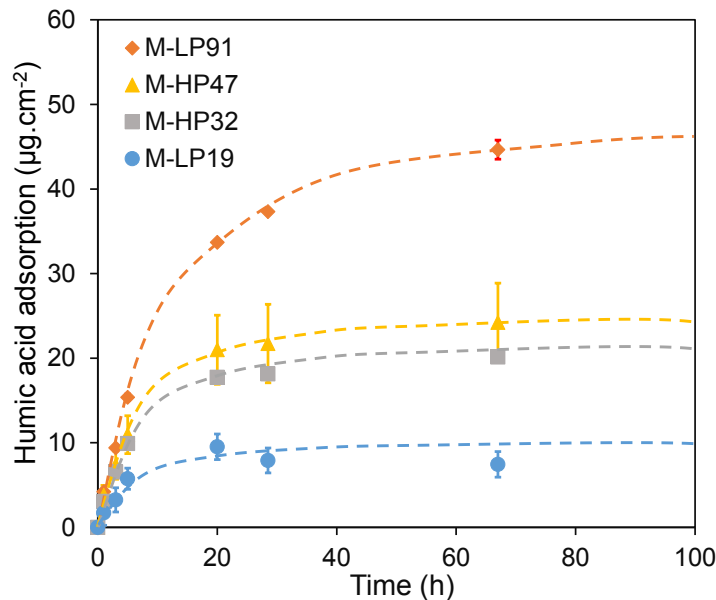


Figure 66: Kinetics of humic acid adsorption on different PVDF membranes

While adsorption kinetics was not significantly different between the membranes, very different adsorption equilibriums were measured. M-LP91 demonstrated the highest amount of adsorbed particles with $45 \mu\text{g}\cdot\text{cm}^{-2}$ in 72 hours whereas only $8 \mu\text{g}\cdot\text{cm}^{-2}$ was adsorbed on M-

LP19 in 72 hours. Regarding M-HP32 and M-HP47, they had the same adsorption kinetics and equilibrium. The amount of adsorbed particles was approximately $20 \mu\text{g}\cdot\text{cm}^{-2}$ in 72 hours. Pictures of the pristine membranes and at the adsorption equilibrium (after 200 hours static adsorption) were taken (Figure 67). Visual observation confirmed the UV-spectroscopy measurements: M-LP91 was the fiber that adsorbed the most and had the more intense brownish color whereas M-LP19 was the one that adsorbed the less and had the lighter color.



Figure 67: Pictures of pristine hollow-fiber membranes (top) and hollow-fiber membranes after 200 hours static adsorption (bottom).

Measurement of the retention on a fiber at the humic acid adsorption equilibrium revealed much lower retention of the humic acid as described in Table 23.

Table 23: Humic acid retention at the adsorption equilibrium during filtration at constant pressure $TMP=0.8$ bar

Fiber	Retention (on clean membrane)	Retention (at adsorption equilibrium)
M-LP91	89 %	78 %
M-LP19	74 %	68%

At adsorption equilibrium, the retention of humic acid fell by 11 % for M-LP91 and 6% for M-LP19. Due to a stronger adsorption of humic acid, M-LP91 showed higher retention but when equilibrium of adsorption was reached, the retention decreased. Adsorption has therefore a significant effect on the retention of humic acid particles.

As the membrane permeabilities were varying from one fiber to another (see Table 14). The filtration time, during which fibers were exposed to humic acid, was different. The amount of adsorbed humic acid was calculated from kinetics adsorption (Figure 66) for an average filtration time and for each membrane (see on Table 24).

Table 24: Amount of humic acid adsorbed during the filtration for each fiber.

Fiber	Filtration time (h)	Adsorbed humic acid ($\mu\text{g}\cdot\text{cm}^{-2}$)
M-LP91	0.4	1.7
M-HP47	0.3	1.1
M-HP32	0.3	0.9
M-LP19	1.4	2.0

The filtration time for M-LP19 was the longest due to its low permeability (110 LMBH at $\text{TMP}=0.8$ bar). M-LP19 was therefore the most exposed to humic acid during filtration. Though its low adsorption of humic acid (the lowest adsorption equilibrium see Figure 66), M-LP19 adsorbed the largest amount of humic acid during its exposure to the solution. However, these results were estimated since dynamic adsorption (during filtration) might be different from static adsorption. Indeed, during filtration the concentration of polarization increases the adsorption at the membrane surface [66].

5.3.3 Hydraulic resistance

5.3.3.1 Membrane hydraulic resistance

During ultra-pure water filtration, the membrane hydraulic resistance is inversely proportional to the membrane permeability. Therefore, membrane hydraulic resistance for each fiber in outside-in and inside-out mode were obtained from permeability measurements from Figure 33 (see on Figure 68). The membrane hydraulic resistance in inside-out (see on Figure 69) was measured at each backwash pressure using Eq. 13.

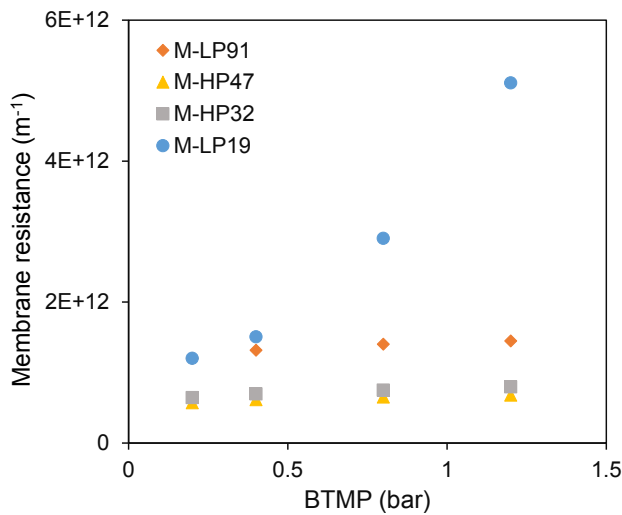


Figure 68: Pressure effect on membrane hydraulic resistance in outside-in mode (TMP=[0.2-1.2] bar)

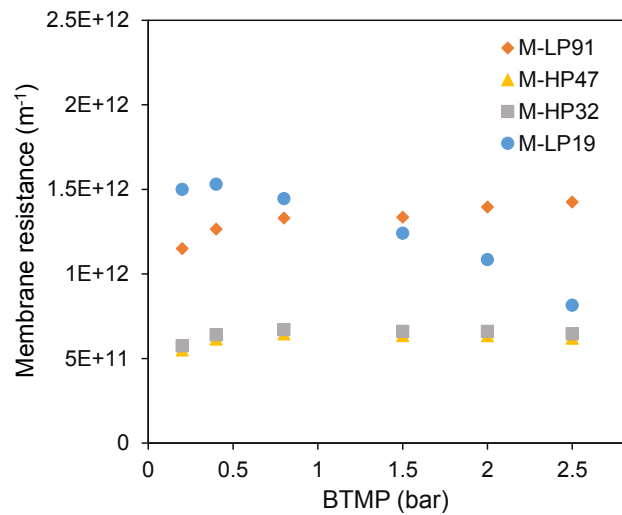


Figure 69: Pressure effect on membrane hydraulic resistance in inside-out mode (BTMP= [0.2-2.5] bar)

In outside-in mode and at constant TMP=0.8 bar, M-LP19 had the highest membrane hydraulic resistance whereas M-HP32 and M-HP47 had the lowest membrane resistance (Figure 68). In inside-out mode, the membrane resistance was increasing when increasing the BTMP for M-LP91, was slightly increasing for M-HP32 and M-HP47 and was decreasing for M-LP19. As explained in 3.4.3, membrane permeability and therefore hydraulic resistance was highly dependent on the mechanical properties of the membrane and its deformation. M-LP19 had the highest membrane hydraulic resistance at TMP=0.8 bar in outside-in mode whereas it had the same low resistance than M-HP32 and M-HP47 at BTMP=2.5 bar in inside-out mode.

5.3.3.2 Hydraulic resistance of bentonite cakes

The filtration of different bentonite feed suspensions induced the formation of different cakes with unique structure and properties. The cake resistance was also dependent on the cake thickness, therefore on the filtration time and permeate volume. Filtration operating conditions were adjusted for each membrane to produce identical filter cakes (with the same thickness and hydraulic resistance) on membranes having different mass transfer properties. Darcy's law (Eq. 5) was used for the cake hydraulic resistance calculations. Throughout the dead-end filtration of the bentonite suspensions, the cake resistance was increasing linearly until the end of the filtration (Figure 70). This observation confirms that fouling was governed by cake deposition only and that Equation Eq. 7 was valid.

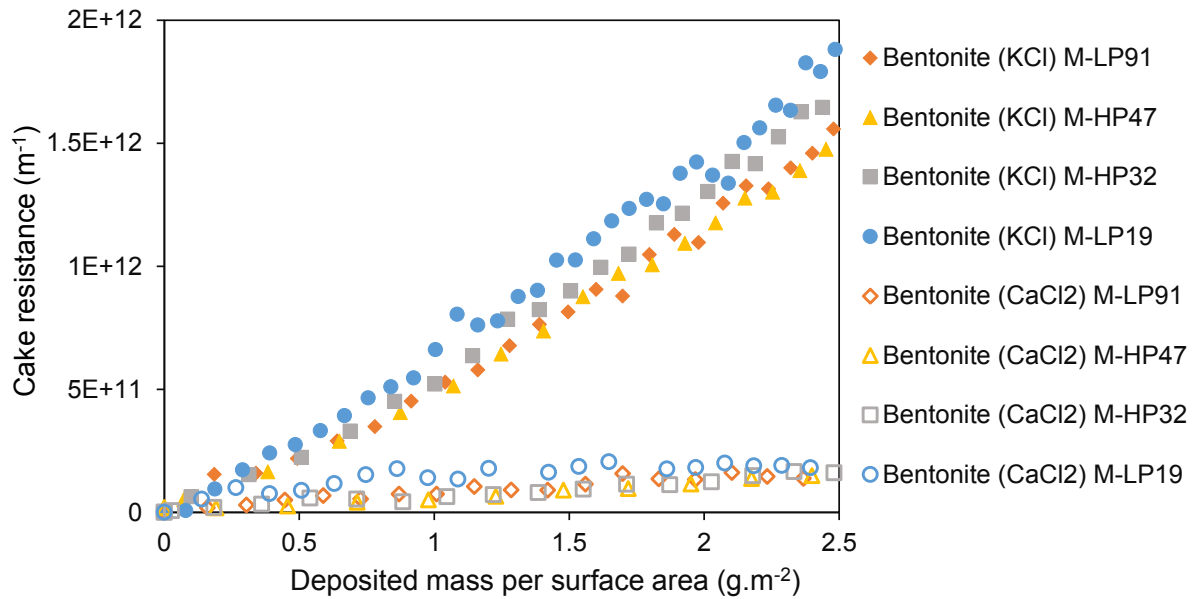


Figure 70 : Evolution of the bentonite (KCl) and bentonite (CaCl₂) cake resistance during filtration at constant TMP=0.8 bar

Due to same filtration operating pressure and identical cake thickness formed on each membrane, the cake resistance at the end of the filtration was expected to be similar between the different fouled membranes for a same feed solution. The mean cake resistance was determined on all hollow-fiber membranes: two different values of cake resistance were measured, a first one at the end of the filtration ($R_{c,f}$) and a second one after rinsing the membrane ($R_{c,r}$). The rinsing step (described in details in 2.4.2.4) using water at ionic strength of 10^{-3} M (adjusted with KCl or CaCl₂) was not supposed to affect the cake resistance. However, a non-negligible decrease of the bentonite (KCl) cake resistance was observed when the membrane was rinsed (see on Figure 71). Visual observations confirmed that during the rinsing, small fragments of bentonite (KCl) cake peeled off at the inlet of the rinsing solution probably due to shear stress on membrane surface induced by a more turbulent flow at this location. This amount of removed cake was insignificant for mass balance calculation (<10 %) but can strongly influence the hydraulic resistance. Bentonite (KCl) cake was the only deposit to be damaged during the rinsing step due to the lack of cohesion of the deposit. Only the value of cake resistance after rinsing was taking into account for the backwash calculations, therefore R_c was chosen equal to $R_{c,r}$ (as listed in Table 25).

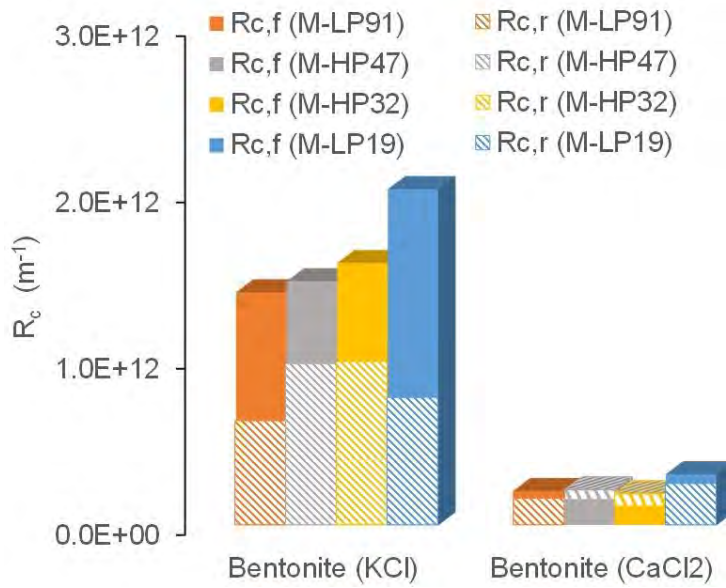


Figure 71: Bentonite cake resistance at the end of the filtration ($R_{c,f}$) and after rinsing ($R_{c,r}$) on each membrane

An averaged value of the cake resistance for all membrane was reported in Table 25 for bentonite solutions. Low standard deviations were obtained between the different hollow-fiber membranes indicating similar cake thickness for each fouled fiber. Because of a continuous compaction of M-LP19 under pressure due to its elastic properties (see on Figure 32), the membrane hydraulic resistance was changing over filtration time and affected the calculations of cake resistance. This could explain why the cake resistance on M-LP19 was always the highest between the membranes for each filtration.

Table 25: Mean cake resistance after filtration $R_{c,f}$ and after rinsing the fouled membrane $R_{c,r}$.

Cake	$R_{c,f}$ ($\times 10^{11} \text{ m}^{-1}$)	$R_{c,r}$ ($\times 10^{11} \text{ m}^{-1}$)
Bentonite (KCl)	16 ± 1	8 ± 0.5
Bentonite (CaCl ₂)	2 ± 0.5	2 ± 0.5

Changing the nature of the salt added to the suspension offers different cake resistances. For instance, the bentonite (KCl) cake resistance was 8 times higher than the cake resistance of bentonite (CaCl₂) after filtration. These differences may be explained by the modification of the cake structure. In his work Lelievre [197] explained why the filtration of laponite (MgCl₂), a clay from the smectite group, form a more permeable cake than laponite (NaCl). Small angle neutron scattering measurements showed that the structure of laponite (NaCl) cake was much more ordered than in the case of Laponite (MgCl₂) cake. In the presence of a monovalent and inert salt, the interactions between particles were mainly repulsive leading to the formation of an ordered and low-permeable cake structure under pressure. Whereas in the case of a divalent

salt, the interaction forces between particles were less repulsive and the distances between particles were not regular leading to a disordered and permeable cake structure under pressure.

5.3.3.3 Specific bentonite cake resistance

From filtration data recording and using Eq. 6, it can be drawn real-time curves of the specific cake resistance evolution as a function of the deposited mass per surface area for all the different fibers as shown on Figure 72. It can be observed a rapid stabilization of the specific resistance around a common value for all fibers but specific to each feed composition. This value gives information on the structure and properties of the bentonite cake and is independent of the cake thickness, contrary to the cake resistance values.

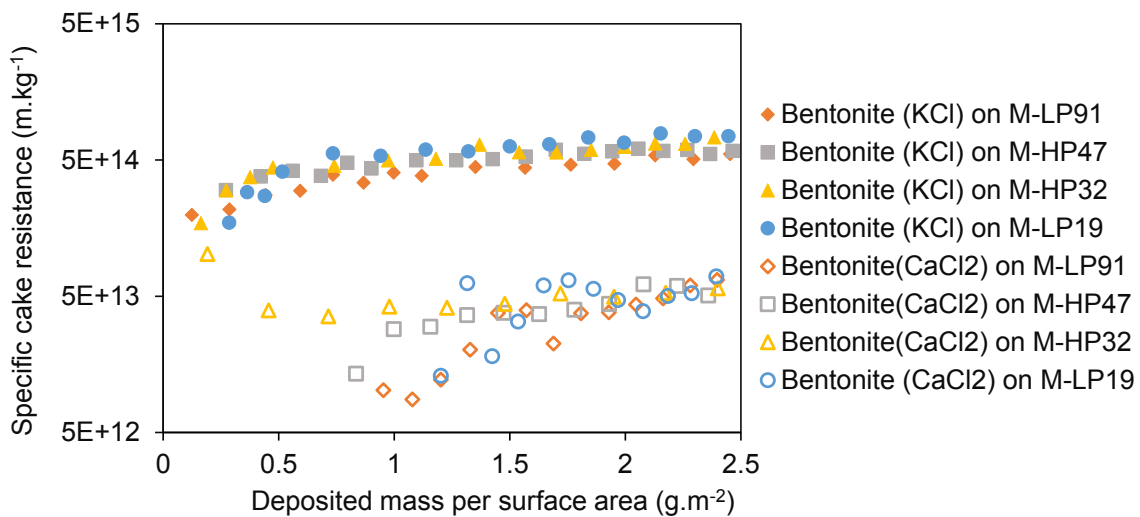


Figure 72: Evolution of the specific resistance for bentonite (KCl) and bentonite (CaCl₂) cake during filtration at constant pressure TMP=0.8 bar

Specific cake resistances values were calculated using Eq. 6 and reported in Table 26.

Table 26: Specific cake resistance for bentonite (KCl) and bentonite (CaCl₂) filtration at TMP=0.8 bar

Cake	α ($\times 10^{13}$ m.kg ⁻¹)
Bentonite (KCl)	70 \pm 11
Bentonite (CaCl ₂)	7 \pm 3

The specific resistance for bentonite (CaCl₂) cake was 10 times lower than bentonite (KCl) cake meaning that calcium chloride induces a more permeable bentonite cake structure than potassium chloride as explained in the previous section (5.3.3.2).

5.3.3.4 Hydraulic resistance for humic acid filtration

In the case of humic acid filtration the increase in fouling resistance was not linear as shown on Figure 73 and was different on each hollow-fiber membrane suggesting other fouling mechanisms in addition of cake deposition such as pore blocking and adsorption of humic substances.

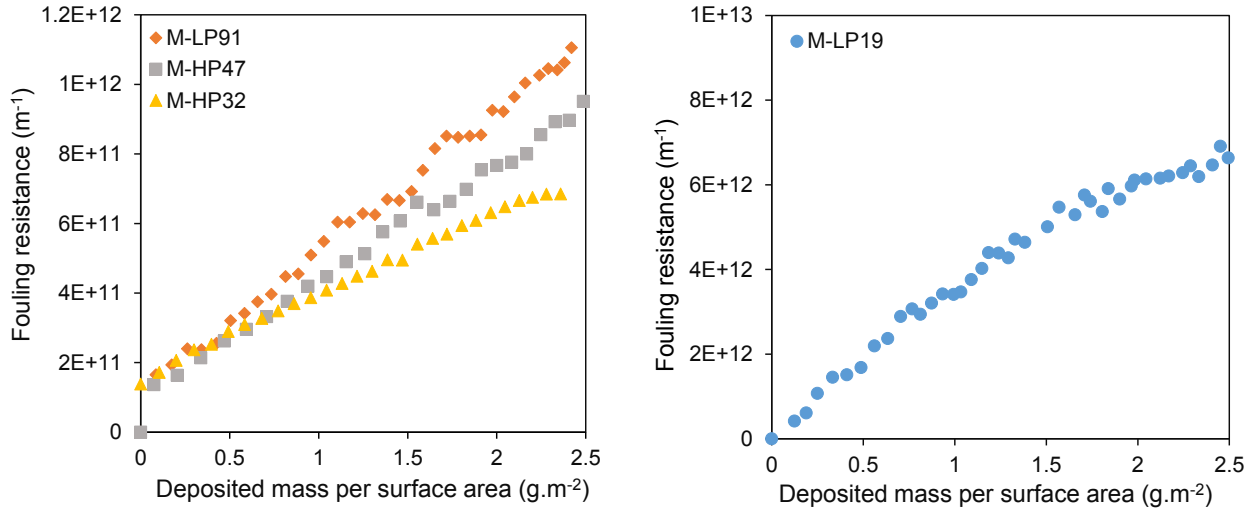


Figure 73 : Evolution of the humic acid (CaCl_2) fouling resistance during filtration at constant $\text{TMP} = 0.8$ bar

Therefore, it was more appropriate to talk about fouling resistance than cake resistance since each mechanism contributed to the fouling resistance. The mean fouling resistance was determined for each hollow-fiber membranes after filtration $R_{f,f}$ and after rinsing $R_{f,r}$ (as shown in Table 27). Contrary to bentonite (KCl) filtration, the rinsing step had here no effect on the bentonite (CaCl_2) cake resistance. The value of cake resistance after rinsing was taken into account for backwash calculations, therefore R_f was chosen equal to $R_{f,r}$.

Table 27: Mean fouling resistance after filtration $R_{f,f}$ and after rinsing the fouled membrane $R_{f,r}$

Cake	$R_{f,f}$ ($\times 10^{11} \text{ m}^{-1}$)	$R_{f,r}$ ($\times 10^{11} \text{ m}^{-1}$)
M-LP91	11 ± 2	10 ± 1
M-HP47	9 ± 2	9 ± 1
M-HP32	7 ± 1	7 ± 1
M-LP19	71 ± 8	66 ± 2

A portion of humic acid particles was passing through the membrane and cause inevitably pore blocking which led to a rapid increase of the fouling resistance [196]. Due to initial high membrane resistance for M-LP19 (Figure 68), the calculated fouling resistance was very high

compared to the other calculated resistances (> 7 times higher) even at the beginning of the filtration. However, the measurements of cake height observed by camera (Figure 74) confirmed that the same amount of humic acid was deposited on M-LP19 than on M-LP91. The cake resistances on the different fibers were then assumed in the same order of magnitude and lower than the maximum fouling resistance observed on M-HP32, $R_{c,f} < 7.10^{11} \text{ m}^{-1}$ (from Table 27).

5.3.4 Measurement of the cake thickness

The objective of this section is to measure the cake thickness for bentonite and humic acid suspensions for different membranes during the filtration step to understand the different cake structure and evaluate its influence on cake removal. The measured cake thickness was plotted as a function of the permeate volume per membrane surface area as shown in Figure 74 to compare cake formation on membranes with different dimensions.

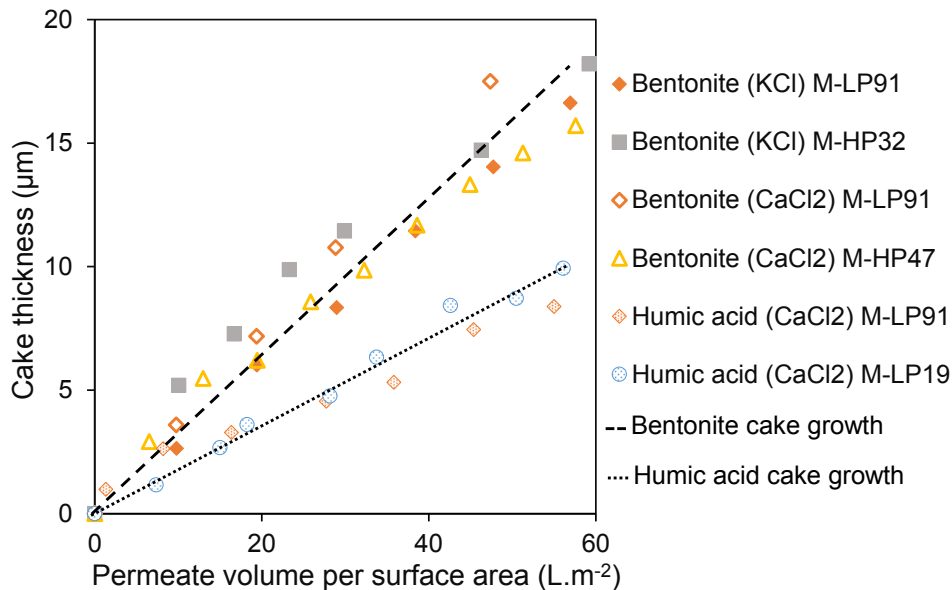


Figure 74: Observation of bentonite and humic acid cake formation on different membranes at constant pressure, $TMP=0.8 \text{ bar}$

As expected in dead-end filtration mode, a linear increase of the cake thickness was observed with the increase of permeate volume. The filtration of 60 L.m^{-2} of bentonite feed solution formed a cake with a thickness of $17 \pm 3 \mu\text{m}$ bentonite cake whereas the filtration of 60 L.m^{-2} of humic acid feed solution formed a cake with a thickness of $10 \pm 3 \mu\text{m}$. The cake growth appeared to be identical for a same feed and if compared between two different membranes as illustrated on Figure 74 confirming that cake deposition was independent of the membrane properties.

Furthermore, the cake growth was also independent of the type of salt added to the bentonite suspensions. Indeed bentonite (KCl) and bentonite (CaCl₂) cakes showed the same cake thickness increase with permeate volume meaning that the cake density was close for the two filtrations. Regarding the cake growth from humic acid particles, for a same permeate volume per surface area the thickness was approximately 60 % the value of the bentonite cake thickness. This lower thickness was firstly explained by the low retention of humic acid particles at the membrane surface (see Table 22) compared to bentonite particles. However, the observed cake thickness depended also on the cake density, which is function of its porosity, its swelling ability in water, and its compressibility under pressure. The cake thickness was plotted as a function of the calculated deposited mass per surface area on Figure 75. The mass of particle retained and deposited on the surface was calculated by Eq. 7.

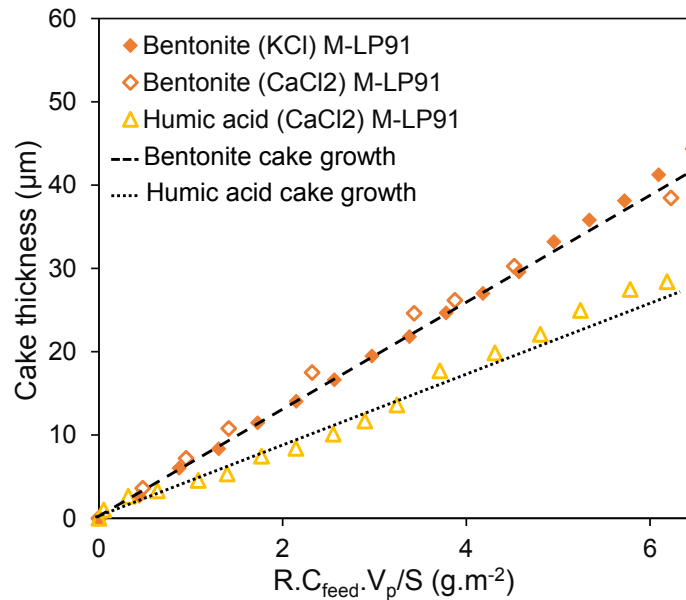


Figure 75: Evolution of the cake thickness on long-term during filtration of the different suspensions on M-LP91 at constant TMP=0.8 bar as a function of the calculated mass deposited per surface area.

The concentration of particle in the cake was calculated by Eq. 34 and reported in Table 28 :

$$C_{cake} = \frac{m_d}{h_f * S_{ext}} \quad \text{Eq. 34}$$

With C_{cake} the concentration of particles in the cake (kg.m⁻³)

Table 28: Particle concentration in the bentonite and humic acid cake.

Cake	C_{cake} (g.L ⁻¹)
Bentonite (KCl)	150
Bentonite (CaCl ₂)	150
Humic acid (CaCl ₂)	290

From the particle concentration values (Table 28), the bentonite cake was composed of 85% of water compared to the humic acid cake, which contained 71% of water. The same particle concentration was found for bentonite (KCl) and bentonite (CaCl₂) cake and therefore the salt used was not affecting cake structure and density. The particle concentration in humic acid (CaCl₂) cake was twice higher than bentonite cakes indicating a cake with higher compacity and probably less porous.

5.3.5 Conclusions

As a conclusion, the fouling step was controlled by the amount of permeate volume filtered per surface area. Indeed a linear increase of the cake thickness was observed during filtration and identical cake height could be formed on the different membranes. A cake thickness of 17 μm for bentonite and 10 μm for humic acid was measured when filtering a volume per surface area of 60 L.m⁻² for each membrane. This controlled thickness was essential for the comparison of the backwash efficiency between the different membranes (as demonstrated in the next section 5.4). The study of fouling mechanisms revealed that fouling resistance did not depend on the membrane properties in the case of bentonite filtrations: identical cake hydraulic resistances were indeed obtained on different membranes for a specific feed suspension. However, the cake hydraulic resistance was varying depending on the salt added to the suspension (here, KCl or CaCl₂). The specific cake resistance of bentonite (CaCl₂) was 10 times lower than bentonite (KCl) due to the build-up of a more disordered structure. Fouling mechanisms were more complex during humic acid filtration. Indeed, fouling resistance depended on the membrane properties. Indeed as particles were not completely retained by the membrane, pore blockage occurred. Furthermore, humic substances were adsorbed on the membrane surface and within the pore. These fouling mechanisms were largely contributing to the increase of the observed

fouling resistance and overcame the cake hydraulic resistance that was assumed identical on each membrane.

5.4 Fouling removal analysis

Once the membrane was fouled, the flow of permeate was reversed to perform a backwash at constant pressure to remove the cake and recover the initial permeability.

Backwash at fixed transmembrane pressure (BTMP) was chosen to study the influence of the membrane mechanical properties on the backwash efficiency. Membrane deformation (pore and diameter) was indeed function of the applied stress or pressure. Backwash was performed at different pressures from 0.2 to 2.5 bar for each fouled membrane.

Permeability recovery is usually used to compare cleaning efficiency. However, it is difficult to predict backwash efficiency by this method on a few cycles of filtration/backwash. The mass balance method was used to assess the backwash efficiency on a single cycle and for comparison between membrane performances.

5.4.1 Influence of the cake thickness

0.05 g.L⁻¹ or 0.5 g.L⁻¹ bentonite (KCl) suspension was filtered on M-LP91 and M-LP19 to form a deposit with a thickness from 17 to 170 μm. Calculations of the specific resistance for the cakes verified that the cake structure was independent both of the cake thickness and the feed concentration.

Backwash was performed at constant BTMP=0.4 bar for 60 seconds on each fouled membrane. The percentage of removed cake during backwash was plotted as function of the thickness of the deposited cake in Figure 76.

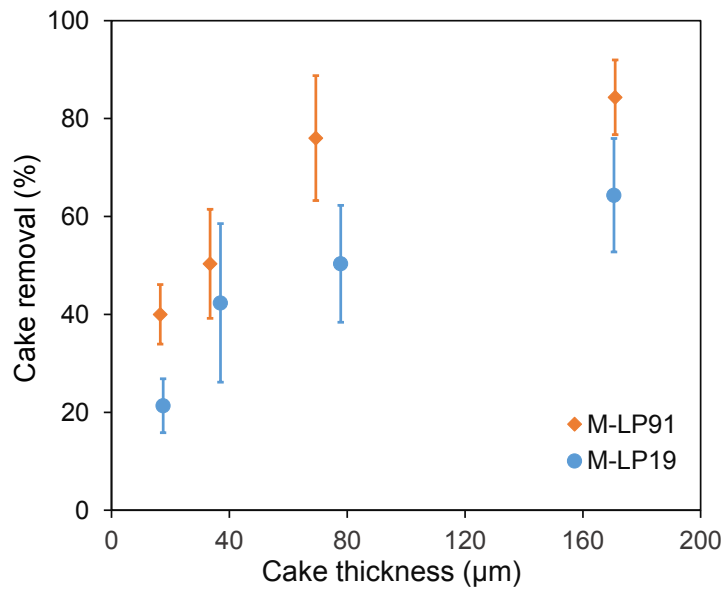


Figure 76: Influence of bentonite cake thickness on the cake removal during backwash at constant pressure, $BTMP=0.4$ bar, on M-LP91 and M-LP19

For both studied membranes, higher fouling removal was measured for thicker cake. Indeed, only [20-40]% of bentonite (KCl) cake was removed when the deposit thickness was 17 μm , whereas [60-80]% was removed in the case of 170 μm thick cake. Furthermore, M-LP19 demonstrated lower cake removal than M-LP91 for each cake thickness. Further analysis of the results was carried out in section 5.5.2.

Measurements of permeability after the backwash gave information on the permeability recovery (see Figure 77). The permeability recovery could also be correlated to the cake removal as shown in Figure 78.

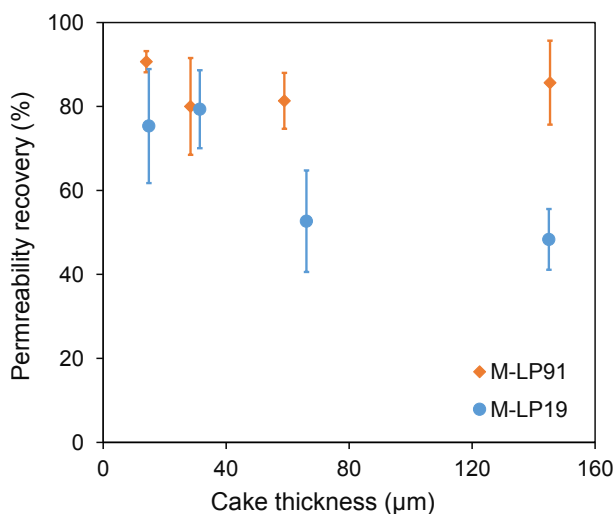


Figure 77: Permeability recovery after backwash at constant pressure, $BTMP=0.4$ bar, on M-LP91 and M-LP19 for several bentonite cake thicknesses

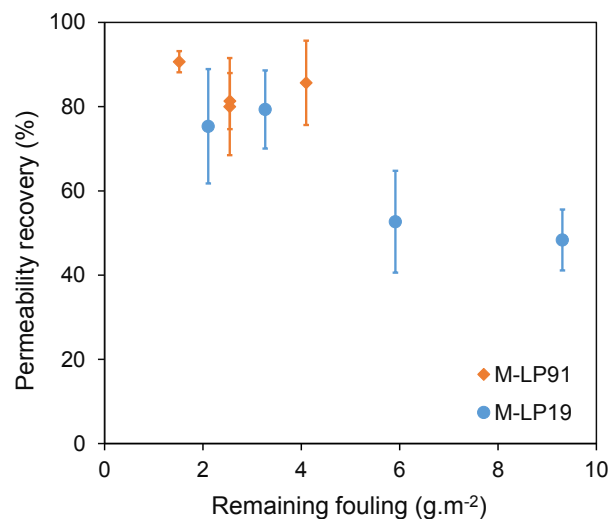


Figure 78: Permeability recovery as a function of the remaining fouling after backwash at constant pressure, $BTMP=0.4$ bar, on M-LP91 and M-LP19

The idea that the higher the fouling removal, the higher the permeability recovery was not verified in this case since different mass of particles was deposited on the surface. Figure 76 and Figure 77 showed that only 50% of the M-LP19 initial permeability was recovery when 60% of a 170 μm thick bentonite cake was removed whereas 75% of the permeability was recovered when 20% of 17 μm thick bentonite cake was removed. This result was explained by the remaining fouling on the membrane, which was calculated by the subtraction of the removed cake mass to the deposited cake mass. The higher the remaining fouling the lower was the permeability recovery. A strong decline of the permeability recovery was observed when more than 5 $\text{g}\cdot\text{m}^{-2}$ remained on the fiber after backwash. Cake removal results were therefore consistent with the permeability recovery results.

5.4.2 Study on a 17 μm thick bentonite (KCl) cake

The objective of the following part was to compare backwash efficiency between different membranes and at different backwash pressures. Choosing to depose a thin deposit with a thickness of 17 μm allowed a larger range of cake removal percentage between 3 and 98% in the range of BTMP from 0.2 to 1.5 bar for the bentonite (KCl) and bentonite (CaCl_2). Furthermore, according to Figure 76 the results were the most reproducible for a thickness of 17 μm .

5.4.2.1 Amount of cake removed during backwash at different BTMP

The fouled membrane was backwashed and the amount of cake removal was compared between the different hollow-fiber membranes (Figure 79). An increase of the percentage of cake removal with increasing the backwash pressure was observed for all membranes. A low percentage of removal below 40% was observed in the case of M-LP91 and M-LP19 membranes at low BTMP [0.2-0.4 bar] whereas at BTMP=1.5 bar, the removal percentage reached 70%. Low BTMP were however sufficient to remove the cake formed on M-HP32 and M-HP47 since 70% of the cake was removed at BTMP=0.4 bar. A good reproducibility of the results was obtained for each membrane and pressure.

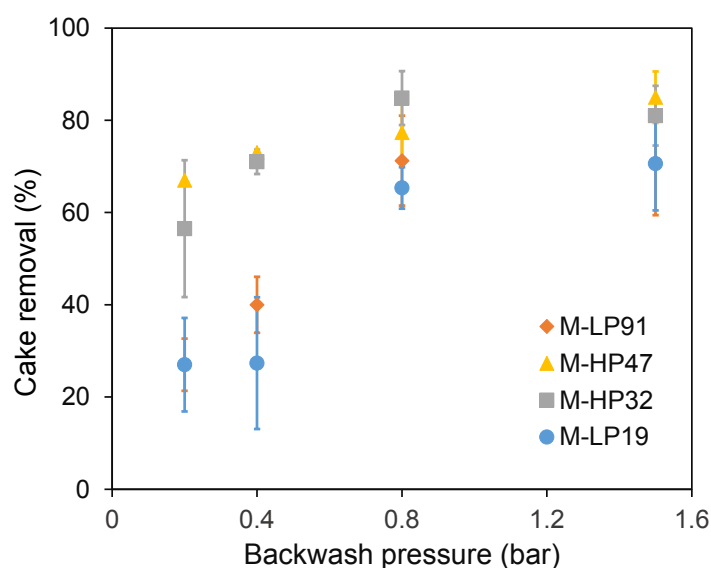


Figure 79: Effect of backwash pressure on bentonite (KCl) cake removal

Global backwash performances were lower for M-LP19 and M-LP91 than for M-HP47 and M-HP32. The main differences between these two groups of membranes were their permeability and their hydrophilicity (see Table 14 and Table 13). As first assumption, a more permeable and/or a more hydrophilic membrane might conduct to higher backwash efficiency.

5.4.2.2 Permeability recovery after backwash

Permeability recovery was plotted as a function of backwash pressure as shown in Figure 83. It can be observed a lower permeability recovery at low BTMP than at high BTMP and the lowest permeability recovery were obtained for M-LP19. However, the permeability recovery differences between the membranes were not significant, indeed the maximal difference (between low and high BTMP) was 25%, with an averaged standard deviation between measurements of 10%. Unlike the method of permeability recovery, the method of mass balance demonstrated maximal percentage differences up to 60 % (see on Figure 79) making the comparison between the fibers easier. The backwash efficiency based on permeability measurements was more representative of the fouling removal when calculating the gain of permeability using Eq. 3. Indeed Figure 81 shows larger differences between fibers and results were more consistent with the ones obtained by mass balance method (Figure 79). Both mass balance method and gain of permeability calculation seemed appropriate to evaluate the backwash efficiency on a single filtration-backwash cycle.

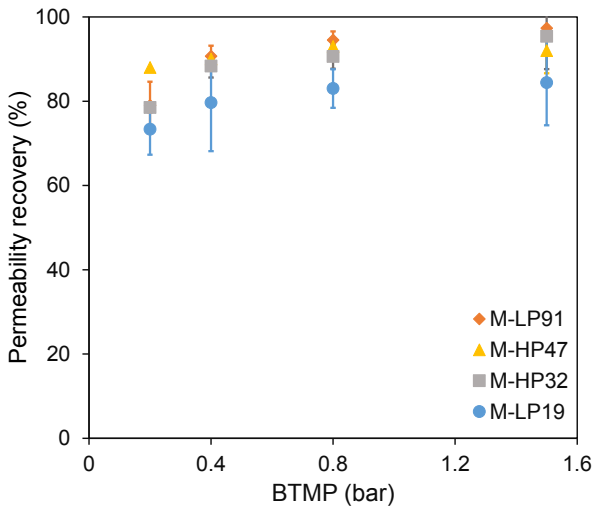


Figure 80: Effect of backwash pressure on membrane permeability recovery after bentonite (KCl) fouling

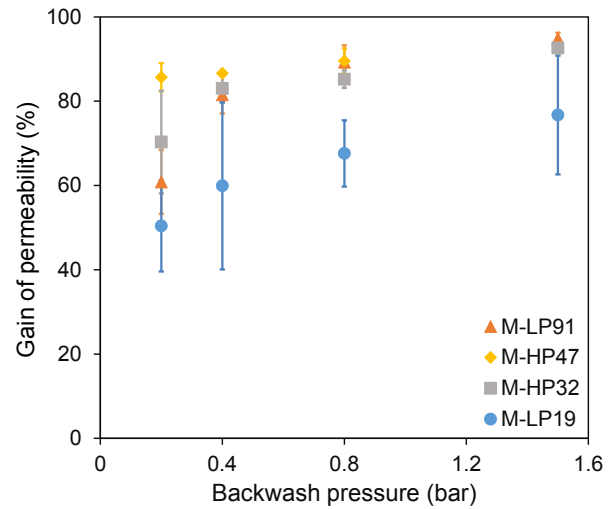


Figure 81: Effect of backwash pressure on permeability gain after bentonite (KCl) fouling

The difference of percentage between these two methods can be interpreted from Figure 82. Permeability recovery rapidly increased to 60% even at a low percentage of cake removal of 30%. Indeed, when a fragment of the cake was detached, the local hydraulic resistance strongly decreases and it becomes a preferential path for water to go through. Thus, even low cake removal percentage could lead to high permeability recovery as illustrated in Figure 82.

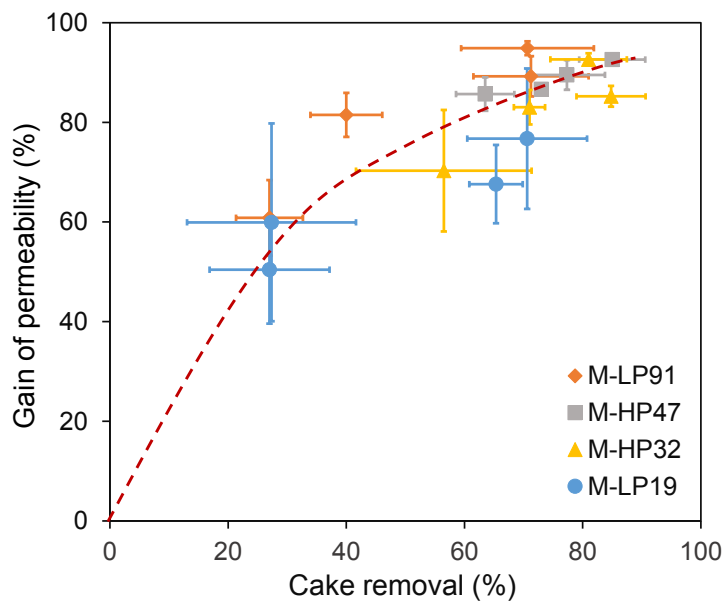


Figure 82: Correlation between gain of permeability and bentonite (KCl) cake removal during backwash

5.4.3 Study on a 17 μm thick bentonite (CaCl_2) cake

5.4.3.1 Amount of cake removed during backwash at different BTMP

The experiments were reproduced in the exact same conditions but with bentonite (CaCl_2) feed solution. The same increase of the amount of cake removed with BTMP can be observed on Figure 83 during the backwash step. Contrary to the deposit with KCl, the deposit here was not removed at all at low BTMP, indeed less than 5% was removed at 0.2 bar for all fibers and less than 30% at 0.4 bar for most fibers (except M-HP32). Furthermore, at high pressure the removal percentages were higher than in the case of cake made from bentonite (KCl). One of the assumption was a stronger cohesion of the bentonite (CaCl_2) cake in the presence of CaCl_2 [198]. As observed on Figure 89, either the cake remained intact or it broke off as large fragments leading to extremely low or high cake removal. Moreover, bentonite (CaCl_2) cake was not affected by rinsing step contrary to bentonite (KCl) one. This could explain why higher cake removal percentages (Figure 83), than in the case of bentonite (Figure 79), were measured at BTMP=1.5 bar.

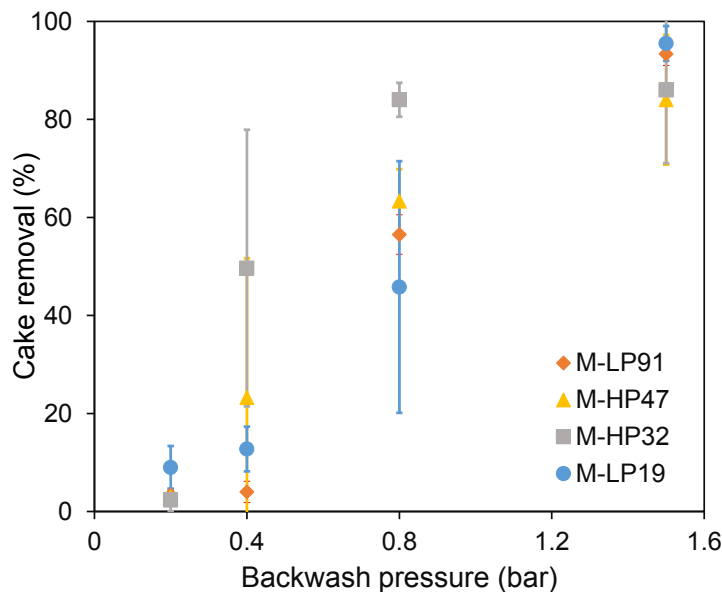


Figure 83: Effect of backwash pressure on bentonite (CaCl_2) cake removal

5.4.3.2 Permeability recovery after backwash

The permeability recovery and gain of permeability were plotted as a function of the backwash pressure for the bentonite (CaCl_2) fouling. According to the results presented in 5.3.1 the hydraulic resistance of the bentonite (CaCl_2) fouled membrane was mainly led by the

membrane hydraulic resistance and not by the cake resistance, that is why even if less than 5% of cake was removed, the permeability recovery was superior to 70%. This confirmed that mass balance method was preferable to evaluate backwash efficiency. However, Figure 85 shows the gain of permeability and variations seemed more consistent with Figure 83 than Figure 84. Gain of permeability was indeed very low at low BTMP and significantly increased when increasing BTMP.

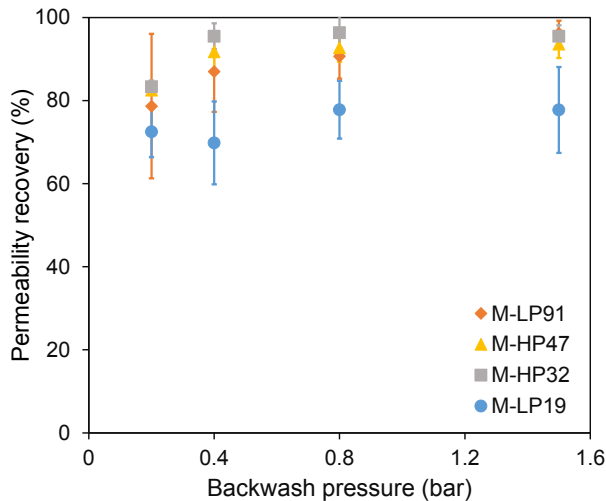


Figure 84: Effect of backwash pressure on permeability recovery after bentonite (CaCl_2) fouling

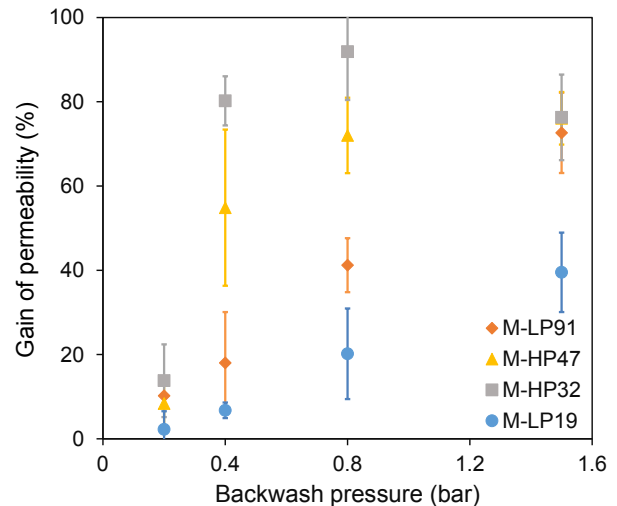


Figure 85: Effect of backwash pressure on permeability gain after bentonite (CaCl_2) fouling

5.4.4 Study on a 10 μm thick humic acid (CaCl_2) cake

5.4.4.1 Amount of cake removed during backwash at different BTMP

Membranes fouled with humic acid were much harder to clean hydraulically than bentonite fouled membranes, as shown on Figure 86. Extremely low percentages of cake were removed from M-LP91, M-HP47 and M-HP32 (less than 20% of cake removal) even when increasing BTMP up to 2.5 bar. However, M-LP19 demonstrated a remarkable increase of cake removal percentage with increasing the BTMP. The cake removal was 20 % at BTMP=0.4 bar and reached more than 60% at BTMP=2.5 bar. While backwash efficiency of M-LP19 was lower than the other membranes for bentonite cake removal (see on Figure 79 and Figure 83), in the case of humic acid the backwash performances were much greater for M-LP19 (Figure 86).

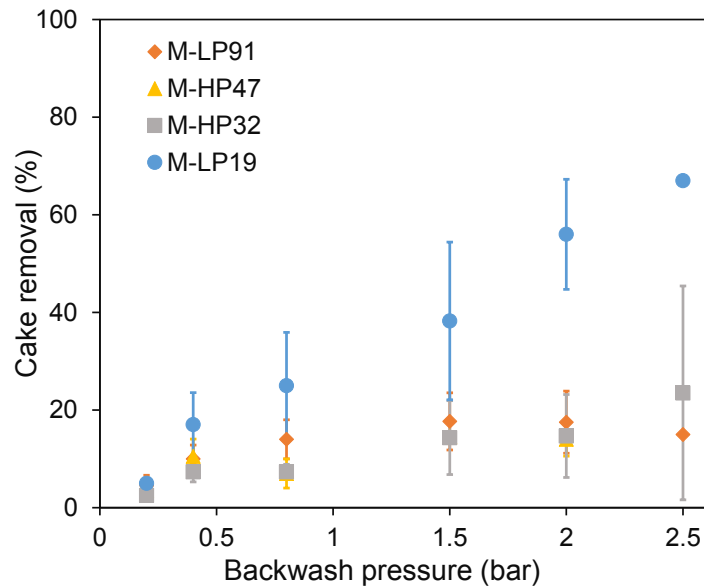


Figure 86: Effect of backwash pressure on humic acid (CaCl_2) cake removal

5.4.4.2 Permeability recovery after backwash

Permeability recovery was lower for humic acid filtration than bentonite filtrations. Furthermore, only 50% of the initial permeability could be recovered for M-LP19 (see on Figure 87) while more than 60 % of the humic cake was removed at 2.5 bar (see on Figure 86). This low recovery could be compared to the strong fouling resistance of the M-LP19 after filtration indicating a pore blocking or adsorption within the pore that was partially irreversible. Even if M-LP91, M-HP47 and M-HP32 showed better permeability recovery than M-LP19, between 60 and 80 %, results were very different if the gain of permeability (Eq. 3) was plotted as a function of the backwash pressure as shown in Figure 88. M-LP19 demonstrated indeed a higher gain of permeability than the others did on a single filtration backwash cycle and results were therefore comparable to the ones obtained by the mass balance method (Figure 86). It might be assumed that M-LP19 would become the membrane with the best hydraulic performances when performing on several cycles.

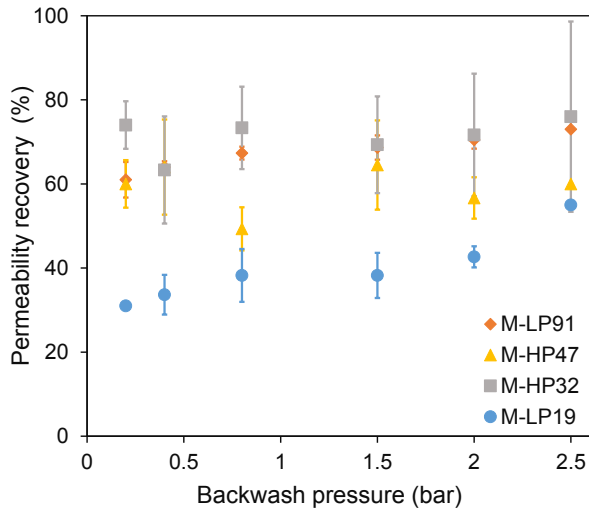


Figure 87: Effect of backwash pressure on permeability recovery after humic acid (CaCl_2) fouling

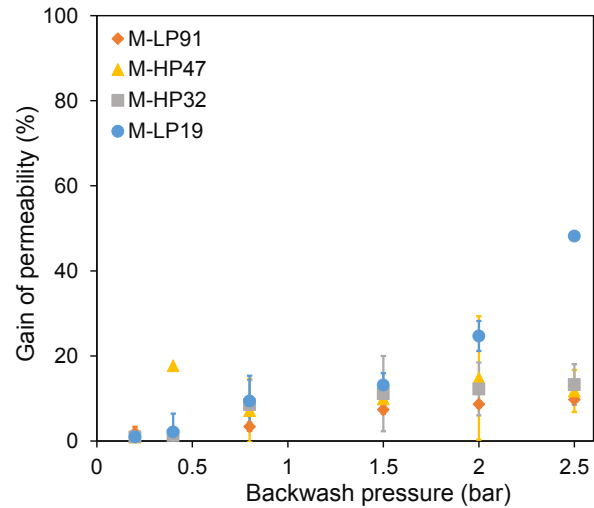


Figure 88: Effect of backwash pressure on permeability gain after humic acid (CaCl_2) fouling

5.4.1 Effect of cation valency and visual observation of cake removal

Electrostatic interactions were strongly influenced by the presence of a salt. While monovalent salts (i.e. KCl) were considered inert to the membrane and bentonite particles, bivalent salts (i.e. CaCl_2) could interact and adsorb on negative surfaces. Calcium cations have indeed interesting chelating properties [199][200] and could bridge negatively charged montmorillonite particles [198][72] and humic acid particles [200][70][110]. This bridging effect would reinforce the cohesion and the breaking strength of bentonite (CaCl_2) and humic acid (CaCl_2) cake. Furthermore, Li et al. [108] demonstrated Ca^{2+} adsorption on PES/PVP hollow-fiber membrane. This adsorption would promote the adhesion of particles on the membrane surface and the cake might be more difficult to remove during backwash as seen on Figure 83 and Figure 86.

Bentonite cake fragmentation explained in Section 5.4.3 was confirmed by visual observations of the cake removal during backwash at BTMP=0.8 bar (see on Figure 89). Bentonite (CaCl_2) cake looks to break off from the surface only as large fragments (size >1 mm) at high pressure whereas bentonite (KCl) cake was breaking into small pieces (size <1 mm) at low and high pressures (illustrated on Figure 89).

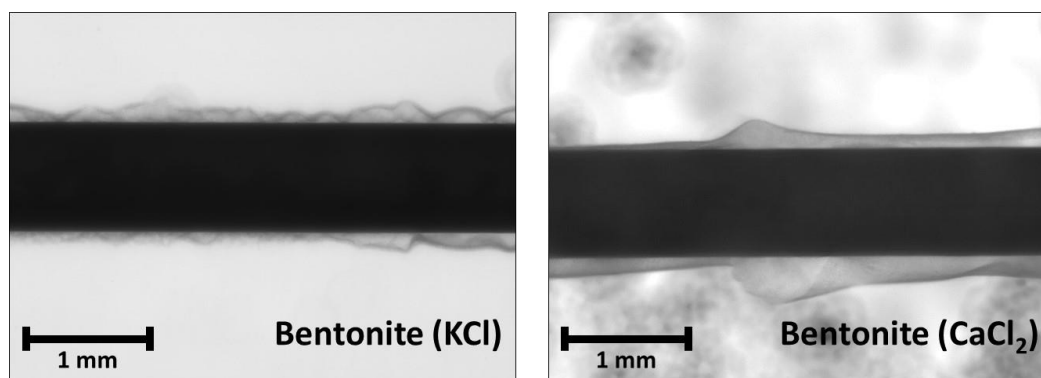


Figure 89: Pictures of bentonite (KCl) (left) and bentonite (CaCl₂) (right) cake fragments during backwash at constant pressure, BTMP=0.8 bar

Regarding humic acid (CaCl₂) cake, it was removed at very high pressure BTMP=2.0 bar and only from M-LP19 (see Figure 86). During backwash, varying sizes of the fragments were observed and most of them presented a long and thin shape (Figure 90). Even if the cake seemed to detach from the surface, a significant proportion of fragments remained attached after backwash to the surface through binding sites as observed on Figure 90. Yoon *et al.* [70] explained that free humic acid was bound to the adsorbed humic on the membrane surface through calcium ions.

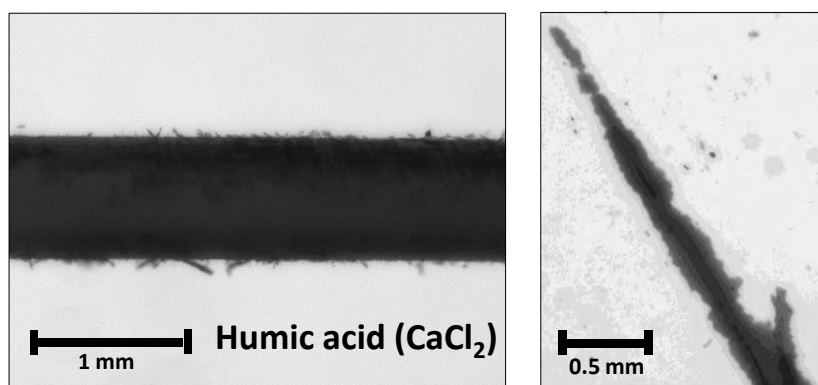


Figure 90: Pictures of humic acid (CaCl₂) cake removal on M-LP19 (left) and cake fragment (right) during backwash at constant pressure, BTMP=2.0 bar

5.4.2 Conclusions

Mass balance was the most appropriate method to evaluate the amount of cake removed during backwash and therefore the backwash efficiency on a single filtration-backwash cycle. The calculation of permeability gain was also very consistent with the cake removal percentage and offer better insight into the backwash efficiency than permeability recovery. In the case of bentonite filtration, an increase of the percentage of removed cake was observed with

increasing the backwash pressure. For both bentonite suspensions, the fouling removal performance seemed related to the mass transfer properties of the membranes: M-LP91 and M-LP19, the low permeability membranes, demonstrated lower backwash efficiency than M-HP47 and M-HP32, the high permeability membranes. However, opposite results were obtained in the case of humic acid filtration. At high backwash pressures, M-LP19 was indeed the membrane with the greatest backwash efficiency. Visual observations under camera of the different cake removals confirmed the mass balance results and revealed information about the fouling mechanisms and the interesting chelating properties of Ca^{2+} .

It was difficult to draw conclusions from the other membrane properties: surface and mechanical properties. However further investigations were conducted on the fouling removal mechanisms in the following part (see on 5.5.1) to have a comprehensive understanding of the role of mass transfer and mechanical properties.

5.5 Fouling removal mechanisms

5.5.1 Existence of a critical backwash flux for bentonite filtration

As summarized in 5.4.2, membrane with higher permeability (from 400 to 700 LMBH) showed a better fouling removal than low permeability membranes (from 100 to 400 LMBH) in the case of bentonite filtration. The primary difference between the backwash efficiencies for the selected membranes could come from their mass transfer properties. This strong assumption was confirmed by plotting the cake removal as a function of the calculated backwash flux (see on Figure 91 and Figure 92). For both bentonite suspensions, a generalized trend was indeed observed whatever the fiber but specific to the feed composition. In the case of bentonite ultrafiltration, neither the membrane structure, dimensions, mechanical, surface nor mass transfer properties affected the fouling removal mechanisms but only the backwash flux (J_{bw}) was causing the elimination of the bentonite cake during the backwash.

During backwash, bentonite cake removal was thus controlled by the hydraulic vector and the cake properties as differences were observed between bentonite (KCl) on Figure 91 and bentonite (CaCl_2) on Figure 92.

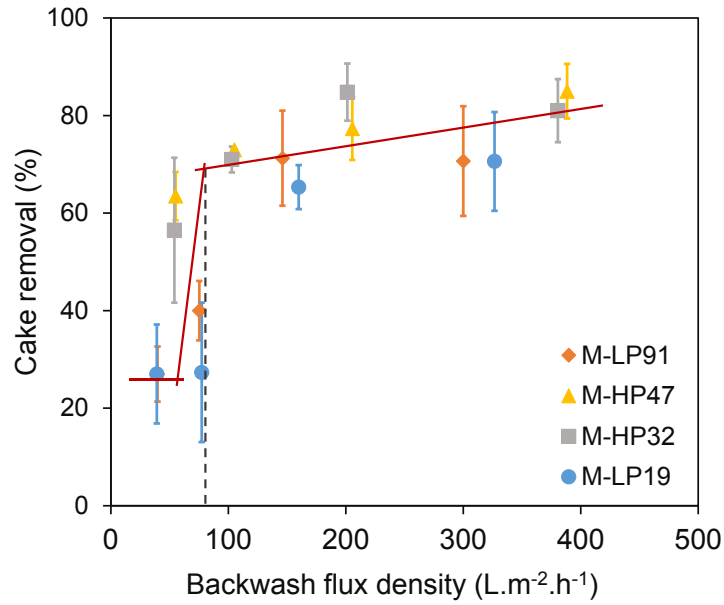


Figure 91: Critical backwash flux after bentonite (KCl) fouling

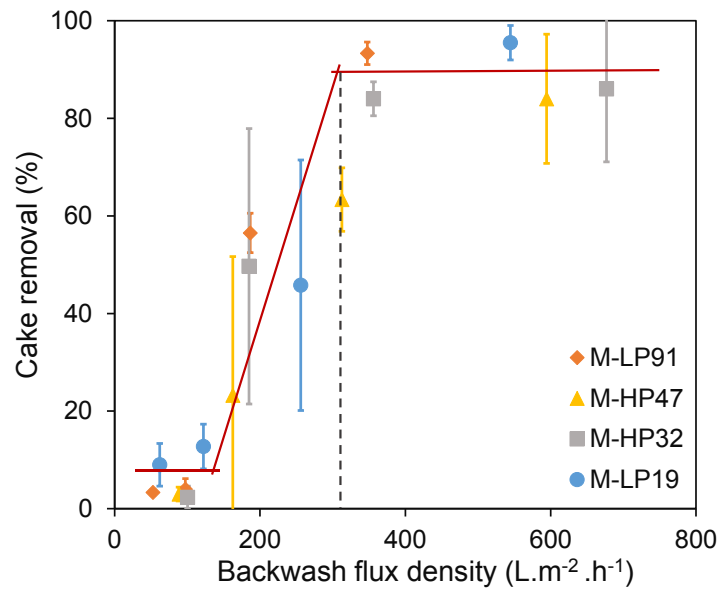


Figure 92: Critical backwash flux after bentonite (CaCl₂) fouling

Three distinguished parts of the curve were identified from Figure 91 and Figure 92: a plateau at low J_{bw} where low removal occurred; a transition zone where the cake removal increased drastically and a plateau at high J_{bw} where significant amount of cake was removed but the increase of cake removal was low.

One can define a critical backwash flux ($J_{bw,crit}$) as the minimal backwash flux to reach the plateau and from which the backwash reached its maximal (or close to) efficiency.

In the case of bentonite (KCl) deposit, the critical backwash flux was 80 L.m⁻².h⁻¹ whereas in the case of bentonite (CaCl₂) deposit, it was 310 L.m⁻².h⁻¹. The critical backwash flux was 4 times

higher when the hydraulic resistance after rinsing ($R_{c,r}$) was 4 times lower (as seen on Table 25). This higher $J_{bw,crit}$ (CaCl_2) meant a cake that was more difficult to remove as shown previously in Figure 83 in comparison with Figure 79. This higher $J_{bw,crit}$ was obtained for more permeable cake (i.e. less resistant, see Table 25) suggesting a potential relationship between $J_{bw,crit}$ and cake properties (demonstrated in the following section, Eq. 38). This $J_{bw,crit}$ depended on the cake properties, which were the result of filtration operating conditions (here, feed composition).

5.5.2 Critical pressure for the detachment of bentonite cakes

The critical backwash flux is also closely related to a critical pressure required to detach and remove the bentonite cake. Indeed the applied backwash transmembrane pressure generates a backwash flux, thus the critical backwash pressure (BTMP_{crit}) is also calculated from the critical backwash flux by Eq. 35.

$$\text{BTMP}_{crit} = \frac{J_{bw,crit}}{Lp'_f} \quad \text{Eq. 35}$$

However, BTMP was not the pressure that acted directly on the cake. We defined the inter cake-membrane pressure (ICMP) as the pressure at the interface between the cake and the outer surface of the membrane (Figure 93). This pressure, or constraint, was indeed really applied on the cake surface during backwash. ICMP was obviously different from the backwash transmembrane pressure as the membrane offered hydraulic resistance to the water flux. ICMP was obtained from flow conservation for incompressible fluid and resistances in series model (Eq. 36).

Considering Figure 93 and according to flow conservation for an incompressible fluid:

$$Q = Q_{memb} = Q_{cake}$$

with Q the total flow ($\text{m}^3 \cdot \text{s}^{-1}$), Q_{memb} the flow through the membrane ($\text{m}^3 \cdot \text{s}^{-1}$) and Q_{cake} the flow through the cake ($\text{m}^3 \cdot \text{s}^{-1}$).

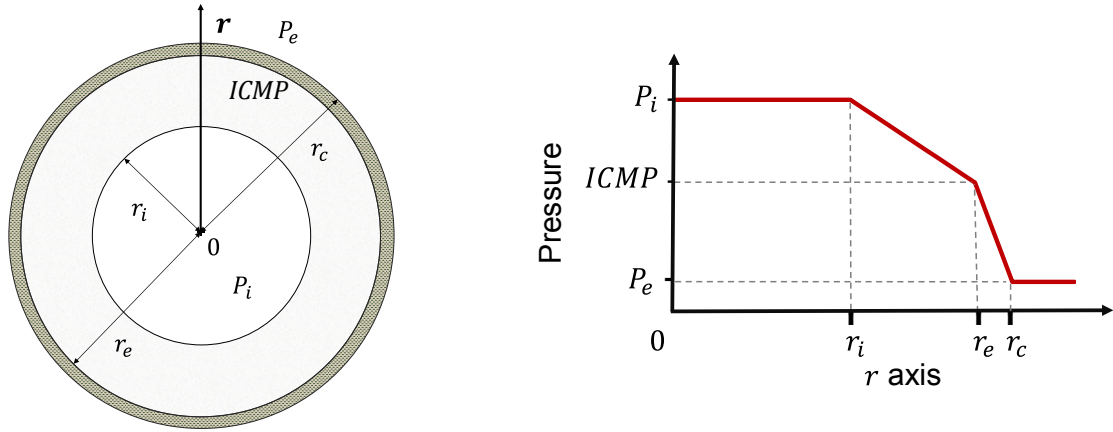


Figure 93: Fouled membrane and qualitative evolution of pressure as a function of the distance from the hollow-fiber center (ICMP: inter cake-membrane pressure (bar) and r_c : external cake radius (m))

As the cake thickness ($\sim 17 \mu\text{m}$) was negligible compared to the fiber radius, it was assumed that the external surface of the fouled membrane was equal to the external surface of membrane.

According to Darcy's law, the flow through a porous media is described by:

$$Q = S_{ext} * \frac{(P_i - P_e)}{\mu * (R'_m + R_c)}$$

$$Q_{memb} = S_{ext} * \frac{(P_i - ICMP)}{\mu * R'_m}$$

$$Q_{cake} = S_{ext} * \frac{(ICMP - P_e)}{\mu * R_c}$$

Therefore,

$$\frac{P_i - P_e}{R'_m + R_c} = \frac{P_i - ICMP}{R'_m} = \frac{ICMP - P_e}{R_c}$$

It could be deduced the following expression:

$$ICMP = \frac{R_c}{R'_m + R_c} * (P_i - P_e) + P_e$$

With $ICMP$ the inter cake-membrane pressure (bar)

In our case, $P_e = 0$ (relative pressure) and $P_i = BTMP$

$$ICMP = \frac{R_c}{R'_m + R_c} * BTMP \quad \text{Eq. 36}$$

The inter cake-membrane pressure depends only on the cake and membrane hydraulic resistance and the backwash pressure. In this study, the hydraulic cake resistance was found constant for each fiber (Table 25) for a given feed while the membrane resistance changes for each fiber.

The critical inter-cake membrane pressure $ICMP_{crit}$ can be calculated by:

$$ICMP_{crit} = \frac{R_c}{R'_m + R_c} * BTMP_{crit} \quad Eq. 37$$

By using Eq. 35 and Eq. 37, the critical backwash transmembrane pressure ($BTMP_{crit}$) and critical inter cake-membrane pressure ($ICMP_{crit}$) were calculated at the critical backwash flux. $BTMP_{crit}$ and $ICMP_{crit}$ for each membrane and feed solution are listed in Table 29.

Table 29: Critical backwash transmembrane pressure and inter cake-membrane pressure

Fiber	Bentonite (KCl)		Bentonite (CaCl ₂)	
	$BTMP_{crit}$ (bar)	$ICMP_{crit}$ (bar)	$BTMP_{crit}$ (bar)	$ICMP_{crit}$ (bar)
M-LP19	0.41		0.85	
M-HP32	0.30		0.70	
M-HP47	0.29	0.17	0.79	0.16
M-LP91	0.43		1.34	

While large variations of $BTMP_{crit}$ were observed between fibers and the treated feed, $ICMP_{crit}$ was independent of the membrane and converged to a common value for both bentonite suspensions (with KCl or CaCl₂) as seen in Table 29. Indeed, the mean inter cake-membrane pressure at $BTMP_{crit}$ was equal to 0.17 bar. This $ICMP_{crit}$ reflected the pressure, as a mechanical constraint, needed for the detachment and removal of bentonite cakes, which was independent of the nature of the added salt as observed on Figure 94.

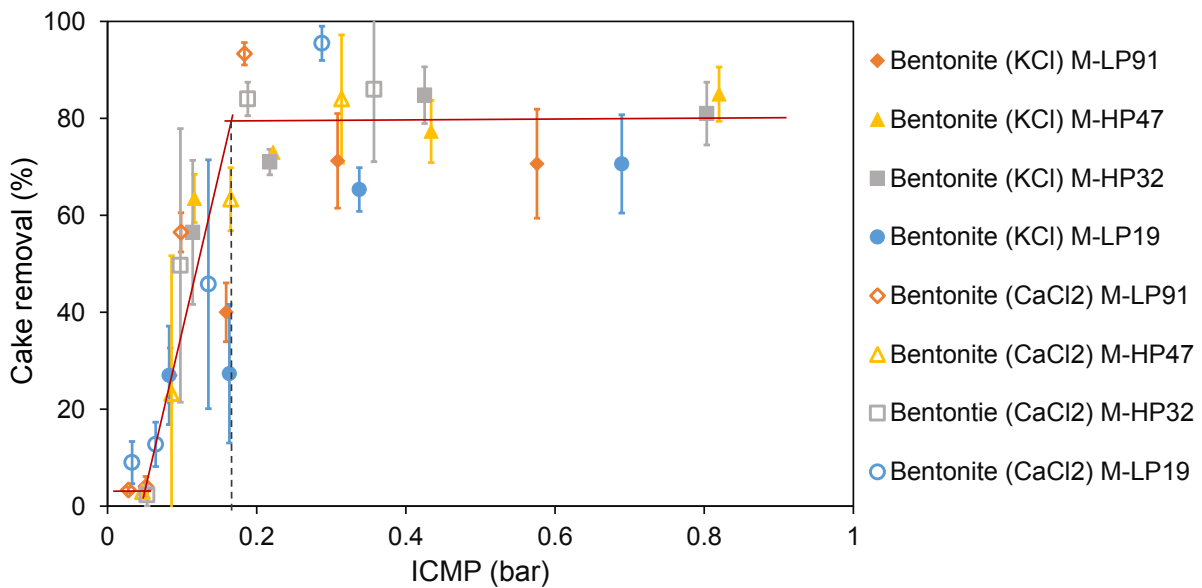


Figure 94: Critical pressure at the cake-membrane interface for detachment and removal of bentonite (CaCl₂ or KCl) cakes

The same value of $ICMP_{crit}$ for two different cake hydraulic resistances indicates that the fouling removal mechanism was closely related to the ICMP. Bentonite (KCl) or bentonite (CaCl₂) cakes had different hydraulic resistances and they might have different mechanical properties as observed by the fragmentation of the deposit (Figure 89). However, they might have the same adherence (or in the same order) to the membrane despite different hydrophilicity of membrane surface (see Table 13). Therefore, the same pressure (i.e. same constraint) at the interface membrane-cake was able to detach the bentonite cake from the membrane surface (Figure 94).

The same observation was made when the gain of permeability was plotted as a function of ICMP confirming the role of the inter cake-membrane pressure in the detachment of bentonite cakes. Values for M-LP19 deviated a little bit from the trend and the strong compression of the membrane might be responsible of the lower permeability gain values.

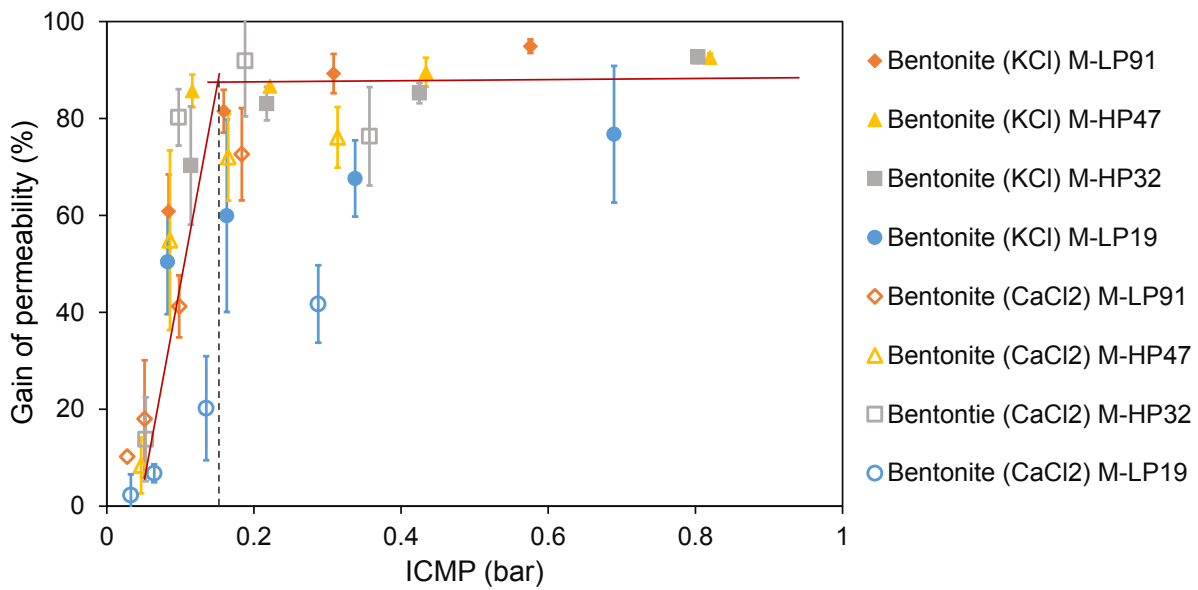


Figure 95: Critical pressure at the cake-membrane interface for detachment and gain of permeability (CaCl₂ or KCl) cakes

Therefore, according to Darcy's law, the critical backwash flux can be determined by Eq. 38 by measuring the hydraulic resistance of the cake in the case of bentonite cake. This equation was assumed valid for other bentonite cakes (with different hydraulic resistances or salt nature) if the adhesion of the cake to the membrane remained the same.

$$J_{bw,crit} = \frac{ICMP_{crit}}{R_c * \mu} \quad Eq. 38$$

Adherence and mechanical properties of the cake were playing an important role in the cake removal. Further investigation was needed to extend the concept of the ICMP to other fouling cake and have a better understanding of the fouling removal mechanism.

Previously, it was observed from Figure 76 in section 5.4.1 that the percentage of cake removal was influenced by the bentonite cake thickness. Indeed, bentonite cakes removed easier than thin bentonite cakes. As explained in this section the ICMP seemed to be responsible for the cake detachment and removal. During filtration, the cake resistance was increasing with the increase in cake thickness whereas membrane resistance remained constant. At constant backwash pressure, the ICMP was therefore higher for thicker cake than for thin bentonite cake as represented on Figure 96 by the full lines. Furthermore, higher cake removal was observed during backwash for higher cake thickness and therefore higher ICMP as shown on Figure 96. The pressure at the inter cake-membrane also tended to the backwash pressure (BTMP=0.4

bar) at high cake thickness based on Eq. 36. It was observed that cake removal was also tending to its maximal efficiency at high cake thickness. The difference in backwash efficiency for different thicknesses of bentonite (KCl) cake confirmed that force acting at the cake-membrane interface, the ICMP, was playing a major role in the fouling removal mechanism.

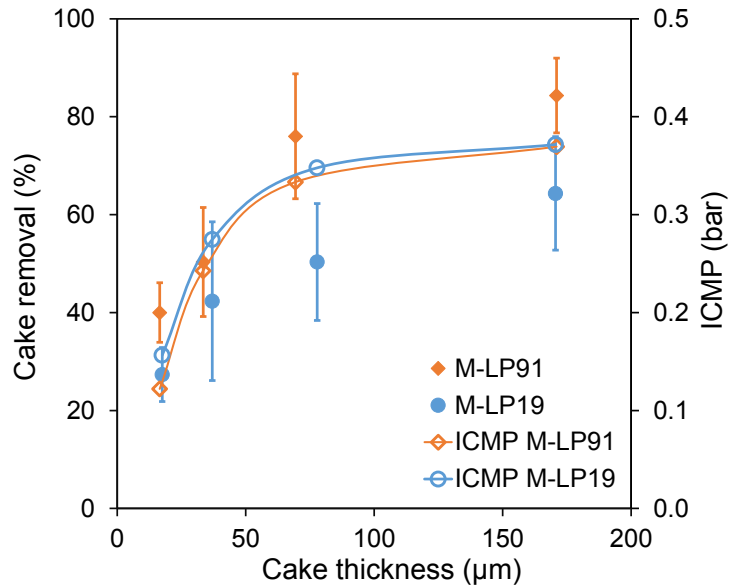


Figure 96: Influence of bentonite cake thickness on the cake removal and ICMP during backwash at constant pressure, BTMP=0.4 bar, on M-LP91 and M-LP19

5.5.3 Effect of membrane surface deformation on humic acid cake

Fouling removal mechanisms for humic acid cakes were different from the bentonite cakes due to different fouling mechanisms. Indeed, adsorption and pore blocking should also be considered in addition of cake deposition in the case of humic acid filtration. At low backwash pressure (less than 1.0 bar) the humic cake was not removed for all membranes suggesting a cake with a stronger adhesion to the membrane surface or/and a greater cohesion compared to bentonite cakes. Figure 97 shows that the cake removal was not led by the mass transfer properties as it was demonstrated for bentonite cakes since no critical backwash flux was observed. Actually, the hydraulic backwash was only able to clean M-LP19. Irreversible fouling was strongly assumed on the other membranes.

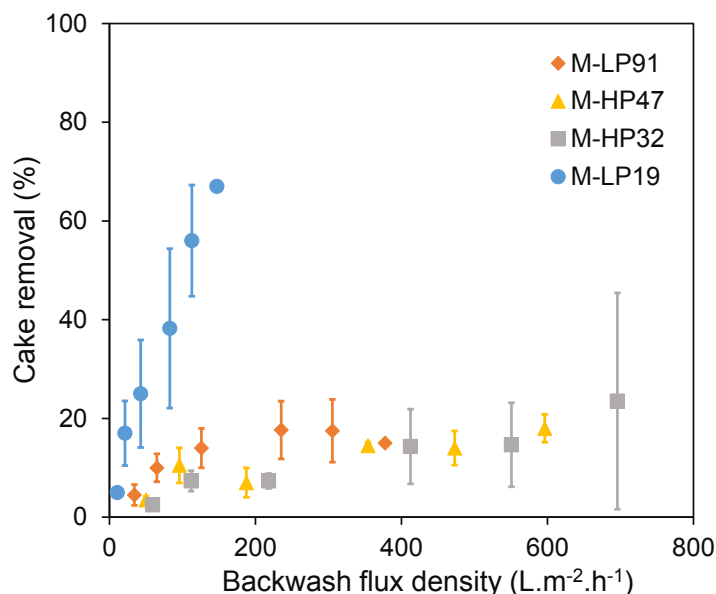


Figure 97: Evolution of cake removal as a function of the backwash flux after humic acid (CaCl_2) fouling.

Mechanical properties of the membrane and especially the elasticity was assumed to play a key role in fouling removal. Indeed, M-LP19 had the lowest Young's modulus (see Table 12) and demonstrated the best backwash efficiency (Figure 86). As explained previously in 1.4.3.3, the deformation of the membrane would create shear stress at the cake-membrane interface and would cause or help fouling removal. This was the strongest assumption to explain the fouling removal mechanism for humic acid filtration.

In addition of the water pressure exerted on the cake-membrane interface during the backwash (section 5.5.2), the membrane undergoes a reversible deformation (up to a certain limit) of its external surface. This deformation was observed and calculated for each hollow-fiber membrane in Chapter 4 (Figure 45). Figure 98 and Figure 99 show the effect of small and large membrane deformation on the humic acid (CaCl_2) cake removal. While the influence of small membrane deformations did not significantly increase the cake removal (Figure 98), a profound effect of larger membrane deformation on the cake removal was observed (Figure 99). In the area of small deformations, below 2% of external surface strain, the humic acid (CaCl_2) cake removal percentages were very low, below 30%. Even if a slight increase of the backwash efficiency could be noticed on Figure 98, the results were not particularly striking and could be related to the backwash flux. However, increasing the membrane deformation led to higher fouling removal for M-LP19, indeed more than 60% of the humic acid (CaCl_2) cake was removed at a membrane deformation of 15%. Due to its elastic properties, M-LP19 was the only hollow-fiber membrane that could deform above 5 % and up to 15%. Results on large

deformation effect were then exclusively based on M-LP19 but other membranes with similar mechanical properties were expected to demonstrate the same performances.

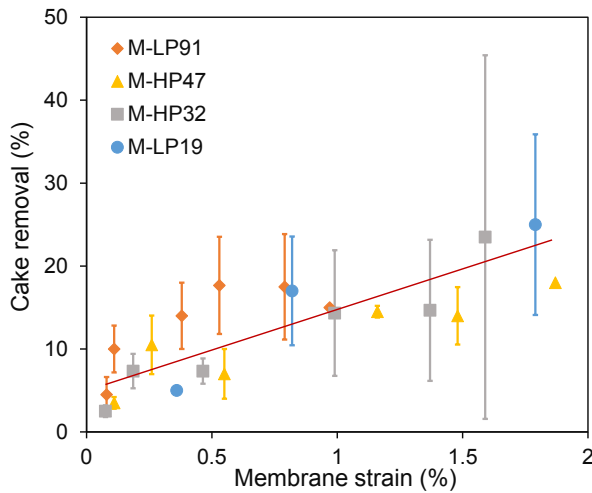


Figure 98: Effect of small membrane deformation on humic acid (CaCl_2) cake removal

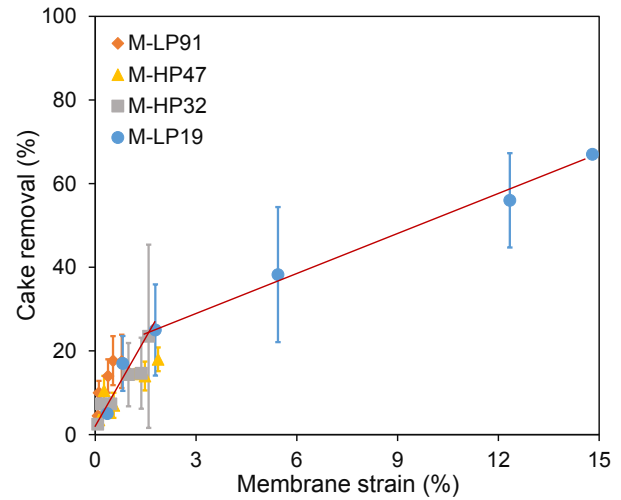


Figure 99: Effect of large membrane deformation on humic acid (CaCl_2) cake removal

This results could be compared to the ones obtained in the articles [146][145][143] published in the biology area (presented in 1.4.3.2) in which the biofilm removal was caused by the substrate deformation. In his paper Levering *et al.* [146] demonstrated that a critical strain and strain rate were required to effectively detach the biofilm. More than 80 % of the biofilm was detached at a strain of 25 % and a strain rate of 40 % per second (the substrate was consecutively strained 10 times). Lower operating conditions were however not sufficient to detach the biofilm. These results could be compared to humic acid fouling removal where a strain of 15 % was required to remove at least 60 % of the cake. These results demonstrated that hollow-fiber membrane deformation could help for the fouling removal when the cake was not hydraulically reversible from typical membranes. However, it seemed that the effect was significant only in the case of large membrane deformation (>15%).

5.5.4 Multiple and combined mechanisms

In this chapter, some fouling removal mechanisms were outlined via different model feed solutions of bentonite and humic acid. However, in the case of real fluid filtration (mainly composed of sludge, organic substances, micro-organisms and minerals), the fouling and fouling removal mechanisms are more complex and a combination of factors lead to fouling removal.

In industry a lot of techniques have been implemented to improve backwash efficiency such as the adjustment of backwash operating conditions [9] (i.e. pressure [107], time and frequency [4]) or the introduction of shear stress at the membrane surface while backwashing (i.e. cross-flow velocity [156], air bubble [117][201], vibration[87]).

Fouling removal was therefore caused by multiple forces and constraints and influenced by both membrane and feed properties as well as filtration and backwash operating conditions.

5.5.4.1 Shear stress

The shear stress is defined by the force vector parallel to the membrane surface. Shear stresses are mechanical forces near the membrane surface, which are usually generated by cross-flow velocity [156], air bubbles [117][201] or scouring agents [82] during membrane filtration. Various shear stress profiles can be generated depending on hydrodynamic conditions and system geometry [202]. In membrane filtration units, these shear stresses help prevent fouling and can greatly improve the membrane cleaning and backwash efficiency.

5.5.4.2 Interfacial normal and shear stresses

The interfacial normal and shear stresses were respectively defined by the force vector perpendicular or parallel to the membrane surface and located at the interface cake-membrane. These mechanical stresses acted on the cake and could trigger the cake detachment and removal.

During the backwash, the backwash flux was perpendicular to the membrane surface and the generated interfacial normal stress was closely related to the inter-cake membrane pressure defined in section 5.5.2. The interfacial normal stress could lead to the detachment of the cake if the force exceeds the adhesion force between the cake and the membrane. The cake removal was however possible only if the cake sufficiently deformed up to breaking point. Fragments were then evacuated away from the membrane if the shear and normal forces near the membrane were high enough. This normal interfacial stress generated during the backwash explains the cause of fouling removal of bentonite cakes and correlated with the pressure of detachment (Figure 94).

However, a different fouling removal mechanism was observed in the case of humic acid cake. The most likely cause of its removal was the deformation of the membrane. During the deformation of the membrane, interfacial shear stress could be generated if the cake and the membrane do not have the same mechanical properties (i.e. Young's modulus, strain and stress at break, elastic limit, strain rate). However, the fouling layers are soft and usually present high elastic properties. It is then assumed that the presence of rigid bonds or domains could hinder the homogenous deformation and induce some interfacial shear stress. Their formation could come from the foulant or membrane composition and structure. Indeed humic acid substances could be able to create rigid bonds with the membrane surface and within particles due to the presence of bivalent cations as explained in section 5.4.1. Furthermore, M-LP19 was made from copolymers and it might be assumed that micro-domains with different elasticity could form on the membrane surface during the membrane preparation.

5.5.4.3 Adherence of the deposit to the membrane surface

The formation of reversible (removed by backwash) or irreversible (removed using chemicals) deposit on the membrane surface is the result of different types of physico-chemical interactions between the particles and the membrane, and hydrodynamic forces (i.e. TMP, shear stress). The adhesion of foulants on the membrane surface is a preliminary step to the cake growth and membrane fouling. Adhesion between two solids is explained by the Derjaguin–Landau–Verwey–Overbeek (DLVO) theory, which combines the Van der Waals forces and electrostatic repulsions. However, hydrophilic interaction and ion bridging should also be considered since they contribute to particle adhesion and fouling propensity [203]. Fouling removal can be related in the same way to the energy of adhesion. Determining the required energy to detach the adhered fouling cake from the membrane surface will offer insight into fouling removal mechanisms.

The adhesion of a foulant particle to the membrane surface can be described with the extended DLVO theory (XDLVO) taking into account the Lifshitz-van der Waals (LW), Lewis acid-base (AB) and electrostatic double-layer (EL) free energies. The electrostatic energy is smaller than the two others and can be neglected, giving the following equation [204]:

$$\Delta G_{mwf}^{Tot} = \Delta G_{mwf}^{LW} + \Delta G_{mwf}^{AB}$$

With ΔG_{mwf}^{Tot} the total free energy of adhesion between the membrane and the foulant, ΔG_{mwf}^{LW} the LW free energy component, and ΔG_{mwf}^{AB} the AB free energy component, all in $\text{mJ}\cdot\text{m}^{-2}$.

If $\Delta G_{mwf}^{Tot} < 0$ then the interactions between the membrane and the foulant are attractive: the lower the energy, the stronger the adhesion. Whereas if $\Delta G_{mwf}^{Tot} > 0$ the interactions between the membrane and the foulant are repulsive: the higher the energy, the stronger the repulsion. However due to other interactions (e.g. ionic strength and ion bridging) the values of free energy were more qualitative than quantitative and were used to compare the adhesion between the membrane and humic acid/bentonite foulants.

The developed expression of the total free energy of adhesion between the membrane and the foulant is demonstrated in [205]:

$$\Delta G_{mwf}^{Tot} = 2 * \left[\left(\sqrt{\gamma_w^{LW}} - \sqrt{\gamma_m^{LW}} \right) * \left(\sqrt{\gamma_f^{LW}} - \sqrt{\gamma_w^{LW}} \right) + \sqrt{\gamma_w^+} * \left(\sqrt{\gamma_f^-} + \sqrt{\gamma_m^-} - \sqrt{\gamma_w^-} \right) \right. \\ \left. + \sqrt{\gamma_w^-} \left(\sqrt{\gamma_f^+} + \sqrt{\gamma_m^+} - \sqrt{\gamma_w^+} \right) - \sqrt{\gamma_f^+ * \gamma_m^-} - \sqrt{\gamma_f^- * \gamma_m^+} \right] \quad \text{Eq. 39}$$

With γ_i^{LW} the LW component of surface tension, γ_i^+ the Electron acceptor component of surface tension and γ_i^- the electron donor component of surface tension, all in $\text{mJ}\cdot\text{m}^{-2}$, and $i = m, w$ or f for membrane, water and foulant respectively.

The surface tension (γ_i^{tot}) and its polar (γ_i^+ and γ_i^-) and dispersive (γ_i^{LW}) components can be determined by measuring contact angle with at least three referenced liquids (for example: water, diiodomethane and glycerol). Values for water, two PVDF membranes, and foulants (bentonite, humic acid and humic acid (CaCl_2) with ionic strength at $I=1.5 \times 10^{-3}$ M) were found in the literature and reported in Table 30.

Table 30: Water contact angle (WCA), surface tension and components of the surface tension found in literature

Material	WCA	γ_i^{tot}	γ_i^{LW}	γ_i^+	γ_i^-	[Ref]
Water	/	72.8	21.8	25.5	25.5	[206]
PVDF M1	65	34.3	28.6	0.4	22.3	[43]
PVDF M2	18	61	34	4.1	44	[42]
Bentonite (Wyoming)	43	53.9	40.7	1.5	29.2	[206]

Humic acid	42	37.4	30.8	3.6	12.7	[207]
Humic acid + Ca ²⁺	39	38	38	50.8	0	[110]

Two types of membrane were chosen to compare the literature values with the membranes studied in this research: PVDF M1 with a WCA of 65° and a much more hydrophilic membrane, PVDF M2 with a WCA of 18°. The measurements of water contact angle for M-LP19, M-LP91, M-LP32 and M-LP47 varied from 37 to 54° (see on Table 13). Free energy of adhesion was calculated between the PVDF membranes and the foulants (bentonite, humic acid and humic acid (CaCl₂) with ionic strength at I=1.5x10⁻³ M). The calculated values are presented in Table 31.

Table 31: Calculated free energy of adhesion between the membrane and foulant

Foulant	Bentonite	Humic acid	Humic acid + Ca ²⁺
Membrane	Membrane-foulant ΔG_{mwf}^{Tot} (mJ.m ⁻²)		
PVDF M1	-1.7	-16.4	-45.3
PVDF M2	10.3	-1.0	-40.6

Negative energy of adhesion was found between the foulants and PVDF M1 meaning that attraction was predominant and adhesion occurred. However, for the most hydrophilic membrane (PVDF M2) the adhesion energy was positive with bentonite and negative for humic acid indicating a lower adhesion or even no adhesion for bentonite particles. It verifies that increasing the hydrophilicity of membrane reduces the adhesion force and improves the antifouling ability [204].

For both membranes, the energy of adhesion for PVDF/humic acid was lower than the energy of adhesion for PVDF/bentonite and therefore stronger adhesion between PVDF/humic acid than PVDF/bentonite was predicted by XDLVO theory. Furthermore, the addition of Ca²⁺ to the humic acid solution drastically decreased the free energy indicating a more severe adhesion than for humic acid alone. This strong adhesion was observed during the experiments of humic acid (CaCl₂) cake removal (Figure 86).

The required energy to detach the deposit was the opposite of adhesion energy according to the laws of thermodynamics. In theory, it was assumed that an energy per surface area of at least 2 mJ.m^{-2} was required to detach bentonite cake and 46 mJ.m^{-2} for humic acid (CaCl_2) cake. The calculated energies were very low and probably underestimated since they do not include the electrostatic interactions and the bridge effect caused by calcium cations between the membrane and the foulant.

These adhesion energies could be compared to the backwash energy released during backwash and that really acts on the cake, defined by Eq. 40:

$$E_{bw} = J_{bw} * S_{ext} * ICMP * t_{bw} \quad \text{Eq. 40}$$

With E_{bw} , the backwash energy released during backwash (J).

According to the previous section 5.5.2, a minimum backwash flux and a critical inter cake-membrane pressure were required to eliminate most of the bentonite deposit and reach maximal backwash efficiency. Writing Eq. 40 in these conditions gives the critical energy required for maximal backwash efficiency per surface area:

$$\frac{E_{bw,crit}}{S_{ext}} = J_{bw,crit} * ICMP_{crit} * t_{bw}$$

With $E_{bw,crit}$, the critical backwash energy required for cake removal (J).

In the case of bentonite (KCl), the critical backwash energy per surface area was 20 J.m^{-2} whereas for bentonite (CaCl_2), it reached 90 J.m^{-2} . These energy requirements were much higher than the calculated adhesion energies by the XDLVO method suggesting that the adhesion mechanism might not be predominant in cake removal mechanisms. However, the energy was calculated for the total duration of the backwash (1 minute) but detachment of the cake might occur at the very beginning of the backwash process. Indeed, the critical backwash energy calculated for 0.1 s was 40 mJ.m^{-2} for bentonite (KCL) and 150 mJ.m^{-2} for bentonite (CaCl_2).

5.5.4.4 Mechanical properties of the cake

5.5.4.4.1 Cake strain under camera

The mechanical properties of the cake were estimated by plotting the stress-strain curves for each filter cake based on the method described in 2.7.1. The stress-strain curve was constructed

by plotting the calculated ICMP (Eq. 36) as a function of the measured cake elongation as shown on Figure 100. Young's modulus was calculated from these curves for each cake (on bentonite (KCl), bentonite (CaCl₂) and humic acid (CaCl₂) cakes) and reported on Table 32. Further tests should be carried out to confirm the results. Moreover, this method is limited by the approximation of the applied stress on the cake. Indeed, as explained previously (4.4.3), there is a gradient of pressure in a porous media and therefore pressure or stress is varying in the cake layer and is not equal to ICMP.

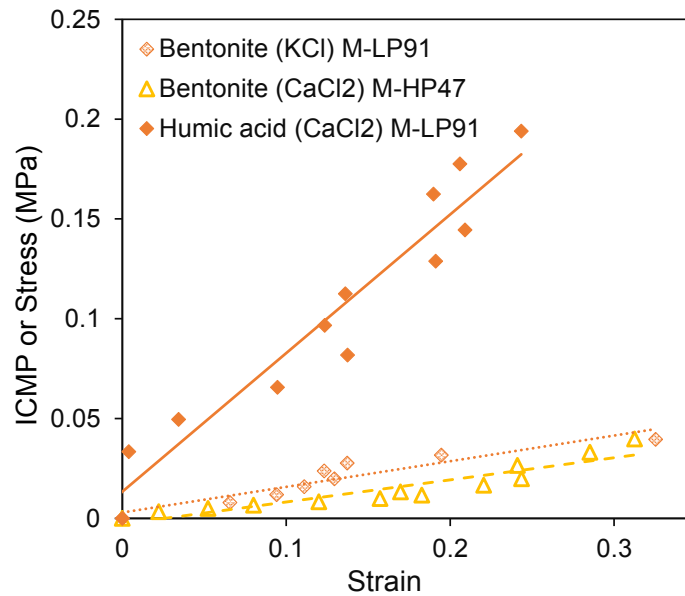


Figure 100: Stress-strain curves for bentonite (KCl), bentonite (CaCl₂) and humic acid (CaCl₂) cake

Linear deformation of the cake with the applied pressure was observed for the three types of cakes and estimated Young's modulus could be calculated in Table 32.

Table 32: Estimation of Young's modulus for bentonite (KCl), bentonite (CaCl₂) and humic acid (CaCl₂) cake based on strain measurement with pressure under camera

Cake	(Camera) Young's modulus (MPa)
Bentonite (KCl)	0.1
Bentonite (CaCl ₂)	0.1
Humic acid (CaCl ₂)	0.7

According to the measurements, the type of salt did not significantly influence the Young's modulus of bentonite cake. However, according to the visual observation of the cake removal during backwash (on Figure 89), the cohesion of the cake was much higher for bentonite (CaCl₂)

(large fragments) than bentonite (KCl) (small fragments). Furthermore, the type of particles had a great effect on the mechanical properties. Humic acid showed much higher Young's modulus than the bentonite cakes. Therefore, the humic acid cake was assumed more rigid and more difficult to break and remove.

However, the cake Young's modulus remained very low compared to the membrane Young's modulus suggesting higher elasticity of the cake. This confirmed the results presented in section 5.5.4.2 and strengthened the assumption of the presence of binding sites between the cake and the membrane.

5.5.4.4.2 Atomic force microscopy measurements

Mechanical properties of filter cakes of bentonite (KCl), bentonite (CaCl₂) and humic acid (CaCl₂) were determined by AFM measurements. The different suspensions of bentonite and humic acid were filtered on a PVDF flat-sheet membrane at constant pressure (TMP=0.8 bar) to form a 40 μm thick cake. Each sample surface was analyzed by AFM using mapping of force curves (between 200 and 3000 measurements) to determine the mechanical properties of the filter cake. The force-tip motion curve for each cake is shown on Figure 101.

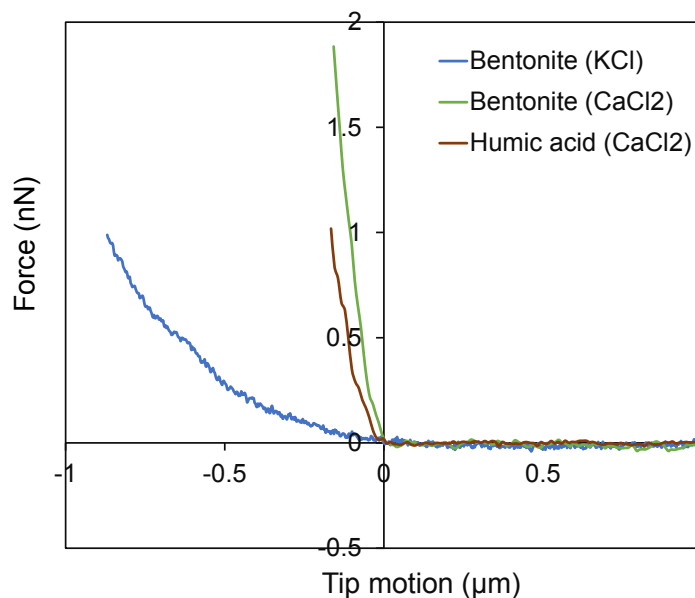


Figure 101: Applied force as a function of the tip motion (indentation) for bentonite (KCl), bentonite (CaCl₂) and humic acid (CaCl₂) cake.

The Young's modulus distribution, calculated using Eq. 14 and the force curve mapping, is shown on Figure 102. Mean Young's modulus was calculated for bentonite (KCl), bentonite (CaCl₂) and humic acid (CaCl₂) cake and reported in Table 33.

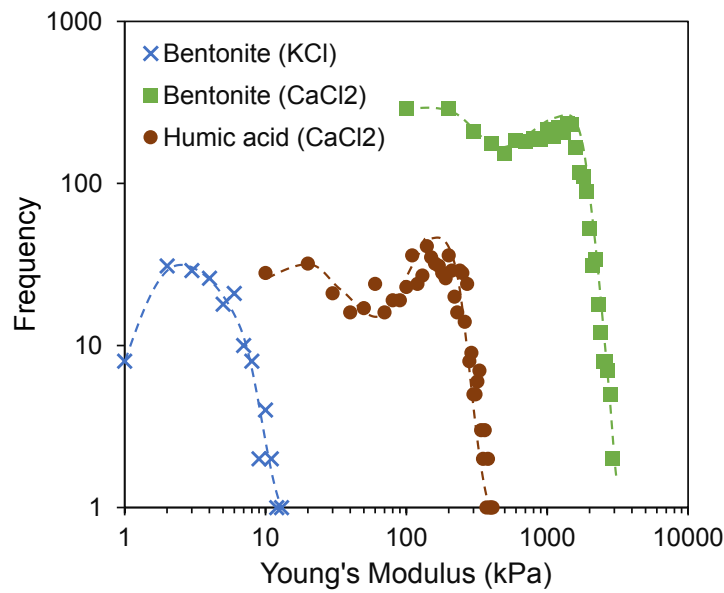


Figure 102: Young's modulus distribution for bentonite (KCl), bentonite (CaCl₂) and humic acid (CaCl₂) cake determined by AFM using mapping of force curves

Table 33: Mean Young's modulus for bentonite (KCl), bentonite (CaCl₂) and humic acid (CaCl₂) cake based on AFM measurements

Cake	(AFM) Young's modulus (MPa)
Bentonite (KCl)	0.004
Bentonite (CaCl₂)	0.9
Humic acid (CaCl₂)	0.2

The order of magnitude of Young's modulus could be compared between the different cakes even if the error of the measurement was relatively high (standard deviation as high as the mean Young's modulus). These errors might be due to the material fragility (breakage during indentation) or due to a non-homogenous deposit. Bentonite (KCl) was much softer than bentonite (CaCl₂) with a mean Young's modulus 200 times lower. These results were in accordance with the visual observations (as seen in Figure 89) since stronger cohesion of bentonite (CaCl₂) cake was observed compared to bentonite (KCl). A mean Young's modulus of 200 kPa was found for humic acid (CaCl₂) cake.

AFM measurement gave interesting cake properties and might provide better accuracy than the strain measurements with pressure under camera (see 5.5.4.4.1).

5.5.5 Calculation of critical strain

Several authors [143] [146] have demonstrated that stretching a biofilm-covered substrate could lead to the biofilm detachment (described in 1.4.3.2) when exceeding a critical strain. Shivapooja *et al.* [143] proposed a mechanism involved in the detachment of the biofilm. Indeed, the biofilm is simultaneously deforming along with the silicon substrate strain since the biofilm has a lower Young's Modulus and higher elasticity than the substrate. During deformation, the biofilm is storing elastic energy per surface unit, which is expressed by:

$$e_{elastic} = \frac{1}{2} h_f \frac{E_f}{1 - \nu_f^2} \varepsilon^2$$

With $e_{elastic}$ the stored elastic potential energy per surface unit ($J.m^{-2}$)

The stored elastic energy is released when it exceeds the adhesion energy of the biofilm to the substrate leading to the detachment of the biofilm. Therefore, a critical strain could be calculated for the biofilm detachment.

In this thesis work, humic acid cake had also a lower Young's Modulus than the membrane and was strongly adhered to the membrane surface. The critical strain could be estimated based on the mechanism for the biofilm detachment using humic acid cake properties and adhesion energy. The adhesion between humic acid ($CaCl_2$) and PVDF was calculated from literature data (Table 31), fouling layer thickness was measured under camera (5.3.4) and Young's modulus of the humic acid ($CaCl_2$) cake was measured by AFM (Table 33). Therefore, the critical strain could be estimated using Eq. 1:

$$\varepsilon_c = \left(\frac{2\Delta G_{mwf}^{Tot} (1 - \nu_f^2)}{h_f E_f} \right)^{\frac{1}{2}} \quad Eq. 1$$

A critical strain of 18% was obtained using Eq. 1 and a Poisson's ratio of the fouling layer of 0.5 (typical value used in numerical model with assumption of elastic isotropy and incompressibility [145]). It was noticed that the calculated critical strain remarkably supported the experimental results on humic acid cake removal. Indeed, an efficient detachment of humic acid ($CaCl_2$) cake from PVDF membrane (M-LP19) was measured when the membrane experienced a deformation higher than 15%. As adhesion energy between bentonite and PVDF membrane is extremely low (see on Table 31), calculated critical strain is close to 0 and other driving parameters that the deformation might lead to the removal (as demonstrated in 5.5.1). However, these calculations have to be interpreted with care as errors on theoretical data or

measurements could modify the critical strain value. Indeed a variation of 50% of one of the calculating parameters (ΔG_{mwf}^{Tot} or h_f or E_f) results in a 30% change of the critical strain value.

5.5.6 Analysis of membrane permeability on the long term in the case of humic acid filtration

5.5.6.1 Filtration-backwash cycles of humic acid suspension

Several filtration-backwash cycles were carried out on M-LP91, M-HP32 and M-LP19 to determine if M-LP19 was a relevant candidate for ultrafiltration on the long term. The normalized permeability was plotted as a function of the number of cycles on Figure 103. The membrane permeability after backwash kept decreasing with increasing the number of cycles for all fibers. This decrease on the long term came from irreversible fouling caused by humic substances.

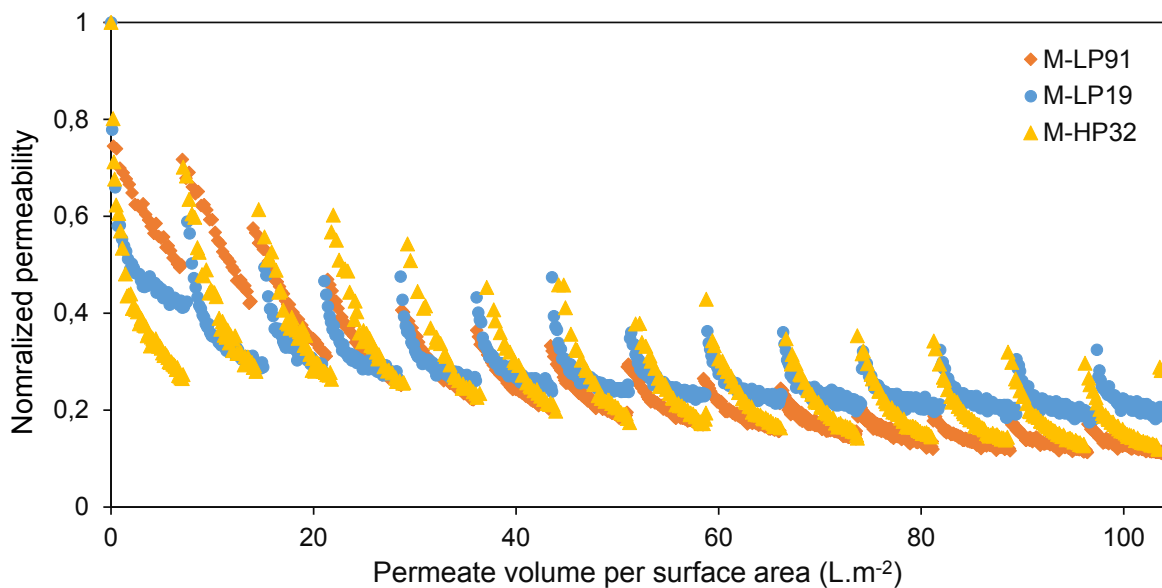


Figure 103: Normalized permeability for M-LP91, M-HP32 and M-LP19 during several cycles of humic acid (CaCl₂) filtration at constant TMP=0.5 bar and backwash at constant BTMP= 2.0 bar

Backwash efficiency was assessed here from permeability measurements on several cycles as shown on Figure 104.

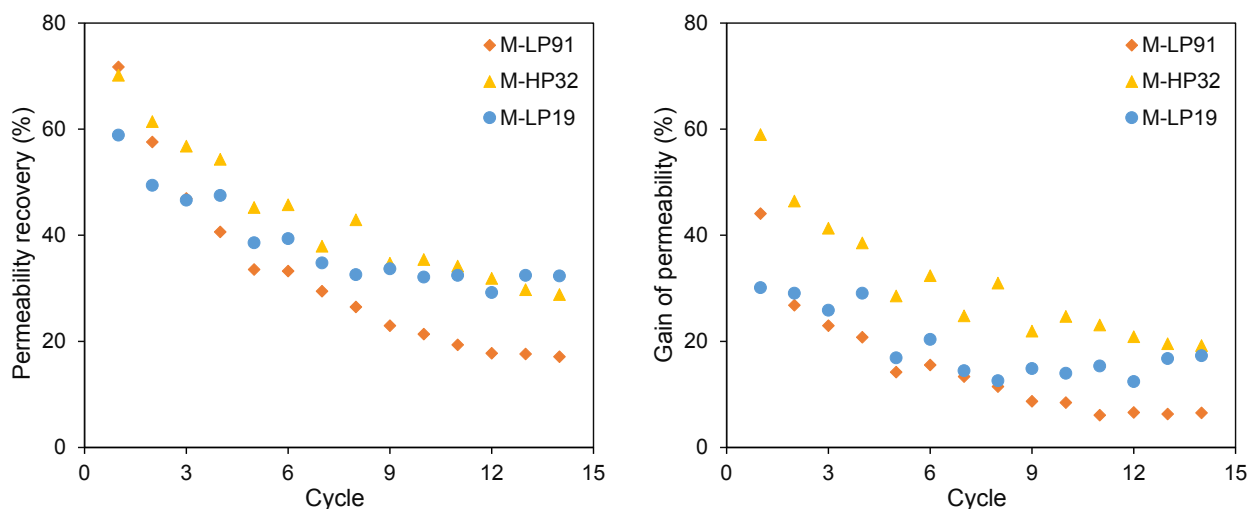


Figure 104: Permeability recovery (left) and gain of permeability (right) for M-LP91, M-HP32 and M-LP19 as function of the number of cycle of humic acid (CaCl₂) filtration at constant TMP=0.5 bar and backwash at constant BTMP= 2.0 bar

A strong decrease of the permeability recovery and gain of permeability was observed during the first cycles of filtration for all fibers (Figure 104), this decrease was mainly attributed to irreversible fouling such as adsorption and pore blockage [196]. The permeability recovery seemed then to stabilize after a few cycles, from the 6th cycle the decrease of membrane permeability during filtration might be caused by cake deposition. However, the permeability recovery was still slightly decreasing for M-HP32 and M-LP91 even at the 14th cycle whereas for M-LP19 it remained stable after 6 cycles. The presence of remaining fouling on M-HP32 and M-LP91 after backwash might be responsible of this decrease of permeability recovery. The great backwash performances of M-LP19 in the case of humic acid cakes (Figure 86) were responsible of the stable permeability recovery observed from the 8th cycle. Visual observation also confirmed that a fouling layer remained on the membranes M-HP32 and M-LP91 at the end of the 14th backwash whereas M-LP19 looked much cleaner (see on Figure 105).

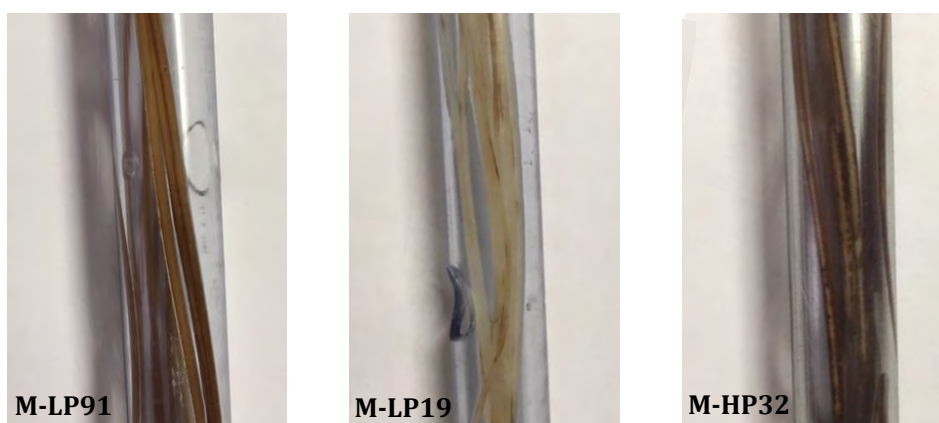


Figure 105: Pictures of M-LP91, M-LP19 and M-HP32 membranes after 14th filtration-backwash cycle of humic acid suspension

Even if M-LP19 showed lower permeability recovery than M-LP91 on the first cycles (from 1st to 5th cycle), the reverse was observed on the long-term. Indeed, from the 5th cycle the permeability recovery for M-LP19 was better than M-LP91. These results proved that M-LP19 showed better performances of filtration-backwash on the long term.

However, these results should be interpreted with care since permeability measurement were normalized and differences were not very significant. Due to the much lower initial permeability of M-LP19, M-LP91 and M-HP32 still had higher permeate flux after 14 cycles of filtration as observed on Figure 106.

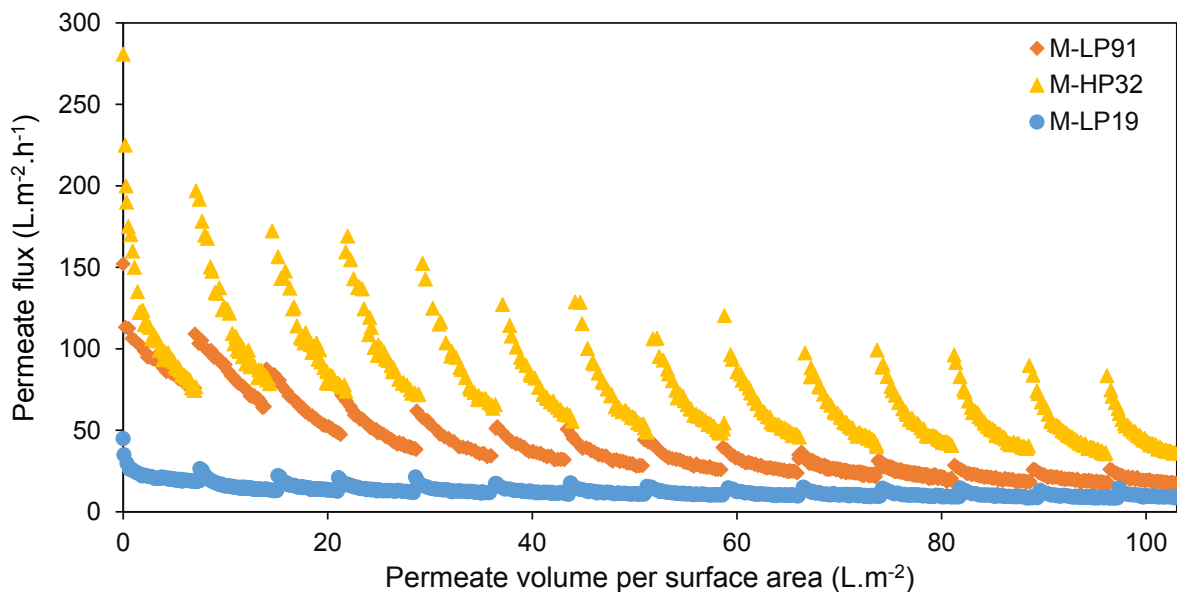


Figure 106: Permeate flux for M-LP91, M-HP32 and M-LP19 during several cycles of humic acid (CaCl_2) filtration at constant $\text{TMP}=0.5$ bar and backwash at constant $\text{BTMP}=2.0$ bar

A study on more cycles might show higher flux for M-LP19 but this needs further investigation. Also if the initial membrane permeability of M-LP19 would have been as high as M-HP32, higher permeate flux might be obtained for M-LP19 after a few cycles.

5.5.6.2 Filtration-backwash cycles of real wastewaters

It was important to test the different membranes on real fluids to compare the laboratory and industrial environment. The same experiment on the long term was therefore reproduced with real wastewaters. Comparable results with humic acid filtration-backwash (Figure 103) were obtained for the wastewater treatment even if the differences were less significant. From Figure 107 and Figure 108, it can be noticed that M-LP19 showed better filtration-backwash

performances than M-LP91 from the 9th cycle. However, M-HP32 showed better performances than M-LP19 with higher permeability recovery on each cycle (Figure 108). Differences were less significant on Figure 109 and experiments should be carried out on longer term to allow better comparison. The permeability recovery of M-LP19 was more stable during cycles than M-HP32 and M-LP91 as seen on Figure 108 and it was expected higher permeability recovery for M-LP19 on longer term. Therefore, fouling removal seemed also improved by the membrane deformation in the case of wastewater filtrations.

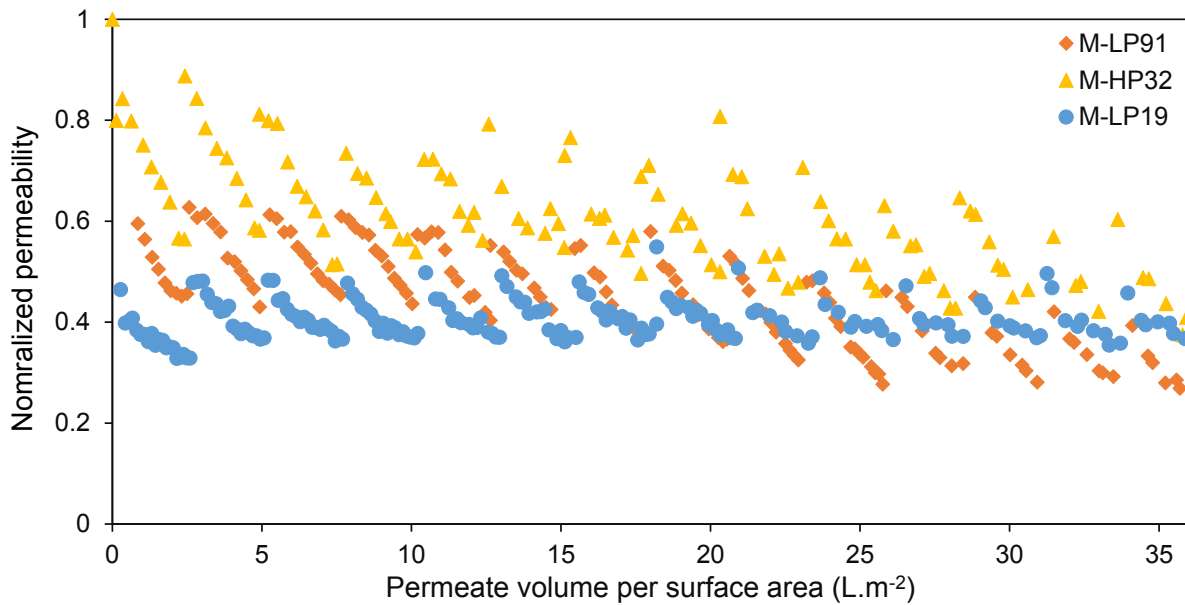


Figure 107: Normalized permeability for M-LP91, M-HP32 and M-LP19 during several cycles of real wastewaters filtration at constant $TMP=0.5$ bar and backwash at constant $BTMP= 2.0$ bar

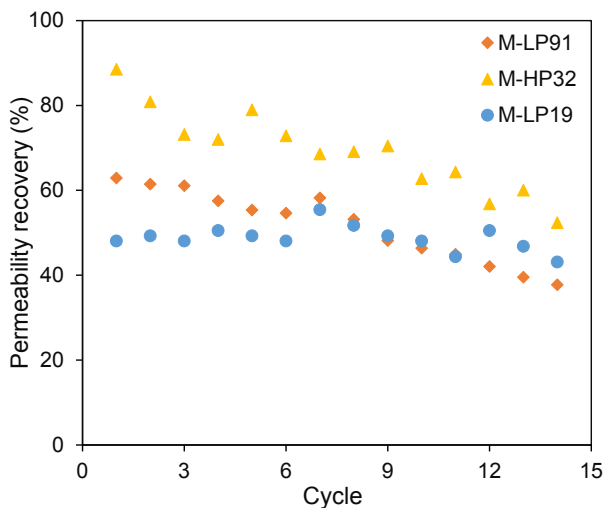


Figure 108: Permeability recovery for M-LP91, M-HP32 and M-LP19 as function of the number of cycle of real wastewater filtration at constant $TMP=0.5$ bar and backwash at constant $BTMP= 2.0$ bar

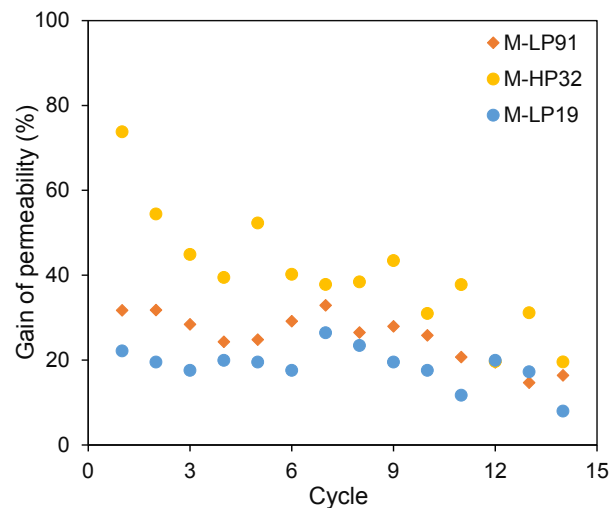


Figure 109: Gain of permeability for M-LP91, M-HP32 and M-LP19 as function of the number of cycle of real wastewater filtration at constant $TMP=0.5$ bar and backwash at constant $BTMP= 2.0$ bar

5.5.7 Economic benefits

As defined previously, the critical backwash flux was the minimal backwash flux necessary to reach high backwash efficiency for a specific filtration unit. Using a backwash flux much higher than the critical backwash flux leads to a higher use of permeate water and a higher energy consumption with a low gain on the cake removal. The knowledge of the critical backwash flux is then a key parameter to optimize economically the backwash step.

As it is seen in Figure 110, the backwash efficiency reaches a high stationary value when plotted as a function of the energy ($\frac{e_{bw}}{S_{ext}}$) and permeate volume ($\frac{V_{bw}}{S_{ext}}$) per surface area consumed during a backwash. For example, in the case of bentonite (CaCl₂) cake and for a single backwash of 60 seconds duration, the requirements of energy and water for optimal cake removal were 1000 J.m⁻² and 6 L.m⁻² respectively. This energy consumption during backwash was significant since it represents 20% of the energy consumption of the filtration step of bentonite suspension (details about consumed energy and permeate calculations are given in Appendix 1). A backwash flux that is twice as high would result in an extra 20 % of energy contribution to the energy consumed for the filtration. Energy consumption and net water production are therefore optimized if the membrane is cleaned at the critical backwash flux.

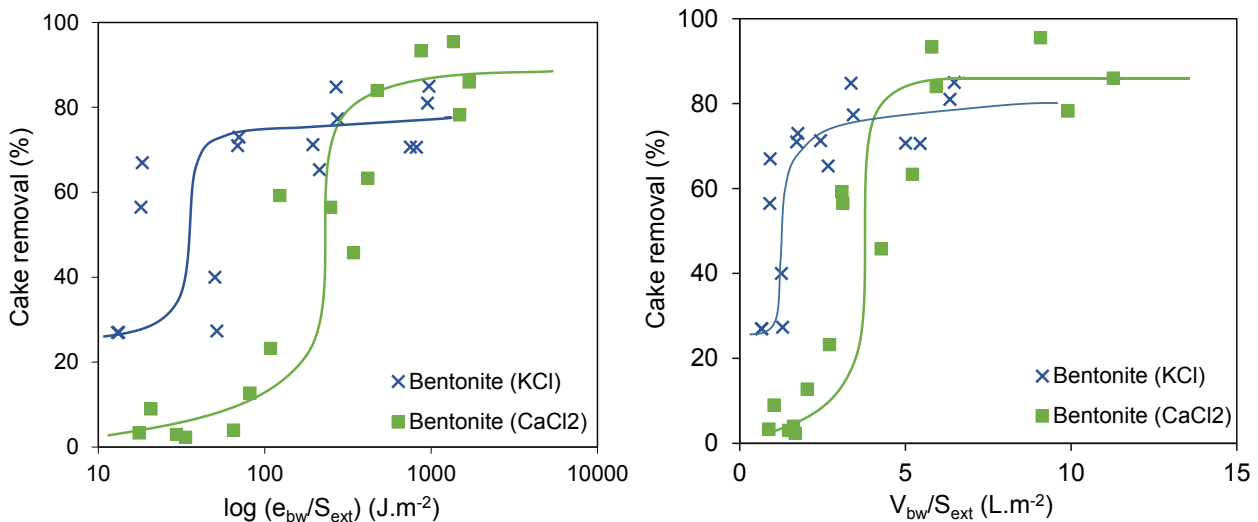


Figure 110: Backwash efficiency per consumed energy and permeate.

5.6 General conclusion

Fouling mechanisms and fouling removal mechanisms were extensively studied in this chapter on different model feed suspensions (bentonite and humic acid). The ionic strength of the

suspensions was chosen below the C.C.C for higher control of ultrafiltration and cake deposition.

For bentonite filtrations, fouling was exclusively governed by the cake deposition and was not influenced by the membrane properties. However, bentonite cake properties were dependent on the added salt and Ca^{2+} ions strongly decreased its hydraulic resistance compared to KCl. For humic acid filtrations, fouling was the result of different mechanisms such as cake deposition, pore blockage and adsorption. Thus, different fouling resistance were measured for the membranes, however identical humic acid cake height was measured between the membranes.

During backwash, different cake removal mechanisms were identified for bentonite and humic acid filtrations. The bentonite cake removal was triggered by the constraint applied at the cake-membrane interface induced by the backwash flux. We defined a critical backwash flux from which backwash reaches its highest efficiency and removes most of the deposit. This critical backwash flux was related to the cake hydraulic resistance and was independent of the membrane properties in the case of bentonite deposits. The pressure at the interface cake-membrane while backwashing was calculated for the two types of feed and interesting results suggest that a critical pressure is required to lift and eliminate the bentonite cake. Bentonite cake removal was thus controlled by the backwash operating conditions and hydrodynamic forces. Furthermore, the critical pressure of detachment was not related to the bentonite cake properties and might be closer related to the adherence to the membrane. This also suggests that the new studies on backwash efficiency and performances of low fouling membranes should be conducted at the same ICMP in order to correctly evaluate and compare the efficiency between membranes as the hydraulic vector (here the backwash flux) is related to the membrane permeability.

However, hydrodynamic forces were not sufficient to detach and remove humic acid cakes. XDLVO theory predicted stronger adhesion of humic acid cake to the membrane and the addition of Ca^{2+} cation would reinforce this adhesion and the cake cohesion due to its bridging effect. Interesting results demonstrated that humic acid cake removal was better related to the membrane properties than to hydrodynamics. Indeed, more than 60 % of the cake was removed in specific conditions where the membrane underwent a deformation exceeding 15%. It seems that the deformation of the external surface of the hollow-fiber membrane was responsible for the cake detachment. Only M-LP19 was able to deform of this magnitude, due to its great elastic

properties, and showed the greatest backwash efficiency for humic acid filtration. A critical strain of 18% at which the fouling layer should be efficiently removed was calculated from theoretical and analytical data and was fully consistent with the measured backwash efficiency. On several filtration-backwash cycles, M-LP19 showed higher normalized permeability recovery for humic acid filtration than M-LP91 and M-HP32 but initial water permeability of M-LP19 should be improved to compete with high permeable membranes. Regarding the treatment of real wastewaters, both the backwash hydrodynamics and the ability of the fiber to deform were assumed to improve the backwash efficiency. Differences were however not very significant in the case of a dozens of filtration-backwash cycles and experiments should be carried out on longer time to verify conclusions. Highly permeable membrane with large reversible deformation under pressure would be therefore a competitive candidate for ultrafiltration of industrial or domestic wastewaters.

General conclusions and perspectives

This dissertation was focused on membrane fouling in water filtration and particularly on fouling removal during backwash. The objective was to determine the key factors causing cake removal to better understand the mechanisms involved in fouling removal during the backwash. Determining the role of hollow-fiber membrane properties was essential to explain the detachment and elimination of the filter cake.

Several hollow-fiber membranes were firstly prepared by dry-wet spinning using different PVDF grades, additives and spinning operating conditions. A few membranes were selected for this research based on their shape, permeability and first and foremost for their mechanical properties. These membranes had indeed different tensile elasticities with a Young's modulus comprised between 19 and 91 MPa. Membranes with low Young's modulus were much more sensitive to pressure operations than membranes with high Young's modulus. Indeed, the permeability of the membrane with a Young's modulus of 19 MPa was decreasing from 300 to 50 L.m⁻².h⁻¹.bar⁻¹ when applied pressure increased from 0.2 to 2.4 bar in outside-in mode. On the contrary, it was increasing from 500 to 800 L.m⁻².h⁻¹.bar⁻¹ when applied pressure increased from 0.2 to 2.4 bar in inside-out mode. These strong variations were likely caused by the deformation of the membrane surface and the compaction or expansion of the membrane pores even at low pressure.

The deformation of the membrane during filtration and backwash operations have therefore been further investigated by in-situ direct observation technique and by modelling. A camera equipped with optical lens was mounted on a filtration pilot to observe the hollow-fiber membrane deformation when subjected to external or internal pressure. This high resolution technique could measure the membrane deformation with an accuracy of 0.7 μm. The membrane with the lowest Young's modulus of 19 MPa showed remarkable compression during filtration (outside-in) and expansion during backwash (inside-out) with membrane strain reaching 15% under a backwash pressure of 2.4 bar. The deformation was however partially irreversible when the strain exceeded 5%. Other membranes experienced small deformations, below 2 % in the same range of pressure. A numerical model based on the mechanical deformation of a pressurized thick-walled cylinder could fit the in-situ measurements of the external membrane surface strain if adjusting the simulated results with a single factor. Indeed, numerical results underestimated the real deformations of the membranes. This model was assumed valid for non-porous material, it is therefore thought that

a pressure gradient within the porous membrane might promote the wall deformation and consecutively the external surface deformation.

A complete examination of membrane properties and deformation behavior during filtration and backwash with ultrapure water was a preliminary step to the ultrafiltration of particle suspensions. In order to study the basic mechanisms involved during fouling and fouling removal, model suspensions prepared from bentonite or humic acid particles with addition of potassium or calcium chloride were filtered at constant pressure in outside-in mode. In the case of bentonite filtration, fouling was governed by cake deposition with a linear growth on the membrane surface. The cake hydraulic resistances were not affected by the membrane properties but were strongly modified by the nature of the added salt. In the case of humic acid filtration, fouling behavior is more complex and depended on the membrane properties as pore blocking and adsorption mechanisms were added to cake deposition. However, direct observation of cake growth supported the linear growth of a humic cake, which was identical on each membrane. Fouling removal was studied on each fouled membrane during backwash at constant pressure. In the interests of comparability, backwash efficiency was assessed by permeability recovery, mass balance and local scale observations. Two fouling removal behaviors were drawn from these experiments:

- *Bentonite deposits*: Cake removal was caused by the pressure applied at the cake-membrane interface induced by the backwash flux. Backwash flux is perpendicular to the membrane surface generating interfacial normal stress leading to the detachment, rupture and elimination of the deposit.
- *Humic acid deposits*: Cake removal was caused by the membrane surface strain. At the cake-membrane interface, normal stress induced by the backwash flux and shear stress generated by the strain lead to the cake detachment, rupture and elimination.

The difference in removal mechanisms between bentonite and humic acid cake might be related to the adherence of the cake to the membrane surface. As bentonite cakes have relatively low adherence to the membrane surface, the forces generated by the hydraulic vector during backwash are sufficiently high to cause the cake removal. However, humic acid cake was extremely difficult to remove even at high backwash fluxes and therefore considered as irreversible fouling. Moreover, the presence of calcium cations induced a bridging effect between particles and the membrane strengthening the adhesion of the cake to the membrane surface. In this case, high strain might provide sufficient elastic energy in the cake layer to

exceed the adhesion energy leading to its removal. Therefore, humic acid cake removal was better promoted by membrane elasticity than hydrodynamic contrary to bentonite cakes. Amount of humic acid cake removed at high backwash flux reached 60 % when the membrane experienced a deformation of 15% whereas less than 20 % of the cake was removed for deformation lower than 2 %. A critical strain at which the fouling layer should be efficiently removed was calculated from adhesion energy and cake properties. The calculated critical strain of 18% was fully consistent with the measured backwash efficiency.

As a conclusion, critical backwash flux and critical strain, at which backwash reached its maximum efficiency, have been highlighted in this research for the removal of bentonite and humic acid cake respectively. Research findings on these critical parameters provide interesting insights on how to optimize materials in combination with backwash conditions to achieve a more energy-efficient filtration process.

Finally, filtration tests have been carried out on domestic wastewaters from water treatment plant and backwash efficiency was evaluated by permeability recovery on a dozens of filtration/backwash cycles for the different membranes. First results indicated that both hydrodynamic and membrane deformation might help for fouling removal but results should be investigated on longer-term filtration operation to confirm this assumption.

Following this work, multiple research perspectives can be proposed:

- Conducting a study on biofouling removal after filtrating micro-organisms (e.g. algae, bacteria) or growing a biofilm on the membrane surface. Evaluating the driving factors leading to biofilm release. Is the membrane strain during backwash causing the detachment of biofilm in the range of industrial backwash pressures?
- Finding novel membranes with high permeability and the ability to deform under pressure. The membrane deformation has to be high, reversible and should not interfere with membrane selectivity. Elastomeric or cross-linked elastic membranes might be potential candidates. Membranes with various tensile elasticities but the same structure (to keep the same permeability and selectivity) could be prepared by different degree of cross-linking. Cross-linking is processed by adding a crosslinking agent in the dope preparation, then membrane is treated by electron-beam or gamma-ray irradiation at low temperature.

- Performing filtration/backwash cycles on membrane bioreactors on the long-term, as biofouling is the main limitation, ideally using deformable and non-deformable membrane having similar permeability for comparison.
- Modelling the deformation of the membrane and the fouling layer under pressure with finite elements as described in [145]. Computing the shear stress generated at the interface cake-membrane during deformation.
- Evaluating membrane mechanical properties on the long-term (after several filtration/backwash cycles). Modification of the Young's modulus and deformation reversibility? Observation of creep behavior for deformable materials?

This research work was therefore a first approach to improve the physical cleaning efficiency of filtration membranes offering insights on the mechanisms involved in fouling removal and opening the door to new developments and multiple applications.

Appendices

Appendix 1 Technical data sheets of Kynar® PVDF grades

KYNAR® HSV 900

Kynar® resins are fluorinated thermoplastic homopolymers.

Outstanding characteristics: chemical resistance, imperviousness to UV, high barrier properties, high purity, good mechanical and thermo-mechanical properties.

Main applications: Battery, membrane

MAIN CHARACTERISTICS

PROPERTIES	VALUE	UNIT	TEST STANDARD
Melt Viscosity, 230°C, 100 s ⁻¹	48 - 52.5	kPoise	ASTM D3835
Tensile Strength at Yield, 73 °F	40 - 55.2	MPa	ASTM D638
Tensile Strength at Break, 73 °F	34 - 43	MPa	ASTM D638
Elongation at Break, 73 °F	50 - 250	%	ASTM D638
Hardness, Shore D, 73 °F	76 - 80	-	ASTM D2240
Flexural Modulus, 73 °F	1380 - 2210	MPa	ASTM D790
Compressive Strength, 73 °F	68.9 - 103	MPa	ASTM D695
Notched Impact Strength, 73 °F	0.107 - 0.32	kJ/m	ASTM D256
Melting Point, 73 °F	162 - 172	°C	ASTM D3418
Limiting Oxygen Index, 73 °F	44	%	ASTM D2863
Density	1.780	kg/m ³	ISO 1183
Specific Gravity, 73 °F	1.77 - 1.79	-	ASTM D792
Refractive Index @ sodium D line	1.42	-	ASTM D542

Processing

Coating, Casting

Delivery form

Powder

Special Characteristics

Heat Stabilized, UV Stable

Regional Availability

North America, Europe, Asia Pacific, South and Central America, Near East/Africa

Arkema France - A French "société anonyme", registered in the Nanterre (France) Tribunal Commercial Register under the number 319 632 790
5/30/11-2018

Please consult Arkema's disclaimer regarding the use of Arkema's products on <https://www.arkema.com/en/products/product-safety/disclaimer/index.html>

Kynar® is a registered trademark of Arkema
© 2019 Arkema Inc. All rights reserved.

kynar.com

Arkema Inc. – Technical Polymers
900 First Avenue
King of Prussia, PA 19406
Tel.: +1 610 205 7000
Fax: +1 610 205 7497
arkema-america.com

KYNAR®
BY ARKEMA

Headquarters: Arkema France
420, rue d'Estienne d'Orves
92705 Colombes Cedex – France
Tel.: +33 1 49 00 80 80
Fax: +33 1 49 00 83 96
arkema.com

KYNAR® MG15

Kynar® resins are fluorinated thermoplastic homopolymers.

Kynar® MG15 resin is a crystalline high viscosity polymer of polyvinylidene difluoride. It is an engineering polymer with an outstanding balance of physical strength and high chemical resistance which make it ideal for micro and ultra-filtration membranes for durable water purification and other applications.

Kynar® MG15 resin is soluble in selected solvents and can be used in solution processing applications. It is especially recommended for hollow fiber and flat sheet membranes.

Kynar® MG15 resin has NSF, FDA, and USP Class VI certifications for use in potable water, food processing, and bio-pharma applications.

MAIN CHARACTERISTICS

PROPERTIES	VALUE	UNIT	TEST STANDARD
Melt Viscosity, 230°C, 100 s-1	33 - 39	kPoise	ASTM D9835
Tensile Modulus, 73 °F	1380 - 2310	MPa	ASTM D638
Tensile Strength at Yield, 73 °F	44.8 - 55.2	MPa	ASTM D638
Flexural Modulus, 73 °F	1380 - 2310	MPa	ASTM D790
Melting Temperature, 10°C/min	168	°C	ISO 11357-1/-3
Melting Point, 73 °F	162 - 172	°C	ASTM D3418
Glass Transition Temperature, 10°C/min	-40	°C	ISO 11357-1/-2
Water Absorption	≤ 0.04	%	ASTM D570
Density	1.780	kg/m ³	ISO 1183
Specific Gravity, 73 °F	1.77 - 1.79	-	ASTM D792
Refractive Index @ sodium D line	1.42	-	ASTM D542
Solution Viscosity, 20°C, #3 Brookfield	≥ 1500	cps	10% NMP Solution Spindle@20 RPM Spindle Viscometer

Processing

Casting

Delivery form

Powder

Regional Availability

North America, Europe, Asia Pacific, South and Central America, Near East/Africa

Please consult Arkema's disclaimer regarding the use of Arkema's products on <https://www.arkema.com/en/products/product-safety/disclaimer/index.html>

Kynar® is a registered trademark of Arkema
© 2019 Arkema Inc. All rights reserved.

kynar.com

Arkema Inc. – Technical Polymers

900 First Avenue
King of Prussia, PA 19406
Tel.: +1 610 205 7000
Fax: +1 610 205 7497
arkema-america.com

KYNAR®
BY ARKEMA

Headquarters: Arkema France

420, rue d'Estienne d'Orves
92705 Colombes Cedex – France
Tel.: +33 1 49 00 80 80
Fax: +33 1 49 00 83 96
arkema.com

Arkema France - A French "société anonyme", registered in the Commerce (France) National Companies Register under the number 319 432 790
5/20/11-2018

KYNAR FLEX® 2801-00

Kynar Flex® resins are fluorinated thermoplastic copolymers.

Outstanding characteristics: chemical resistance, imperviousness to UV, high barrier properties, high purity, good mechanical and thermo-mechanical properties.

Main applications: corrosion protection in the chemical industry, coating (painting, co-extrusion), off shore, wire and cable.

Kynar Flex® 2801 resin is the powder form of the Kynar Flex® 2800-00 resin. To be used as an additive in LLDPE to improve the extrusion rate.

MAIN CHARACTERISTICS

PROPERTIES	VALUE	UNIT	TEST STANDARD
Melt Volume-Flow Rate, MVR	0.5	cm ³ /10min	ISO 1133
Temperature	230	°C	-
Load	5	kg	-
Melt Flow Rate	3 - 8	g/10min	ASTM D1238
Temperature	230	°C	-
Load	12.5	kg	-
Melt Viscosity, 230°C, 100 s⁻¹	23 - 27	kPoise	ASTM D3835
Tensile Modulus	700	MPa	ISO 527-1/-2
Tensile Modulus, 73 °F	552 - 896	MPa	ASTM D638
Yield stress	27	MPa	ISO 527-1/-2
Tensile Strength at Yield, 73 °F	20 - 34.5	MPa	ASTM D638
Yield strain	15	%	ISO 527-1/-2
Elongation at Yield, 73 °F	10 - 20	%	ASTM D638
Nominal Strain at Break	>50	%	ISO 527-1/-2
Tensile Strength at Break, 73 °F	17.2 - 34.5	MPa	ASTM D638
Elongation at Break, 73 °F	100 - 300	%	ASTM D638
Taber Abrasion, CS 17 1000g:pad	16 - 19	mg/1000 cycles	ASTM-G195-13A
Hardness, Shore D, 73 °F	60 - 70	-	ASTM D2240
Flexural Modulus, 73 °F	483 - 758	MPa	ASTM D790
Flexural Strength @ 5% Strain, 73 °F	20.7 - 34.5	MPa	ASTM D790
Compressive Strength, 73 °F	31 - 41.4	MPa	ASTM D695
Unnotched Impact Strength, 73 °F	N	kJ/m	ASTM D256
Notched Impact Strength, 73 °F	0.534 - 1.07	kJ/m	ASTM D256
Coefficient of Friction, Static vs. Steel, 73 °F	0.33	-	ASTM D1894
Coefficient of Friction, Dynamic vs. Steel, 73 °F	0.33	-	ASTM D1894
Melting Temperature, 10°C/min	143	°C	ISO 11357-1/-3
Melting Point, 73 °F	140 - 145	°C	ASTM D3418
Glass Transition Temperature, 10°C/min	-40	°C	ISO 11357-1/-2
Glass Transition Temperature (T_g)	-41.1 - -39.4	°C	ASTM D7028

Arkema France - A French "société anonyme", registered in the Marne-la-Vallée (France) Trade and Companies Register under the number 319 037 770 25071-2018

Please consult Arkema's disclaimer regarding the use of Arkema's products on <https://www.arkema.com/en/products/product-safety/disclaimer/index.html>

KYNAR FLEX
BY ARKEMA

KYNAR FLEX® 2801-00

Temperature Rating	130	°C	UL R11
Temp. of Deflection Under Load, 1.80 MPa	48	°C	ISO 75-1/-2
Heat Deflection Temperature, 264 Psi, 248 °F/hr	40 - 55	°C	ASTM D648
Heat Deflection Temperature, 66 Psi, 248 °F/hr	60 - 75	°C	ASTM D648
Vicat Softening Temperature, 50°C/h 50N	79	°C	ISO 306
Coeff. of Linear Thermal Expansion, parallel	160	E-6/K	ISO 11359-1/-2
Coefficient of Thermal Expansion, 73 °F	12.6 - 18.5	10E-5/°C	ASTM D696
Burning Behav. at 1.5 mm Nominal Thickness	V-0	class	IEC 60695-11-10
Thickness Tested	1.5	mm	-
Yellow Card available	yes	-	-
Burning Behav. at Thickness h	V-0	class	IEC 60695-11-10
Thickness Tested	0.8	mm	-
Oxygen Index	43	%	ISO 4589-1/-2
Limiting Oxygen Index, 73 °F	42	%	ASTM D2863
Thermal Conductivity	0.144 - 0.18	W/(m K)	ASTM D433
Specific Heat	745 - 958	J/(kg K)	DSC
Thermal Decomposition TGA, in air	375	°C	1% wt. loss
Thermal Decomposition TGA, in nitrogen	410	°C	1% wt. loss
Relative Thermal Index, Mechanical	130	°C	UL 746B
Relative Thermal Index, Electrical	130	°C	UL 746B
Relative Permittivity, 1MHz	7	-	IEC 60250
Dielectric Constant, 1 kHz	3.5 - 10.6	-	ASTM D150
Dissipation Factor, 1MHz	2330	E-4	IEC 60250
Dissipation Factor, 100 kHz	0.02 - 0.21	-	ASTM D150
Volume Resistivity	2E12	Ohm*m	IEC 60093
Volume Resistivity, DC 68 °F, 65% R.H.	2E14	Ohm*cm	ASTM D257
Dielectric Strength, 73 °F	1.3 - 1.5	kV/mm	ASTM D149
Water Absorption	0.03	%	Sim. to ISO 62
Density	1780	kg/m ³	ISO 1183
Specific Gravity, 73 °F	1.77 - 1.8	-	ASTM D792
Refractive Index @ sodium D line	1.41	-	ASTM D542

Arkema Fluoro - A French "société anonyme", registered in the Marne (France) Trade and Companies Register under the number 319 832 790
SIC(1)-2018

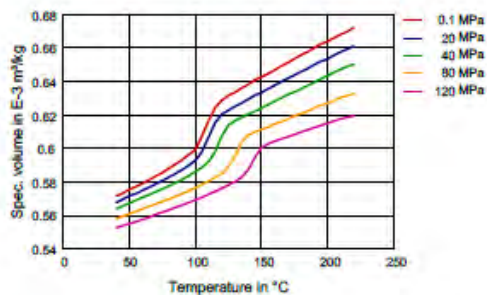
Please consult Arkema's disclaimer regarding the use of Arkema's products on <https://www.arkema.com/en/products/product-safety/disclaimer/index.html>

KYNAR FLEX®
BY ARKEMA

KYNAR FLEX® 2801-00

Diagrams

Specific volume-temperature (pvT)



Delivery form

Powder

Special Characteristics

Heat Stabilized, Light stabilized or stable to light, UV Stable

Regional Availability

North America, Europe, Asia Pacific, South and Central America, Near East/Africa

Arkema France - Arkema "Kynar" est une marque déposée, enregistrée en France. Arkema France est enregistrée au Registre du Commerce et des Sociétés sous le numéro 319 632 790 502/11/2016

Please consult Arkema's disclaimer regarding the use of Arkema's products on <https://www.arkema.com/eia/products/product-safety/disclaimer/index.html>

Kynar Flex® is a registered trademark of Arkema
© 2019 Arkema Inc. All rights reserved.

kynar.com

KYNAR FLEX®

BY ARKEMA

Arkema Inc. – Technical Polymers
900 First Avenue
King of Prussia, PA 19406
Tel.: +1 610 205 7000
Fax: +1 610 205 7497
arkema-america.com

Headquarters: Arkema France
420, rue d'Estienne d'Orves
92705 Colombes Cedex – France
Tel.: +33 1 49 00 80 80
Fax: +33 1 49 00 83 96
arkema.com

Kynar®RC10312

This is a provisional data sheet for a developmental product. Specifications may be changed without notice.

Kynar®RC10312 is a high viscosity VF2-HFP copolymer resin. It is supplied as a fine powder, readily soluble in strong polar aprotic solvents such as N-methylpyrrolidone, N,N-dimethylacetamide, and dimethylsulfoxide. It is suitable for casting hollow fiber membranes by the non-solvent induced phase separation process (NIPS). RC10312 has excellent chemical resistance to acids, chlorinated solvents, hydrocarbons, and can be used up to pH 13.

TYPICAL PROPERTIES

PROPERTY	METHOD	CONDITIONS	ENGLISH / COMMON UNITS	VALUE
Specific Gravity	D792	23°C	-	1.77 - 1.79
Melt Viscosity	D3835	232°C, 100 sec ⁻¹	Kpoise	39 - 44
Solution viscosity	10% NMP solution @ 20 rpm	20°C, #3 spindle Brookfield DHBV rheometer	cps	> 1800
Melting Temperature	D3418	-	°C	155 - 160
Water Absorption	D570	20°C	%	0.03 - 0.05

The statements, technical information and recommendations contained herein are believed to be accurate as of the date hereof. Since the conditions and methods of use of the product and of the information referred to herein are beyond our control, ARKEMA expressly disclaims any and all liability as to any results obtained or arising from any use of the product or reliance on such information; NO WARRANTY OF FITNESS FOR ANY PARTICULAR PURPOSE, WARRANTY OF MERCHANTABILITY OR ANY OTHER WARRANTY, EXPRESSED OR IMPLIED, IS MADE CONCERNING THE GOODS DESCRIBED OR THE INFORMATION PROVIDED HEREIN.

The information provided herein relates only to the specific product designated and may not be applicable when such product is used in combination with other materials or in any process. The user should thoroughly test any application before commercialization. Nothing contained herein constitutes a license to practice under any patent and it should not be

construed as an inducement to infringe any patent and the user is advised to take appropriate steps to be sure that any proposed use of the product will not result in patent infringement. See SDS for Health & Safety Considerations. Arkema has implemented a Medical Policy regarding the use of Arkema products in Medical Devices applications that are in contact with the body or circulating bodily fluids:

<http://www.arkema.com/en/social-responsibility/responsible-product-management/medical-device-policy/index.html>

Arkema has designated Medical grades to be used for such Medical Device applications. Products that have not been designated as Medical grades are not authorized by Arkema for use in Medical Device applications that are in contact with the body or circulating bodily fluids. In addition, Arkema strictly prohibits the use of any Arkema products in Medical Device applications that are implanted in the body or in contact with bodily fluids or tissues for greater than 30 days. The Arkema trademarks and the Arkema name shall not be used in conjunction with customers' medical devices, including without limitation, permanent or temporary implantable devices, and customers shall not represent to anyone else, that Arkema allows, endorses or permits the use of Arkema products in such medical devices.

It is the sole responsibility of the manufacturer of the medical device to determine the suitability (including biocompatibility) of all raw materials, products and components, including any medical grade Arkema products, in order to ensure that the final end-use product is safe for its end use; performs or functions as intended; and complies with all applicable legal and regulatory requirements (FDA or other national drug agencies) It is the sole responsibility of the manufacturer of the medical device to conduct all necessary tests and inspections and to evaluate the medical device under actual end-use requirements and to adequately advise and warn purchasers, users, and/or learned intermediaries (such as physicians) of pertinent risks and fulfill any postmarket surveillance obligations. Any decision regarding the appropriateness of a particular Arkema material in a particular medical device should be based on the judgment of the manufacturer, seller, the competent authority, and the treating physician.

Appendix 2 Dope and bore fluid compositions and spinning operating conditions

In-situ observation of fouling and fouling removal behavior on hollow-fiber membranes requires a specific filtration cell design. Indeed, a specific filtration cell design is required for optimal observation as reported in Table A 3.

The detailed dope and bore fluid composition (Table A 1) and the spinning operating conditions (Table A 2) were given for M-LP91 and M-LP19. The formulations and spinning operating conditions for the other membranes were provided by Arkema S.A. and confidential.

Table A 1: Detailed compositions of dope solution and bore fluid for M-LP91 and M-LP19 hollow-fiber membranes.

Fiber Name	Dope composition			Bore fluid composition	
	Polymer	Solvent	Additive	Solvent	Non-solvent
M-LP91	15 wt.% Kynar® HSV 900	82 wt.% NMP	3 wt.% LiCl	15 wt.% NMP	85 wt.% water
M-LP19	20 wt.% Kynar Flex® 2801-00	68 wt.% DMSO	12% PEG ($M_w=10\ 000$ $g.mol^{-1}$)	-	100 wt.% water

Table A 2: Detailed spinning operating conditions for M-LP91 and M-LP19 hollow-fiber membranes.

Fiber Name	Dope flow rate (ml.min ⁻¹)	Bore fluid flow rate (ml.min ⁻¹)	Dope temperature (°C)	Bore fluid temperature (°C)	Water coagulation bath temperature (°C)	Air gap (cm)	Take-up speed (m.min ⁻¹)
M-LP91	8.5	2.1	50	50	50	18	8
M-LP19	6.2	6.0	50	50	50	20	22

Appendix 3 Filtration cell design and hydrodynamic

In-situ observation of fouling and fouling removal behaviors on hollow-fiber membranes requires a specific filtration cell design as described in Table A 3.

Table A 3: Filtration cell design requirements and matching solutions for cell prototype.

Requirement	Solution
Transparent cell for optical observation.	An observation window (66 x 16 mm) was made from glass microscope slide glued on both sides of the cell.
Horizontal and stable cell for precise measurements.	A support made from polylactic acid was specifically designed to support and stabilize the cell.
Homogenous hydrodynamic flow for uniform particle deposition on the membrane surface.	The cell geometry was designed to improve the fluid hydrodynamic from the inlet to the membrane surface. Coat-hanger flow channel design of the filtration cell may help to evenly distribute the particle solution and limit dead-zone formation and boundary effects.
Controlled distance between the fiber and the microscopic lens. Indeed, this distance depends on the focus length of the objective to allow high resolution on the fiber surface. As the fiber is constrained in the filtration cell, short distance between the fiber and the module glass wall is required. Moreover, increasing this distance loses sharpness as feed solution is not clear.	The channel height between the two glass slides was 5 mm. The hollow-fiber was centered in the channel. The distance between the membrane outer surface and the glass slide was comprised between 1.8 and 2.1 mm (depending on fiber dimensions). The turbidity of the feed solution was lower than 40 NTU.

The filtration cell was made from aluminum by 3D-printing technique. Prior to be printed, the 3D cell was meshed on Blender software meeting the requirements (Table A 3). The mesh and the different views of the cell are displayed on Figure A 1.

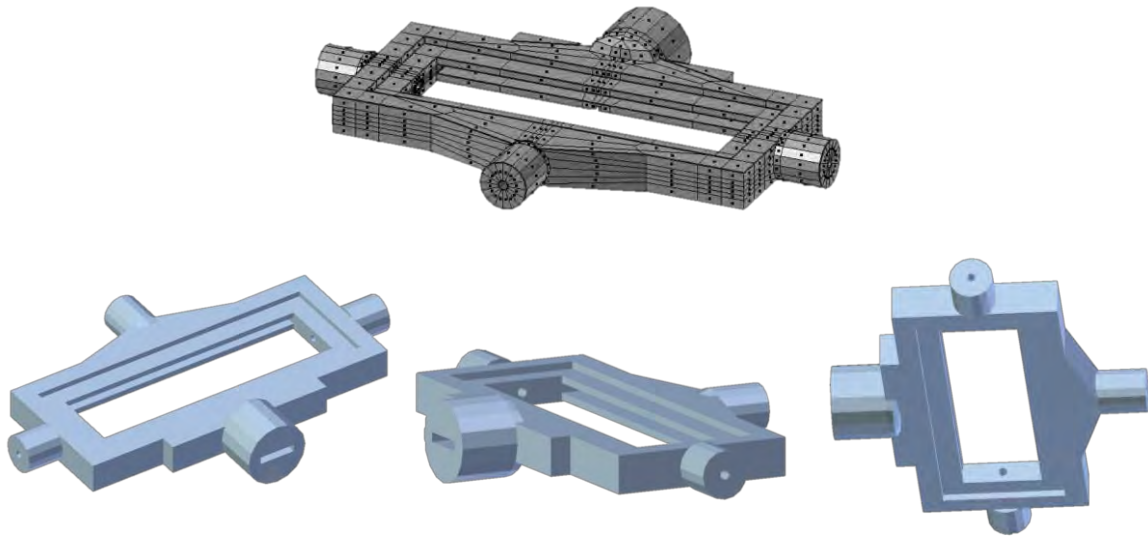


Figure A 1: Mesh display (top) and different 3D views of the Blender cell (bottom)

Post treatments were applied as supplementary finishes such as polishing and threading once the cell was printed. Finally, two glass microscope slides were glued with epoxy on both sides of the 3D-printed cell and left for curing during 48 hours into oven at 60°C to improve the sealing (see on Figure A 2).



Figure A 2: Experimental 3D-printed cell after post treatment and with glued microscope slides

Hydrodynamic in the filtration cell was simulated by finite elements using COMSOL Multiphysics® software to verify that water flow was homogenized through the cell. The 3D-model included the inside volume of the filtration cell and a centered hollow-fiber membrane. The geometry of the inside of the filtration cell and its dimensions were modelled in 3D on COMSOL whereas the volume of the fiber was subtracted to the cell volume to obtain the external surface of the fiber only. The model size was reduced using symmetries. Simplified cell was modelled with two planes of symmetry: xy and zy-plane (see on Figure A 3).

The hydrodynamic of water fluid through the inlet of the filtration cell to the outlet of the hollow-fiber membrane was simulated once boundary conditions were set. The pressure at the

inlet was set to 0.8 bar (blue surface on Figure A 3) as used during our filtration experiments. The water flux at the external membrane surface was limited by the membrane flux. The outlet was therefore represented by the external membrane surface area (red surface Figure A 3) and set to an outlet flux of $6.10^{-5} \text{ m.s}^{-1}$ ($=215 \text{ L.m}^2.\text{h}^{-1}$).

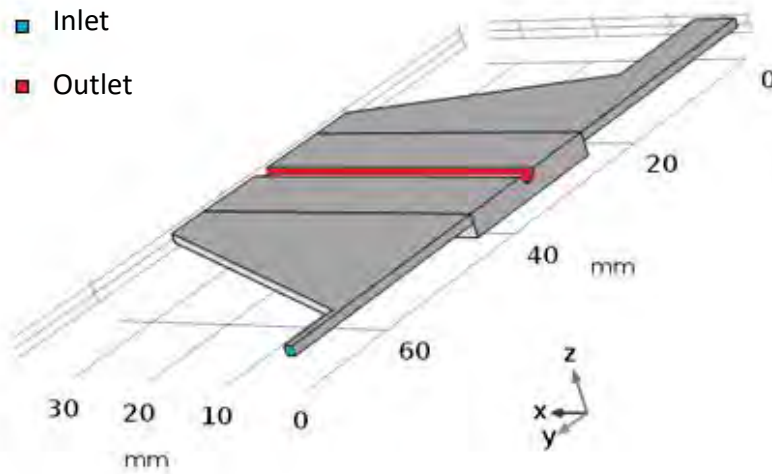


Figure A 3: Simplified cell model on COMSOL with two planes of symmetry (*xy* and *zy*-plane). Boundary conditions set at the inlet, $P=0.8 \text{ bar}$ and outlet, $J=6.10^{-5} \text{ m.s}^{-1}$.

Water flux through the cell was computed within the cell as shown on Figure A 4. It was observed a high flux at the fluid inlet mainly explained by the narrow channel. However, the water flux seemed to homogenize when getting closer to the membrane surface, especially in the observation window (brown rectangle).

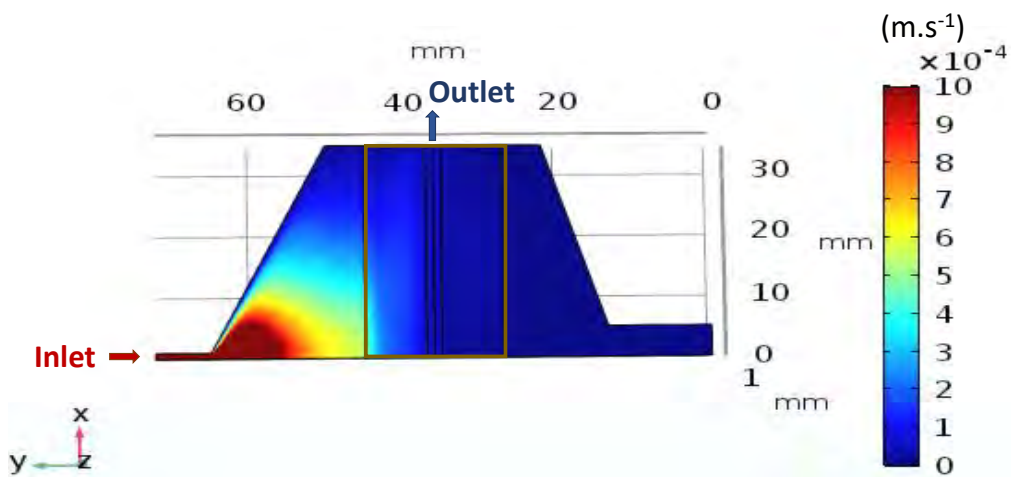


Figure A 4: Flux hydrodynamic simulation by finite elements with water solution. Boundary conditions set at the inlet, $P=0.8 \text{ bar}$ and outlet, $J=6.10^{-5} \text{ m.s}^{-1}$. Brown rectangle represents the observation window.

Appendix 4 Valve control for filtration of feed solutions

Experimental designs of filtration unit A and unit B are shown on Figure 19 and Figure 20 respectively. The operating mode for valve control to perform filtration of model suspensions on single filtration/backwash cycle is given in Table A 4.

Table A 4: Experimental operations with valve control for fouling of model suspension on a single filtration/backwash cycle on filtration unit A and B

Step	Valve		
	V ₁	V ₂	V ₃
Conditioning	A	Close	A
Permeability measurement			
<i>Draining and refilling with feed solution</i>	B	Open	Close
Filtration	B	Close	A
<i>Rinsing step with saline solution</i>	A	Open	Close
Permeability measurement	A	Close	A
1st Backwash	Close	Open	B
<i>Rinsing step with saline solution</i>	A	Open	Close
Permeability measurement	A	Close	A
2nd Backwash	Close	Open	B
<i>Rinsing step with saline solution</i>	A	Open	Close
Permeability measurement	A	Close	A

The operating mode for valve control to perform filtration of feed solutions on several filtration/backwash cycles is given in Table A 5.

Table A 5: Experimental operations with valve control for fouling of feed solutions on several filtration/backwash cycles on filtration unit A

Step	Valve		
	V ₁	V ₂	V ₃
Conditioning	A	Close	A
Permeability measurement	A	Close	A
<i>Draining and refilling with feed solution</i>	B	Open	Close
1st Filtration cycle	B	Close	A
1st Backwash cycle	Close	Open	B
<i>Rinsing step with feed solution</i>	B	Open	Close
2nd Filtration cycle	B	Close	A
2nd Backwash cycle	Close	Open	B
<i>Rinsing step with feed solution</i>	B	Open	Close
⋮			
14th Filtration cycle	B	Close	A
14th Backwash cycle	Close	Open	B
<i>Rinsing step with feed solution</i>	B	Open	Close

Appendix 5 Pore size and pore distribution

The pore size and pore distribution (Figure A 5) were measured by BET analysis. The pore distribution was very similar for all analyzed membrane as shown on Figure A 5. Most of the pores had a size between 2 and 5 nm and were assumed located at the membrane surface. Indeed, the smallest pores are formed in the skin layer during the phase inversion process. This pore size was close to the pore size of ultrafiltration membranes [208][209]. Xu *et al.* [209] measured a pore size from 7 to 20 nm on the surface of Tröger's base UF membrane by SEM and a rejection of humic acid of 90%. By comparison, the measured selectivity of the studied membranes (see on Table 22) was consistent with the measured pore size of a few nanometers.

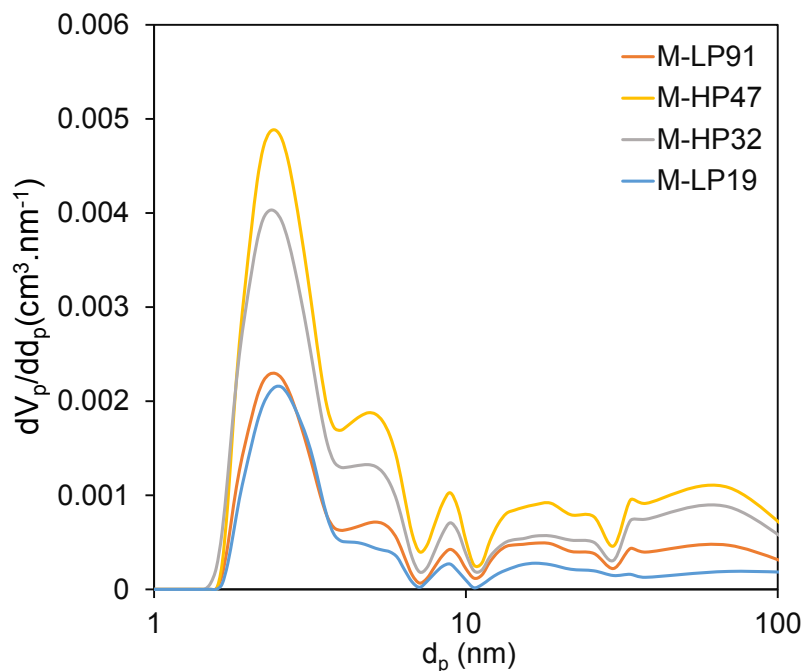


Figure A 5: Pore size distribution of the Kynar® PVDF hollow-fiber membranes based on N₂ adsorption isotherm

The BET specific surface area was also measured for each membrane and reported in Table A 6 as supplementary data.

Table A 6: BET specific surface area for each Kynar® PVDF hollow-fiber membrane

Fiber Name	$S_{\text{BET}}(\text{m}^2\cdot\text{g}^{-1})$
M-LP91	12.0
M-HP47	26.2
M-HP32	20.5
M-LP19	10.9

Appendix 6 Loading-unloading cycles

Hollow-fiber membranes were subjected to several tensile loading-unloading cycles to evaluate the reversibility of the tensile strain. Different maximum strains were chosen to identify the limit of the elastic domain where the strain was expected completely reversible. Ten loading-unloading cycles were successively performed on M-LP19, M-LP91 and M-HP47. Only the first cycle (C1) and the tenth cycle (C10) were represented for each fiber as observed on Figure A 6, Figure A 7 and Figure A 8. A hysteresis loop was observed during the loading-unloading cycle representing the dissipated energy as heat during the deformation-recovery cycle. This hysteresis loop was typically observed for viscoelastic materials such as PVDF. The accumulation of residual strain over successive loading-unloading cycles shifted the stress-strain curve to the right as observed when comparing C1 and C10 for each fiber. A residual strain was observed for each fiber and in all strain conditions as reported in Table A 7. Indeed, even at very low applied strain (up to 0.3%) the reversibility was not complete (as seen on Table A 7 Figure A 6).

Table A 7: Measured elastic recovery and residual strain from stress-strain curve for M-LP19, M-LP91 and M-HP47 at each applied strain during loading-unloading cycle.

Fiber Name	Applied strain (%)	Elastic recovery (%)	Residual strain (%)
M-LP19	0.3	0.25	0.05
	1.2	0.81	0.39
	1.8	1.10	0.70
	3.0	1.92	1.08
	6.0	3.73	2.27
	10.0	4.83	5.17
M-LP91	0.3	0.25	0.05
	1.2	0.96	0.24
	1.8	1.41	0.39
M-HP47	0.3	0.25	0.01
	1.2	0.83	0.37
	1.8	1.31	0.49

The residual strain was composed of a viscoelastic and a plastic component [177][178]. The viscoelastic recovery was time dependent and was not measured during these loading-

unloading cycles. Most part of the residual strain was supposed viscoelastic when the deformation was lower than 2% as high reversibility of the deformation (in radial direction) was observed under camera as reported in Table 19, and if assuming that the viscoelastic behavior was the same in axial and radial directions.

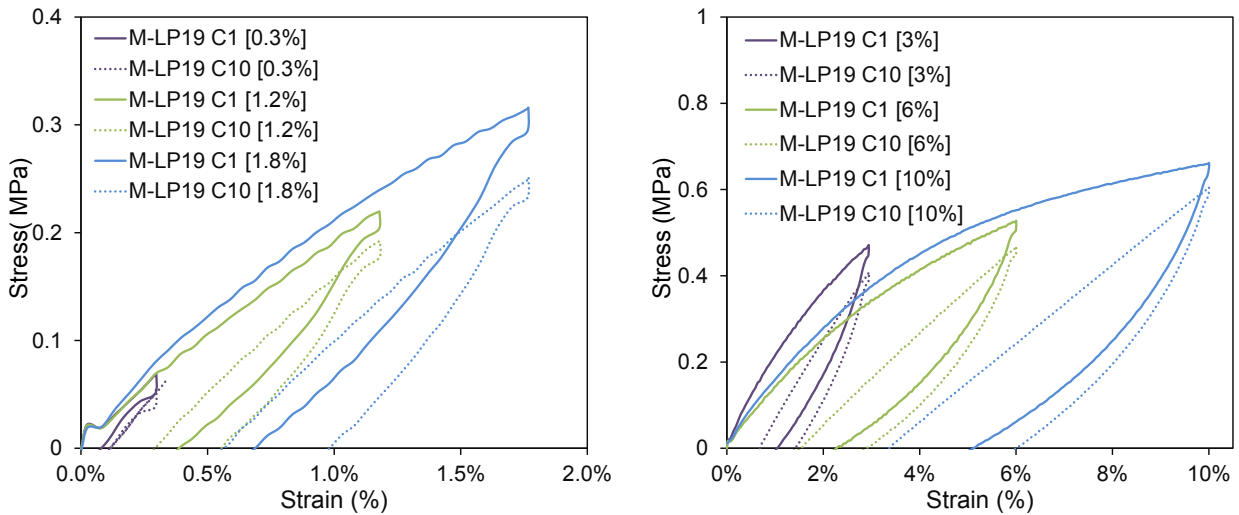


Figure A 6: Stress-strain curves for M-LP19 at 1st (C1) and 10th (C10) loading-unloading cycle with applied strains between 0.3 and 1.8 % (on the left) and between 3 and 10% (on the right) at a strain rate of 50 mm.min-1 and specimen length of 85 mm

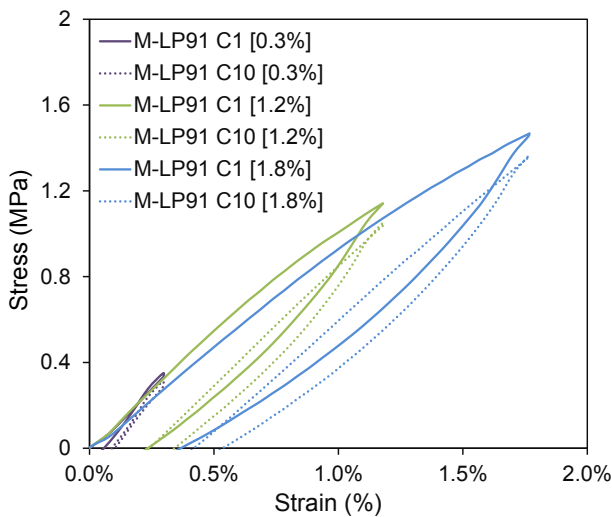


Figure A 7: Stress-strain curves for M-LP91 at 1st (C1) and 10th (C10) loading-unloading cycle with applied strains between 0.3 and 1.8 % at a strain rate of 50 mm.min-1 and specimen length of 85 mm

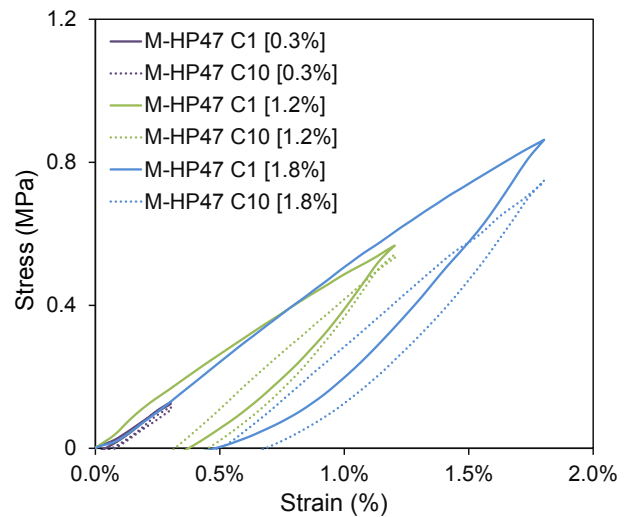


Figure A 8: Stress-strain curves for M-HP45 at 1st (C1) and 10th (C10) loading-unloading cycle with applied strains between 0.3 and 1.8 % at a strain rate of 50 mm.min-1 and specimen length of 85 mm

Appendix 7 Estimation of the consumed energy and permeate

The permeate volume per surface area filtered during a single filtration was 60 L.m⁻². The consumed energy per surface area during a single filtration was calculated by:

$$\frac{e_f}{S_{ext}} = \frac{V_p}{S_{ext}} * TMP$$

With $\frac{e_f}{S_{ext}}$ the energy consumed during a filtration per surface area (mJ.m⁻²), $\frac{V_p}{S_{ext}}$ the permeate volume per surface area produced during the filtration (L.m⁻²) and TMP the transmembrane pressure (Pa).

For all filtrations, 4800 J.m⁻² was consumed to filter 60L m⁻² of permeate volume per surface area.

The real permeate volume per surface area consumed during a single backwash was calculated by:

$$\frac{V_{bw}}{S_{ext}} = \int_0^{t_{bw}} J_{bw} dt_{bw}$$

With $\frac{V_{bw}}{S_{ext}}$ the permeate volume consumed per surface area during the backwash (L.m⁻²), J_{bw} the backwash flux (L.m⁻².h⁻¹) and t_{bw} the backwash duration (h).

Indeed, due to the gradual elimination of the cake the backwash flux was increasing during backwash. The equation was simplified for ease of use by considering J_{bw} constant:

$$\frac{V_{bw}}{S_{ext}} = J_{bw} * t_{bw}$$

A permeate volume per surface area of 2 and 6 L.m⁻² was consumed to reach maximal backwash efficiency for bentonite (KCl) and bentonite (CaCl₂) cake respectively (calculated using critical backwash fluxes found in 5.5.1).

The energy per surface area consumed during a single backwash was calculated by:

$$\frac{e_{bw}}{S_{ext}} = J_{bw} * BTMP * t_{bw}$$

With $\frac{e_{bw}}{S_{ext}}$ the energy consumed per surface area for a single backwash ($\text{mJ}\cdot\text{m}^{-2}$), J_{bw} the backwash flux ($\text{L}\cdot\text{m}^{-2}\cdot\text{h}^{-1}$) and $BTMP$ the backwash transmembrane pressure (Pa).

An energy per surface area of 100 and 1000 J m^{-2} was consumed to reach maximal backwash efficiency for bentonite (KCl) and bentonite (CaCl_2) cake respectively.

The energy contribution of the backwash step compared to the filtration step was calculated by the ratio of the consumed backwash energy on the consumed filtration energy ($\frac{e_{bw}}{e_f}$).

References

-
- [1] S. Atkinson, "The history of the industry. A brief history of membrane science," *Filtr. Sep.*, vol. 36, no. 1, p. 28, 1999.
- [2] S. Loeb and S. Sourirajan, "Sea water demineralization by means of an osmotic membrane," *Adv. Chem.*, vol. 38, pp. 117–132, 1963.
- [3] R. Baker, "Membrane technology and applications," McGraw-Hil, 1999, ISBN: 9780071354400.
- [4] L. Li, H. E. Wray, R. C. Andrews, and P. R. Bérubé, "Ultrafiltration Fouling: Impact of Backwash Frequency and Air Sparging," *Sep. Sci. Technol.*, vol. 49, no. 18, pp. 2814–2823, 2014.
- [5] O. Ferrer, B. Lefèvre, G. Prats, X. Bernat, O. Gibert, and M. Paraira, "Reversibility of fouling on ultrafiltration membrane by backwashing and chemical cleaning: differences in organic fractions behaviour," *Desalin. Water Treat.*, vol. 57, no. 19, pp. 8593–8607, 2016.
- [6] F. Meng, S. Zhang, Y. Oh, Z. Zhou, H. S. Shin, and S. R. Chae, "Fouling in membrane bioreactors: An updated review," *Water Res.*, vol. 114, pp. 151–180, 2017.
- [7] W. Gao, H. Liang, J. Ma, M. Han, Z. lin Chen, Z. shuang Han, and G. bai Li, "Membrane fouling control in ultrafiltration technology for drinking water production: A review," *Desalination*, vol. 272, no. 1–3, pp. 1–8, 2011.
- [8] F. Prézéus, "Ecodesign of ultrafiltration membranes for drinking water production: a modelling and experimental approach," PhD Dissertation, University of Toulouse Paul Sabatier, 2019.
- [9] H. Chang, H. Liang, F. Qu, B. Liu, H. Yu, X. Du, G. Li, and S. A. Snyder, "Hydraulic backwashing for low-pressure membranes in drinking water treatment: A review," *J. Memb. Sci.*, vol. 540, pp. 362–380, 2017.
- [10] N. Kalboussi, J. Harmand, A. Rapaport, T. Bayen, F. Ellouze, and N. Ben Amar, "Optimal control of physical backwash strategy - towards the enhancement of membrane filtration process performance," *J. Memb. Sci.*, vol. 545, pp. 38–48, 2018.
- [11] K. J. Hwang, C. S. Chan, and K. L. Tung, "Effect of backwash on the performance of submerged membrane filtration," *J. Memb. Sci.*, vol. 330, no. 1–2, pp. 349–356, 2009.

- [12] X. Zhao, H. Zhang, and J. Wang, "Filtering surface water with a polyurethane-based hollow fiber membrane: Effects of operating pressure on membrane fouling," *Chinese J. Chem. Eng.*, vol. 22, no. 5, pp. 583–589, 2014.
- [13] "Arkema Website." [Online]. Available: <https://www.arkema.com/en/markets-and-solutions/markets-overview/water-and-environment/>. [Accessed: 07-Jan-2020].
- [14] "Marketsandmarkets Website." [Online]. Available: <https://www.marketsandmarkets.com/Market-Reports/membrane-filtration-market-68840418.html>. [Accessed: 07-Jan-2020].
- [15] J. Davey and A. I. Schäfer, "Ultrafiltration to supply safe drinking water in developing countries: A review of opportunities," in *Appropriate Technologies for Environmental Protection in the Developing World*, Yanful E., Ed. Springer science, 2009, pp. 151–168.
- [16] A. K. Fard, G. McKay, A. Buekenhoudt, H. Al Sulaiti, F. Motmans, M. Khraisheh, and M. Atieh, "Inorganic membranes: Preparation and application for water treatment and desalination," *Materials*, vol. 11, no. 1, 2018.
- [17] J.-C. Remigy and S. Desclaux, "Filtration membranaire (OI, NF, UF) - Présentation des membranes et modules," *Tech. l'ingénieur*, vol. 33, no. 0, 2007.
- [18] D. M. Warsinger *et al.*, "A review of polymeric membranes and processes for potable water reuse," *Prog. Polym. Sci.*, vol. 81, pp. 209–237, 2018.
- [19] F. Liu, N. A. Hashim, Y. Liu, M. R. M. Abed, and K. Li, "Progress in the production and modification of PVDF membranes," *J. Memb. Sci.*, vol. 375, no. 1–2, pp. 1–27, 2011.
- [20] J. Zhang, Z. Wang, Q. Wang, J. Ma, J. Cao, W. Hu, and Z. Wu, "Relationship between polymers compatibility and casting solution stability in fabricating PVDF/PVA membranes," *J. Memb. Sci.*, vol. 537, pp. 263–271, 2017.
- [21] J. Mijović, H. Luo, and C. D. Han, "Property-morphology relationships of polymethylmethacrylate/polyvinylidene fluoride blends," *Polym. Eng. Sci.*, vol. 22, no. 4, pp. 234–240, 1982.
- [22] L. Shi, R. Wang, Y. Cao, C. Feng, D. T. Liang, and J. H. Tay, "Fabrication of

- poly(vinylidene fluoride-co-hexafluoropropylene) (PVDF-HFP) asymmetric microporous hollow fiber membranes," *J. Memb. Sci.*, vol. 305, no. 1–2, pp. 215–225, 2007.
- [23] S. Wongchitphimon, R. Wang, R. Jiraratananon, L. Shi, and C. H. Loh, "Effect of polyethylene glycol (PEG) as an additive on the fabrication of polyvinylidene fluoride-co-hexafluoropropylene (PVDF-HFP) asymmetric microporous hollow fiber membranes," *J. Memb. Sci.*, vol. 369, no. 1–2, pp. 329–338, 2011.
- [24] S. Kaur, S. Sundarrajan, D. Rana, R. Sridhar, R. Gopal, T. Matsuura, and S. Ramakrishna, "Review: The characterization of electrospun nanofibrous liquid filtration membranes," *J. Mater. Sci.*, vol. 49, no. 18, pp. 6143–6159, 2014.
- [25] D. M. Wang and J. Y. Lai, "Recent advances in preparation and morphology control of polymeric membranes formed by nonsolvent induced phase separation," *Curr. Opin. Chem. Eng.*, vol. 2, no. 2, pp. 229–237, 2013.
- [26] X. M. Tan and D. Rodrigue, "A review on porous polymeric membrane preparation. Part II: Production techniques with polyethylene, polydimethylsiloxane, polypropylene, polyimide, and polytetrafluoroethylene," *Polymers*, vol. 11, no. 8, p. 1310, 2019.
- [27] A. Bottino, G. Camera-Roda, G. Capannelli, and S. Munari, "The formation of microporous polyvinylidene difluoride membranes by phase separation," *J. Memb. Sci.*, vol. 57, no. 1, pp. 1–20, 1991.
- [28] D. J. Lin, K. Beltsios, T. H. Young, Y. S. Jeng, and L. P. Cheng, "Strong effect of precursor preparation on the morphology of semicrystalline phase inversion poly(vinylidene fluoride) membranes," *J. Memb. Sci.*, vol. 274, no. 1–2, pp. 64–72, 2006.
- [29] I. Pinnau and W. J. Koros, "Structures and gas separation properties of asymmetric polysulfone membranes made by dry, wet, and dry/wet phase inversion," *J. Appl. Polym. Sci.*, vol. 43, no. 8, pp. 1491–1502, 1991.
- [30] P. Sukitpaneenit and T. S. Chung, "Molecular elucidation of morphology and mechanical properties of PVDF hollow fiber membranes from aspects of phase inversion, crystallization and rheology," *J. Memb. Sci.*, vol. 340, no. 1–2, pp. 192–205, 2009.

- [31] L. P. Cheng, "Effect of temperature on the formation of microporous PVDF membranes by precipitation from 1-Octanol/DMF/PVDF and water/ DMF/PVDF systems," *Macromolecules*, vol. 32, no. 20, pp. 6668–6674, 1999.
- [32] Y. Tang, N. Li, A. Liu, S. Ding, C. Yi, and H. Liu, "Effect of spinning conditions on the structure and performance of hydrophobic PVDF hollow fiber membranes for membrane distillation," *Desalination*, vol. 287, pp. 326–339, 2012.
- [33] D. Wang, K. Li, and W. K. Teo, "Preparation and characterization of polyvinylidene fluoride (PVDF) hollow fiber membranes," *J. Memb. Sci.*, vol. 163, no. 2, pp. 211–220, 1999.
- [34] F. P. Cuperus, D. Bargeman, and C. A. Smolders, "Characterization of anisotropic UF-membranes: top layer thickness and pore structure," *J. Memb. Sci.*, vol. 61, no. C, pp. 73–83, 1991.
- [35] T. Savart, "Conception et réalisation de fibres creuses industrielles," PhD Dissertation, University of Toulouse Paul Sabatier, 2013.
- [36] E. Saljoughi and T. Mohammadi, "Cellulose acetate (CA)/polyvinylpyrrolidone (PVP) blend asymmetric membranes: Preparation, morphology and performance," *Desalination*, vol. 249, no. 2, pp. 850–854, 2009.
- [37] H. C. Kim and B. A. Dempsey, "Removal of organic acids from EfOM using anion exchange resins and consequent reduction of fouling in UF and MF," *J. Memb. Sci.*, vol. 364, no. 1–2, pp. 325–330, 2010.
- [38] W. Zhang, M. Wahlgren, and B. Sivik, "Membrane Characterization by the Contact Angle Technique," *Desalination*, vol. 72, no. 3, pp. 263–273, 1989.
- [39] N. A. Ahmad, C. P. Leo, A. L. Ahmad, and W. K. W. Ramli, "Membranes with great hydrophobicity: A review on preparation and characterization," *Sep. Purif. Rev.*, vol. 44, no. 2, pp. 109–134, 2015.
- [40] Y. W. Guo, W. W. Cui, W. H. Xu, Y. Jiang, H. H. Liu, J. Y. Xu, Z. Q. Gao, and L. Z. Liu, "Effect of PVP hydrophilic additive on the morphology and properties of PVDF porous membranes," *Adv. Mater. Res.*, vol. 981, pp. 891–894, 2014.
- [41] E. Fontananova, M. A. Bahattab, S. A. Aljlil, M. Alowairdy, G. Rinaldi, D. Vuono, J. B.

- Nagy, E. Drioli, and G. Di Profio, "From hydrophobic to hydrophilic polyvinylidene fluoride (PVDF) membranes by gaining new insight into material's properties," *RSC Adv.*, vol. 5, no. 69, pp. 56219–56231, 2015.
- [42] N. Subhi, A. R. D. Verliefde, V. Chen, and P. Le-Clech, "Assessment of physicochemical interactions in hollow fibre ultrafiltration membrane by contact angle analysis," *J. Memb. Sci.*, vol. 403–404, pp. 32–40, 2012.
- [43] F. Gao, J. Wang, H. Zhang, M. A. Hang, Z. Cui, and G. Yang, "Interaction energy and competitive adsorption evaluation of different NOM fractions on aged membrane surfaces," *J. Memb. Sci.*, vol. 542, pp. 195–207, 2017.
- [44] C. S. Ong, W. J. Lau, P. S. Goh, B. C. Ng, T. Matsuura, and A. F. Ismail, "Effect of PVP Molecular Weights on the Properties of PVDF-TiO₂ Composite Membrane for Oily Wastewater Treatment Process," *Sep. Sci. Technol.*, vol. 49, no. 15, pp. 2303–2314, 2014.
- [45] J. S. Kang, K. Y. Kim, and Y. M. Lee, "Preparation of PVP immobilized microporous chlorinated polyvinyl chloride membranes on fabric and their hydraulic permeation behavior," *J. Memb. Sci.*, vol. 214, no. 2, pp. 311–321, 2003.
- [46] I. M. Wienk, E. E. B. Meuleman, Z. Borneman, T. van den Boomgaard, and C. A. Smolders, "Chemical treatment of membranes of a polymer blend: Mechanism of the reaction of hypochlorite with poly(vinyl pyrrolidone)," *J. Polym. Sci. Part A Polym. Chem.*, vol. 33, no. 1, pp. 49–54, 1995.
- [47] Y. Kourde-Hanafi, P. Loulergue, A. Szymczyk, B. Van der Bruggen, M. Nachtnebel, M. Rabiller-Baudry, J. L. Audic, P. Pölt, and K. Baddari, "Influence of PVP content on degradation of PES/PVP membranes: Insights from characterization of membranes with controlled composition," *J. Memb. Sci.*, vol. 533, pp. 261–269, 2017.
- [48] B. Pellegrin, F. Mezzari, Y. Hanafi, A. Szymczyk, J. C. Remigy, and C. Causserand, "Filtration performance and pore size distribution of hypochlorite aged PES/PVP ultrafiltration membranes," *J. Memb. Sci.*, vol. 474, pp. 175–186, 2015.
- [49] M. O. Mavukkandy, M. R. Bilad, A. Giwa, S. W. Hasan, and H. A. Arafat, "Leaching of PVP from PVDF/PVP blend membranes: impacts on membrane structure and fouling in membrane bioreactors," *J. Mater. Sci.*, vol. 51, no. 9, pp. 4328–4341, 2016.

- [50] A. Bottino, G. Capannelli, S. Munari, and A. Turturro, "High performance ultrafiltration membranes cast from LiCl doped solutions," *Desalination*, vol. 68, no. 2-3, pp. 167-177, 1988.
- [51] L. Shi, R. Wang, Y. Cao, D. T. Liang, and J. H. Tay, "Effect of additives on the fabrication of poly(vinylidene fluoride-co-hexafluoropropylene) (PVDF-HFP) asymmetric microporous hollow fiber membranes," *J. Memb. Sci.*, vol. 315, no. 1-2, pp. 195-204, 2008.
- [52] E. Fontananova, J. C. Jansen, A. Cristiano, E. Curcio, and E. Drioli, "Effect of additives in the casting solution on the formation of PVDF membranes," *Desalination*, vol. 192, no. 1-3, pp. 190-197, 2006.
- [53] J. Ma, Z. Wang, M. Pan, and Y. Guo, "A study on the multifunction of ferrous chloride in the formation of poly(vinylidene fluoride) ultrafiltration membranes," *J. Memb. Sci.*, vol. 341, no. 1-2, pp. 214-224, 2009.
- [54] M. Khayet and T. Matsuura, "Preparation and characterization of polyvinylidene fluoride membranes for membrane distillation," *Ind. Eng. Chem. Res.*, vol. 40, no. 24, pp. 5710-5718, 2001.
- [55] M. Khayet, C. Y. Feng, K. C. Khulbe, and T. Matsuura, "Study on the effect of a non-solvent additive on the morphology and performance of ultrafiltration hollow-fiber membranes," *Desalination*, vol. 148, no. 1-3, pp. 321-327, 2002.
- [56] M. Khayet, "The effects of air gap length on the internal and external morphology of hollow fiber membranes," *Chem. Eng. Sci.*, vol. 58, pp. 3091-3104, 2003.
- [57] N. Awanis Hashim, Y. Liu, and K. Li, "Stability of PVDF hollow fibre membranes in sodium hydroxide aqueous solution," *Chem. Eng. Sci.*, vol. 66, no. 8, pp. 1565-1575, 2011.
- [58] L. Y. Wang, W. F. Yong, L. E. Yu, and T. S. Chung, "Design of high efficiency PVDF-PEG hollow fibers for air filtration of ultrafine particles," *J. Memb. Sci.*, vol. 535, pp. 342-349, 2017.
- [59] T. S. Chung, J. J. Qin, and J. Gu, "Effect of shear rate within the spinneret on morphology, separation performance and mechanical properties of ultrafiltration polyethersulfone hollow fiber membranes," *Chem. Eng. Sci.*, vol. 55, no. 6, pp. 1077-

- 1091, 2000.
- [60] J.-M. Berland and C. Juery, "Les procédés membranaires pour le traitement de l'eau," *Ministère de l'agriculture, de l'alimentation, de la pêche et des affaires rurales*, pp. 1–71, 2002.
- [61] M. Peter-Varbanets, C. Zurbrügg, C. Swartz, and W. Pronk, "Decentralized systems for potable water and the potential of membrane technology," *Water Res.*, vol. 43, no. 2, pp. 245–265, 2009.
- [62] G. E. Wetterau, M. M. Clark, and C. Anselme, "A dynamic model for predicting fouling effects during the ultrafiltration of a groundwater," *J. Memb. Sci.*, vol. 109, no. 2, pp. 185–204, 1996.
- [63] J. Xu, G. Ruan, X. Gao, X. Pan, B. Su, and C. Gao, "Pilot study of inside-out and outside-in hollow fiber UF modules as direct pretreatment of seawater at low temperature for reverse osmosis," *Desalination*, vol. 219, no. 1–3, pp. 179–189, 2008.
- [64] K. J. Howe, D. W. Hand, J. C. Crittenden, R. R. Trussel, and G. Tchobanoglous, "Principles of Water Treatment," John Wiley & Sons, 2012, ISBN: 978-0470405383.
- [65] P. Bacchin, "Principes de base des Technologies à Membranes," *Sciences et Technologies à Membranes*, 2005, hal- 00201760.
- [66] J. D. Nikolova and M. A. Islam, "Contribution of adsorbed layer resistance to the flux-decline in an ultrafiltration process," *J. Memb. Sci.*, vol. 146, no. 1, pp. 105–111, 1998.
- [67] W. Guo, H. H. Ngo, and J. Li, "A mini-review on membrane fouling," *Bioresour. Technol.*, vol. 122, pp. 27–34, 2012.
- [68] G. Collet, "Étude et modélisation du colmatage de membrane d'ultrafiltration par des suspensions de matières organiques et de particules minérales," PhD Dissertation, University of Poitiers, 2013.
- [69] K. Katsoufidou, S. G. Yiantsios, and A. J. Karabelas, "A study of ultrafiltration membrane fouling by humic acids and flux recovery by backwashing: Experiments and modeling," *J. Memb. Sci.*, vol. 266, no. 1–2, pp. 40–50, 2005.
- [70] S. H. Yoon, C. H. Lee, K. J. Kim, and A. G. Fane, "Effect of calcium ion on the fouling of nanofilter by humic acid in drinking water production," *Water Res.*, vol. 32, no. 7,

- pp. 2180–2186, 1998.
- [71] S. Hong and M. Elimelech, “Chemical and physical aspects of natural organic matter (NOM) fouling of nanofiltration membranes,” *J. Memb. Sci.*, vol. 132, no. 2, pp. 159–181, 1997.
- [72] D. Niriella and R. P. Carnahan, “Comparison study of zeta potential values of bentonite in salt solutions,” *J. Dispers. Sci. Technol.*, vol. 27, no. 1, pp. 123–131, 2006.
- [73] H. Choi, K. Zhang, D. D. Dionysiou, D. B. Oerther, and G. A. Sorial, “Influence of cross-flow velocity on membrane performance during filtration of biological suspension,” *J. Memb. Sci.*, vol. 248, no. 1–2, pp. 189–199, 2005.
- [74] L. Ren, S. Yu, J. Li, and L. Li, “Pilot study on the effects of operating parameters on membrane fouling during ultrafiltration of alkali/surfactant/polymer flooding wastewater: optimization and modeling,” *RSC Adv.*, vol. 9, no. 20, pp. 11111–11122, 2019.
- [75] B. J. Bellhouse, G. Costigan, K. Abhinava, and A. Merry, “The performance of helical screw-thread inserts in tubular membranes,” *Sep. Purif. Technol.*, vol. 22–23, pp. 89–113, 2001.
- [76] H. S. Abid, D. J. Johnson, R. Hashaikeh, and N. Hilal, “A review of efforts to reduce membrane fouling by control of feed spacer characteristics,” *Desalination*, vol. 420, pp. 384–402, 2017.
- [77] C. C. V. Chan, P. R. Bérubé, and E. R. Hall, “Shear profiles inside gas sparged submerged hollow fiber membrane modules,” *J. Memb. Sci.*, vol. 297, no. 1–2, pp. 104–120, 2007.
- [78] N. Ratkovich, C. C. V. Chan, P. R. Berube, and I. Nopens, “Experimental study and CFD modelling of a two-phase slug flow for an airlift tubular membrane,” *Chem. Eng. Sci.*, 2009.
- [79] S. Laborie, C. Cabassud, L. Durand-Bourlier, and J. M. Lainé, “Fouling control by air sparging inside hollow fibre membranes - effects on energy consumption,” *Desalination*, vol. 118, no. 1–3, pp. 189–196, 1998.
- [80] C. Cabassud, S. Laborie, L. Durand-Bourlier, and J. M. Lainé, “Air sparging in

- ultrafiltration hollow fibers: Relationship between flux enhancement, cake characteristics and hydrodynamic parameters," *J. Memb. Sci.*, vol. 181, no. 1, pp. 57–69, Jan. 2001.
- [81] Z. F. Cui, S. Chang, and A. G. Fane, "The use of gas bubbling to enhance membrane processes," *J. Memb. Sci.*, vol. 221, no. 1–2, pp. 1–35, 2003.
- [82] M. Aslam, A. Charfi, G. Lesage, M. Heran, and J. Kim, "Membrane bioreactors for wastewater treatment: A review of mechanical cleaning by scouring agents to control membrane fouling," *Chem. Eng. J.*, vol. 307, pp. 897–913, 2017.
- [83] Q. Yang, J. Chen, and F. Zhang, "Membrane fouling control in a submerged membrane bioreactor with porous, flexible suspended carriers," *Desalination*, vol. 189, pp. 292–302, 2006.
- [84] T. Kurita, K. Kimura, and Y. Watanabe, "Energy saving in the operation of submerged MBRs by the insertion of baffles and the introduction of granular materials," *Sep. Purif. Technol.*, vol. 141, pp. 207–213, 2015.
- [85] M. J. Van Der Waal, P. M. Van Der Velden, J. Koning, C. A. Smolders, and W. P. M. Van Swaay, "Use of fluidised beds as turbulence promoters in tubular membrane systems," *Desalination*, vol. 22, no. 1–3, pp. 465–483, 1977.
- [86] M. Y. Jaffrin, L. H. Ding, O. Akoum, and A. Brou, "A hydrodynamic comparison between rotating disk and vibratory dynamic filtration systems," *J. Memb. Sci.*, vol. 242, no. 1–2, pp. 155–167, 2004.
- [87] T. Li, A. W. K. Law, M. Cetin, and A. G. Fane, "Fouling control of submerged hollow fibre membranes by vibrations," *J. Memb. Sci.*, vol. 427, pp. 230–239, 2013.
- [88] J. A. Howell, "Sub-critical flux operation of microfiltration," *J. Memb. Sci.*, vol. 107, no. 1–2, pp. 165–171, 1995.
- [89] P. Bacchin, P. Aimar, and R. W. Field, "Critical and sustainable fluxes: Theory, experiments and applications," *J. Memb. Sci.*, vol. 281, no. 1–2, pp. 42–69, 2006.
- [90] Y. Bessiere, N. Abidine, and P. Bacchin, "Low fouling conditions in dead-end filtration: Evidence for a critical filtered volume and interpretation using critical osmotic pressure," *J. Memb. Sci.*, vol. 264, no. 1–2, pp. 37–47, 2005.

- [91] B. Espinasse, P. Bacchin, and P. Aimar, "On an experimental method to measure critical flux in ultrafiltration," *Desalination*, vol. 146, no. 1–3, pp. 91–96, 2002.
- [92] A. Idris and L. K. Yet, "The effect of different molecular weight PEG additives on cellulose acetate asymmetric dialysis membrane performance," *J. Memb. Sci.*, vol. 280, no. 1–2, pp. 920–927, 2006.
- [93] J. Zhang, Z. Xu, M. Shan, B. Zhou, Y. Li, B. Li, J. Niu, and X. Qian, "Synergetic effects of oxidized carbon nanotubes and graphene oxide on fouling control and anti-fouling mechanism of polyvinylidene fluoride ultrafiltration membranes," *J. Memb. Sci.*, vol. 448, pp. 81–92, 2013.
- [94] S. Arefi-Oskoui, V. Vatanpour, and A. Khataee, "Development of a novel high-flux PVDF-based ultrafiltration membrane by embedding Mg-Al nanolayered double hydroxide," *J. Ind. Eng. Chem.*, vol. 41, pp. 23–32, 2016.
- [95] J. Shen, Q. Zhang, Q. Yin, Z. Cui, W. Li, and W. Xing, "Fabrication and characterization of amphiphilic PVDF copolymer ultrafiltration membrane with high anti-fouling property," *J. Memb. Sci.*, vol. 521, pp. 95–103, 2017.
- [96] N. A. Hashim, F. Liu, and K. Li, "A simplified method for preparation of hydrophilic PVDF membranes from an amphiphilic graft copolymer," *J. Memb. Sci.*, vol. 345, no. 1–2, pp. 134–141, 2009.
- [97] I. Sadeghi, A. Aroujalian, A. Raisi, B. Dabir, and M. Fathizadeh, "Surface modification of polyethersulfone ultrafiltration membranes by corona air plasma for separation of oil/water emulsions," *J. Memb. Sci.*, vol. 430, pp. 24–36, 2013.
- [98] J.-C. Remigy, "Membranes fibres creuses innovantes: conception, élaboration, applications," Habilitation à Diriger les Recherches, University of Paul Sabatier Toulouse, 2012.
- [99] M. Taniguchi, J. E. Kilduff, and G. Belfort, "Low fouling synthetic membranes by UV-assisted graft polymerization: Monomer selection to mitigate fouling by natural organic matter," *J. Memb. Sci.*, vol. 222, no. 1–2, pp. 59–70, 2003.
- [100] R. Ma, Y. L. Ji, X. D. Weng, Q. F. An, and C. J. Gao, "High-flux and fouling-resistant reverse osmosis membrane prepared with incorporating zwitterionic amine monomers via interfacial polymerization," *Desalination*, vol. 381, pp. 100–110,

- 2016.
- [101] M. Abedi, M. P. Chenar, and M. Sadeghi, "Surface modification of PAN hollow fiber membrane by chemical reaction," *Fibers Polym.*, vol. 16, no. 4, pp. 788–793, 2015.
- [102] X. Shi, G. Tal, N. P. Hankins, and V. Gitis, "Fouling and cleaning of ultrafiltration membranes: A review," *J. Water Process Eng.*, vol. 1, pp. 121–138, 2014.
- [103] P. J. Smith, S. Vigneswaran, H. H. Ngo, R. Ben-Aim, and H. Nguyen, "A new approach to backwash initiation in membrane systems," *J. Memb. Sci.*, vol. 278, no. 1–2, pp. 381–389, 2006.
- [104] R. Villarroel, S. Delgado, E. González, and M. Morales, "Physical cleaning initiation controlled by transmembrane pressure set-point in a submerged membrane bioreactor," *Sep. Purif. Technol.*, vol. 104, pp. 55–63, 2013.
- [105] E. H. Bouhabila, R. Ben Aïm, and H. Buisson, "Fouling characterisation in membrane bioreactors," *Sep. Purif. Technol.*, vol. 22–23, pp. 123–132, 2001.
- [106] H. Huang, N. Lee, T. Young, A. Gary, J. C. Lozier, and J. G. Jacangelo, "Natural organic matter fouling of low-pressure, hollow-fiber membranes: Effects of NOM source and hydrodynamic conditions," *Water Res.*, vol. 41, no. 17, pp. 3823–3832, 2007.
- [107] P. J. Remize, C. Guigui, and C. Cabassud, "Evaluation of backwash efficiency, definition of remaining fouling and characterisation of its contribution in irreversible fouling: Case of drinking water production by air-assisted ultrafiltration," *J. Memb. Sci.*, vol. 355, no. 1–2, pp. 104–111, 2010.
- [108] S. Li, S. G. J. Heijman, J. Q. J. C. Verberk, P. Le Clech, J. Lu, A. J. B. Kemperman, G. L. Amy, and J. C. van Dijk, "Fouling control mechanisms of demineralized water backwash: Reduction of charge screening and calcium bridging effects," *Water Res.*, vol. 45, no. 19, pp. 6289–6300, 2011.
- [109] S. Li, S. G. J. Heijman, J. Q. J. C. Verberk, A. R. D. Verliefde, A. J. B. Kemperman, J. C. Van Dijk, and G. Amy, "Impact of backwash water composition on ultrafiltration fouling control," vol. 344, pp. 17–25, 2009.
- [110] H. Chang, F. Qu, B. Liu, H. Yu, K. Li, S. Shao, G. Li, and H. Liang, "Hydraulic irreversibility of ultrafiltration membrane fouling by humic acid: Effects of

- membrane properties and backwash water composition," *J. Memb. Sci.*, vol. 493, pp. 723–733, 2015.
- [111] A. J. Abrahamse, C. Lipreau, S. Li, and S. G. J. Heijman, "Removal of divalent cations reduces fouling of ultrafiltration membranes," vol. 323, pp. 153–158, 2008.
- [112] P. Le-Clech, V. Chen, and T. A. G. Fane, "Fouling in membrane bioreactors used in wastewater treatment," *J. Memb. Sci.*, vol. 284, no. 1–2, pp. 17–53, 2006.
- [113] C. Psoch and S. Schiewer, "Critical flux aspect of air sparging and backflushing on membrane bioreactors," *Desalination*, vol. 175, pp. 61–71, 2005.
- [114] Z. Cui and T. Taha, "Enhancement of ultrafiltration using gas sparging: A comparison of different membrane modules," *J. Chem. Technol. Biotechnol.*, vol. 78, no. 2–3, pp. 249–253, 2003.
- [115] C. Guigui, M. Mougnot, and C. Cabassud, "Air sparging backwash in ultrafiltration hollow fibres for drinking water production," *Water Sci. Technol. Water Supply*, vol. 3, no. 5–6, pp. 415–422, 2003.
- [116] H. Nagaoka, A. Tanaka, and Y. Toriizuka, "Measurement of effective shear stress working on flat-sheet membrane by air-scrabbling," *Water Sci. Technol. Water Supply*, vol. 3, no. 5–6, pp. 423–428, 2003.
- [117] C. Serra, L. Durand-Bourlier, M. J. Clifton, P. Moulin, J. C. Rouch, and P. Aptel, "Use of air sparging to improve backwash efficiency in hollow-fiber modules," *J. Memb. Sci.*, vol. 161, no. 1–2, pp. 95–113, 1999.
- [118] Y. Bessiere, C. Guigui, P. J. Remize, and C. Cabassud, "Coupling air-assisted backwash and rinsing steps: a new way to improve ultrafiltration process operation for inside-out hollow fibre modules," *Desalination*, vol. 240, no. 1–3, pp. 71–77, 2009.
- [119] I. Ruigómez, E. González, S. Guerra, L. E. Rodríguez-Gómez, and L. Vera, "Evaluation of a novel physical cleaning strategy based on HF membrane rotation during the backwashing/relaxation phases for anaerobic submerged MBR," *J. Memb. Sci.*, vol. 526, pp. 181–190, 2017.
- [120] N. P. De Souza and O. D. Basu, "Comparative analysis of physical cleaning operations for fouling control of hollow fiber membranes in drinking water treatment," *J.*

- Memb. Sci.*, vol. 436, pp. 28–35, 2013.
- [121] Z. Wang, J. Ma, C. Y. Tang, K. Kimura, Q. Wang, and X. Han, “Membrane cleaning in membrane bioreactors: A review,” *J. Memb. Sci.*, vol. 468, pp. 276–307, 2014.
- [122] J. P. Chen, S. L. Kim, and Y. P. Ting, “Optimization of membrane physical and chemical cleaning by a statistically designed approach,” *J. Memb. Sci.*, vol. 219, no. 1–2, pp. 27–45, 2003.
- [123] H. Liang, W. Gong, J. Chen, and G. Li, “Cleaning of fouled ultrafiltration (UF) membrane by algae during reservoir water treatment,” *Desalination*, vol. 220, no. 1–3, pp. 267–272, 2008.
- [124] C. C. Tarazaga, M. E. Campderrós, and A. P. Padilla, “Physical cleaning by means of electric field in the ultrafiltration of a biological solution,” *J. Memb. Sci.*, vol. 278, no. 1–2, pp. 219–224, 2006.
- [125] W. R. Bowen, R. S. Kingdon, and H. A. M. Sabuni, “Electrically enhanced separation processes: the basis of in situ intermittent electrolytic membrane cleaning (IEMC) and in situ electrolytic membrane restoration (IEMR),” *J. Memb. Sci.*, vol. 40, no. 2, pp. 219–229, 1989.
- [126] H. M. Huotari, G. Trägårdh, and I. H. Huisman, “Crossflow membrane filtration enhanced by an external DC electric field: A review,” *Chem. Eng. Res. Des.*, vol. 77, no. 5, pp. 461–468, 1999.
- [127] X. Li, J. Yu, and A. G. A. Nnanna, “Fouling mitigation for hollow-fiber UF membrane by sonication,” *Desalination*, vol. 281, no. 1, pp. 23–29, 2011.
- [128] I. Masselin, X. Chasseray, L. Durand-Bourlier, J. M. Lainé, P. Y. Syzaret, and D. Lemordant, “Effect of sonication on polymeric membranes,” *J. Memb. Sci.*, vol. 181, no. 2, pp. 213–220, 2001.
- [129] M. Kallioinen and M. Mänttari, “Influence of ultrasonic treatment on various membrane materials: A review,” *Sep. Sci. Technol.*, vol. 46, no. 9, pp. 1388–1395, 2011.
- [130] D. Jun, Y. Kim, S. Hafeznezami, K. Yoo, E. M. V. Hoek, and J. Kim, “Biologically induced mineralization in anaerobic membrane bioreactors: Assessment of membrane

- scaling mechanisms in a long-term pilot study," *J. Memb. Sci.*, vol. 543, pp. 342–350, 2017.
- [131] P. Lipp, M. Witte, and C. Baldaui, "Treatment of reservoir water with a backwashable MF / UF spiral wound membrane," vol. 179, pp. 83–94, 2005.
- [132] J. Decarolis, S. Hong, and J. Taylor, "Fouling behavior of a pilot scale inside-out hollow fiber UF membrane during dead-end filtration of tertiary wastewater," *J. Memb. Sci.*, vol. 191, no. 1–2, pp. 165–178, 2001.
- [133] E. Arkhangelsky, D. Kuzmenko, N. V. Gitis, M. Vinogradov, S. Kuiry, and V. Gitis, "Hypochlorite cleaning causes degradation of polymer membranes," *Tribol. Lett.*, vol. 28, no. 2, pp. 109–116, 2007.
- [134] S. Rouaix, C. Causserand, and P. Aimar, "Experimental study of the effects of hypochlorite on polysulfone membrane properties," *J. Memb. Sci.*, vol. 277, no. 1–2, pp. 137–147, 2006.
- [135] E. Arkhangelsky, D. Kuzmenko, and V. Gitis, "Impact of chemical cleaning on properties and functioning of polyethersulfone membranes," *J. Memb. Sci.*, vol. 305, no. 1–2, pp. 176–184, 2007.
- [136] J. Ravereau, A. Fabre, A. Brehant, R. Bonnard, C. Sollogoub, and J. Verdu, "Ageing of polyvinylidene fluoride hollow fiber membranes in sodium hypochlorite solutions," *J. Memb. Sci.*, vol. 505, pp. 174–184, 2016.
- [137] S. Krause, B. Zimmermann, U. Meyer-Blumenroth, W. Lamparter, B. Siembida, and P. Cornel, "Enhanced membrane bioreactor process without chemical cleaning," *Water Sci. Technol.*, vol. 61, no. 10, pp. 2575–2580, 2010.
- [138] B. Chu, B. S. Hsiao, and Y. Su, "Elastic Membrane-Based Membrane Bioreactor with High-Efficiency for Fouling Control," Patent US2017/0157565, 2017.
- [139] T. W. Beck, H. J. J. Drummond, M. B. Lee, C. V. Kopp, and W. T. Johnson, "Cleaning of hollow fibre membranes," Patent 6,159,373, 2000.
- [140] D. L. Ford, E. W. Anderson, and C. V. Kopp, "Cooling hollow fibre cross-flow separators," Patent 4,816,160, 1989.
- [141] E. Akhondi, F. Zamani, A. W. K. Law, W. B. Krantz, A. G. Fane, and J. W. Chew,

- “Influence of backwashing on the pore size of hollow fiber ultrafiltration membranes,” *J. Memb. Sci.*, vol. 521, pp. 33–42, 2017.
- [142] E. Akhondi, F. Wicaksana, W. B. Krantz, and A. G. Fane, “Evaporimetry determination of pore-size distribution and pore fouling of hollow fiber membranes,” *J. Memb. Sci.*, vol. 470, pp. 334–345, 2014.
- [143] P. Shivapooja, Q. Wang, B. Orihuela, D. Rittschof, G. P. López, and X. Zhao, “Bioinspired surfaces with dynamic topography for active control of biofouling,” *Adv. Mater.*, vol. 25, no. 10, pp. 1430–1434, 2013.
- [144] P. Shivapooja, Q. Wang, L. M. Szott, B. Orihuela, D. Rittschof, X. Zhao, and G. P. López, “Dynamic surface deformation of silicone elastomers for management of marine biofouling: laboratory and field studies using pneumatic actuation,” *Biofouling*, vol. 31, no. 3, pp. 265–274, 2015.
- [145] G. Limbert, R. Bryan, R. Cotton, P. Young, L. Hall-Stoodley, S. Kathju, and P. Stoodley, “On the mechanics of bacterial biofilms on non-dissolvable surgical sutures: A laser scanning confocal microscopy-based finite element study,” *Acta Biomater.*, vol. 9, no. 5, pp. 6641–6652, 2013.
- [146] V. Levering, Q. Wang, P. Shivapooja, X. Zhao, and G. P. López, “Soft robotic concepts in catheter design: An on-demand fouling-release urinary catheter,” *Adv. Healthc. Mater.*, vol. 3, no. 10, pp. 1588–1596, 2014.
- [147] M. K. Chaudhury, J. A. Finlay, Y. C. Jun, M. E. Callow, and J. A. Callow, “The influence of elastic modulus and thickness on the release of the soft-fouling green alga *Ulva linza* (syn. *Enteromorpha linza*) from poly(dimethylsiloxane) (PDMS) model networks,” *Biofouling*, vol. 21, no. 1, pp. 41–48, 2005.
- [148] M. G. Stafford-Smith, “Sediment-rejection mechanisms of 42 species of Australian scleractinian corals,” *Mar. Biol.*, vol. 243, pp. 229–243, 1993.
- [149] N. Porcelli and S. Judd, “Effect of cleaning protocol on membrane permeability recovery: A sensitivity analysis,” *J. Am. Water Works Assoc.*, vol. 102, no. 12, pp. 78–86, 2010.
- [150] R. Bogati, C. Goodwin, K. Marshall, K. T. Leung, and B. Q. Liao, “Optimization of Chemical Cleaning for Improvement of Membrane Performance and Fouling

- Control in Drinking Water Treatment," *Sep. Sci. Technol.*, vol. 50, no. 12, pp. 1835–1845, 2015.
- [151] J. Li, S. He, S. Xia, C. Qiu, Y. Zhang, and J. Xuan, "The Membrane Fouling Monitored by Scanning Electron Microscopy (SEM) in a Submerged Membrane Bioreactor," vol. 4, no. 3, pp. 159–166, 2014.
- [152] Y. H. Lin, K. L. Tung, S. H. Wang, Q. Zhou, and K. K. Shung, "Distribution and deposition of organic fouling on the microfiltration membrane evaluated by high-frequency ultrasound," *J. Memb. Sci.*, vol. 433, pp. 100–111, 2013.
- [153] M. Rabiller-Baudry, L. Bégoïn, D. Delaunay, L. Paugam, and B. Chaufer, "A dual approach of membrane cleaning based on physico-chemistry and hydrodynamics. Application to PES membrane of dairy industry," *Chem. Eng. Process.*, vol. 47, no. 3, pp. 267–275, 2008.
- [154] Y. Marselina, P. Le-Clech, R. Stuetz, and V. Chen, "Detailed characterisation of fouling deposition and removal on a hollow fibre membrane by direct observation technique," *Desalination*, vol. 231, no. 1–3, pp. 3–11, 2008.
- [155] Y. Marselina, L. Lifa, P. Le-Clech, R. M. Stuetz, and V. Chen, "Characterisation of membrane fouling deposition and removal by direct observation technique," *J. Memb. Sci.*, vol. 341, no. 1–2, pp. 163–171, 2009.
- [156] S. Lorenzen, Y. Ye, V. Chen, and M. L. Christensen, "Direct observation of fouling phenomena during cross-flow filtration: Influence of particle surface charge," *J. Memb. Sci.*, vol. 510, pp. 546–558, 2016.
- [157] S. Chang and A. G. Fane, "Characteristics of microfiltration of suspensions with inter-fiber two-phase flow," *J. Chem. Technol. Biotechnol.*, vol. 75, no. 7, pp. 533–540, 2000.
- [158] J. Li, D. K. Hallbauer, and R. D. Sanderson, "Direct monitoring of membrane fouling and cleaning during ultrafiltration using a non-invasive ultrasonic technique," *J. Memb. Sci.*, vol. 215, no. 1–2, pp. 33–52, 2003.
- [159] K. L. Tung, S. Wang, W. M. Lu, and C. H. Pan, "In situ measurement of cake thickness distribution by a photointerrupt sensor," *J. Memb. Sci.*, vol. 190, no. 1, pp. 57–67, 2001.

- [160] P. Z. Çulfaz, S. Buetehorn, L. Utu, M. Kueppers, B. Bluemich, T. Melin, M. Wessling, and R. G. H. Lammertink, "Fouling behavior of microstructured hollow fiber membranes in dead-end filtrations: Critical flux determination and NMR imaging of particle deposition," *Langmuir*, vol. 27, no. 5, pp. 1643–1652, 2011.
- [161] S. Buetehorn, L. Utu, M. Küppers, B. Blümich, T. Wintgens, M. Wessling, and T. Melin, "NMR imaging of local cumulative permeate flux and local cake growth in submerged microfiltration processes," *J. Memb. Sci.*, vol. 371, no. 1–2, pp. 52–64, 2011.
- [162] M. Hamachi and M. Mietton-Peuchot, "Experimental investigations of cake characteristics in crossflow microfiltration," *Chem. Eng. Sci.*, vol. 54, no. 18, pp. 4023–4030, 1999.
- [163] J. Mendret, C. Guigui, P. Schmitz, C. Cabassud, and P. Duru, "An optical method for in situ characterization of fouling during filtration," *AIChE*, vol. 53, no. 9, pp. 2265–2274, 2007.
- [164] L. M. F. dos Santos and A. G. Livingston, "Membrane-attached biofilms for VOC wastewater treatment I: Novel in situ biofilm thickness measurement technique," *Biotechnol. Bioeng.*, vol. 47, no. 1, pp. 82–89, 1995.
- [165] Y. Ye, V. Chen, and P. Le-Clech, "Evolution of fouling deposition and removal on hollow fibre membrane during filtration with periodical backwash," *Desalination*, vol. 283, pp. 198–205, 2011.
- [166] H. Li, A. G. Fane, H. G. L. Coster, and S. Vigneswaran, "Direct observation of particle deposition on the membrane surface during crossflow microfiltration," *J. Memb. Sci.*, vol. 149, no. 1, pp. 83–97, 1998.
- [167] S. R. Santiwong, J. Guan, and T. D. Waite, "Effect of ionic strength and pH on hydraulic properties and structure of accumulating solid assemblages during microfiltration of montmorillonite suspensions," *J. Colloid Interface Sci.*, vol. 317, no. 1, pp. 214–227, 2008.
- [168] Y. Bessiere, "Filtration Frontale sur membrane : mise en évidence du volume filtre critique pour l'anticipation et le contrôle du colmatage," PhD Dissertation, University of Toulouse Paul Sabatier, 2005.

- [169] A. Rushton, A. S. Ward, and R. G. Holdich, "Solid-Liquid Filtration and Separation Technology," Wiley-VCH, 1996, ISBN: 3-527-28613-6.
- [170] E. Elele, Y. Shen, J. Tang, Q. Lei, B. Khusid, G. Tkacik, and C. Carbrello, "Mechanical properties of polymeric microfiltration membranes," *J. Memb. Sci.*, vol. 591, p. 117351, 2019.
- [171] T. H. Young, L. P. Cheng, D. J. Lin, L. Fane, and W. Y. Chuang, "Mechanisms of PVDF membrane formation by immersion-precipitation in soft (1-octanol) and harsh (water) nonsolvents," *Polymer*, vol. 40, no. 19, pp. 5315–5323, 1999.
- [172] A. Idris, A. F. Ismail, M. Noorhayati, and S. J. Shilton, "Measurement of rheologically induced molecular orientation using attenuated total reflection infrared dichroism in reverse osmosis hollow fiber cellulose acetate membranes and influence on separation performance," *J. Memb. Sci.*, vol. 213, no. 1–2, pp. 45–54, 2003.
- [173] P. Aptel, N. Abidine, F. Ivaldi, and J. P. Lafaille, "Polysulfone hollow-fibers-Effect of spinning conditions on ultrafiltration properties," *J. Memb. Sci.*, vol. 22, pp. 199–215, 1985.
- [174] S. J. Shilton, "Flow profile induced in spinneret during hollow fiber membrane spinning," *J. Appl. Polym. Sci.*, vol. 65, no. 7, pp. 1359–1362, 1997.
- [175] J. Qin and T. Chung, "Effect of dope flow rate on hollow fiber ultrafiltration," *J. Memb. Sci.*, vol. 157, pp. 35–51, 1999.
- [176] D. Li, T.-S. Chung, J. Ren, and R. Wang, "Thickness Dependence of Macrovoid Evolution in Wet Phase-Inversion Asymmetric Membranes," *Ind. Eng. Chem. Res.*, vol. 43, no. 6, pp. 1553–1556, 2004.
- [177] S. Iio, A. Yonezu, H. Yamamura, and X. Chen, "Deformation modeling of polyvinylidenedifluoride (PVDF) symmetrical microfiltration hollow-fiber (HF) membrane," *J. Memb. Sci.*, vol. 497, pp. 421–429, 2016.
- [178] A. Yonezu, S. Iio, T. Itonaga, H. Yamamura, and X. Chen, "Tensile deformation of polytetrafluoroethylene hollow fiber membranes used for water purification," *Water Sci. Technol.*, vol. 70, no. 7, pp. 1244–1250, 2014.
- [179] D. B. Mosqueda-Jimenez and R. M. Narbaitz, "Membrane Fouling Test : Apparatus

- Evaluation Membrane Fouling Test : Apparatus Evaluation,” vol. 130, no. 1, 2015.
- [180] D. B. Mosqueda-Jimenez, R. M. Narbaitz, T. Matsuura, G. Chowdhury, G. Pleizier, and J. P. Santerre, “Influence of processing conditions on the properties of ultrafiltration membranes,” *J. Memb. Sci.*, vol. 231, no. 1–2, pp. 209–224, 2004.
- [181] S. Stade, M. Kallioinen, A. Mikkola, T. Tuuva, and M. Mänttari, “Reversible and irreversible compaction of ultrafiltration membranes,” *Sep. Purif. Technol.*, vol. 118, pp. 127–134, 2013.
- [182] J. Sierke and A. V. Ellis, “Cross-linking of dehydrofluorinated PVDF membranes with thiol modified polyhedral oligomeric silsesquioxane (POSS) and pure water flux analysis,” *J. Memb. Sci.*, vol. 581, pp. 362–372, 2019.
- [183] K. M. Persson, V. Gekas, and G. Trägårdh, “Study of membrane compaction and its influence on ultrafiltration water permeability,” *J. Memb. Sci.*, vol. 100, no. 2, pp. 155–162, 1995.
- [184] H.-J. Muller and D. Mulette, “Membrane Polymer Compositions,” Patent US 2004/0191894 A1, 2004.
- [185] S. Timoshenko, “Strength of Materials Part II Advanced Theory and Problems,” D. Van Nostrand Company, 1956, ISBN: 978-0898746211.
- [186] S. Silvano, “Mathematical model of Lamé Problem for Simplified Elastic Theory applied to Controlled-Clearance Pressure Balances,” *The Simplified Elastic Theory applied to controlled-clearance pressure balances*, pp. 1–20, 2010.
- [187] Q. Saeed Masikh, M. Tariq, and P. Kumar Sinha, “Analysis of a thin and thick walled pressure vessel for different materials,” *Int. J. Mech. Eng. Technol.*, vol. 5, no. 10, pp. 9–19, 2014.
- [188] S. N. J. Dargahi, “A novel tactile sensor for use in medical imaging,” in *Advances in Dynamics, Instrumentation and Control*, 2004, pp. 433–442.
- [189] B. Pellegrin, F. Mezzari, Y. Hanafi, A. Szymczyk, J. C. Remigy, and C. Causserand, “Filtration performance and pore size distribution of hypochlorite aged PES/PVP ultrafiltration membranes,” *J. Memb. Sci.*, vol. 474, pp. 175–186, 2015.
- [190] P. Bacchin, “Formation et résistance au transfert d’un dépôt de colloïdes sur une

- membrane d'ultrafiltration," PhD Dissertation, University of Toulouse Paul Sabatier, 1994.
- [191] N. Malikova, "Dynamics of water and ions in montmorillonite clays by microscopic simulation and quasi-elastic neutron scattering," PhD Dissertation, University of Pierre et Marie Curie - Paris VI, 2005.
- [192] J. S. Gaffney, N. A. Marley, and S. B. Clark, "Humic and Fulvic Acids and Organic Colloidal Materials in the Environment," *ACS Symp. Ser.*, vol. 651, 1996.
- [193] F. J. Stevenson, "Humus Chemistry - Genesis, composition, reactions," John Wiley & Sons, 1982, ISBN: 978-0471594741.
- [194] C. Y. Tang, T. H. Chong, and A. G. Fane, "Colloidal interactions and fouling of NF and RO membranes: A review," *Adv. Colloid Interface Sci.*, vol. 164, no. 1–2, pp. 126–143, 2011.
- [195] J. P. Hsu and B. T. Liu, "Critical coagulation concentration of a colloidal suspension at high particle concentrations," *J. Phys. Chem. B*, vol. 102, no. 2, pp. 334–337, 1998.
- [196] W. Yuan, A. Kocic, and A. L. Zydney, "Analysis of humic acid fouling during microfiltration using a pore blockage-cake filtration model," *J. Memb. Sci.*, vol. 198, no. 1, pp. 51–62, 2002.
- [197] Vincent Lelievre, "Rhéologie et filtration de dispersions aqueuses de nanoparticules d'hectorite en relation avec la structuration des dépôts," PhD Dissertation, University of Grenoble INPG, 2005.
- [198] R. M. Pashley and J. N. Israelachvili, "DLVO and Hydration Forces between Mica Surfaces in γ , Ca^{2+} , Sr^{2+} , and Ba^{2+} Chloride Solutions," *J. Colloid Interface Sci.*, vol. 97, no. 2, p. 446, 1984.
- [199] M. E. Parolo, M. J. Avena, G. R. Pettinari, and M. T. Baschini, "Influence of Ca^{2+} on tetracycline adsorption on montmorillonite," *J. Colloid Interface Sci.*, vol. 368, no. 1, pp. 420–426, 2012.
- [200] A. Majzik and E. Tombácz, "Interaction between humic acid and montmorillonite in the presence of calcium ions I. Interfacial and aqueous phase equilibria: Adsorption and complexation," *Org. Geochem.*, vol. 38, no. 8, pp. 1319–1329, 2007.

- [201] C. Cabassud, S. Laborie, L. Durand-Bourlier, and J. M. Lainé, "Air sparging in ultrafiltration hollow fibers: Relationship between flux enhancement, cake characteristics and hydrodynamic parameters," *J. Memb. Sci.*, vol. 181, no. 1, pp. 57–69, 2001.
- [202] B. G. Fulton, J. Redwood, M. Tourais, and P. R. Bérubé, "Distribution of surface shear forces and bubble characteristics in full-scale gas sparged submerged hollow fiber membrane modules," *Desalination*, vol. 281, no. 1, pp. 128–141, 2011.
- [203] R. Oliveira, "Understanding adhesion: A means for preventing fouling," *Exp. Therm. Fluid Sci.*, vol. 14, no. 4, pp. 316–322, 1997.
- [204] X. Wang, M. Zhou, X. Meng, L. Wang, and D. Huang, "Effect of protein on PVDF ultrafiltration membrane fouling behavior under different pH conditions: interface adhesion force and XDLVO theory analysis," *Front. Environ. Sci. Eng.*, vol. 10, no. 4, 2016.
- [205] C. C. van Oss, "Acid-base interfacial interactions in aqueous media," *Colloids Surfaces A Physicochem. Eng. Asp.*, vol. 78, pp. 1–49, 1993.
- [206] R. F. Giese, C. J. Van Oss, J. Norris, and P. M. Costanzo, "Surface energies of some smectite clay minerals," *Sci. Geol. - Mem.*, vol. 86, pp. 33–41, 1990.
- [207] X. Meng, W. Tang, L. Wang, X. Wang, D. Huang, H. Chen, and N. Zhang, "Mechanism analysis of membrane fouling behavior by humic acid using atomic force microscopy: Effect of solution pH and hydrophilicity of PVDF ultrafiltration membrane interface," *J. Memb. Sci.*, vol. 487, pp. 180–188, 2015.
- [208] H. Sun, B. Tang, and P. Wu, "Hydrophilic hollow zeolitic imidazolate framework-8 modified ultrafiltration membranes with significantly enhanced water separation properties," *J. Memb. Sci.*, vol. 551, pp. 283–293, 2018.
- [209] Z. Xu, J. Liao, H. Tang, J. E. Efome, and N. Li, "Preparation and antifouling property improvement of Tröger's base polymer ultrafiltration membrane," *J. Memb. Sci.*, vol. 561, pp. 59–68, 2018.

Abstract

Kynar® PVDF ultrafiltration hollow fiber membranes with various properties (permeability and mechanical properties) were selected for the study of fouling removal mechanisms in the case of model suspension filtrations (bentonite and humic acid cake). The aim of this project is to improve backwash efficiency by optimizing materials and operating conditions for an energy-efficient backwash process.

The deformation of the external surface of the hollow fiber during pressure operations was measured under camera. The deformation, which can reach 15% during backwash, was numerically calculated using a mechanical deformation model of a thick-walled cylinder under pressure.

The experimental study of the bentonite cake removal percentage, as a function of backwash pressure and the different membranes or feed suspension, showed the existence of a critical backwash flux from which the backwash reached its maximal efficiency. However, detachment of humic acid cake, which is more adherent and causes irreversible fouling, is not affected by the backwash flux but seems to be affected by the strong deformation of external surface of the hollow-fiber (>10%). Mechanisms of cake removal during backwash are therefore linked to the mechanical stresses (normal and shear stress) acting at the cake-membrane interface.

Résumé

Des membranes fibres creuses d'ultrafiltration Kynar® PVDF possédant diverses caractéristiques (perméabilité et propriétés mécaniques) ont été sélectionnées pour étudier les mécanismes de décolmatage dans le cas de filtration de suspensions modèles (dépôt de bentonite ou d'acide humique). L'objectif de ce travail est d'améliorer l'efficacité du rétrolavage en optimisant les matériaux et les conditions opératoires dans le but de réduire le coût énergétique de cette opération.

Des mesures expérimentales sous caméra ont permis d'étudier la déformation de la surface externe des fibres creuses lors des opérations sous pression. Ces déformations qui peuvent atteindre 15% lors des étapes de rétrolavage ont été modélisées par la déformation mécanique d'un tube cylindrique à paroi épaisse sous pression.

L'étude expérimentale du taux d'élimination de dépôt de bentonite, fonction de la pression de rétrolavage et des différentes membranes ou suspension filtrée, a permis de montrer l'existence d'un flux critique de rétrolavage pour lequel l'efficacité maximum est atteinte. En revanche, le détachement des dépôts d'acide humique qui sont plus adhérent et responsable d'un colmatage irréversible, n'est pas impacté par le flux de rétrolavage mais semble être affecté par la forte déformation (>10%) de surface externe de la fibre. Les mécanismes de décolmatage des dépôts lors du rétrolavage sont donc liés aux contraintes mécaniques (contrainte normale et de cisaillement) s'exerçant à l'interface dépôt-membrane.